Inaugural dissertation
for
obtaining the doctoral degree
of the
Combined Faculty of Mathematics, Engineering and Natural Sciences
of the
Ruprecht - Karls - University
Heidelberg

Presented by
M.Sc. Tiago Daniel Gomes Nunes

born in: Canhestros, Ferreira do Alentejo, Portugal

Oral examination: 07/07/2022

Linking stomatal function and anatomy for efficient gas exchange in the model grass *Brachypodium distachyon*

Referees:

Prof. Dr. Karin Schumacher

Prof. Dr. Michael Raissig

Acknowledgements

First, I would like to thank my supervisor Michael, since without him I would have not written these pages. Thank you for giving me the opportunity, for your mentoring, for supporting these projects and for pushing me to become a better scientist. It was not always an easy journey, but I am very grateful with all I learnt from you and very proud of the science we created. I hope this experience was as enriching to you as it was for me.

I would like to thank Heike, for your support, for your help in many stressful moments and for creating a safe and inclusive environment. Thanks for listening to my endless stories about Eurovision and for joining me on watching it, even if virtually during the pandemic.

I would like to thank my lab mate Dan Zhang. Without you this experience would have not followed these lines. Together since day one, we were not just lab mates but the best friends and partners in crime. Thank you for your unconditional support and for being the joy of my days. You were my safe harbour, and I will never forget all the moments we lived together.

I would also like to thank my TAC members for your feedback, advice, and support throughout my PhD, and to thank everyone in the lab and at COS for creating a safe and supportive working environment.

I would like to thank Rashmi, for your friendship and unceasing support. Thank you for the endless serious and silly conversations.

I would like to thank Magda, Lea, and Xin, for your support, kindness, and friendship. This experience would have not been the same without you.

A big thank you to Paula, Upendo and Zaida for your advice, patience and all the coffee breaks that made the hard days much easier.

A huge thank you to my friend Luz, for being present and for bringing light to my life. I am so grateful for your unconditional support. You are one of my biggest inspirations and someone that understands me the most without judgements. I hope we continue to share our next adventures together. Gracias!

Also, a huge thank you to the best Rita, who has been by my side since day one when we started our bachelor studies in Portugal. Thanks for the happiness, for your patience and for being always up for any crazy plan. I hope that in the future we can again be closer to each other. Obrigado!

I will also always be grateful to my former mentors Bea, Nacho, Luis, and Monica as my academic journey in the world of plant sciences started with them. A big thank you for your trust, unconditional support, and kindness.

Thank you, Sara, Charlie, Mathias, Melissa and Nia for your friendship, for listening to my stories and follow my journey even if at a distance.

Finally, my eternal and colossal thank you to my mum and dad, for all the sacrifices so I could follow my dreams, and for all the unconditional love. Thank you for believing in me, for always waiting for me with open arms and for giving me strength. Eternal thanks to my family for caring and supporting me unconditionally.

Abstract

Stomata are cellular pores on the leaf epidermis that regulate CO_2 uptake for photosynthesis and limit water vapour loss. Stomata can open and close in response to different environmental triggers and the speed of stomatal movements defines how efficiently plants exchange gas and save water in fluctuating environments. Therefore, stomatal speed and water use efficiency (ratio between assimilated carbon and lost water through stomata) are important traits for plant productivity and tolerance to environmental stresses.

Grasses such as wheat, and rice and the model species *Brachypodium distachyon* are the plant group displaying the fastest stomatal movements, a trait that is associated with their unique stomatal morphology. Grass stomata are formed by two dumbbell-shaped guard cells (GCs) flanked by two subsidiary cells (SCs). This morphology seems to result in optimal mechanics that facilitate the stomatal movements and the SCs appear to contribute with quick exchange of ions and water required for turgor-driven stomatal opening and closure. Still, the molecular mechanisms behind the efficient form and function of grass stomata remain highly unexplored. A comparison of the leaf transcriptome between wildtype *B. distachyon* (Bd21-3) and *bdmute* mutant plants, which lack SCs and show defective stomatal function, allowed identifying candidate genes potentially associated with grass stomata form and function. Therefore, I established a leaf-level gas exchange phenotyping platform to perform a reverse genetic screen to identify phenotypes associated with defective stomatal kinetics and water use efficiency.

First, I characterized stomatal movements and gas exchange efficiency in wild-type *B. distachyon* with 120 individuals and verified that environmental fluctuations (e.g., light intensity, temperature) systemically affected leaf-level gas exchange measurements and stomatal anatomy, and observed significant correlations between stomatal anatomy and function.

Secondly, the reverse genetic screen of 60 mutant lines yielded a few promising candidates from which I selected *BdPRX76/BdPOX*, a class III peroxidase for further characterization. *bdpox* mutants displayed lower intrinsic water-use efficiency and higher stomatal conductance levels due to increased stomatal size. Interestingly, *bdpox* mutants presented longer stomata but no differences in stomatal density. Therefore, this resulted in a unique disruption in the negative correlation between stomatal density and size. Contrary to stomata, prickle hair cells were reduced in *bdpox* mutants. Surprisingly, *BdPOX* was exclusively expressed in hair cells which suggested that *BdPOX* cell-autonomously promote prickle hair cell size and non-cell-autonomously constricts stomatal elongation.

The analysis of cell wall autofluorescence and lignin stainings suggested that BdPOX acts in the lignification/hydroxycinnamates cross-linking at the hair cell base to support cell outgrowth. Finally, ectopic expression of *BdPOX* in the stomatal lineage restricted stomatal elongation by increasing phenolic content in the guard cells. Overall, these results suggest a coordination between stomata and prickle hair cell formation to optimize leaf functionality.

Zusammenfassung

Stomata sind zelluläre Poren in der Blattepidermis, die die CO_2-Aufnahme für Photosynthese regulieren und den Verlust von Wasserdampf einschränken. Stomata öffnen und schließen als Antwort auf verschiedene umweltbedingte Auslöser und die Geschwindigkeit der stomatalen Bewegungen bestimmt, wie effizient Pflanzen in fluktuierenden Umgebungen Gase austauschen und Wasser sparen. Daher sind stomatale Geschwindigkeit und Wassernutzungseffizienz (Verhältnis zwischen assimiliertem Kohlenstoff und Wasserverlust über Stomata) wichtige Eigenschaften für die Produktivität von Pflanzen und Toleranz gegenüber Umweltstressoren.

Gräser wie Weizen, Reis oder die Modell-Spezies Brachypodium distachyon sind die Pflanzengruppe mit den schnellsten stomatalen Bewegungen; ein Merkmal, das mit ihrer einzigartigen stomatalen Morphologie assoziiert ist. Gras-Stomata bestehen aus zwei hantelförmigen Schließzellen ("guard cells", GCs) flankiert von zwei Nebenzellen ("subsidiary cells", SCs). Diese Morphologie scheint in optimalen Mechanismen zu resultieren, die die stomatalen Bewegungen vereinfachen und die SCs tragen ihren Teil dazu bei, indem sie schnellen Austausch von Ionen und Wasser unterstützen, die für turgor-getriebenes stomatales Öffnen und Schließen benötigt werden. Nichtsdestotrotz sind die molekularen Mechanismen im Hintergrund dieser effizienten Form und Funktionalität von Gras-Stomata noch weitgehend unerforscht. Ein Vergleich der Blatt-Transkriptome von Wildtyp *B. distachyon* (Bd21-3) und bdmute Mutanten, die keine SCs haben und defektive stomatale Funktionalität aufweisen, ermöglichte die Identifizierung von Kandidatengenen, die potenziell mit der Form und Funktionalität von Gras-Stomata assoziiert werden können. Daher habe ich eine Phänotypisierungsplattform für Blattlevel-Gasaustausch etabliert, um einen reverse genetic screen zur Identifizierung von Phänotypen durchzuführen, die in Verbindung mit defektiver stomataler Kinetik und Wassernutzungseffizienz stehen.

Zuerst charakterisierte ich stomatale Bewegungen und Gasaustauschseffizienz in 120 Individuen vom Wildtyp *B. distachyon* und verifizierte, dass Umweltfluktuationen (z.B. Lichtintensität, Temperatur) Blattlevel-Gasaustauschsmessungen und stomatale Anatomie systemisch beeinflussten und beobachtete signifikante Korrelationen zwischen stomataler Anatomie und Funktionalität.

Des Weiteren lieferte der reverse genetic screen von 60 Mutantenlinien ein paar vielversprechende Kandidaten, aus denen ich *BdPRX76/BdPOX*, eine Peroxidase der Klasse III, für weitere Charakterisierung auswählte. *bdpox* Mutanten präsentieren längere Stomata, aber keine Differenzen in stomataler Dichte. Daher resultiert dies in einer einzigartigen Störung der negativen Korrelation zwischen stomataler Dichte und Größe. Im Gegensatz zu Stomata waren die stacheligen Haarzellen in *bdpox* Mutanten verkleinert. Überraschenderweise war *BdPOX* ausschließlich in Haarzellen exprimiert, was darauf hindeutet, dass *BdPOX* zell-autonomisch eine Vergrößerung der stacheligen Haarzellen und non-zell-autonomisch die stomatale Elongation fördert.

Die Analyse von Zellwand-Autofluoreszenz und Lignin-Färbungen wies darauf hin, dass BdPOX in der Lignifizierung und Verlinkung von Hydroxycinnamaten an der Haarzell-Basis involviert ist, um den Zellauswuchs zu unterstützen. Abschließend führte ektopische Expression von *BdPOX* in der stomatalen Linie zu eingeschränkter stomatalen

Elongation, indem der Anteil an Phenolen in Schließzellen erhöht wurde. Zusammengefasst deuten diese Ergebnisse auf eine Koordinierung zwischen der Formierung von Stomata und stacheligen Haarzellen hin, um Blatt-Funktionalität zu optimieren.

Table of contents

List of figures 11

List of tables 15

1. General Introduction 17

1.1 Stomata 19

1.2 Stomatal functioning in grasses 20

1.2.1 Perceiving and signalling environmental cues to trigger stomatal responses 20

1.2.2 Translating signalling into osmotic changes 25

1.2.3 Osmotic changes inducing turgor changes 28

1.2.4 Cell wall properties to sustain turgor changes 29

1.3 Morphological stomatal categories and contribution of subsidiary cells for stomatal movements 32

1.4 Stomatal formation in grasses for optimal functionality 37

2. Aims of the study 43

3. Results and discussion – Chapter I 45

3.1 Introduction 47

3.2 Material and methods 49

3.2.1 Plant material and growth conditions 49

3.2.2 Leaf-level gas exchange measurements: light-responses 49

3.2.3 Leaf-level gas exchange measurements: physiological $g_s$max 50

3.2.4 Stomatal anatomy measurements 51

3.2.5 Correlation analysis and statistics 51

3.2.6 Morphometric analysis of graminoid stomatal complexes 52

3.2.7 Anatomical $g_s$max calculations 53

3.2.8 Comparison between anatomical and physiological $g_s$max 53

3.3 Results 54

3.3.1 Leaf-level gas exchange measurements in *Brachypodium distachyon* are robust and revealed fast and efficient stomatal responses to fluctuating light 54

3.3.2 Environmental conditions vary daily and seasonally in glasshouse settings 55

3.3.3 Environmental fluctuations systemically influence gas exchange measurements 58

3.3.4 Higher iWUE occurs in the warm season due to seasonal variations in A and g_{sw} 63

3.3.5 Seasonal changes in glasshouse growth conditions affect stomatal anatomical traits and gas exchange 65

3.3.6 Changes in stomatal anatomy influence gas exchange and stomatal kinetics 67

3.3.7 Adjustments on anatomical $g_s$max calculations for graminoid stomata 70

3.3.8 Testing adjusted anatomical $g_s$max calculations 72

3.3.9 Seasonal variation in anatomical $g_s$max in *Brachypodium distachyon* 74

3.3.10 Assessing stomatal anatomy and $g_s$max in other grass species 74

3.4 Discussion 77

4. Results and discussion – Chapter II 87

4.1 Introduction 89

4.2 Material and methods 92

4.2.1 RNA-seq and identification of mutant lines for the candidate genes 92

4.2.2 Plant material and growth conditions 92

4.2.3 Leaf-level gas exchange measurements and data analysis 92

4.2.4 CRISPR cloning of selected candidate genes 93

4.3 Results 95

4.3.1 Identification of candidate genes and mutants **95**
4.3.2 Stomatal kinetics phenotypes **109**
4.3.3 Intrinsic water-use efficiency (iWUE) phenotypes **109**
4.3.4 *BdPRX19* and *SCS/EF-HAND CALCIUM BINDING PROTEIN* **110**
4.3.5 *CST1* **111**
4.3.6 *BdPRX76* **111**
4.3.7 *HKT1/HKT2.4* **112**
4.4 Discussion **146**
5. Results and discussion – Chapter III **157**
5.1 Introduction **159**
5.2 Material and methods **161**
5.2.1 Plant material and growth conditions **161**
5.2.2 Cloning of reporter lines **161**
5.2.3 Generation and analysis of transgenic lines **164**
5.2.4 Leaf-level gas exchange measurements **165**
5.2.5 Microscopy analysis of stomatal anatomy **165**
5.2.6 Cell wall phenolics autofluorescence and lignin stainings **166**
5.3 Results **168**
5.3.1 *bdpox* mutants show higher stomatal conductance and lower intrinsic water use efficiency **168**
5.3.2 The negative correlation between stomatal size and density is disrupted in *bdpox* **169**
5.3.3 Cell size defects in *bdpox* are not exclusive to stomata but also found in prickle hair cells **171**
5.3.4 *BdPOX* was specifically expressed in hair cells and its expression occurs before stomatal elongation **173**
5.3.5 Mutant complementation with *BdPOXp:BdPOX:mCitrine* rescued cell-size and gas exchange phenotypes **176**
5.3.6 *BdPOX* positively regulates prickle hair cell outgrowth by cell wall phenolic modifications at the base of PHCs **178**
5.3.7 BdPOX plays a lignification or hydroxycinnamates crosslinking function in prickle hair cells **180**
5.3.8 *BdPOX* overexpression driven by maize ubiquitin promoter does not rescue phenotypes in *bdpox-1* **184**
5.3.9 *BdPOX* specific expression in the stomatal lineage rescues stomatal phenotype **185**
5.3.10 Supplementary figures **188**
5.4 Discussion **199**
6. Conclusions **207**
7. Study limitations and outlook **208**
8. Appendix **211**
9. Bibliography **217**

List of figures

Introduction

Figure 0.1 – Grass stomata morphology and turgor-driven stomatal movements in grass stomata.

Figure 0.2 – Known molecular players involved in the regulation stomatal movements in grasses and their location determined by the analysis of reporter lines and/or gene expression.

Figure 0.3 – Proposed contributions of SCs for improved stomatal movements in grasses.

Figure 0.4 – Model of stomatal development in grasses.

Results and discussion – Chapter I

Figure 1.1 – Leaf-level gas exchange measurements in response to changing light intensity in *Brachypodium distachyon.*

Figure 1.2 – Characterization of stomatal movements and gas exchange in *Brachypodium distachyon.*

Figure 1.3 – Daily and seasonal variation in temperature, light intensity and relative humidity registered during LI-6800 measurements of the 120 individuals.

Figure 1.4 – Correlations between intrinsic water-use efficiency and environment.

Figure 1.5 – Correlations between stomatal closure/opening half-times and environment.

Figure 1.6 – Correlations between stomatal gas exchange, stomatal half-times and environment.

Figure 1.7 – Seasonal variation in stomatal speed, intrinsic water-use efficiency and gas exchange).

Figure 1.8 – Seasonal variation in stomatal anatomy and correlations with environment.

Figure 1.9 – Correlations between stomatal anatomy, stomatal speed and intrinsic water-use efficiency.

Figure 1.10 – Relations between stomatal anatomy and gas exchange.

Figure 1.11 – Characterization of graminoid stomatal pores, optimization of anatomical $g_s$max calculations and seasonal variation in $g_s$max.

Figure 1.12 – Stomatal anatomy and maximum stomatal conductance in different grass species.

Results and discussion – Chapter II

Figure 2.1 – Gene ontology analysis for annotated keywords (UniPROT).

Figure 2.2 – Gene ontology analysis (GO terms for cellular component and molecular function) of *Arabidopsis thaliana* homologues.

Figure 2.3 – RNA-seq comparison between B21-3 (WT) and *bdmute.*

Figure 2.4 – Comparison of stomatal speed (rate constant, k) in the three light transitions (I, 1000-100 PAR; II 100-1000 PAR and III, 1000-0 PAR) between WT and mutant lines.

Figure 2.5 – Comparison of iWUE at 100 and 1000 PAR between WT and mutant lines.

Figure 2.6 – Gas exchange phenotyping of mutant line 2 (NaN175).

Figure 2.7 – Gas exchange phenotyping of mutant line 3 (NaN342).

Figure 2.8 – Gas exchange phenotyping of mutant line 4 (NaN344).

Figure 2.9 – Gas exchange phenotyping of mutant line 7 (NaN326).

Figure 2.10 – Gas exchange phenotyping of mutant line 8 (NaN358).

Figure 2.11 – Gas exchange phenotyping of mutant line 10 (NaN401).

Figure 2.12 – Gas exchange phenotyping of mutant line 11 (JJ3084).

Figure 2.13 – Gas exchange phenotyping of mutant line 12 (JJ12454).

Figure 2.14 – Gas exchange phenotyping of mutant line 13 (JJ19779).

Figure 2.15 – Gas exchange phenotyping of mutant line 14 (JJ8807).

Figure 2.16 – Gas exchange phenotyping of mutant line 15 (NaN1673).

Figure 2.17 – Gas exchange phenotyping of mutant line 16 (NaN373).

Figure 2.18 – Gas exchange phenotyping of mutant line 18 (NaN1942).

Figure 2.19– Gas exchange phenotyping of mutant line 19 (NaN1911).

Figure 2.20 – Gas exchange phenotyping of mutant line 22 (NaN218).

Figure 2.21 – Gas exchange phenotyping of mutant line 23 (NaN353).

Figure 2.22 – Gas exchange phenotyping of mutant line 26 (NaN1534).

Figure 2.23 – Gas exchange phenotyping of mutant line 29 (NaN319).

Figure 2.24 – Gas exchange phenotyping of mutant line 30 (NaN224).

Figure 2.25 – Gas exchange phenotyping of mutant line 31 (NaN356).

Figure 2.26 – Gas exchange phenotyping of mutant line 32 (NaN428).

Figure 2.27 – Gas exchange phenotyping of mutant line 34 (NaN245).

Figure 2.28 – Gas exchange phenotyping of mutant line 36 (NaN263).

Figure 2.29 – Gas exchange phenotyping of mutant line 37 (NaN1588).

Figure 2.30 – Gas exchange phenotyping of mutant line 40 (NaN403).

Figure 2.31 – Gas exchange phenotyping of mutant line 41 (NaN251).

Figure 2.32 – Gas exchange phenotyping of mutant line 42 (NaN307).

Figure 2.33 – Gas exchange phenotyping of mutant line 46 (NaN132).

Figure 2.34 – Gas exchange phenotyping of mutant line 47 (NaN427).

Figure 2.35 – Gas exchange phenotyping of mutant line 48 (NaN2038).

Figure 2.36 – Gas exchange phenotyping of mutant line 49 (NaN1954).

Figure 2.37 – Gas exchange phenotyping of mutant line 52 (NaN2106).

Figure 2.38 – Gas exchange phenotyping of mutant line 53 (NaN1541).

Figure 2.39 – Gas exchange phenotyping of mutant line 55 (NaN170).

Figure 2.40 – Gas exchange phenotyping of mutant line 1 (NaN51).

Figure 2.41– Gas exchange phenotyping of mutant line 5 (NaN407).

Figure 2.42 – Gas exchange phenotyping of mutant line 6 (NaN1459).

Figure 2.43 – Gas exchange phenotyping of mutant line 9 (NaN514).

Figure 2.44 – Gas exchange phenotyping of mutant line 17 (JJ2380).

Figure 2.45 – Gas exchange phenotyping of mutant line 20 (NaN1997).

Figure 2.46 – Gas exchange phenotyping of mutant line 21 (NaN1843).

Figure 2.47 – Gas exchange phenotyping of mutant line 24 (NaN86).

Figure 2.48 – Gas exchange phenotyping of mutant line 25 (NaN34).

Figure 2.49 – Gas exchange phenotyping of mutant line 27 (NaN69).

Figure 2.50 – Gas exchange phenotyping of mutant line 28 (NaN1599).

Figure 2.51 – Gas exchange phenotyping of mutant line 33 (NaN379).

Figure 2.52 – Gas exchange phenotyping of mutant line 35 (NaN1550).

Figure 2.53 – Gas exchange phenotyping of mutant line 38 (NaN68).

Figure 2.54 – Gas exchange phenotyping of mutant line 39 (NaN369).

Figure 2.55 – Gas exchange phenotyping of mutant line 43 (NaN255).

Figure 2.56 – Gas exchange phenotyping of mutant line 44 (NaN1457).

Figure 2.57 – Gas exchange phenotyping of mutant line 45 (NaN1485).

Figure 2.58 – Gas exchange phenotyping of mutant line 50 (NaN2049).

Figure 2.59 – Gas exchange phenotyping of mutant line 51 (NaN375).

Figure 2.60 – Gas exchange phenotyping of mutant line 54 (NaN1963).

Figure 2.61 – Gas exchange phenotyping of mutant line 56 (NaN397).

Figure 2.62 – Gas exchange phenotyping of mutant lines 57 (NaN1528) and 58 (NaN1508).

Figure 2.63 – Gas exchange phenotyping of mutant lines 59 (NaN570) and 60 (NaN553).

Figure 2.64 - Hypothetical localization and function of genes identified in the RNA-seq which mutants displayed impaired stomatal function.

Results and discussion – Chapter III

Figure 3.1 – Identification of *bdpox* mutants and leaf-level gas exchange.

Figure 3.2 – Stomatal closure and opening speed (k) in WT, NaN1508^{BdPOX}, *bdpox-1* and *bdpox-2*.

Figure 3.3 – Stomatal anatomical traits in WT, NaN1508^{BdPOX}, *bdpox-1* and *bdpox-2*.

Figure 3.4 – Stomatal morphometry and maximum stomatal conductance in Stomatal anatomical traits in WT, NaN1508^{BdPOX} and *bdpox* mutants.

Figure 3.5 – Pavement cells and prickle hair cells in WT, NaN1508^{BdPOX}, *bdpox-1* and *bdpox-2*.

Figure 3.6 – *BdPOX* expression pattern.

Figure 3.7 – *BdPOX* complementation experiments.

Figure 3.8 – PHC cell wall autofluorescence in WT, *bdpox-1* and complementation lines.

Figure 3.9 – Basic-fuchsin lignin staining in WT, *bdpox-1* and complementation lines.

Figure 3.10 – Safranin-o lignin staining in WT, *bdpox-1* and complementation lines.

Figure 3.11 – Phenotyping of ubiquitin promoter-driven *BdPOX* overexpression (ZmUbip:BdPOX(CDS)-mCitrine).

Figure 3.12 – Effect of *BdPOX* expression in stomatal lineage (*BdMUTEp:BdPOX(CDS)-mCitrine*) in GC autofluorescence and stomatal size.

Figure 3.13 – Cell division defects in *BdMUTEp:BdPOX-mCitrine* expressed in *bdpox-1*.

Figure 3.14 – Model for the coordination between PHC and stomatal development.

Figure 3.15 – Suggested mechanism for *BdPOX* on promoting PHC growth and limiting stomatal size.

Figure S0 – Stages of *BdPOX* expression in relation with stomatal development.

Figure S1 – *BdPOX* expression and stomatal density in complementation experiments.

Figure S2 – Additional confocal imaging of three T0 reporter lines (*BdPOXp:BdPOX-mCitrine* in WT).

Figure S3 – Additional confocal imaging from T0 complementation lines (*BdPOXp:BdPOX-mCitrine* in *bdpox-1*).

Figure S4 – Additional confocal imaging from T0 WT; *BdMUTEp:BdPOX(CDS)-mCitrine* lines.

Figure S5 – Additional confocal imaging from T0 WT; *BdMUTEp:BdPOX(CDS)-mCitrine* lines.

Figure S6 – Additional confocal imaging of four independent T0 *bdpox-1*; *ZmUbip:BdPOX(CDS)-mCitrine* lines.

Figure S7 – Example of PHCs of WT, *bdpox-1* and in three complementation lines (*bdpox-1; BdPOXp:BdPOX-mCitrine*_#1, #2 and #3) stained by basic fuchsin (lignin stain).

Figure S8 – Cell wall autofluorescence and lignin staining of mature stomata in WT and *bdpox-1,* and cell wall autofluorescence in elongating stomata (step 6i, 6ii and 6iii) in WT, NaN1508^{BdPOX} and *bdpox-1*.

Figure S9 – Example of PHCs of WT, *bdpox-1* and in three complementation lines (*bdpox-1; BdPOXp:BdPOX-mCitrine*_#1, #2 and #3) stained with safranin-o (lignin stain).

Figure S10 – Prickle hair cell size and numbers in *bdpox*-1 and *bdmute* mutants.

List of tables

Table 1 – Comparison between exact pore depth and GC width at the centre and at the apex of fully open and closed the stomatal complexes.

Table 2 – Ratio between stomatal pore length/width and guard cell (GC) length.

Table 3 – Significantly downregulated genes in *bdmute.*

Table 4 – Candidate genes and respective identified and screened mutant lines, amino acid (AA) change and location of the mutation in the protein (domain accession).

1. General Introduction

1.1 Stomata

Stomata are microscopic cellular valves on plant epidermis that originated over 400 million years ago and their evolution facilitated the continental plant expansion by allowing efficient plant–atmosphere gas exchange and maintaining hydration in plant tissues (Chater et al. 2016; Chater et al. 2017; McAdam and Brodribb 2012; Brodribb and McAdam 2017; McAdam et al. 2021). It is estimated that 20 % of the global atmospheric CO_2 enters through stomata to be assimilated annually (Hetherington and Woodward 2003). Furthermore, a massive amount of water is cycled by the vegetation via stomatal transpiration, accounting for 80-90 % of the total terrestrial evapotranspiration (Jasechko et al. 2013). Therefore, stomata can be considered crucial gatekeepers at the plant-atmosphere interface that both perceive and drive global atmospheric dynamics (Franks et al. 2017; Clifton et al. 2020).

Guard cells (GCs) form the cellular core of stomatal complexes and can regulate the size of the stomatal pore to control the rate of gas exchange. The regulation of the stomatal pore size is achieved by changes in GC turgor. Increasing GC turgor results in stomatal opening, while turgor loss results in stomatal closure. Turgor-driven stomatal movements are regulated by a plethora of environmental stimuli such as light intensity and quality, relative humidity, soil water content, temperature, CO_2 concentrations and even the occurrence of pathogens or atmospheric pollutants (Lawson and Matthews 2020; Kim et al. 2010; Kollist et al. 2014; Daloso et al. 2017) (Fig. 0.1).

The speed of stomatal movements is crucial for how efficiently plants exchange gas and save water (Lawson and Blatt 2014; Leakey et al. 2019; McAusland et al. 2016). The rate of assimilated carbon per water loss is defined as water-use efficiency (WUE) and is an important parameter for plant productivity and stress tolerance. Quick stomatal responses to adjust stomatal pore apertures allow therefore an efficient balance between CO_2 uptake and water vapour loss providing an advantage under changing environmental conditions (Eyland et al. 2021; Lawson and Vialet-Chabrand 2019).

Grasses (Family *Poaceae*) are the plant group with the fastest stomatal movements which is associated with their unique stomatal morphology consisting of elongated dumbbell-shaped GCs and two lateral subsidiary cells (SCs) (Franks and Farquhar 2007; Raissig et al. 2017; Chen et al. 2017; McAusland et al. 2016) (Fig. 0.1). While stomatal form-function relations and the molecular

machinery of stomatal movements have been well investigated in the model eudicot plant *Arabidopsis thaliana* (Ando and Kinoshita 2018; Hu et al. 2010; X. Wang et al. 2019; Kinoshita et al. 2001; Hõrak et al. 2016; Sierla et al. 2018; Vahisalu et al. 2008; Ronzier et al. 2014; Batool et al. 2018; Andrés et al. 2014; Dow et al. 2014), the molecular mechanisms behind the improved stomatal function and morphology in grasses remain less explored. Therefore, in my doctoral thesis I introduce current genetic and mechanistic knowledge regarding grass stomatal functioning, and experimentally contribute with novel knowledge on the form and functionality of grass stomata using the grass model *Brachypodium distachyon*.

1.2 Stomatal functioning in grasses

1.2.1 Perceiving and signalling environmental cues to trigger stomatal responses

Blue light is the primary environmental cue inducing stomatal opening in C_3/C_4 plant species. In *Arabidopsis thaliana*, blue light is perceived by phototropins. Phototropins are blue light-protein kinases associated to the plasma membrane that activate plasma membrane H^+-ATPases such as AHA1, via phosphorylation cascades (Inoue and Kinoshita 2017; Yamauchi et al. 2016). The activation of plasma membrane H^+-ATPases induces proton pumping that causes a hyperpolarization of the plasma membrane leading to the opening of inward rectifying K^+ channels and inhibits S-type anion channels (Marten et al. 2007). The consequent ion influx promotes water influx into the GCs increasing the turgor pressure and culminating in stomatal opening (Inoue and Kinoshita 2017).

While the photoreceptors mediating blue light responses in grasses remain unknown, some studies in rice shown that H^+-ATPases (OSAs) regulate stomatal opening in *Oryza sativa* (Toda et al. 2016). *OSA7* is one of the major *OSA* isoforms and homologue to the *Arabidopsis AHA1* and *AHA2* (Toda et al. 2016). *OSA7* was preferentially expressed in GCs, but potentially expressed in SCs (Fig. 0.2). *osa7* mutants exhibited affected responsivity to blue light resulting in lower stomatal conductance (Toda et al. 2016). These findings suggest that blue light-responsive signalling regulating stomatal opening is present in the family *Poaceae*.

Besides blue light, stomata can also open in response to red light, but solely at high light intensity that promotes photosynthesis. This light signal triggers a drop in internal CO_2 concentration in the substomatal cavities perceived by the GCs and induces stomatal opening (Ando and Kinoshita 2018; Roelfsema et al. 2002).

Stomatal closure can result from a plethora of environmental cues such as darkness (in C_3 and C_4 plants), low humidity, high CO_2 concentrations or the presence of pathogens (Lawson and Matthews 2020; Kim et al. 2010; Kollist et al. 2014; Daloso et al. 2017; Sierla et al. 2018; Pitaloka et al. 2021; Merilo et al. 2014). In *Arabidopsis thaliana*, two carbonic anhydrases *AtCA1* and *AtCA4* were shown to mediate stomatal closure in response to changing CO_2 concentrations by converting CO_2 to HCO_3^- (Hu et al. 2010). Similarly, loss of function mutants of *ZmCA1* and *ZmCA2* or *OsβCA1* resulted in increased stomatal conductance and affected stomatal responsivity to elevated CO_2 in maize and rice, respectively (Kolbe et al. 2018; Chen et al. 2017).

It has been described in *Arabidopsis thaliana* that the environmental signals inducing stomatal closure are integrated by the plant hormone ABA, which has been widely associated with abiotic stress tolerance/responses and a core modulator of stomatal closure (Batool et al. 2018; Munemasa et al. 2015; Merilo et al. 2015).

The PYR1/PYL/RCAR ABA receptors perceive ABA (Ma et al. 2009; Sun et al. 2017; Park et al. 2009) and inhibit the AtABI1 phosphatase, therefore activating the central AtOST1 (Fujii et al. 2009; Umezawa et al. 2009; Saez et al. 2006; Leung et al. 1997). OST1 (SnRK2.6 or SRK2E) is a serine/threonine protein kinase involved in the regulation of stomatal closure. OST1 phosphorylates and activates anion channels (such as SLAC1 and QUAC1) (Geiger et al. 2009; Imes et al. 2013; Acharya et al. 2013) inducing a membrane depolarization which consequently activates K^+ outward rectifiers causing water efflux, turgor loss and therefore stomatal closure (Munemasa et al. 2015; Murata et al. 2015). Additionally, AtOST1 has also been demonstrated to physically interact and inhibit the inward K^+ channel AtKAT1, preventing ion influx (Sato et al. 2009; Acharya et al. 2013).

ABA-induced stomatal closure signalling has also been demonstrated in grasses. OsABCG5/OsRCN1 is a ATP-binding cassette transporter protein involved in ABA accumulation in the GCs (Fig. 0.2) as a response to drought stress, therefore promoting stomatal closure in rice (Matsuda et al. 2016). *OsABCG5/OsRCN1* loss of function mutants presented decreased ABA accumulation in GCs after exposure to ABA and detached leaves displayed faster dehydration rates, suggesting defective stomatal closure capacity (Matsuda et al. 2016). *OsPM1* is an AWPM-19 like family gene that mediates ABA influx into the GCs (Fig. 0.2) to regulate stomatal closure (Yao et al. 2018). RNAi and knockout lines displayed faster water loss rates in detached leaves, while slower water loss rates were observed in overexpression lines, suggesting the function of OsPM1 in promoting ABA-induced stomatal closure in rice (Yao et al. 2018).

Grass homologues of the *Arabidopsis* ABA receptors AtPYR1/PYL/RCAR perceive ABA in GCs and trigger stomatal closure signalling cascades in grass species. *TaPYL4* is a high-affinity ABA receptor and its overexpression increased water use efficiency in wheat, improving grain weight under water-deficit stress conditions (Mega et al. 2019). It has also been suggested that the wheat E3 ligase TaPUB1 is a negative regulator of ABA signalling by interacting with TaPYL4 and PaABI5, therefore affecting stomatal responsiveness (Zhang et al. 2021). Overexpression lines displayed partially impaired stomatal closure, while *TaPUB1*-RNAi lines presented enhanced stomatal closure in response to ABA (Zhang et al. 2021).

The central kinase OST1 involved in stomatal closure has also been described in maize. *ZmOST1* was expressed in GCs and its expression was induced during water-stress and directly by ABA treatments (Wu et al. 2019). *zmost1* mutants presented reduced anion currents and larger stomatal apertures in response to ABA. Furthermore, higher water loss rates were observed in detached leaves of *zmost1* mutants (Wu et al. 2019). In barley, several Hv14-3-3s proteins have been shown to functionally interact with HvOST1 and HvSLAC1 to regulate stomatal and drought responses, suggesting the existence of multi-component protein complexes regulating the activity of anion channels (Jiang et al. 2022). Additionally, suppressing the expression of *Hv14-3-3A* significantly enhanced drought sensitivity, carbon assimilation, stomatal conductance, and stomatal density in barley (Jiang et al. 2022). Also in barley, a cell-type specific transcriptomic analysis suggested that

the serine-threonine phosphatase *HvABI1* and the kinase *HvOST1.1* were strongly expressed only in GCs, suggesting that ABA-related signalling is a molecular feature of GCs (Schäfer et al. 2018).

It has been verified in *Arabidopsis* that ABA-induced stomatal signalling is modulated and enhanced by Ca^{2+} and ROS (Kollist et al. 2014; Sierla et al. 2016; Huang et al. 2019). Besides OST1, several kinases involved in the modulation of ABA signalling, including Ca^{2+}-dependent protein kinases (CPK3, CPK5, CPK6, CPK21, and CPK23), the leucine-rich repeat receptor-like kinase GHR1 and CBL/CIPK complexes, have also been reported as involved in the activation of SLAC1 to trigger stomatal closure in *Arabidopsis* (Geiger et al. 2010; Brandt et al. 2012; Hua et al. 2012; Maierhofer et al. 2014; Sierla et al. 2018; Hõrak et al. 2016; Hsu et al. 2021). AtCPK13 inhibits light-induced stomatal opening and suppresses the currents of the potassium channels AtKAT1 and AtKAT2 (Ronzier et al. 2014). *AtCPK9* has been shown to be expressed in GCs and to be a negative regulator of the ABA-induced stomatal closure by modulating ion channel activities (Chen et al. 2019). AtCPK33 mediates Ca^{2+} sensing during strigolactone-induced stomatal closure (Wang et al. 2019). Interestingly, it was shown that the leucine-rich repeat receptor-like kinase AtGHR1 lacks phosphorylation activity and is therefore a pseudokinase (Sierla et al. 2018). Thus, it was suggested that AtGHR1 mediates AtSLAC1 activation by acting as scaffolding protein to recruit the Ca^{2+}-dependent protein kinase AtCPK3 and other unknown pathway-specific components to regulate stomatal closure in response to different environmental stimuli (Sierla et al. 2018).
Homologous Ca^{2+}-dependent kinases have been also characterized in grasses. In rice, ABA induced the expression of the Ca^{2+}-dependent protein kinase *OsCPK9* (Wei et al. 2014). Knock-down RNAi lines presented faster dehydration rates while overexpression lines lower dehydration rates and consequently enhanced drought resistance (Wei et al. 2014). In maize, two Ca^{2+}-dependent kinases *ZmCPK35* and *ZmCPK37* have been shown to be expressed in GCs and to play a crucial role in stomatal closure by regulating the activity of ZmSLAC1 (Li et al. 2022). Electrophysiological characterization in both maize GCs and *Xenopus* oocytes showed that ZmCPK35 and ZmCPK37 activate ZmSLAC1-mediated chloride and nitrate currents (Li et al. 2022). *zmpk37* mutants displayed impaired anion currents in GCs while *ZmCPK35* and *ZmCPK37* overexpression lines shown increased anion currents (Li et al. 2022). Furthermore, enhancing *ZmCPK35* and

ZmPCK37 expression improved drought tolerance and reduced yield loss caused by drought stress by modifying stomatal control (Li et al. 2022).

Besides Ca^{2+}, ROS signalling is also integrated in stomatal closure pathways (Sierla et al. 2016; Postiglione and Muday 2020; Singh et al. 2017). In maize, water stress increased H_2O_2 levels in stomatal complexes. Closed stomata presented a strongly enhanced H_2O_2 signal in the SCs, again suggesting cell-type specific signalling responses (Yao et al. 2013).

Furthermore, two transcription factors associated with stomatal responses have been identified to regulate the expression of genes that modulate ROS levels in response to drought and salt stress. *OsSNAC1* expression is induced by water stress in both GCs and SCs and overexpression lines displayed significantly improved drought stress tolerance (Hu et al. 2006; You et al. 2014). A direct target of OsSNAC1 is OsSRO1 which promotes H_2O_2 accumulation and stomatal closure in rice (You et al. 2013). Contrarily, OsDST negatively regulates stomatal closure by directly regulating genes related with H_2O_2 homeostasis (Huang et al. 2009). Consequently, *osdst* mutants displayed enhanced stomatal closure which resulted in improved drought and salt stress tolerance by restricting water loss (Huang et al. 2009). Lastly, *OsDCA1* is a transcriptional coactivator of *OsDST*. *OsDCA1* together with *OsDST* activate the H_2O_2 scavenger peroxidase 24 precursor, decreasing H_2O_2 levels and therefore inhibiting ROS-induced stomatal closure (Cui et al. 2015). Therefore, *osdca1* mutants presented higher drought resistance associated with enhanced stomatal closure while *OsDCA1* overexpression lines were hypersensitive to drought stress due to enhanced inhibition of stomatal closure (Cui et al. 2015).

Overall, ABA, Ca^{2+} and ROS are central modules in stomatal closure signalling in grasses. Furthermore, a unique expression of genes associated with ABA import/signalling in GCs and inverse ROS/Ca^{2+} signalling between GCs and SCs may therefore contribute to the inverse osmotic and turgor behaviour of GCs and SCs required during stomatal movements.

1.2.2 Translating signalling into osmotic changes

Cations and anions are osmolytes triggering the osmotic changes in GCs/SCs to drive stomatal movements. Therefore, ion channels act as the cellular effectors of stomatal signalling and play a crucial role in the coordination of osmolytes transport (Jezek and Blatt 2017; Mumm et al. 2011).

Indeed, a key and central component of stomatal closure characterized in *Arabidopsis* is *AtSLAC1*, a S-type slow anion channel (Vahisalu et al. 2008) which is activated by AtOST1 (Geiger et al. 2009; Vahisalu et al. 2010). Homologues of *AtSLAC1* have also been characterised in grass stomata. In rice, OsSLAC1 was described to be a nitrate-selective channel that can be activated by the protein kinase OsSAPK8 by phosphorylation of the OsSLAC1 serine 129 (S129) (Sun et al. 2016). *OsSLAC1* reporters are expressed in both GCs and SCs (Kusumi et al. 2017) (Fig. 0.2). *osslac1* mutants displayed enhanced stomatal conductance which reflects the defective stomatal closure capacity. Consequently, plant productivity was negatively affected in *osslac1* mutants which presented affected in biomass and seed production (Kusumi et al. 2017). Similarly, it was suggested that ZmSLAC1 mediates the nitrate efflux rather than chloride in maize and *zmslac1* mutants displayed inefficient stomatal closure in response to different stomatal closure triggers (Qi et al. 2018). It was demonstrated that barley requires nitrate for ABA-induced stomatal closure achieved by nitrate-dependent gating of HvSLAC1. A tandem amino acid residue motif in SLAC1 monocots channels is responsible for the nitrate-dependent gating of SLAC1 observed in grasses during ABA-induced stomatal closure (Schäfer et al. 2018). While in grasses SLAC1 is nitrate-sensitive, in the eudicot *Arabidopsis* AtSLAC1 is insensitive to nitrate, suggesting that the nitrate-dependent gating evolved from a tandem *motif* after the split between monocots and dicots (Schäfer et al. 2018). Interestingly, replacing the dicot amino acid signature (VV) with the monocot signature (IA) in *Arabidospis*, converted AtSLAC1 into a nitrate-sensitive channels as observed in the grasses rice, maize and barley (Kusumi et al. 2017; Qi et al. 2018; Schäfer et al. 2018). Still, replacing the monocot with the dicot signature did not convert HvSLAC1 into a nitrate-insensitive channel, which suggested that additional features in the monocot SLAC1 are needed for nitrate-sensitive gating (Schäfer et al. 2018).

In addition to SLAC1, AtQUAC1/AtALMT12 is quick anion channel also activated by AtOST1 that acts together with slow anion channels by exporting chloride and organic anions such as malate in *Arabidopsis* (Meyer et al. 2010; Mumm et al. 2013; Imes et al. 2013; Sasaki et al. 2010). In barley, the aluminium-activated malate transporter HvALMT1 has also been associated with anion transport during stomatal closure. *HvALMT1* transcriptional reporter was strongly expressed in GCs (Fig. 0.2) while a faint signal was observed in SCs (Gruber et al. 2010, 2011), and stomatal closure was strongly impaired in *hvalmt1* RNAi mutants (Xu et al. 2015).

It has also been suggested in barley that GC-specific S-type anion channels are activated to trigger stomatal closure in response to biotic factors to avoid pathogen entrance (e.g., mildew hyphae penetrating the leaf cuticle and presence of chitosan, a fungal cell wall component) (Koers et al. 2011).

Recently, a comparison of single-nucleus transcriptome from maize leaf epidermal peels attempted to describe signalling components unique to GCs and to SCs. One of the genes highly enriched in the SC cluster was the nitrate transporter *ZmNTR1.2* which expression in *Xenopus laevis* oocytes demonstrated ABA and nitrate transport activities and therefore provided evidences of SC-specific ion transport (Sun et al. 2022).

Finally, a cell-type-specific regulation of anion channels in GCs and SCs has been also described in maize (Mumm et al. 2011). While in SCs cytosolic alkalinization positively affected anion efflux and high Ca^{2+}concentrations and ABA inhibited anion efflux, cytosolic alkalinization had no impact on anion efflux in GCs, but high Ca^{2+}concentrations promoted anion efflux (Mumm et al. 2011).

Regarding cations, K^+ is the key osmolyte responsible for turgor changes. Electrophysiological studies on maize GC and SC protoplasts identified two classes of K^+ channels: a hyperpolarization-induced class mediating K^+ influx and a depolarization-induced class mediating K^+ efflux (Fairley-Grenot and Assmann 1992; Dreyer et al. 1995). The identical response of K^+ channels observed in both GCs and SCs suggests that the membranes of GCs and SCs need to be inversely polarized to achieve opposite influx/efflux of K^+ in GCs/SCs, potentially explaining why anion channels and

ABA signalling could be restricted to GCs. Still, regarding the composition of K^+ channels in GCs and SCs, transcriptional analysis of GC and SC protoplasts from maize leaves identified not just a common K^+ outward rectifying channel (*ZmZORK*) but also differentially expressed K^+ uptake channels in GCs and SCs (Büchsenschütz et al. 2005) (Fig. 0.2). Furthermore, two KAT1-like shaker K^+ channels (*ZmKZM1* and *ZmKZM2*) have been found in GCs and SCs, while *ZmZMK1* was only expressed in the SCs (Büchsenschütz et al. 2005) (Fig. 0.2). *ZmKZM2* and *ZmKZM3* have also been reported to be highly expressed in maize GCs and to localize in the plasma membrane. RNAi lines against *ZmKZM2* displayed higher stomatal conductance which suggested that ZmKZM2 acts as an inhibitor of stomatal opening (Gao et al. 2017).

Other cation channels associated with stomatal functioning have been identified in rice. *OsKAT2* is an inward rectifying K^+ channel strongly expressed in GCs and weakly in the SCs (Hwang et al. 2013; Hwang et al. 2013) (Fig. 0.2). Similarly, a shaker K^+ channel *OsK5.2* was strongly expressed in GCs and weakly in the SCs. Loss of *OsK5.2* functional expression resulted in higher transpiration rates and defective stomatal closure (Nguyen et al. 2017), highlighting the role of OsK5.2 in the regulation of stomatal movements.

Finally, a cell-type-specific regulation of ion channels in GCs and SCs in response to light and darkness was described in maize. A short hyperpolarization in SCs induced by darkness may result in the activation of inward rectifying channels in SCs, therefore inducing cation influxes and increasing turgor in SCs pressing against GCs (Mumm et al. 2011). A complementary response occurs in GCs, as darkness caused a depolarization of the membrane in GCs (Roelfsema and Hedrich 2002; Kollist et al. 2014). On the other hand, light induced a membrane depolarization in SCs, which putatively results in K^+ efflux and consequently in turgor decrease. This may allow a mechanical accommodation of the opening and turgor-increasing GCs, which membranes are hyperpolarized by light. This hyperpolarization of GCs in response to light putatively induces the influx of K^+ and an increase in turgor culminating in stomatal opening (Mumm et al. 2011; Toda et al. 2016; Roelfsema and Hedrich 2002).

Overall, a cell-type-specific and opposite regulation of membrane polarization and ion channel activity in GCs and SCs underlies the inverse regulation of osmotic potential in the two cell types of grass stomata. Additionally, cell-type-specific expression of transport-associated proteins seems to contribute to the inversed regulation of turgor in GCs and SCs during stomatal movements.

1.2.3 Osmotic changes inducing turgor changes

Aquaporins, such as the plasma membrane intrinsic proteins (PIPs), are hydrophilic channel proteins that facilitate water movement through the plasma membrane and play an essential role in plant-water relations and stomatal functioning (Heinen et al. 2014; Gomes et al. 2009; Cui et al. 2021a; Avila et al. 2020; Grondin et al. 2015; Scharwies and Dinneny 2019). Furthermore, *PIPs* expression is tissue/cell-type specific and environmentally responsive which suggests their relevance for both cell-type specific and ecophysiological responses (Yaneff et al. 2015; Scharwies and Dinneny 2019; Bai et al. 2021; Cui et al. 2021a).

In maize, *ZmPIP1;1*, *ZmPIP1;3* and *ZmPIP2;2* were the most abundant PIP aquaporin transcripts detected in microdissected stomata in maize and their expression was strongly induced during the day, suggesting a role of aquaporins in the diurnal cycles of water transport and stomatal functioning (Heinen et al. 2014). Furthermore, the specific relevance of aquaporin in the coordination of stomatal movements has been recently observed in maize. It was demonstrated that *ZmPIP2;5* is expressed in the epidermis (including GCs and SCs) (Fig. 0.2) and enhances stomatal closure in response to water stress (Ding et al. 2022). In response to mild water-stress or ABA treatments, stomatal conductance decreased more in *ZmPIP2;5* overexpression lines and less in *zmpip2;5* mutants, compared to WT (Ding et al. 2022). Also, in epidermal peels, ABA induced faster stomatal closure in overexpression lines while *zmpip2;5* mutants were irresponsive to ABA (Ding et al. 2022).

In rice, GC protoplasts from two drought-tolerant varieties presented higher osmotic permeability than a drought-sensitive variety (Vinnakota et al. 2016). Despite those differences in the GCs osmotic permeability between drought sensitive and tolerant varieties, only one of the drought-tolerant varieties presented an increased expression

of *OsPIP1;1*, *OsPIP1;2*, *OsPIP2;1*, *OsPIP2;4* and *OsPIP2;5* (Vinnakota et al. 2016). These observations suggest that the change in water permeability between drought and sensitive varieties may rely on either aquaporins expression or in the modulation of aquaporin activity to improve water transport (Vinnakota et al. 2016).

1.2.4 Cell wall properties to sustain turgor changes

Since stomata constantly open and close to optimize gas exchange, stomatal cell walls must be specialized to withstand intense and regular pressurization/depressurization and display tensile strength and flexible properties to endure the changes in cellular turgor and volume (Spiegelhalder and Raissig 2021). Therefore, the biosynthesis of cell wall components must be highly specialized and localized within the cell wall of stomata to result in anisotropic cell wall composition to allow the stomatal movements (Shtein et al. 2017; Marom et al. 2017; Rui et al. 2018). It has been suggested that the orientation and crystallinity of cellulose microfibrils is crucial for the mechanical functioning of stomata (Shtein et al. 2017). While kidney-shaped GCs present a radial cellulose disposition, graminoid GCs rather display a longitudinally organized cellulose microfibrils (Shtein et al. 2017).

Differences in cell wall composition and organization between kidney-shaped GCs and graminoid dumbbell-shaped GCs have been observed (Shtein et al. 2017), and therefore may also contribute to the improve stomatal functioning in grasses. Pectin polymers are a component of the cell walls in GCs that has been shown to be important for stomatal functioning. In *Arabidopsis*, *PME6* is a pectin methylesterase highly expressed in GCs and required for stomatal functioning. *pme6* mutants have cell walls enriched in methylesterified pectin and present impaired stomatal opening and closure dynamics (Amsbury et al. 2016). Complementing *pm6* with *PME6p:PME* rescued GC cell wall pectin methylesterification status and stomatal functioning, demonstrating the importance of gene expression of cell-wall associated genes for the proper cell wall composition and dynamics for functional stomata (Amsbury et al. 2016). A pectin-modifying gene *PLL12* was also shown to be required for stomatal dynamics in *Arabidopsis thaliana* (Chen et al. 2021). *PLL12* is required for regulating cross-linked pectin in GC cell walls and maintain turgor pressure. GC-specific

knockdown of *PLL12* resulted in defective stomatal responses to changing light (Chen et al. 2021). Interestingly, even though grass cell walls generally contain low pectin levels, GC cell walls are abundant in pectin and phenolic esters (Jones et al. 2005) which suggests that pectin is also significant for stomatal movements in grasses as in *Arabidopsis*.

Regarding phenolics, lignin and polyphenolic compounds also occur in the stomatal complexes potentially to provide mechanical support for the stomatal movements (Shtein et al. 2017). While in kidney-shaped GCs lignin and phenolics are located around the stomatal pore, in grass dumbbell-shaped GCs these components are distributed over the entire GC cell wall (Shtein et al. 2017).

Recently, the expression of cell-wall associated genes putatively in SCs has been identified in maize: the ATP-binding cassette *ABCG29*, the glycosyl hydrolase *GH9B8*, the non-specific lipid transfer protein *LTP2*, the glycosyltransferase *GT43*, the xyloglucan/endotransglucosylase *OsXTH25* and the wall-associated receptor kinase *ZmWAK1* which are involved in cell wall modelling processes such as cell wall biosynthesis, lignification, loosening, cuticle and pectin interactions, suggesting a high relevance of cell wall composition not just in GCs but also in SCs for stomatal formation and movements (Sun et al. 2022).

Furthermore, a cell wall glycine-rich protein *ZmGRP6* involved in cell wall expansion was demonstrated to be expressed specifically in grass SCs in maize (Sun et al. 2022). In *Arabidopsis*, *PGX3* has been shown to be involved in cell wall expansion (Rui et al. 2017). In *Arabidopsis* cotyledons, *PGX3* was localized in the cell wall, and was enriched in the stomatal pore formation sites. In adult plants, *PGX3* overexpression accelerated stomatal opening while loss of *PGX3* impaired stomatal closure (Rui et al. 2017), suggesting the relevance of cell wall expansion and loosening for stomatal formation and function. A putative role of expansins in cell wall loosening to adjust stomatal movements has also been suggested. *AtEXPA1* was shown to be expressed in GCs. Increasing *AtEXPA1* expressed resulted in faster stomatal movements, while Anti-EXPA1 antibody treatments reduced stomatal speed (Wei et al. 2011; Zhang et al. 2011). Also, in the eudicot *Vicia faba, VfEXPA1* was detected in GCs and *VfEXPA1* overexpression in tobacco accelerated stomatal opening induced by light and increased gas exchange rates (Wei et al. 2011).

Overall, stomatal cell wall composition seems to be of major relevance for effective stomatal mechanics crucial for turgor-driven stomatal movements and differences in its composition may contribute to the difference in stomatal functioning between eudicots and grasses.

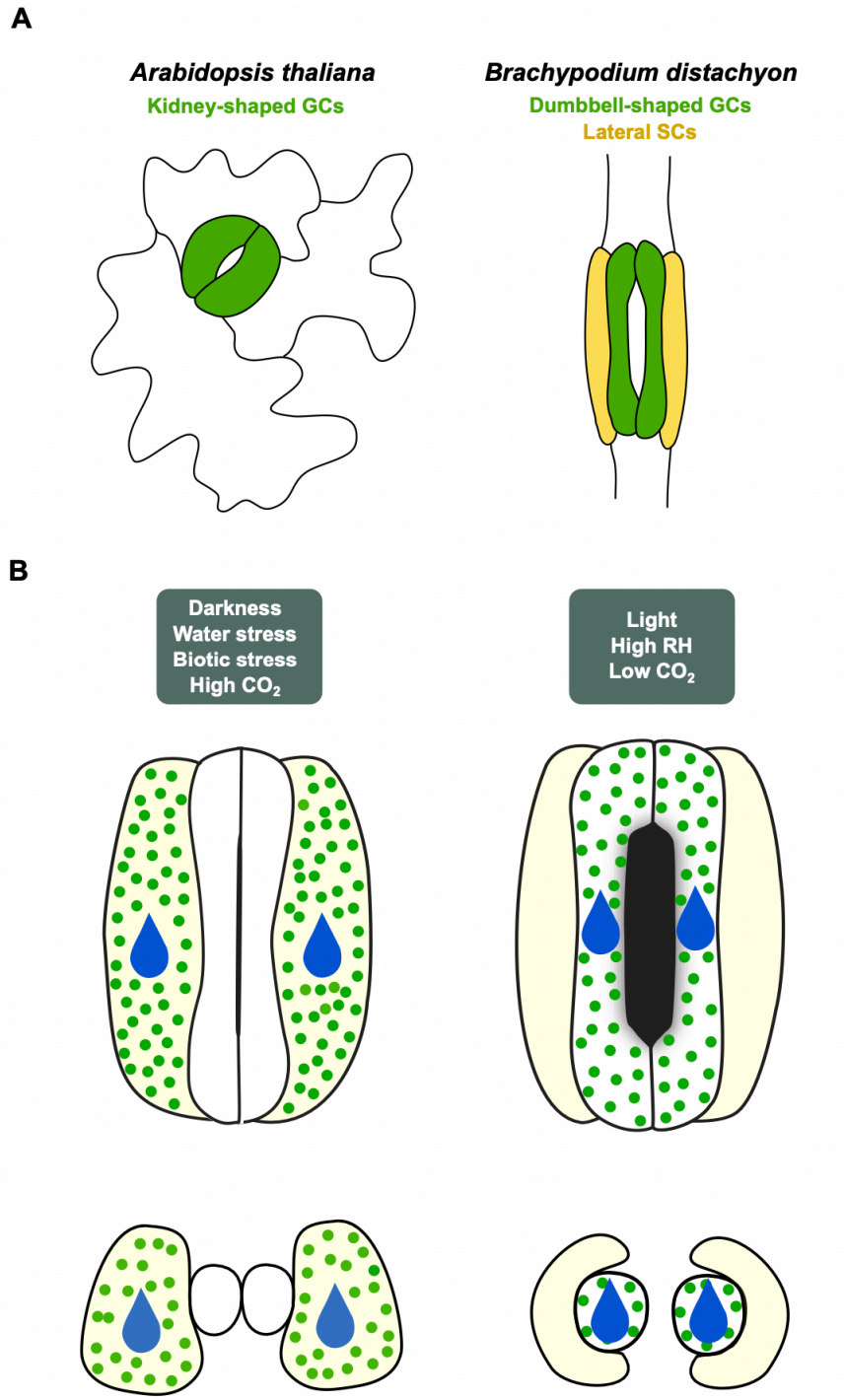


Figure 0.1 – Grass stomata morphology and turgor-driven stomatal movements in grass stomata. Inverse shuffling of osmotic and turgor pressure between GCs and SCs. Darkness, (a)biotic stresses and high carbon dioxide concentration can induce stomatal closure, during which ions (represented as green circles) accumulate in SCs inducing an increase in turgor pressure by an influx of water (represented as a blue drop) into the SCs. On the other hand, in response to light and low CO2, for example, stomata open, which is a result of an increase of osmotic and turgor pressure in the GCs and a reciprocal decrease in osmotic/turgor pressure in the SCs.

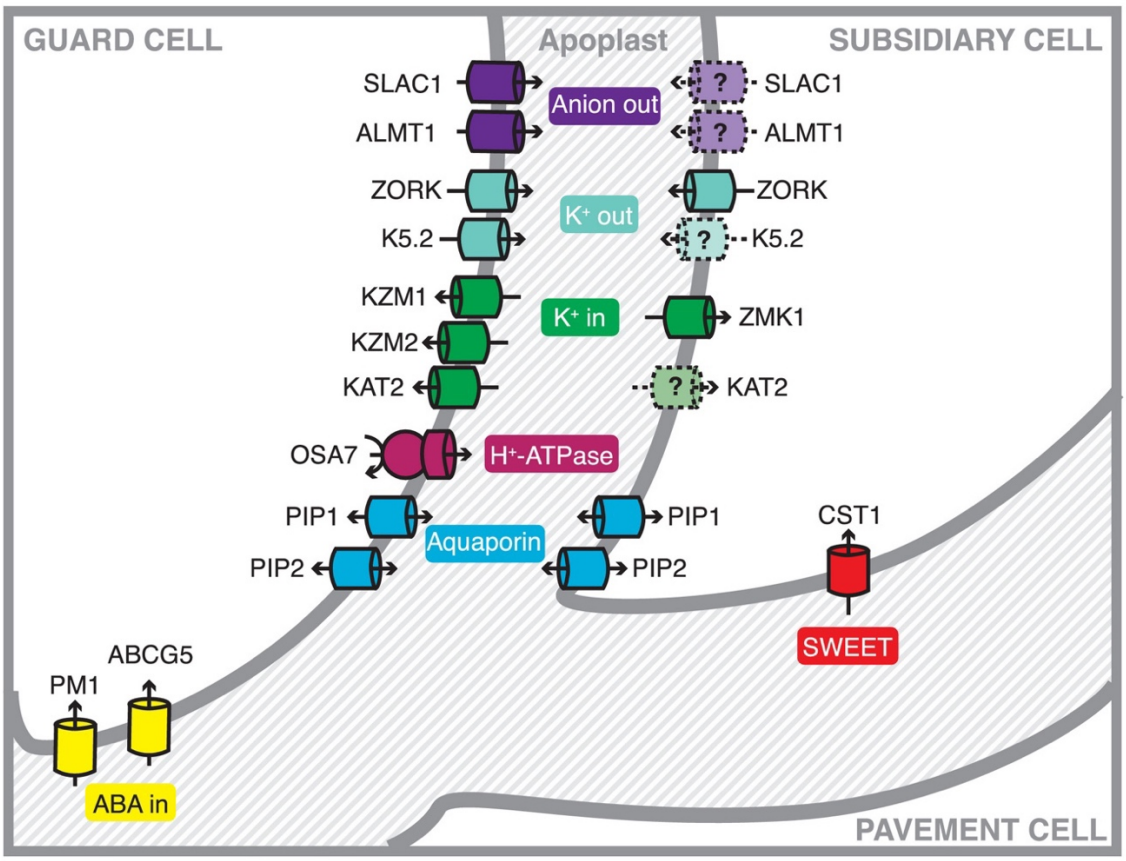


Figure 0.2 - Known molecular players involved in the regulation stomatal movements in grasses and their location determined by the analysis of reporter lines and/or gene expression. Dotted lines represent inconclusive data. Same colours indicate identical molecular function. This figure was created by Michael T. Raissig and myself, and is published in an review article in *The Plant Journal*, which I am co-first author (Nunes et al. 2020) (https://doi.org/10.1111/tpj.14552, open-access (CC BY 4.0).

1.3 Morphological stomatal categories and contribution of subsidiary cells for stomatal movements

Stomata can be classified based on morphology mostly considering if the neighbouring cells are subsidiary cells (based solely if they are morphological different than the other pavement cells). Thus, morphologically, stomata can be classified into seven major classes: (i) anomocyic stomata, consisting of two GCs surrounded by cells that are identical in size, arrangement and shape as the rest of the epidermal pavement cells and therefore not considered (morphologically) SCs, (ii) anisocytic stomata, consisting on two GCs surrounded by three spiralled SCs with different sizes, (iii) paracytic stomata, with two GCs flanked with parallel SCs, (iv) tetracytic stomata, GCs surrounded by two lateral and two apical SCs, (v) diacytic stomata, consisting of GCs surrounded by two perpendicular SCs, (vi) actinocytic stomata, consisting of GCs surrounded by radiating SCs

and (vii) cyclocytic stomata consisting of GCs circularly surrounded by four or more SCs identical in size (Nunes et al. 2020).

When it comes to GC morphology, GCs are generally kidney-shaped, except in grasses which present more elongated and dumbbell-shaped GCs (Fig. 0.1). Due to this unique morphology in grasses, an additional morphological type can be considered and referred as graminoid stomata, consisting of two uniquely dumbbell-shaped GCs flanked by lateral SCs. This morphological type can be considered a subtype of paracytic stomata based on the previously described morphological types, due to the same identical cell arrangement but unique shape.

In *Arabidopsis thaliana*, stomata can be morphologically classified as anomocytic, meaning that they do not feature SCs, but also as anisocytic since some stomata display three neighbouring epidermal cells surrounding the GCs that vary in size (Pillitteri and Dong 2013) (Fig. 0.19. Similarly, stomata in many eudicot families such as *Brassicaceae*, *Solanaceae* and *Crassulaceae* also contain anisocytic stomata (Sampaio et al. 2014; Nurit-Silva et al. 2012; Ahmad 1964). Particularly, anisocytic stomata with highly distinctive shape are found in species of the family *Crassulaceae* such as in *Kalanchoë laxiflora*, where neighbouring cells are smaller, differently shaped than the surrounding epidermal pavement cells and differently arranged and therefore morphologically SCs (Nunes et al. 2020).

In the family *Solanaceae*, multiple stomatal morphological types can in fact be found within the same species and leaf. In species of agriculture and floriculture interest such as *Solanum melongena*, *Capsicum annuum*, *Petunia violaceae* or *Solanum lycopersicum*, the epidermis of mature leaves contains anisocytic, paracytic and anomocytic stomata (Inamdar and Patel 1969). The legumes *Glycine soja*, *Medicago sativa* and *Pisum sativum* contain paracytic, anisocytic and anomocytic stomata (Shah and Gopal 1969). In the *Citrus* genus, *Citrus limon* contains paracytic stomata, while *Citrus sinensis* contains both paracytic and anomocytic stomata (Obiremi and Oladele 2001).

While an enormous effort has been done to establish morphological categories, these tell little about stomatal functioning and the efficiency of stomatal movements. SCs are tendentiously classified as it when displaying distinctive morphologies and then hypothesized to provide support for the GCs movements and stomatal functioning. Still, little is known about their specific contribution at the

molecular level. Stomatal classifications based on stomatal efficiency and a physiological definition for SCs remain inexistent (Gray et al. 2020). Furthermore, it remains unknown whether SCs number, size, shape, or arrangement have a significant impact on stomatal functioning.

In the model plant *Arabidopsis thaliana* and many agriculture-relevant species from the families *Solanaceae* or *Fabaceae*, the neighbouring cells can vary in number, size and/or be rather subtly morphologically different from the rest of the epidermal cells, and thus often not classified as SCs when the morphological definitions are used. Therefore, they are rather commonly referred as neighbouring cells, pavement cells or simply epidermal cells.

Even though *Arabidopsis* neighbouring cells vary in shape and size and do not present a fully consistent pattern as observed in *Brachypodium* or *Kalanchoë*, they may still be physiological relevant since the osmotic and turgor changes occurring in the GCs require a mechanical accommodation and/or a source-sink of solutes and water which may be provided by the neighbouring cells regardless of their morphology. Thus, they may still be real "helper cells" and therefore, functionally SCs, but significantly differing in their functional efficiency.

Until now, only few players have been shown to participate in both *Arabidopsis* GCs and neighbouring cells (or SCs), in an opposite manner in response to environmental stimuli. PATROL1 is Munc13-like protein involved in mediating the translocation of a major H^+-ATPase AHA1 during stomatal movements promoting stomatal opening and CO_2 capture (Hashimoto-Sugimoto et al. 2013; Higaki et al. 2014). The dynamic expression of *PATROL1* in both GCs and in neighbouring cells suggests that neighbouring cells indeed hold a unique molecular identity differentiated from the rest of pavement cells (Higaki et al. 2014). Furthermore, they seem play an active functional role in the regulation of stomatal movements (Higaki et al. 2014; Hashimoto-Sugimoto et al. 2013) which suggests that they should be considered real helper cells and therefore SCs.

AtPIP2;1 aquaporin dynamics were also shown to be regulated in a cell-type specific manner in both *Arabidopsis* GCs and SCs and play a positive role in pathogen-associated responses (Cui et al. 2021a). Furthermore, a non-autonomous stomatal control by pavement cell turgor via the K^+

channel subunit AtKC1 was recently described, highlighting the relevance of integrating the neighbouring epidermal cells in stomatal functioning studies (Nieves-Cordones et al. 2022).

Fluxes of potassium and chloride ions have been early demonstrated between neighbouring cells and GCs in *Commelina communi* (Penny and Bowling 1974; Penny et al. 1976). One study comparing *Citrus limon* (containing paracytic stomata), *Citrus aurantifolia* (paracytic stomata), *Citrus paradisi* (paracytic and hemiparacytic stomata), *Citrus sinensis* (paracytic and anomocytic stomata) and *Citrus reticulata* (paracytic, branchyparacytic and anomocytic stomata) suggested that the level of transpiration may be related with the number of epidermal cells in direct contact with the GCs (Obiremi and Oladele 2001).

Overall, the molecular identity of SCs of non-grass species remains mostly unexplored. Most of the studies in stomatal physiology focus on GC signalling and many studies were performed in epidermal peels where the neighbouring cells are disrupted and the GCs removed from their tissue context, which has contributed to neglecting the relevance of SCs.

In grasses, SCs seem to have been developmentally and functionally improved. Experimental and mathematical models suggest that that grass SCs enhance stomatal responsiveness and gas exchange efficiency by (i) mechanically accommodate the GCs and providing a geometrical advantage resulting in a lower lateral GC displacement to reach large stomatal pore areas due to their elongated shape, (ii) functioning as a source/sink of ions allowing an optimized see-sawing of osmotic/turgor pressure, and (iii) providing additional signalling to improve stomatal reactivity (Fig. 0.3) (Franks and Farquhar 2007; Chen et al. 2017; Nunes et al. 2020). Still, the molecular mechanisms behind these molecular functions remain highly uncharacterized.

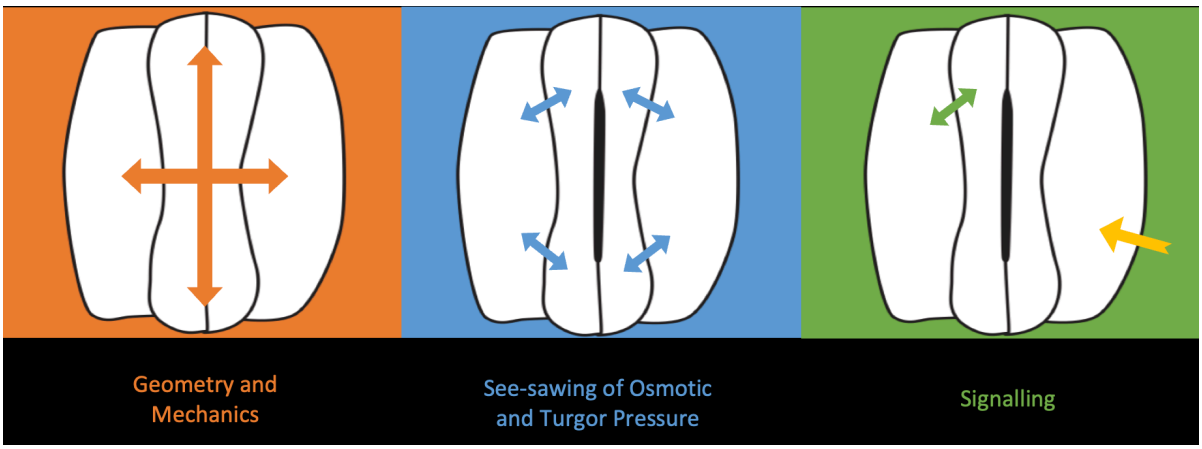


Figure 0.3 – Proposed contributions of SCs for improved stomatal movements in grasses (i) SCs seem to mechanically accommodate GCs during stomatal movements and facilitate the lateral displacement of GCs; (ii) SCs seem to function as a source/sink of ions providing a quick seesawing of osmotic and turgor pressure and (iii) SCs might provide additional signalling to improve stomatal responsiveness.

Regarding mechanical accommodation, grass GCs seem to significantly displace laterally in the direction of the SCs during stomatal opening. SCs seem to be squeezed by the GCs and therefore accommodating and facilitating the inflating GCs during stomatal opening (Fig. 0.1) (Franks and Farquhar 2007). Furthermore, the unique dumbbell-shape of the GCs provides clear geometric advantages for stomatal apertures. The elongated graminoid pores geometrically allow for larger pore area changes with less lateral displacement of the GCs (Franks and Farquhar 2007).

Regarding ion shuffling, stains of the K^+ and Cl^- in the epidermis of maize leaves suggested that an inversed ion shuffling occurs between GCs and SCs during stomatal movements (Raschke and Fellows 1971). Samples adapted to dark displayed closed stomata where an enrichment in ions could be observed in SCs. Oppositely, samples adapted to light conditions displayed opened stomata, in which an enrichment in ions could be observed in GCs (Raschke and Fellows 1971). In barley, it was also shown that K^+ and Cl^- ions shuttle from SCs to GCs during stomatal opening and from GCs to SCs during stomatal closure (Schäfer et al. 2018). It was also observed in maize that exogenous H_2O_2 led to a decrease in cation levels (Ca^{2+} and K^+) in GCs and an increase in the SCs, which resulted in stomatal closure (Zhang et al. 2020). Oppositely DPI (NADPH oxidase inhibitor diphenyleneiodonium) treatments, decreased Ca^{2+} and increased K^+ increased in GCs, but both Ca^{2+} and K^+ decreased in SCs, resulting in stomatal opening (Zhang et al. 2020). These observations suggest that GCs and SCs are osmotically regulated in an inversed manner and that a coordinated seesawing of ions contributed to the enhanced stomatal movements in grasses (Fig. 0.1, 0.2). Furthermore, the dumbbell-shape decreases the volume to surface ratio resulting in reduced requirement of ions and water to trigger turgor changes (Franks and Farquhar 2007).

In *B. distachyon*, it has been demonstrated that SCs are indeed required for fast stomatal movements and wider stomatal pores (Raissig et al. 2017). *bdmute* mutants lacking SCs show highly defective stomatal movements in response to light changes and the stomatal pores in *bdmute* mutants are half of the wild-type pore areas (Raissig et al. 2017). Consequently, maximum stomatal conductance

(the rate of water vapor exiting through stomata when stomata reach their putative maximum stomatal pore areas) is highly reduced in *bdmute* mutants (Raissig et al. 2017).

Regarding signalling, SC-specific signalling for the regulation of stomatal movements in grasses has been recently described. One SC-specific player has been molecularly characterized in maize (Wang et al. 2019). *ZmCST1* is a functional glucose transporter belonging to the SWEET family (Clad I Sugars Will Eventually be Exported Transporters) specifically expressed in SCs. *cst1* mutants display reduced stomatal conductance suggesting that *ZmCST1* positively regulates stomatal opening. Furthermore, it was shown that carbon starvation induces *ZmCST1* expression while accumulation of photoassimilates repress its expression (Wang et al. 2019). These findings suggest that *ZmCST1* function as a signalling link between photosynthetic status and stomatal functioning to optimize stomatal opening according to the necessity of carbon, therefore limiting unnecessary water loss.

Also one receptor-like kinase *ZmRLK1* was found to be expressed specifically in SCs, suggesting the occurrence of Ca^{2+}-dependent SC-specific signalling (Sun et al. 2022).

Regarding SC morphology, two major shapes can be observed in grasses: elongated and triangular SCs. Elongated SCs can be found in stomatal complexes of *Brachypodium distachyon*, *Avena sativa*, *Triticum aestivum* and *Hordeum vulgare* (Brett and Ng 2022). Triangular SCs can be observed in *Oryza sativa* and *Zea mays* (Pitaloka et al. 2021; Wang et al. 2019). Whether this morphological variation has an impact on stomatal functioning remains unknown.

1.4 Stomatal formation in grasses for optimal functionality

The regulation of stomatal numbers and size is essential for optimal stomatal function. The development of the leaf epidermis in grasses is organized in vertical cell files which develop from transversal cell divisions followed by longitudinal cell elongation (Stebbins and Shah 1960; Raissig et al. 2017; Nunes et al. 2020; Kavanová et al. 2006). Only certain files gain the ability to produce stomata (Raissig et al. 2016; Stebbins and Shah 1960).

The core regulators of grass stomatal development have been described in grasses (Raissig et al. 2017; Raissig et al. 2016; Liu et al. 2009; Serna 2021; Wu et al. 2019; Wang et al. 2019) (Fig. 0.4). After

acquiring competence for stomatal development, an asymmetric transversal division generates a smaller distal cell that will further produce GCs, therefore named guard mother cell (GMC). The other cell will generate a pavement cell (Stebbins and Shah 1960). SPCH1 and SPCH2 are two bHLH transcription factors required for the establishment of stomatal files and for GMC identity (Raissig et al. 2016; Wu et al. 2019). In *B. distachyon*, *bdspch1* and *bdspch2* display reduced stomatal density. Interestingly, *bdspch2* mutants have a stronger defect on stomatal density than *bdspch1*, and only double-mutants completely lack stomata which suggests partial redundancy between these stomatal initiation transcription factors (Raissig et al. 2016). *SPCH1* and *SPCH2* seem to act together with a third bHLH transcription factor, *ICE,* since not only *spch1 spch2* double-mutants but also *ice1* mutants lack stomata (Raissig et al. 2016; Wu et al. 2019).

Afterwards, the GMCs induce the lateral neighbouring cells to acquire subsidiary mother cell (SMC) identity and subsequently, an asymmetric longitudinal division forms the flanking SCs. This step is defined by BdMUTE. BdMUTE is a mobile bHLH transcription factor that is initially expressed in GMCs and then moves laterally to specify SMC identity and recruit the SCs (Raissig et al. 2017). *bdmute* mutants lack SCs and displayed smaller stomatal pores and highly irresponsive stomatal movements in response to changing light intensity (Raissig et al. 2017). *BdMUTE* overexpression driven by maize ubiquitous promoter induced SMC-like additional divisions in the pavement cells, resulting in multiple layers of SCs surrounding stomata and prickle hair cells (Raissig et al. 2017).

After SC formation, a symmetrical longitudinal division occurs in GMCs generating the two immature GCs. Afterwards, the stomatal complex undergoes cell elongation and maturation. BdSCRM2 is required for the stomatal differentiation after the final symmetric GMC division (Raissig et al. 2016). Therefore, SCRM2 likely acts together with FAMA, which is the key player to drive stomatal morphogenesis to form the elongated and mature dumbbell-shaped GCs (Liu et al. 2009; Wu et al. 2019). Furthermore, *bdmute* mutants also displayed approximately 30 % of defective GMC divisions and aborted GCs, suggesting an additional role of BdMUTE in GMC progression and GC morphogenesis, as observed in maize and rice since neither GCs or SCs are formed in *osmute* and *zmmute* mutants (Wang et al. 2019; Serna 2021).

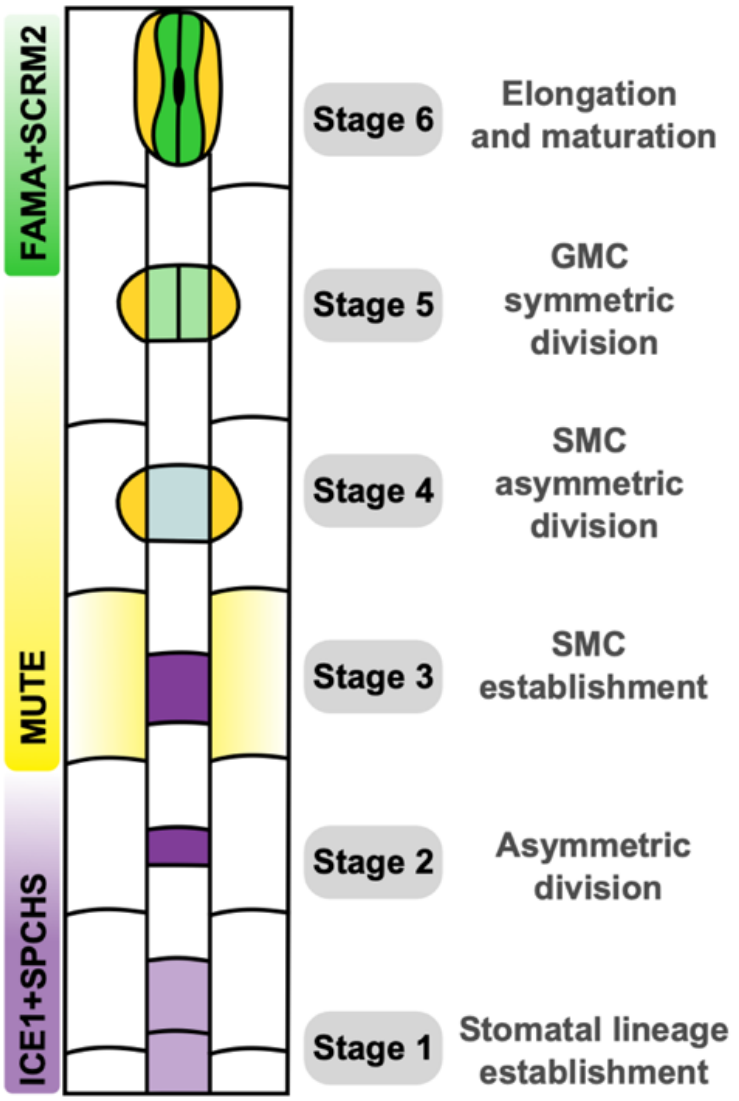


Figure 0.4 – Model of stomatal development in grasses. ICE1, SPCH1 and SPCH2 initiate and establish the stomatal lineage which starts an asymmetric cell vision that generates a smaller cell that originates a guard mother cell (GMC) and a bigger cell that will form a pavement cell (stage 1-2). BdMUTE induces subsidiary mother cell (SMC) identity, and an asymmetric cell division to recruit the subsidiary cells (SCs) (stage 3-4). GMCs undergo a symmetric cell division originating immature GCs (stage 6). FAMA and SCRM2 are involved in the elongation and maturation of the stomatal complexes (stage 6).

While the core genetic programs regulating stomatal development have been described in grasses (Raissig et al. 2017; Liu et al. 2009; Serna 2021; Facette et al. 2015; Wang et al. 2019; Wu et al. 2019) (Fig. 0.4), the interplay between the intrinsic genetic programs and the environmental cues (e.g.,

light intensity, light quality, temperature, relative humidity, CO_2 concentration) remains mostly unexplored.

Light is the environmental cue that has been studied the most in *Arabidopsis*. During light conditions, the red-, far-red- and blue-light receptors phyB, phyA and CRY1/2 inhibit two negative regulators of stomatal development, the E3 ubiquitin-protein ligase COP1 and the phytochrome interacting factor PIF4, therefore inducing stomatal formation (Lee et al. 2017). COP1 seems to induce the degradation of SPCH and ICE1, while PIF4 represses the transcription of *SPCH*, thus inhibiting stomatal formation (Wei et al. 2020; Lee et al. 2017). *SPCH* repression by PIF4 has also been associated with regulation of stomatal development in response to high temperature in *Arabidopsis* (Lau et al. 2018).

Molecular evidence on the mechanisms of light regulation of stomatal development in grasses is limited. It has been shown that *osphyb1* and *osphb2* mutants displayed reduced stomatal density, suggesting that the light receptor phyB is also involved in the perception of light to regulate stomatal development in rice (Liu et al. 2012). The heterologous expression of the rice *OsCOP1* rescued the leaf expansion and stomatal development phenotype in the *Arabidopsis atcop1* mutants (Ranjan et al. 2014). Also, the heterologous expression of the maize *ZmPIF4 and ZmPIF5* could partially or fully rescue the hypocotyl elongation phenotype of *Arabidopsis atpif1;3;4;5* mutants, suggesting that the function of these morphogenesis light-signalling players has been conserved in grasses. Still, if these genes are also directly involved in the regulation of stomatal development in grasses remains unknown. Overall, how the environment influences stomatal development and environmental-responsive genetic programmes regulating stomatal numbers and size remain unexplored in grasses.

Stomatal anatomical traits such as stomatal density and size have a significant impact on stomatal speed and water use efficiency. It has been demonstrated that reducing stomatal numbers in rice, maize, barley and wheat reduced water transpiration, improving water use efficiency and drought tolerance (Caine et al. 2018; Xiang et al. 2020; Hughes et al. 2017; Dunn et al. 2019). On the other hand, it has also been observed that stomatal density increased in response to water deficit, which

positively correlated with water-use efficiency in the perennial grass *Leymus chinensis* (Xu et al. 2008).

Therefore, engineering grass species with higher water-use efficiency and tolerance to abiotic stresses by modifying stomatal formation seems to be a useful approach, but that will still require the integration of known core regulators of stomatal development (e.g., SPCH and MUTE) with environmental-responsive modulators of stomatal development.

2. Aims of the study

The overall aim of this study was to identify and characterize novel players associated with the unique and improved stomatal form and function of graminoid stomata in the grass model *Brachypodium distachyon.* To fulfil this goal, I aimed to:

I. Establish and characterize stomatal kinetics and leaf-level gas exchange in the model grass *B. distachyon* (Chapter I);

II. Quantify the systemic effects of environmental fluctuations on leaf-level gas exchange and stomatal anatomical traits and the relationships between stomatal form and function in *B. distachyon* (Chapter I)*;*

III. Perform a reverse genetics screening to identify genes associated with fast stomatal movements and water-use efficient gas exchange in *B. distachyon* (Chapter II)

IV. Characterize a selected candidate gene associated with grass stomatal form and function for improved and water-use efficient stomatal movements (Chapter III).

3. Results and discussion – Chapter I

Environmental systemic effects on stomatal anatomical and functional traits in *Brachypodium distachyon*

3.1 Introduction

Stomata perceive and integrate an array of fluctuating environmental triggers such as light intensity and quality, relative humidity, temperature, carbon dioxide concentration and also biotic factors like pathogens to optimize carbon dioxide uptake for photosynthesis and save water by limiting transpiration (Engineer et al. 2016; Kollist et al. 2014; Merilo et al. 2014; Murata et al. 2015).

Light is a central environmental factor regulating stomatal movements and highly variable both in daily time scales and among seasons. When light intensity is high, stomata open to supply sufficient carbon dioxide for photosynthesis (in C_3 and C_4 plants). On the contrary, when light intensity decreases and photosynthesis is light-limited, less carbon dioxide is required to saturate photosynthetic reactions and, consequently, stomata close to reduce water vapour loss (Kollist et al. 2014). Therefore, stomatal responsiveness and fast opening and closing stomatal movements can significantly contribute to plant water use efficiency (WUE) which represents the ratio of assimilated carbon to loss water and is an important trait for plant productivity and abiotic stress resistance (McAusland et al. 2016; Leakey et al. 2019; Lawson and Vialet-Chabrand 2019). The grass family *Poaceae* shows faster stomatal movements in comparison to other plant groups which contributes to high water-use efficiency in dynamic environments (Franks and Farquhar 2007; McAusland et al. 2016; Lawson and Matthews 2020; Chen et al. 2017).

Stomata can respond locally to environmental stimuli, which means that different parts of the plant exposed to different conditions can locally optimize their stomatal pores and gas exchange. This allows leaf gas exchange studies (using IRGAs, infra-red gas analysers) to be robust since leaves are placed in a closed leaf chamber and exposed to controlled light, humidity, temperature, and CO_2 concentration regardless of the external ambient conditions. Nonetheless, external ambient conditions may systemically influence the local stomatal responses controlled and measured in the IRGA leaf chamber (Devireddy et al. 2018; Ehonen et al. 2020; Devireddy et al. 2020; Zandalinas et al. 2020). Such systemic effects on stomatal functioning are especially important for gas exchange studies performed in glasshouses or outdoors in the field where environmental conditions highly fluctuate both daily and seasonally. Notwithstanding, the systemic influence of the varying ambient conditions on local leaf-level gas exchange measurements is generally not considered.

Additionally, the speed of stomatal movements, leaf gas exchange levels (carbon assimilation, A and stomatal conductance to water vapor, g_{sw}) and intrinsic water use efficiency (iWUE, A / g_{sw}) seem to be influenced by the stomatal anatomical traits: stomatal density (SD) and stomatal length (SL) (Haworth et al. 2021; Faralli et al. 2019; Lawson and Blatt 2014; Elliott-Kingston et al. 2016; Bertolino et al. 2019; Sun et al. 2014; Bachle and Nippert 2022).

SD and SL are broadly negatively correlated interspecifically and intraspecifically in response to the environmental conditions experienced during plant growth (Bertolino et al. 2019; Franks et al. 2009; Zhang et al. 2021).

The seasonal variation of environmental conditions such as light availability and temperature might significantly alter stomatal anatomical traits. As a result, gas exchange and stomatal behaviour may be affected and, consequently, the results of long-term gas exchange phenotyping studies.

I quantified light-response stomatal kinetics in 120 wildtype *Brachypodium distachyon* (Bd21-3) individuals in a glasshouse over the course of two years (between May 2019 and September 2021). Furthermore, the environmental conditions in the glasshouse (Q_{out}, T, RH) were logged and time of the day (time) when the measurements were performed was registered. I quantified how these environmental parameters affected the leaf-level gas exchange parameters (stomatal opening and closure kinetics, iWUE, A and g_{sw}). I additionally quantified stomatal anatomical traits (SD and SL) from a subset of plants grown in three different periods of the year (representing the seasons summer, autumn, and winter) and further correlated how variations in the stomatal anatomical traits SD and SL influenced leaf-level gas exchange (g_{sw}, A and iWUE), stomatal opening and closing kinetics and maximum stomatal conductance ($g_s$max).

Together with a master student Magdalena W. Slawinska, we calculated anatomical $g_s$max based on anatomical traits and realized that the current approaches to estimate maximum stomatal pore area and stomatal pore depth were not suitable for graminoid stomata. Magdalena W. Slawinska quantified the morphometry of open and closed *B. distachyon* stomata which allowed us to accurately calculate maximum stomatal pore area and pore depth for graminoid stomata in *B. distachyon* and therefore predict of $g_s$max based on the stomatal anatomical traits. Furthermore, me and Magdalena briefly explored other grass species available in the Botanical Garden of the

University of Heidelberg and I discuss the morphological diversity of grass stomata and gas exchange.

Note: The data shown in this chapter has been partially published: Nunes, T.D.G., Slawinska, M.W., Lindner, H., & Raissig, M.T. (2022). Quantitative effects of environmental variation on stomatal anatomy and gas exchange in a grass model. Quantitative Plant Biology, 3, E6. doi:10.1017/qpb.2021.19.

3.2 Material and methods

3.2.1 Plant material and growth conditions

I vernalized wild-type *Brachypodium distachyon* (Bd21-3) seeds in water for two days at 4°C in darkness. Then, I transferred the seeds to pots (one 6 cm X 6 cm X 8 cm pot per plant) containing four parts of soil (Einheitserde CL ED73) and one part of vermiculite. *B. distachyon* plants grew in a glasshouse with a light-dark cycle of 18 h light:6 h darkness, average day temperature = 28°C, average night temperature = 25°C and average relative humidity = 40 %. The glasshouse is in the University of Heidelberg (Centre for Organismal Studies Heidelberg, Im Neuenheimer Feld 360). I performed this study between 01/2019 and 09/2021 and the daily average temperatures outside of the glasshouse seasonally varied as: 3-5°C in winter (from December and February), 8-11°C in spring (March and April), 13-21°C in summer (from May to September) and 6-12°C in Autumn (October and November) (Deutscher Wetterdienst, https://cdc.dwd.de/portal/). Daylight hours varied between 8.3-10.2 hours in winter (from December to February), 11.9-13.8 h in spring (March and April), 12.6-16.2 h in summer (from May to September) and 9.1-10-8 h in autumn (October and November) (Deutscher Wetterdienst, https://cdc.dwd.de/portal/).

3.2.2 Leaf-level gas exchange measurements: light-responses

I performed leaf-level gas exchange measurements on plants three weeks after sowing using a LI-6800 Portable Photosynthesis System (Li-COR Biosciences Inc., Lincoln, NE, USA) equipped with a Multiphase Flash Fluorometer (6800-01A) chamber (2 cm^2). I used the youngest and fully

expanded leaf for the light-response measurements with LI-6800 conditions as follows: flow rate=500 μmol s^{-1}; fan speed=10000 rpm; leaf temperature=28°C; relative humidity (RH)=40 %; [CO_2]=400 μmol mol^{-1}; photosynthetic active radiation (PAR), 1000 – 100 – 1000 – 0 μmol PAR m^{-2} s^{-1}, 20 min per light step (Fig. 1.1). Gas exchange measurements were automatically logged every minute. The first 15 min of the first step (1000 PAR) were discarded as plants were adapting to the leaf-chamber conditions. I performed light-response kinetics on 120 individuals and characterized stomatal movements and water use efficiency in the model grass *B. distachyon*. I calculated relative g_{sw} normalizing g_{sw} to the highest g_{sw} value registered to evaluate stomatal kinetics regardless of variations in absolute g_{sw} and calculated intrinsic water-use efficiency (iWUE) as the A to g_{sw} ratio (A/g_{sw}). Since *B. distachyon* leaves have reduced dimensions and do not fill the 2 cm^2 leaf chamber, I measured the individual leaf area of 35 individuals allowing me to also assess absolute gas exchange parameters (i.e., g_{sw} and A).

Ambient light intensity (Q_{out}) was monitored during the measurements using an external LI-190R PAR Sensor located on top of the LI-6800. Glasshouse ambient temperature and relative humidity were monitored during these experiments using an Onset HOBO U12-O12 4-channel data logger (Onset Computer Corporation, Bourne, MA, USA) that was placed nearby the plants. I did one-phase decay/association non-linear regressions for the stomatal closure transitions I (1000 – 100 PAR) and III (1000 – 0 PAR), and for stomatal opening transition II (100 – 1000 PAR), respectively, to determine half-time ($T_{50\%}$) and rate constant (k) of each light transition.

These leaf-level gas exchange measurements of WT *B. distachyon* (23-1) were performed during the screening of mutant lines described in the next chapter. While early on I observed variations in the LI-6800 measurements and hypothesized these could originate from fluctuations in light intensity and temperature, only *a posteriori* I performed this correlation analysis using the 120 individuals.

3.2.3 Leaf-level gas exchange measurements: physiological $g_s$max

Maximum stomatal conductance measurements (physiological $g_s$max) were performed using the LI-6800 (Li-COR Biosciences Inc., Lincoln, NE, USA) with the following settings: flow rate=500 μmol s^{-1}; fan speed=10000 rpm; leaf temperature=28°C; relative humidity (RH)=68-70 %; [CO_2]

=100 μmol mol^{-1}; PAR=1500 μmol PAR m^{-2} s^{-1}. Measurements were automatically logged every minute and I calculated physiological $g_s$max as the average of the last 5 minutes at steady state.

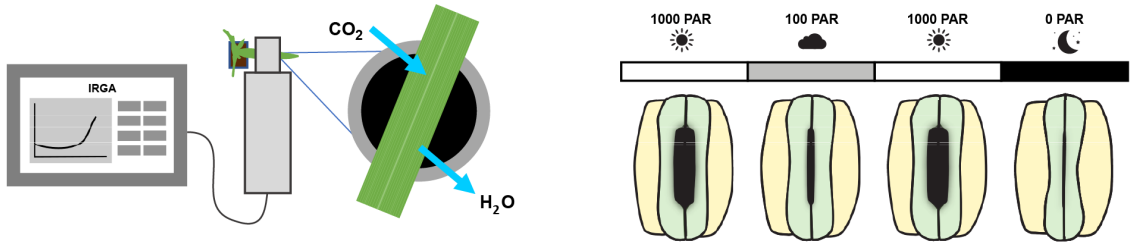


Figure 1.1 - Leaf-level gas exchange measurements in response to changing light intensity in *Brachypodium distachyon*
Experimental setup for measuring leaf-level gas exchange parameters related with carbon assimilation and water vapour loss using an infrared gas analyser (IRGA). Leaf-level gas exchange light-responses as 1000–100–1000–0 PAR. This is an original figure created by myself and adapted from the original published in Quantitative Plant Biology (Nunes et al. 2022) (doi.org/10.1017/qpb.2021.19, open-access (CC BY 4.0).

3.2.4 Stomatal anatomy measurements

I collected leaves from 15 individuals (5 from summer, 6 from autumn and 4 from winter) after the LI-6800 measurements and fixed them in 7:1 ethanol:acetic acid. For microscopy imaging, I rinsed the samples twice in water, mounted them in Hoyer's solution (supplementary table 12) and imaged the abaxial side using a Leica DM5000B microscope. I measured stomatal length (SL) and stomatal width at the apex (W_A) from 4-6 fields of view (0.0725 mm^2, 40X objective) per sample, which resulted in 20 - 70 stomata measured per individual sample. For stomatal density (SD), I counted stomata on 3-5 fields of view (0.290 mm^2, 20X objective) per individual which resulted in 60 - 160 stomata counted per individual.

3.2.5 Correlation analysis and statistics

I performed the correlation analysis including iWUE and half-time ($T_{50\%}$) of stomatal movements using the 120 samples. Additionally, I performed the correlation analysis for absolute gas exchange parameters (i.e., g_{sw} and A) using the 35 individuals for which the individual leaf area was assessed. I averaged the last 5 minutes at steady state of A, g_{sw} and iWUE at the different light steps (100, 1000 and 0 PAR) and their corresponding ambient conditions (Q_{out}, RH and T) for the pearson correlation analysis. For correlations between environment and stomatal anatomy, I obtained pearson correlation matrices using the average stomatal anatomical traits (i.e., SD and SL) and the

respective average environmental growth conditions (T, RH, and day length) of those individual plants.

After obtaining pearson correlation matrices, I represented significant correlations between pairs of parameters by linear or non-linear regressions. I represented statistically significant ($p<0.05$) and non-significant linear regressions with solid and dashed lines, respectively. Non-linear quadratic regressions were applied for the correlations including the variable time of the day, as this method is more adequate to represent this parameter as it contains an axis of symmetry and is more suitable to biologically represent the diurnal rhythms observed in gas exchange in C_3 plant species (Matthews et al 2018; Wu et al. 2019; Rho et al. 2018). I removed outliers using the ROUT method tool on GraphPad Prism (Motulsky and Brown 2006)

To test statistical significance between two groups, I performed unpaired t-tests. I performed one-way ANOVAs followed by Tukey's or Šidák multiple comparison tests to compare more than two groups. I indicated R^2, Sy.x and/or p values directly in the graphs. I performed all statistical analyses using GraphPad Prism version 9.1.0, GraphPad Software, San Diego, California USA, www.graphpad.com.

3.2.6 Morphometric analysis of graminoid stomatal complexes

The stomatal morphometric analysis to optimize anatomical $g_s$max calculations was performed by Magdalena W. Slawinska, as part of her master thesis, with my guidance. For the morphometric characterization of fully open stomata, Magdalena W. Slawinska treated the leaves with 4 μM fusicoccin solution (Cat. No. sc-200754, Santa Cruz Biotechnology, Inc., Dallas, TX, USA) in opening-closing buffer (50 mM KCl, 10 mM MES-KOH). For this, Magdalena W. Slawinska briefly immersed the samples in 70 % ethanol to disrupt hydrophobic forces at the leaf epidermis and infiltrated the samples with the fusicoccin solution using a needleless syringe on the adaxial side until the tissue was visibly saturated with fusicoccin solution. Then, Magdalena W. Slawinska did cut the samples into 3-5 mm long sections and further incubated the samples overnight in fusicoccin solution in the light to fully trigger stomatal opening. To characterise closed stomata, Magdalena W. Slawinska treated the leaves with 50 μM ABA (Product number 90769, Merck,

Darmstadt, Germany) solution in opening-closing buffer (50 mM KCl, 10 mM MES-KOH) as described above for the fusicoccin treatment, but instead the overnight incubation was done in the dark to stimulate fully stomatal closure. Finally, Magdalena W. Slawinska stained the samples with propidium iodide (10 μg/ml) (Cat. No. P3566, Thermo Fisher Scientific, Waltham, MA, USA) and obtained z-stacks using a Leica TCS SP8 confocal microscope (Leica Microsystems, Wetzlar, Germany) for 30 open (fusicoccin-treated samples) and 30 closed (ABA-treated samples) stomatal complexes. For each stoma, Magdalena W. Slawinska measured stomatal pore length (PL), stomatal pore width at the centre of the stoma (PW), GC length (GCL) and stomatal width at the apices (W_A) on z-stack projections (sum slices). The exact stomatal pore area was hand-traced with the polygon selection tool. To assess stomatal pore depth (l), Magdalena W. Slawinska selected the central pore section, resliced from the top and finally measured the stomatal pore depth on z-stack projections (sum slices) from previously resliced images.

3.2.7 Anatomical $g_s$max calculations

For the anatomical maximum stomatal conductance calculations, the anatomical $g_s$max equation from Franks and Farquhar (2001) was used, where SD is the stomatal density (stomata mm^{-2}), a_{max} is the maximum pore area (μm^2), l is the pore depth (μm), d is the diffusivity of water in air (0.0000249 $m^2\ s^{-1}$, at 25°C) and v is the molar volume of air (0.024464 $m^3\ mol^{-1}$, at 25°C).

3.2.8 Comparison between anatomical and physiological $g_s$max

To test if the improved anatomical $g_s$max calculations matched the LI-6800 measurements of $g_s$max, I collected the leaves from which I measured physiological $g_s$max. One section of the leaf was fixed with ethanol:acetic acid 7:1, from which afterwards, I used the Leica DM5000B microscope to image and measure GCL, W_A and W_C (to estimate pore depth and area) from 20-40 stomata per sample and counted stomatal density (SD) in five different 0.290 μm^2 fields of view per sample (20X objective) to calculate anatomical $g_s$max. In parallel, Magdalena W. Slawinska performed the fusicoccin treatments as previously described to induce full stomatal opening and calculated anatomical $g_s$max based on the accurate hand-traced pore depth and area.

3.3 Results

3.3.1 Leaf-level gas exchange measurements in *Brachypodium distachyon* are robust and revealed fast and efficient stomatal responses to fluctuating light

I measured leaf-level gas exchange parameters and light-response stomatal kinetics of 120 wild-type *B. distachyon* individuals (Bd21-3) over the course of two years to characterize stomatal movements in *B. distachyon* and quantify the consistency of leaf-level gas exchange measurements and stomatal kinetics.

To evaluate stomatal kinetics, I normalized stomatal conductance by the highest value to obtained relative stomatal conductance, which revealed consistent and highly reproducible stomatal light-responses (R^2= 0.66-0.76) (Fig. 1.2A, C-E). The first light transition from 1000 to 100 PAR resulted in a 70 % decrease in g_{sw} with a half-time of six minutes ($T_{-50\%}$ I = 6.02 min) (Fig. 1.2C). The second light transition from 100 to 1000 PAR induced stomatal opening with a half-time of less than five minutes ($T_{+50\%}$ II = 4.49 min) which resulted in an increase of g_{sw} to the same levels observed at the initial 1000 PAR light step (Fig. 1.2D). The third and final light transition from 1000 to 0 PAR resulted in rapid stomatal closure with half-time of only approximately three minutes ($T_{-50\%}$ III = 3.361 min) (Fig. 1.2E). The stomatal closure in response to darkness was then the quickest of the stomatal movements (Fig. 1.2E).

Regarding iWUE, 1000 PAR-adapted iWUE was on average 77 μmol CO_2/mol H_2O, while at 100 PAR iWUE was approximately 50 μmol CO_2/mol H_2O (Fig. 1.2B). I observed a significant variability in iWUE among the 120 measurements, particularly at the light-limited step of 100 PAR (Fig. 1.2B).

Regarding stomatal conductance (g_{sw}), I observed that g_{sw} was on average 0.29, 0.10 and 0.015 at 1000, 100 and 0 PAR, respectively (Fig. 1.2F). I observed a considerable variance in g_{sw} particularly at light-limited steps (100 and 0 PAR) (Fig. 1.2F). Finally, I observed an average carbon assimilation (A) of approximately 20 μmol m^{-2} s^{-1} at 1000 PAR and only 4 μmol m^{-2} s^{-1} at 100 PAR (Fig. 1.2G). Overall, I verified that *B. distachyon* presents fast and robust stomatal opening and closing, as generally observed in *Poaceae*. Still, I observed some degree of variability both in stomatal kinetics

(Fig. 1.2A, C-D), iWUE (Fig. 1.2B) and gas exchange levels (g_{sw} and A) (Fig. 1.2F, G). Therefore, I hypothesized that external environmental factors could be systemically influencing the IRGA-based leaf-level gas exchange measurements.

3.3.2 Environmental conditions vary daily and seasonally in glasshouse settings

The ambient environmental conditions varied significantly over the course of the 120 measurements. Temperatures varied between 22 and 34°C (Fig. 1.3A), light intensity between 200 and 500 PAR (Fig. 1.3B) and relative humidity between 30 and 80 % (Fig. 1.3D). I observed variations both at a daily and seasonal scales. A significant increase in temperature was observed during the day from 6:00 to 18:00 h (Fig. 1.3A). The daily variation in light intensity and relative humidity were less significant (Fig. 1.3B, C). Still, higher light intensities may be observed after noon and relative humidity seems to peak at noon (Fig. 1.3B, C).

When looking from a seasonal perspective, I categorized the measurements in warm and cold seasons. Warm season corresponds to spring and summer (may to august) and the cold season corresponds to autumn and winter (September to February). The temperatures and light intensities registered in the warm season were significantly higher than in the cold season (Fig. 1.3D, E). On the other hand, I observed no significant difference in relative humidity between the two seasons (Fig. 1.3F).

With these observations, I hypothesized that leaf-level gas exchange could be systemically influenced by the daily variations in environmental conditions. Furthermore, I also hypothesized that the significant seasonal variation in temperature and light intensity could influence stomatal development and consequently lead to changes in stomatal density and size.

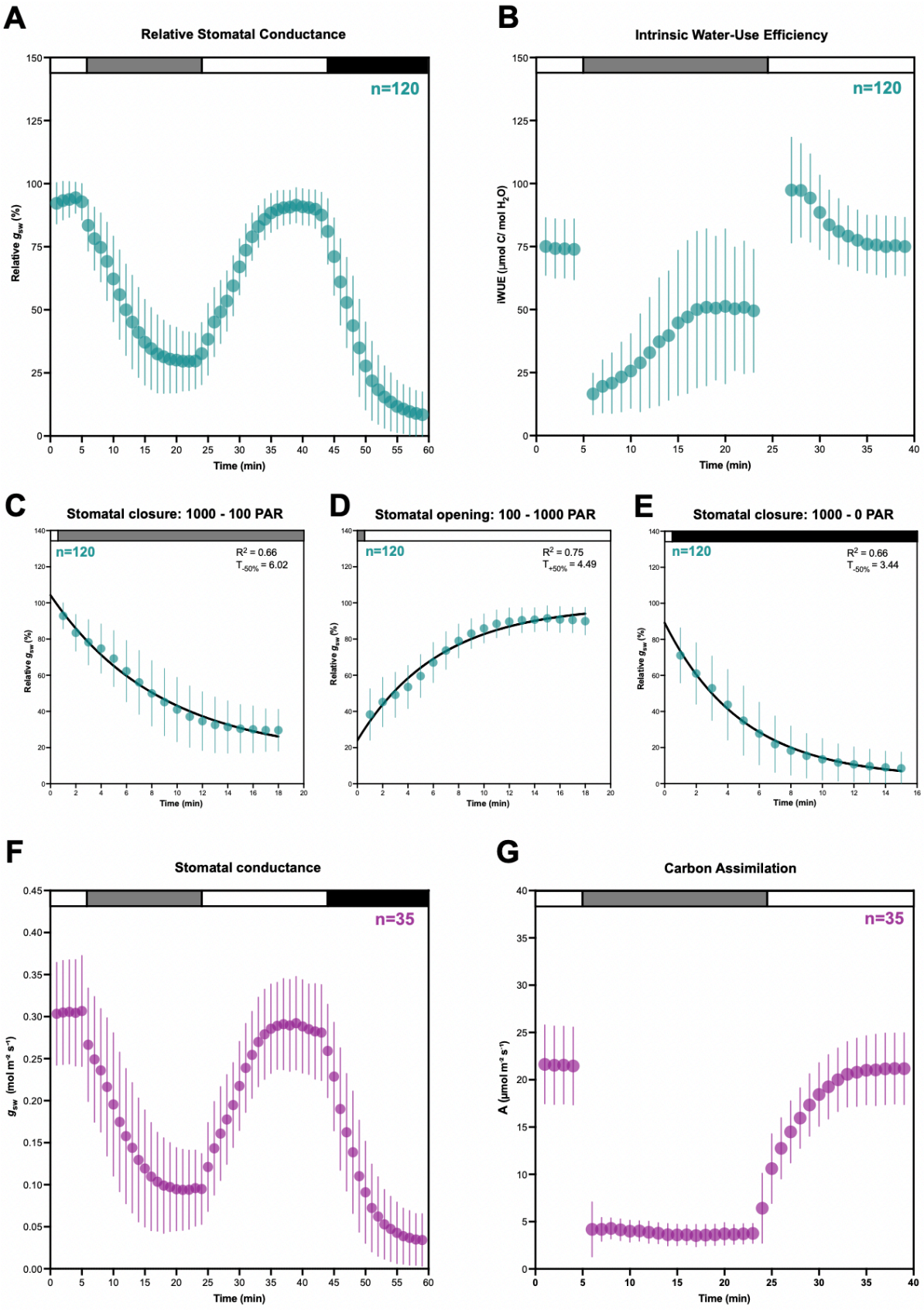


Figure 1.2 – Characterization of stomatal movements and gas exchange in *Brachypodium distachyon* (A) Relative stomatal conductance (Rel g_{sw}) in response to changing light 1000-100-1000-0 PAR (n=120). **(B)** Intrinsic water-use efficiency (iWUE) in

response to changing light 1000-100-1000 PAR (n=120). **(C)** One-phase decay exponential regression for stomatal closure (step I) in response to decreasing light intensity from 1000–100 PAR (n = 120). **(D)** One-phase association exponential regression for stomatal opening (step II) in response to increasing light intensity from 100–1000 PAR (n = 120). **(E)** One-phase decay exponential regression for stomatal closure (step III) in response to increasing light intensity from 1000–0 PAR (n = 120). R^2 and half-times ($T_{\pm 50}$) are indicated in the graphics. **(F)** Absolute stomatal conductance (g_{sw}) in response to changing light 1000-100-1000-0PAR (n=35). **(G)** Carbon assimilation (A) in response to changing light 1000-100-1000-0 PAR (n=35). Error bars represent SD.

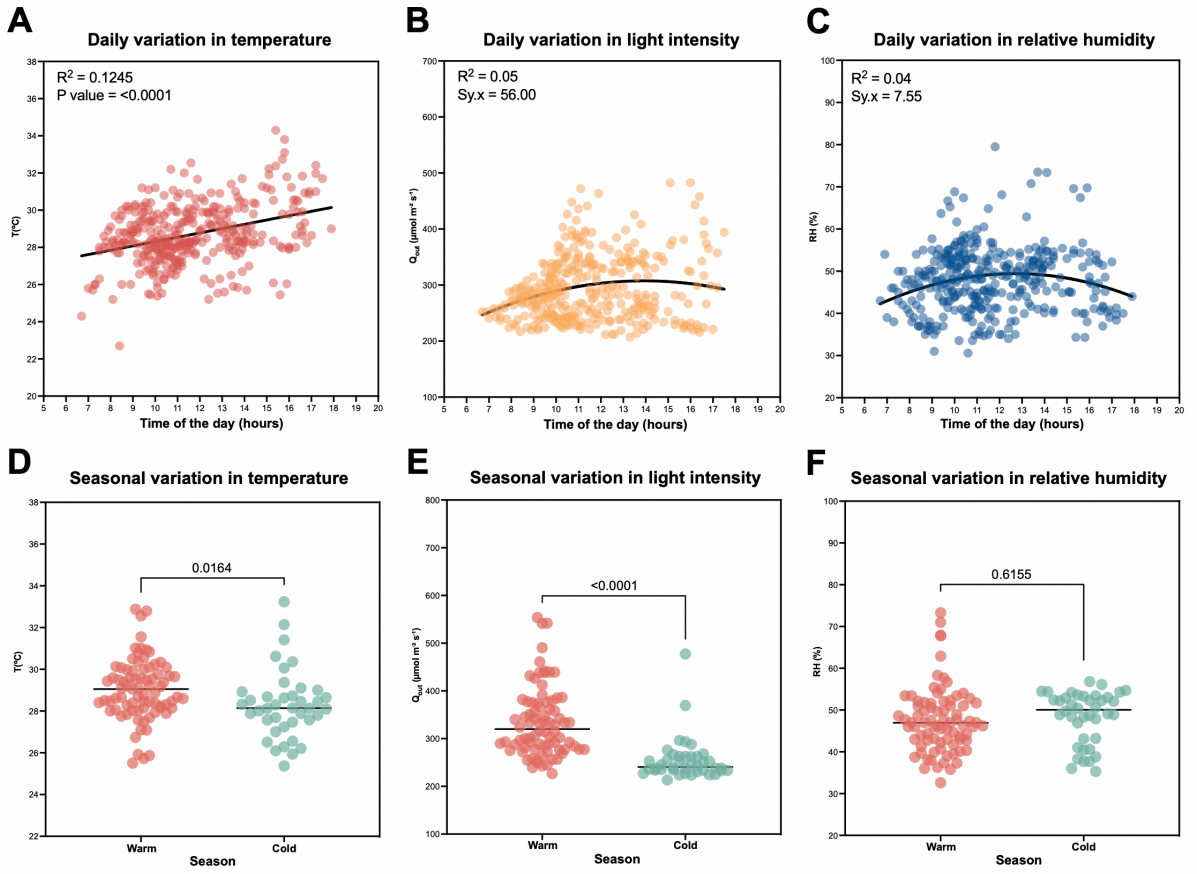


Figure 1.3 – Daily and seasonal variation in temperature, light intensity and relative humidity registered during LI-6800 measurements of the 120 individuals. (A) Daily variation in temperature (T) (n=360 time points). **(B)** Daily variation in light intensity (Q_{out}) (n=360 time points). **(C)** Daily variation in relative humidity (RH) (n=360 time points). **(D)** Seasonal variation in temperature (T) (n=80 in warm season; n=40 in cold; each dot represents the average temperature registered during one LI-6800 measurement). **(E)** Seasonal variation in light intensity (Q_{out}) (n=80 in warm season; n=40 in cold; each dot represents the average temperature registered during one LI-6800 measurement). **(F)** Seasonal variation in relative humidity (RH) (n=80 in warm season; n=40 in cold; each dot represents the average temperature registered during one LI-6800 measurement). P values from unpaired t-tests.

3.3.3 Environmental fluctuations systemically influence gas exchange measurements

To test the systemic effect of varying environmental conditions on leaf-level gas exchange, I performed correlation analysis between gas exchange parameters and environmental conditions (temperature (T), ambient light intensity (Q_{out}), relative humidity (RH) and time of the day (time)) for the three light steps (100 PAR low light, 1000 PAR high light and 0 PAR darkness). I used the 120 samples for the correlation analysis of relative parameters (iWUE and stomatal half-times), while 35 samples were used for correlations including absolute gas exchange parameters (g_{sw} and A). Regarding iWUE, I observed a negative correlation between iWUE and T at both low and high light intensities (pearson correlation coefficient of -0.28 and -0.26, respectively) (Fig. 1.4A, B). This negative correlation can be represented by a significant linear regression ($p<0.05$) with increasing temperatures resulting in decreasing iWUE (Fig. 1.4C, D).

Furthermore, iWUE was also negatively correlated with time at both low and high light conditions (pearson correlation coefficient of -0.22 and -0.31, respectively) (Fig. 1.4A, B). I used non-linear quadratic regressions to represent the correlation between time and iWUE. A quadratic relation mathematically demonstrates that the lowest iWUE values were reached at midday, particularly at low light (Fig. 1.4E) while a weaker correlation was observed at high light (Fig. 1.4F). No significant correlations were found between iWUE and RH or Q_{out} (Fig. 1.4A, B).

When evaluating stomatal kinetics, I observed that stomatal closure but not opening (i.e., half-time) was influenced by diurnal rhythms (i.e., time of the day) (Fig. 1.5A-F). Specifically, I observed slower stomatal closure (longer stomatal half-time) at noon (Fig. 1.5C, F). Furthermore, stomatal closure and opening half-times were strongly positively correlated with initial and/or final g_{sw} levels (Fig. 1.6A). Specifically, stomatal closure triggered by decreasing light from 1000 to 100 or to 0 PAR ($T_{-50\%}$ I and $T_{-50\%}$ III, respectively) dependent on both initial and final g_{sw}, with a stronger dependency on final g_{sw} levels (Fig. 1.6A). On the other hand, stomatal opening half-time in response to an increase in light intensity from 100 to 1000 ($T_{+50\%}$ II) was positively correlated with final step g_{sw} but not with initial g_{sw} (Fig. 1.6A). These results indicate that stomatal closure is slower (higher half-times) when stomatal conductance levels are higher. Stomatal opening seems to be

slower (higher half-times) when stomata must open wider to reach higher final g_{sw}. Overall, stomatal kinetics were conditioned by the steady-state gas exchange parameters.

Regarding steady-state gas exchange, A and g_{sw} showed significant correlations with different environmental parameters (Fig. 1.6B-D). Ambient light intensity (Q_{out}) was positively with both g_{sw} and A at high light (pearson correlation coefficients 0.36 and 0.39, respectively, but not at low light (pearson correlation coefficients 0.17 and 0.11, respectively) (Fig. 1.6B, C). Therefore, increasing ambient light intensity triggered a significant linear increase in A and g_{sw} ($p < 0.05$) at 1000 PAR (Fig. 1.6E, F). No significant correlation was observed between Q_{out} and g_{sw} at 0 PAR (Fig. 1.6D).

Temperature (T) exerted a strong positive influence on g_{sw} in all light conditions (100, 1000 and 0 PAR (pearson correlation coefficient of 0.39, 0.50 and 0.29 respectively), but did not significantly correlate with A (Fig. 1.6B-D). Increasing ambient temperatures resulted in significant linear increases of g_{sw} ($p<0.05$) (Fig. 1.6G-I).

Since both A and g_{sw} were positively influenced by Q_{out}, but only g_{sw} was influenced by T, this observation helps explaining why iWUE ($= A/g_{sw}$) was positively correlated exclusively with T and not with Q_{out} (Fig. 1.4A, B)

Finally, relevant correlations were observed between the time of the day and g_{sw} at all light conditions (100, 1000 and 0 PAR) (Fig. 1.6J-L). Particularly at 100 and 0 PAR, g_{sw} seams to peak at noon (Fig. 1.6J, L), which suggests the influence of systemic diurnal rhythms in stomatal behaviour.

Overall, I verified that variations in ambient temperature and light intensity were perceived by the plants and systemically influenced leaf-level gas exchange measurements and/or stomatal kinetics. Furthermore, diurnal rhythms seem to affect overall stomatal regulation conditioning leaf-level gas exchange measurements, underlining the importance of considering systemic effects of the environmental conditions experienced by the plants outside the leaf chamber during leaf-level gas exchange studies.

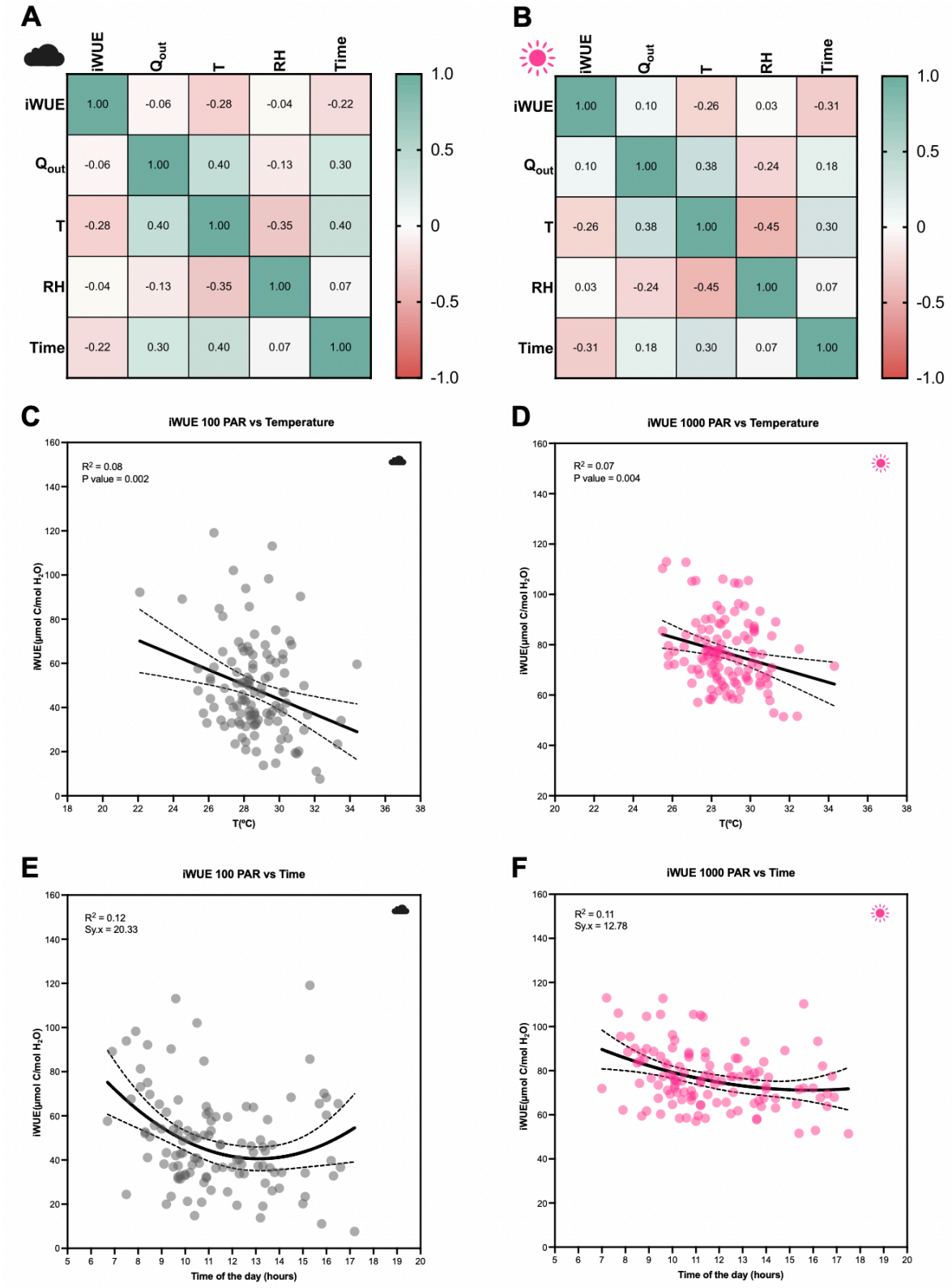


Figure 1.4 – Correlations between intrinsic water-use efficiency and environment. (A) Pearson correlation matrix between iWUE at 100 PAR, ambient light (Q_{out}), temperature (T), relative humidity (RH) and time of the day (time) (n=120). **(B)** Pearson correlation matrix between iWUE at 1000 PAR, Q_{out}, T, RH and time (n=120). **(C)** Linear regression between T and iWUE at 100 PAR (n=120). **(D)** Linear regression between T and iWUE at 1000 PAR (n=120). **(E)** Non-linear regression between time and iWUE at 100 PAR (n=120). **(F)** Non-linear regression between time and iWUE at 1000 PAR (n=120). R^2, p values and/or Sy.x directly in the graphics.

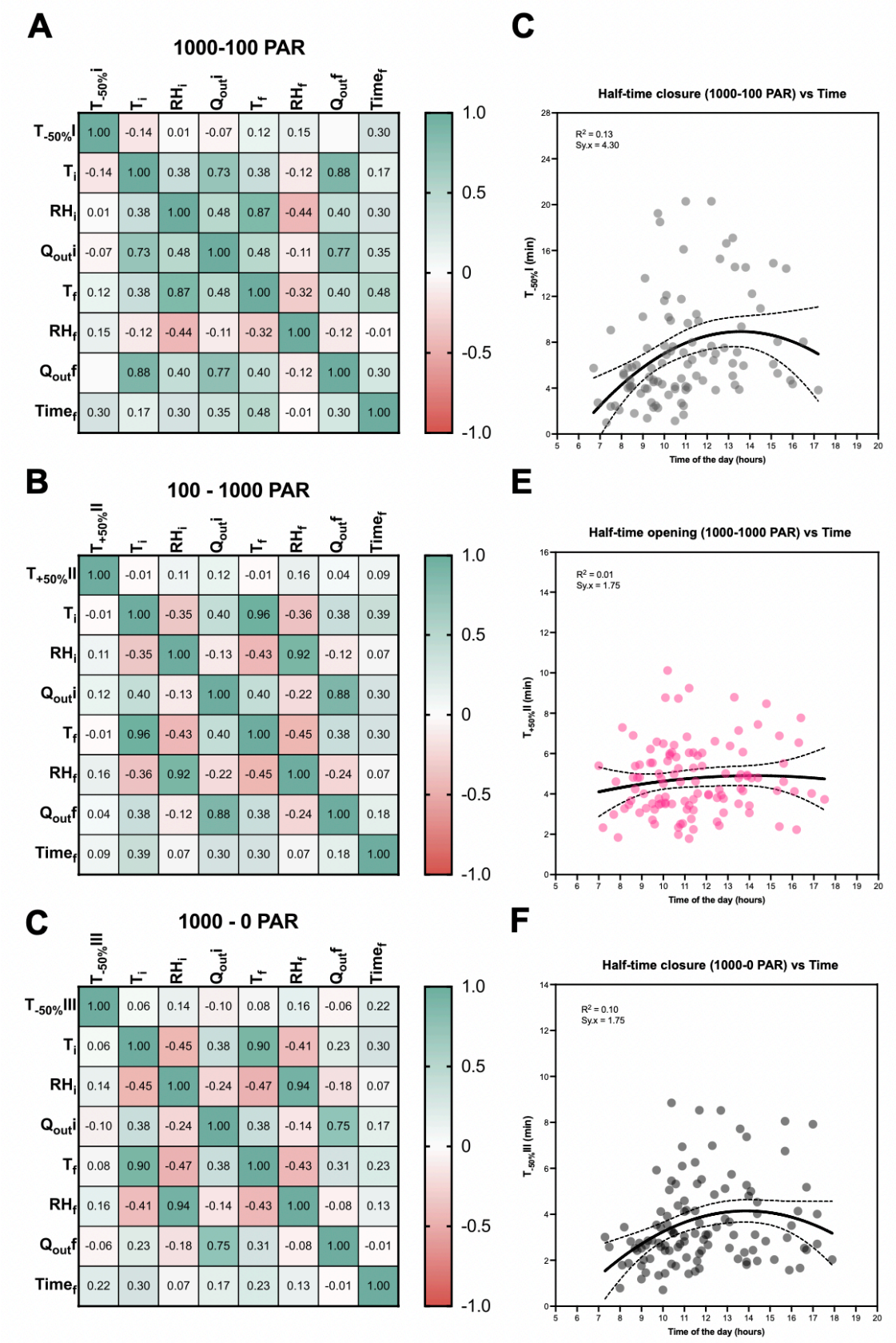


Figure 1.5 – Correlations between stomatal closure/opening half-times and environment. (A) Pearson correlation matrix between half-time stomatal closure I ($T_{-50\%}$ I, response from 1000 to 100 PAR), initial and final ambient light (Q_{out}i, f), temperature

($T_{i,f}$), relative humidity ($RH_{i,f}$) and end time of the day ($time_f$) (n=120). **(B)** Pearson correlation matrix between half-time stomatal opening II ($T_{+50\%}$ II, response from 100 to 1000 PAR), initial and final ambient light (Q_{out}i, f), temperature ($T_{i,f}$), relative humidity ($RH_{i,f}$) and end time of the day ($time_f$) (n=120). **(C)** Pearson correlation matrix between half-time stomatal closure III ($T_{-50\%}$ III, response from 1000 to 0 PAR), initial and final ambient light (Q_{out}i, f), temperature ($T_{i,f}$), relative humidity ($RH_{i,f}$) and end time of the day ($time_f$) (n=120). **(D)** Quadradic regression between time of the day and half-time stomatal closure I ($T_{-50\%}$ I, response from 1000 to 100 PAR) (n=120). **(E)** Quadradic regression between time of the day and half-time stomatal opening II ($T_{+50\%}$ II, response from 100 to 1000 PAR) (n=120). **(F)** Quadradic regression between time of the day and half-time stomatal closure III ($T_{-50\%}$ III, response from 100 to 1000 PAR) (n=120). R^2 and Sy.x directly in the graphics.

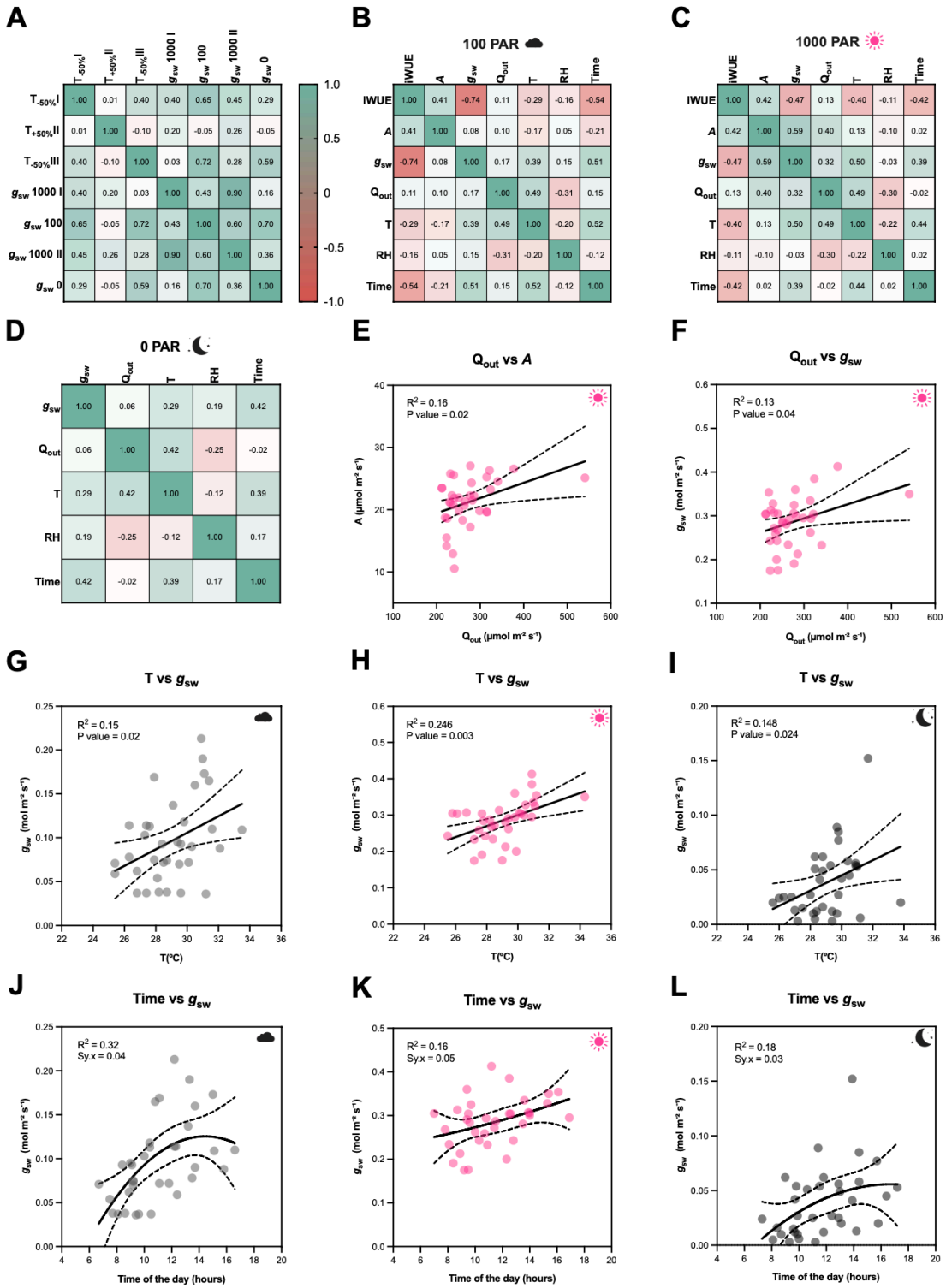


Figure 1.6 – Correlations between stomatal gas exchange, stomatal half-times and environment. (A) Pearson correlation matrix between stomatal half-times ($T_{50\%}$ I, II, III) and g_{sw} (at 1000, 100 and 0 PAR) (n=35). **(B)** Pearson correlation matrix between gas exchange at 100 PAR (iWUE, A, g_{sw}), ambient light (Q_{out}), temperature (T), relative humidity (RH) and time of the day (time) (n=35). **(C)** Pearson correlation matrix between gas exchange at 1000 PAR (iWUE, A, g_{sw}), ambient light (Q_{out}), temperature (T), relative humidity (RH) and time of the day (time) (n=35). **(D)** Pearson correlation matrix between gas exchange at 0 PAR (g_{sw}), ambient light (Q_{out}), temperature (T), relative humidity (RH) and time of the day (time) (n=35). **(E)** Linear regression between Q_{out} and A at 1000 PAR. **(F)** Linear regression between Q_{out} and g_{sw} at 1000 PAR. **(G)** Linear regression between T and g_{sw} at 100 PAR. **(H)** Linear regression between T and g_{sw} at 1000 PAR. **(I)** Linear regression between T and g_{sw} at 0 PAR. **(J)** Non-linear regression between time and g_{sw} at 100 PAR. **(K)** Non-linear regression between time and g_{sw} at 1000 PAR. **(L)** Non-linear regression between time and g_{sw} at 1000 PAR. R^2, p values and/or Sy.x directly in the graphics.

3.3.4 Higher iWUE occurs in the warm season due to seasonal variations in A and g_{sw}

After observing that leaf-level gas exchange and stomatal kinetics significantly vary daily in association with diurnal variations in light and temperature, I decided to check if significant variations were also observed among seasons.

To test if the stomatal opening and closure speed (i.e., half-time) varied seasonally, I assessed stomatal half-times for the three light transitions (1000-100, 100-1000 and 1000-0 PAR) by dividing the 120 samples in two major season groups: warm season (n=80) and cold season (n=40). Surprisingly, I observed significant differences between seasons in stomatal closure but not in stomatal opening (Fig. 1.7A). Specifically in the transition from high light to low light intensity (1000 to 100 PAR), stomatal closure was significantly slower (higher half-time closure) in the cold season (Fig. 1.7A). In the transition from high light to darkness (1000 to 0 PAR), the average stomatal closure half-time was also higher in the cold season, even though not statistically significantly different than in the warm season (Fig. 1.7A).

To test if the steady state gas exchange parameters are generally influenced by the seasonality of environmental conditions occurring in the glasshouse, I assessed the iWUE levels at both low and high light (100 and 1000 PAR, respectively) dividing the 120 samples in the two seasonal groups. Strikingly, significantly higher iWUE was observed in the warm season at both light conditions (Fig. 1.7B).

Additionally, I assessed g_{sw} and A at both low and high light (100 and 1000 PAR, respectively) from the data subset of 35 individuals where these absolute parameters were obtained after an exact correction for sample leaf area. The 35 samples were equally divided in warm season (n=17) and

cold season (n=18). Regarding *A*, while no differences were observed at 100 PAR as expected due to the light limitation of photosynthesis, although significantly higher *A* was observed in the warm season at 1000 PAR (Fig. 1.7C). Oppositely, I observed higher g_{sw} at 100 PAR in the cold season however non statistically significant, and no difference at 1000 PAR between seasons (Fig. 1.7D). These observations indicate that the higher iWUE in the warm season may derive from lower g_{sw} at 100 PAR and from the higher *A* at 1000 PAR.

After observing significant seasonal variation in leaf-level gas exchange, I speculated that this could be a result of seasonal changes in stomatal anatomical traits caused by different environmental conditions during growth.

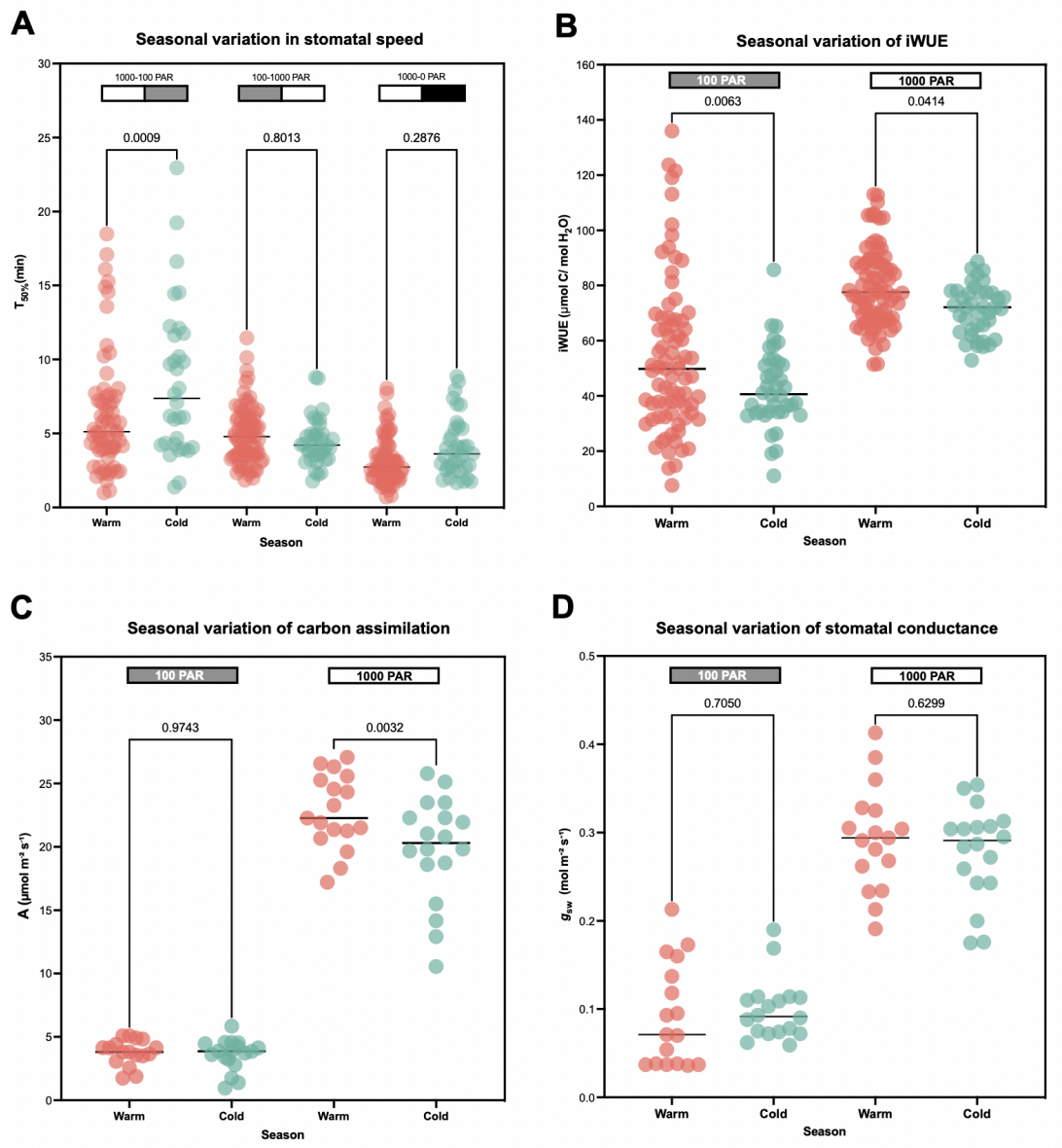


Figure 1.7 – Seasonal variation in stomatal speed, intrinsic water-use efficiency, and gas exchange. (A) Seasonal variation in stomatal half-time (T50%) for the three light transitions 1000-100 PAR, 100-1000 PAR and 1000-0 PAR (n=80 warm season; n=40 cold season). **(B)** Seasonal variation in iWUE at 100 and 1000 PAR (n=80 warm season; n=40 cold season). **(C)** Seasonal variation in carbon assimilation (A) at 100 and 1000 PAR (n=80 warm season; n=40 cold season). **(C)** Seasonal variation in carbon assimilation (A) at 100 and 1000 PAR (n=17 warm season; n=18 cold season). **(D)** Seasonal variation in stomatal conductance (g_{sw}) at 100 and 1000 PAR (n=17 warm season; n=18 cold season). P values obtained from one-way ANOVAs followed by Šídák's multiple comparisons test for the selected groups.

3.3.5 Seasonal changes in glasshouse growth conditions affect stomatal anatomical traits and gas exchange

Temperature and relative humidity significantly varied in the glasshouse between seasons. Additionally, the artificial light systems in the glasshouse allow only a partial regulation of light intensity and light-darkness cycles. Due to the contribution of external sunlight intensity and day length, light intensity in the glasshouse is highly variable not only daily but also seasonally.

Since light and temperature have been described as environmental cues potentially regulating stomatal numbers, and both stomatal density and size are influenced by the environmental conditions perceived by the plants during growth, I hypothesized that the stomatal anatomical traits in *B. distachyon* growing in the glasshouse could vary among seasons and therefore contribute to the seasonal variation in gas exchange that I observed.

Thus, to study the seasonal plasticity of stomatal anatomical traits in *B. distachyon* (21-3), I quantified stomatal length (SL) and stomatal density (SD) from 15 individuals grown in different seasons from which I collected leaf material after LI-6800 measurements. These 15 individuals were categorized in three meteorological seasons: summer (May – June, n=5), autumn (October – November, n=6) and winter (January – February, n=4). Furthermore, the anatomical traits were correlated with the average growth environmental conditions registered during the three weeks between sowing and leaf collection (temperature, relative humidity, and day length).

I observed significant differences in stomatal length (SL) and density (SD) among seasons (Fig. 1.8A, B). In summer, SL was approximately 10 % lower than in autumn or winter (Fig. 1.8A). On the other hand, SD was approximately 40 % higher in summer than in autumn or winter (Fig. 1.8B). No significantly differences were observed in the anatomical traits between autumn and winter (Fig. 1.8A, B), although a lower average SD can be noticed in the winter season (Fig. 1.8B).

When dissecting the correlation between growth environmental factors and anatomical traits, I observed a strong correlation between stomatal anatomical traits and the different environmental parameters (Fig. 1.8C). An opposite effect of the environmental parameters on SD and SL lead to a strong negative correlation between SD and SL (Fig. 1.8C, D), which has been well observed among species (Franks and Beerling 2009; Zhang et al. 2021; Haworth et al. 2021). A significant difference between those seasons is the length of the days, which can greatly alter the illumination conditions in the glasshouse. Indeed, the stomatal anatomical traits correlated significantly with the length of the days (Fig. 1.8C, E, F). Longer days associated with the shorter stomata and higher stomatal densities observed in summer, while shorter days associated with longer stomata and lower stomatal densities.as observed in autumn and winter (Fig. 1.8E, F), suggesting a significant effect of light availability on stomatal formation.

Furthermore, ambient temperature also significantly correlated with the stomatal anatomical straits (Fig. 1.8C). Increasing temperatures were associated with higher SD and shorter stomata. Oppositely, lower temperatures were associated with lower SD and longer stomata, observed in autumn in winter (Fig. 1.8G, H). As temperature and relative humidity were strongly negatively correlated, relative humidity correlated in an inversed manner with SD and SL (Fig. 1.8I, J).

Overall, plants growing in summer during longer days exposed to higher ambient light intensity, higher T, and lower RH developed higher stomatal numbers but shorter stomata. On the other hand, plants growing in autumn/winter during shorter days with lower ambient light intensity, lower T and higher RH developed lower stomatal numbers but longer stomata.

While light and temperature are described to promote stomatal numbers, it remains unclear if the changes in stomatal anatomy were primarily caused by a single parameter or by the combination of different environmental cues.

In conclusion, stomatal anatomical traits of *B. distachyon* were remarkably plastic and variable among seasons in a glasshouse, which likely contributes to the seasonal variation in gas exchange and stomatal kinetics.

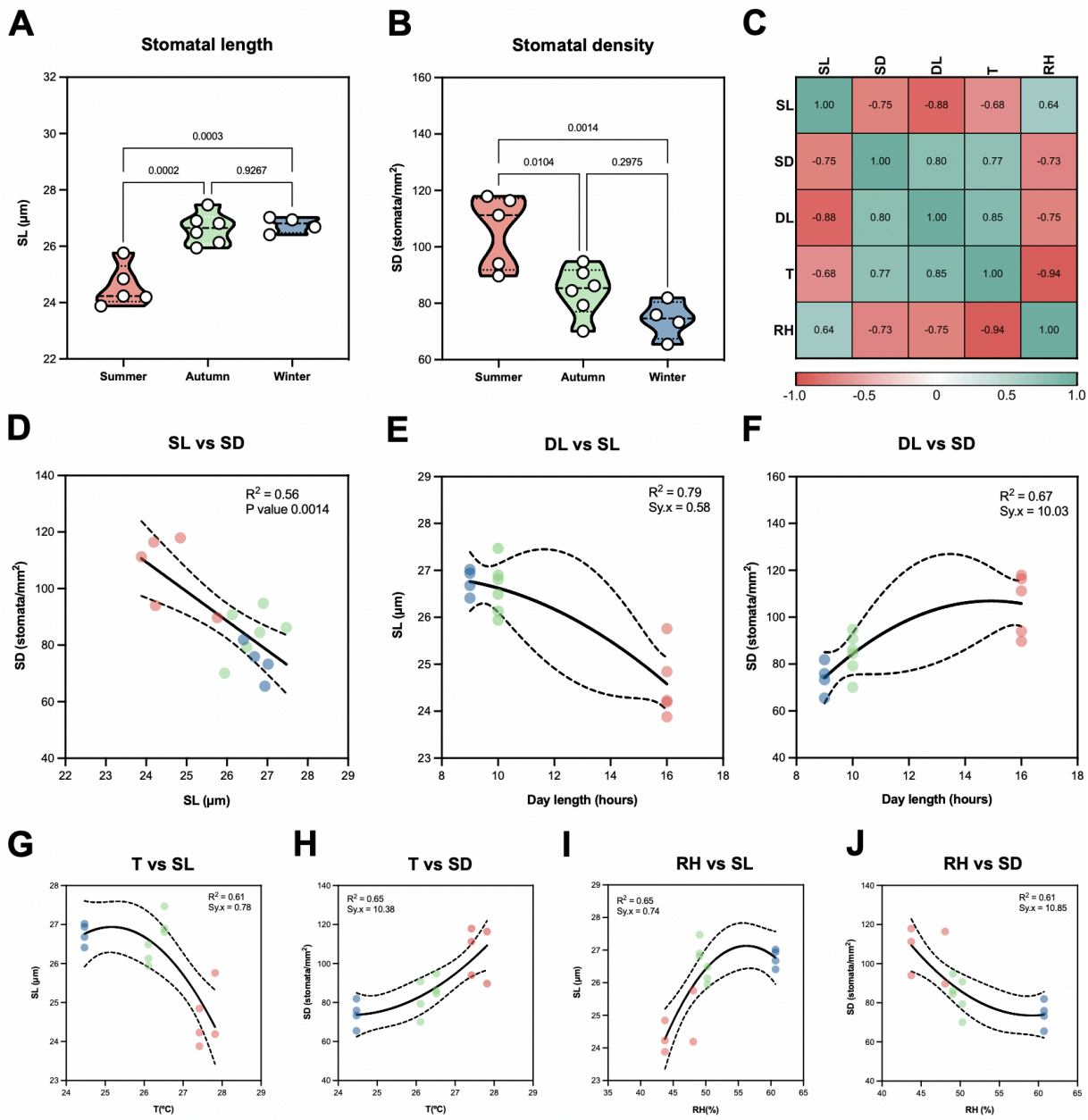


Figure 1.8 – Seasonal variation in stomatal anatomy and correlations with environment (A) Seasonal variation in stomatal length (SL) (n=5 in summer, n=6 in autumn, n=4 in winter). **(B)** Seasonal variation in stomatal density (SD) (n=5 in summer, n=6 in autumn, n=4 in winter). **(C)** Pearson correlation matrix of SL, SD, day length (DL), temperature (T) and relative humidity (RH). **(D)** Linear correlation between SL and SD (n=15). **(E)** Linear correlation between DL and SL (n=15). **(F)** Linear correlation between DL and SD (n=15). **(G)** Non-linear correlation between T and SL (n=15). **(H)** Non-linear correlation between T and SD (n=15). **(I)** Non-linear correlation between RH and SL (n=15). **(J)** Non-linear correlation between RH and SD (n=15). Summer, autumn, and winter represented in red, green and blue colours, respectively. R^2, p values and/or Sy.x represented directly on the graphics.

3.3.6 Changes in stomatal anatomy influence gas exchange and stomatal kinetics

Since I observed a seasonal variation in stomatal anatomy and stomatal function, I therefore investigated how the variation in anatomy correlated with changes in stomatal function.

I correlated stomatal length (SL) and stomatal density (SD) with stomatal opening/closure half-times ($T_{-50\%}$I, $T_{+50\%}$ II and $T_{-50\%}$ III) and steady-state gas exchange parameters (g_{sw}, A and iWUE) at the different light conditions.

Regarding stomatal opening and closure half-times ($T_{50\%}$), I found no significant effect of SL on opening nor on closure speediness (Fig. 1.9A). Surprisingly, while I only observed a weak influence of SD on stomatal opening ($T_{+50\%}$ II), SD significantly correlated and influenced stomatal closure half-times ($T_{-50\%}$ I and $T_{-50\%}$ III) (Fig. 1.9B).

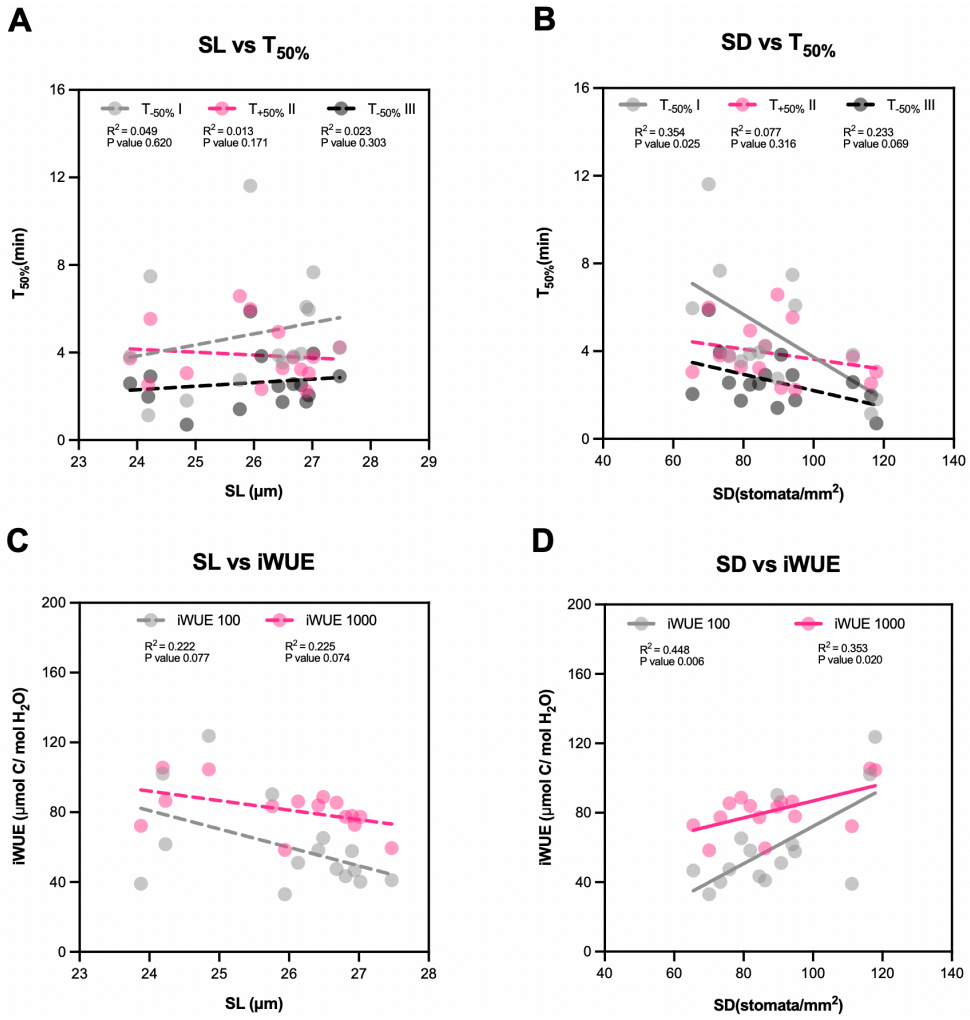


Figure 1.9– Correlations between stomatal anatomy, stomatal speed and intrinsic water-use efficiency (A) Linear regressions between stomatal length (SL) and half-time ($T_{-50\%}$ I in response to 1000-100 PAR, $T_{+50\%}$ II in response to 100-1000 PAR and $T_{-50\%}$ III in response to 1000-0 PAR) (n=15). **(B)** Linear regressions between stomatal density (SD) and half-time ($T_{-50\%}$ I in response to 1000-100 PAR, $T_{+50\%}$ II in response to 100-1000 PAR and $T_{-50\%}$ III in response to 1000-0 PAR) (n=15). **(C)** Linear regressions between stomatal length (SL) and iWUE at 100 and 1000 PAR (n=15). **(D)** Linear regressions between stomatal density (SD) and iWUE at 100 and 1000 PAR (n=15). R^2 and p values represented directly on graphics.

Faster stomatal closures (smaller $T_{50\%}$ values) were observed in the samples with the highest SD, particularly in the transition from high light to low light (1000 to 100 PAR) (Fig. 1.9B). These findings corroborate the significantly faster stomatal closure in response to decreasing light intensity from 1000 to 100 PAR in the 80 samples from warm season (higher SD), in comparison with the 40 samples from the cold season (lower SD) (Fig. 1.7A).

Regarding iWUE, lower SL and higher SD resulted in higher iWUE at both 100 and 1000 PAR, although SD was the anatomical trait with stronger effect on iWUE (Fig. 1.9C, D). Therefore, the higher iWUE observed in the warm season (Fig. 1.7B) might result from higher SD and lower SL. Since higher stomatal numbers were strongly correlated with both higher iWUE and faster stomatal closure, high SD seems to be the anatomical trait that directly and indirectly contributes to water-use efficiency in fluctuating environmental conditions.

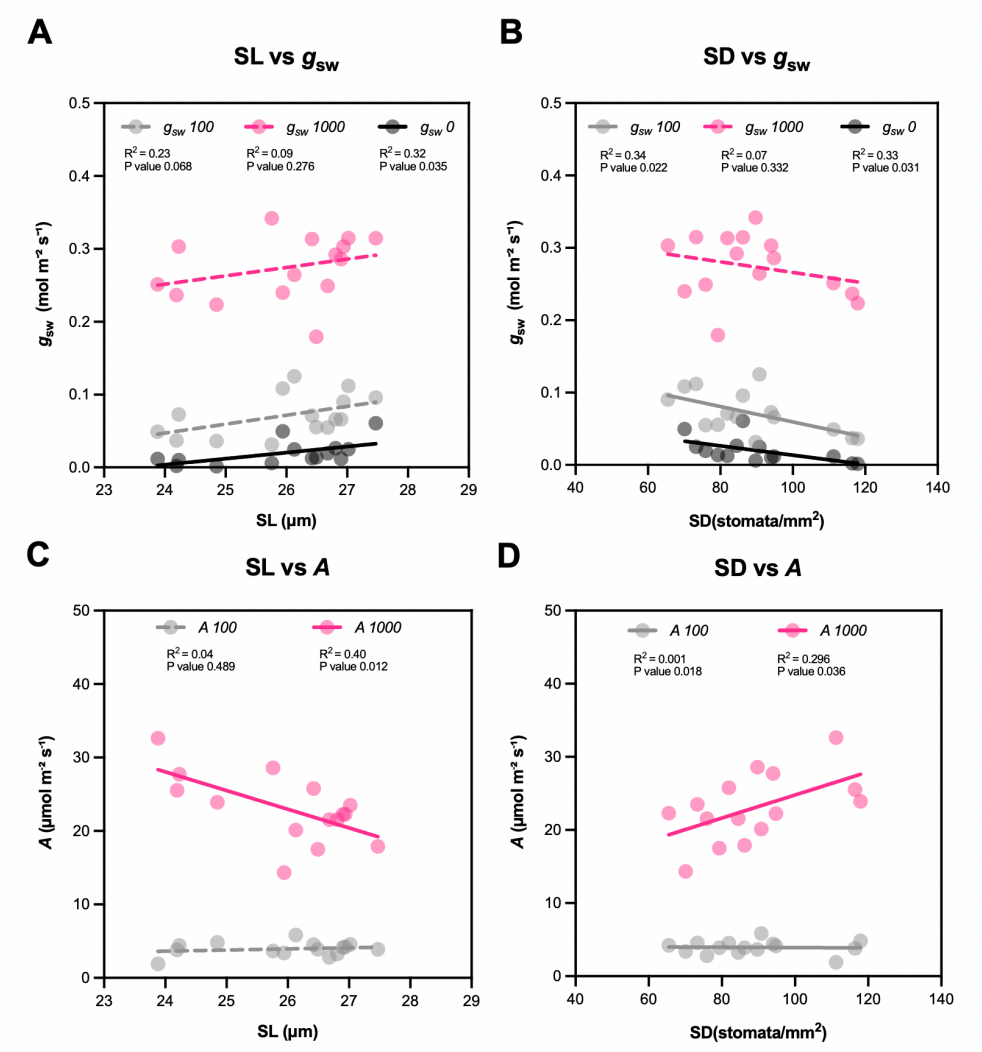


Figure 1.10– Relations between stomatal anatomy and gas exchange. (A) Linear regressions between stomatal length (SL) and stomatal conductance (g_{sw}) at 100 and 1000 PAR (n=15). **(B)** Linear regressions between stomatal density (SD) and stomatal conductance (g_{sw}) at 100 and 1000 PAR (n=15). **(C)** Linear regressions between stomatal length (SL) and carbon assimilation (A) at 100 and 1000 PAR (n=15). **(D)** Linear regressions between stomatal density (SD) and carbon assimilation (A) at 100 and 1000 PAR (n=15). R^2 and p values represented directly on graphics.

Regarding stomatal conductance, g_{sw} was negatively correlated with SD and positively correlated with SL to a lesser extent (Fig. 1.10A, B). SD and SL were therefore linearly associated with g_{sw} particularly at light limited conditions (100 and 0 PAR) (Fig. 1.10A, B). These correlations corroborate the previous observation that g_{sw} at 100 PAR was higher in winter (Fig. 1.7D), which is the season where SD is lower (Fig. 1.8B).

Oppositely, A was negatively correlated with SD and positively correlated with SL at 1000 PAR (Fig. 1.10C, D). Higher SD and lower SL were linearly associated with increased A at 1000 PAR (Fig. 1.10C, D). On the contrary, no correlation between stomatal anatomy occurred with A at light limited conditions (100 PAR) (Fig. 1.10C, D). These results also corroborate the previous finding that A levels were higher at 1000 PAR but not at 100 PAR in summer (Fig. 1.7C), which is the season with higher SD and lower SL (Fig. 1.8A, B).

Overall, the seasonal variations in stomatal anatomy seem to explain the seasonal variations observed in leaf-level gas exchange and in stomatal kinetics, suggesting therefore a major association between stomatal anatomy and function.

3.3.7 Adjustments on anatomical $g_s$max calculations for graminoid stomata

Due to the major association between stomatal anatomy and function, I wanted to mathematically estimate the maximum stomatal conductance based on the stomatal anatomical traits in *B. distachyon*. The maximum stomatal conductance ($g_s$max) can be assessed with IRGA-based gas-exchange measurements by providing the leaf with combined environmental triggers to induce full stomatal opening (high light intensity, high relative humidity, and low CO_2), which I refer to as physiological $g_s$max (also referred as diffusive $g_s$max in the literature (Dow et al. 2014)). Alternatively, $g_s$max can be estimated by calculating the theoretical $g_s$max using an established equation that integrates physical constants of gas and water diffusion with stomatal anatomical traits such as stomatal density (SD), stomatal length (SL), maximum pore area (a_{max}) and pore depth

(l) (Dow et al. 2014; Franks and Farquhar 2001). Still, the formulas to calculate maximum pore area (a_{max}) and pore depth (l) were optimized for kidney-shaped GCs as found in *Arabidopsis thaliana*, which form ellipsoid pores (Franks and Farquhar 2001; Dow et al. 2014) (Fig. 1.11A). Initial calculations of anatomical $g_s$max highly deviated from physiological $g_s$max measurements, and due to the unique shape of grass stomata I hypothesized that the formulas established for *Arabidopsis* do not accurately describe the geometry of graminoid stomatal pores.

Together with Magdalena W. Slawinska, we characterized the graminoid stomatal complexes of *B. distachyon* using confocal microscopy to optimize the anatomical $g_s$max calculations in *B. distachyon*. After fusicoccin treatments to induce stomatal opening in *B. distachyon* leaves, high-resolution confocal stacks of fully open stomata revealed hexagonal rather than elliptical pores (Fig. 1.11B). Additionally, ABA treatments were performed to observe fully close stomatal complexes.

Magdalena W. Slawinska measured GC length (GCL), stomatal pore length (PL), stomatal pore width (PW), GC width at the centre of the stoma (GCW_C) and stomatal width at the apex of the stoma (W_A) in fully open and close stomatal complexes. Moreover, Magdalena W. Slawinska hand-traced and measured pore areas of fully open stomatal complexes to attempt to geometrically define a_{max} of graminoid stomata. Calculating a_{max} as an ellipse with major axis equal to pore length and minor to half the pore length resulted in a significant pore area overestimation compared to the exact pore area assessed by hand-tracing of the fully open stomatal pores (Fig. 1.11C).

We verified that the *B. distachyon* hexagonal stomatal pore areas could accurately be calculated as 90 % of a rectangle (width equal to the stomatal pore width and length equal to the stomatal pore length) (Fig. 1.11D).

After the morphological characterization of graminoid stomata in *B. distachyon*, we calculated anatomical $g_s$max using hand-traced a_{max} and estimated a_{max} geometrically defined as i) ellipses or ii) rectangular pores multiplied by the correction factor 0.9. Pore depth (l) was measured from orthogonal resliced confocal stacks and stomatal density was determined from 3-5 different fields of view using light microscopy. While anatomical $g_s$max calculations based on ellipsoid pores deviated from the hand-traced a_{max}-based calculations (R^2= 0.5970) (Fig. 1.11E), the latter strongly

correlated with anatomical $g_s$max based on rectangular pores multiplied by the correction factor 0.9 (R^2=0.9262) (Fig. 1.11F).

From light microscopy images of leaf samples fixed in 7:1 ethanol:acetic acid, it is impossible to calculate a_{max} since it is hard to observe the stomatal pores. Therefore, Magdalena W. Slawinska calculated coefficients to estimate pore length (l) and width from GC length and to estimate pore depth (l) from GC width, which are parameters easily measured from light microscopy images of fixed material (Fig. 1.11G, H).

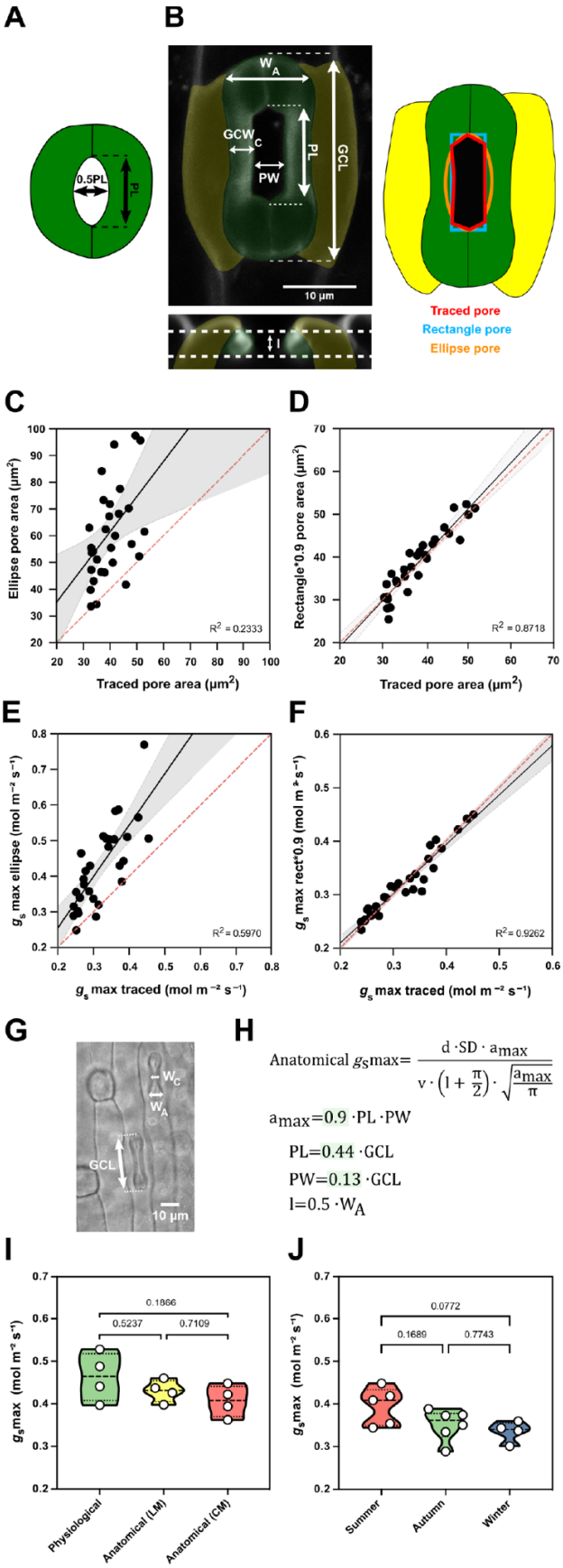
Regarding pore depth (l), Magdalena W. Slawinska determined that the average exact pore depth measured from orthogonal resliced confocal stacks (3.37±0.4μm) matched the average GC width at the centre of the stoma (GCW_C) (3.23±0.3μm) in fully opened stomata from fusiccocin-treated samples (Table 1). Oppositely, in closed stomata (ABA-treated samples), the average exact pore depth approximates the GC width at the stomatal apex (W_A) (3.52±0.6μm) instead of the average GCW_C (2.48±0.3μm) (Table 1). Therefore, if not exactly measured from orthogonal sections, pore depth (l) could be approximated as central GC width of fully open stomata (e.g., in fusiccocin-treated samples) or apex GC width of closed stomata (e.g., in fixed leaves with 7:1 ethanol:acetic acid).

Thus, for fixed material as a standardly used, pore depth (l) can be defined as 0.5* W_A, since stomata are generally closed in fixed material (Fig. 1.11 G, H).

Regarding pore width (PW) and length (PL), Magdalena W. Slawinksa calculated the ratios between GCL, PL, and PW in the confocal-based images and found that PL is approximately 44 % of GCL and PW is 13 % of GCL (Table 2). Therefore, PW can be estimated as 0.13*GCL and PL as 0.44*GCL and (Fig. 1.11G, H).

3.3.8 Testing adjusted anatomical $g_s$max calculations

To test if our adjustments on the calculations of anatomical $g_s$max could be used to predict physiological $g_s$max in *B. distachyon*, Magdalena W. Slawinska and I together performed physiological $g_s$max measurements using the LI-6800, and subsequently collected the measured leaf areas, and assessed the stomatal anatomical traits from segments of those samples. I imaged the



samples using light microscopy after sample fixation with 7:1 ethanol:acetic acid, while Magdalena W. Slawinska used confocal microscopy after treating the collected fresh leaf material with fusicoccin. We saw no significant differences between physiological $g_s$max and anatomical $g_s$max based on the estimated anatomical parameters assessed with light microscopy (LM) or with confocal microscopy (CM) (Fig. 1.11I). Thus, I conclude that the optimized formulas to calculate maximum pore area and pore depth in graminoid stomata can be used to calculate anatomical $g_s$max and reliably predict physiological $g_s$max in *B. distachyon*.

Figure 1.11 – Characterization of graminoid stomatal pores, optimization of anatomical $g_s$max calculations and seasonal variation in $g_s$max. (A) Kidney-shaped guard cells and ellipsoid stomatal pores present in most plant species as in the model eudicot *Arabidopsis thaliana*. **(B)** Stomatal complexes in *Brachypodium distachyon* and anatomical traits measured in the morphometric analysis. W_A represents stomatal width at the apex, GCL represents guard cell length, PL represents stomatal pore length, PW represents stomatal pore width, GCW_C represents guard cell width at the centre of the stoma and l represents stomatal pore depth. Scheme represents three approaches to measure stomatal pore area (hexagonal hand-traced pore in red, rectangular pore in blue and ellipsoid pore in orange). **(C)** Comparison between hand-traced pore area and ellipsoid pore area. **(D)** Comparison between hand-traced pore area and rectangular pore area corrected with a 0.9 correction factor to fit the hexagonal graminoid stomatal pore. **(E)** Correlation between anatomical $g_s$max calculated considering the hand-traced pore area and considering an ellipsoid stomatal pore. **(F)** Correlation between anatomical $g_s$max calculated considering the hand-traced pore area and considering 90 % of a rectangular stomatal pore (0.9 correction factor). **(G)** Light microscopy view of stomata and anatomical measurements required for calculation of anatomical $g_s$max: guard cell length (GCL), stomatal width

at the apex (W_A) in the case of closed stomata and at the centre (WC) in the case of open stomata. **(H)** Anatomical $g_s$max formula and adjustments to calculate maximum pore area (a_{max}), pore length (PL), pore width (PW) and pore depth (l). **(I)** Comparison between physiological gsmax measurements performed with the LI-6800 and anatomical gsmax calculated based on the adjusted formula in H and the traits obtained from light microscopy in G and based on traced pores and anatomical traits obtained from confocal microscopy. **(J)** Seasonal variation in anatomical $g_s$max (n=5 for summer, n=6 for autumn and n=4 for winter). p values from one-way ANOVA followed by Tukey's multiple comparisons. Data produced jointly with Magdalena W. Slawinska. This figure is an original from Magdalena W. Slawinska and myself, originally published in *Quantitative Plant Biology* in an article which I am first author (Nunes et al 2022) (doi.org/10.1017/qpb.2021.19, open-access (CC BY 4.0)).

Table 1 – Comparison between exact pore depth and guard cell (GC) width at the centre and apex of fully open and closed the stomatal complexes. Different letters represent significant differences ($p<0.05$ obtained from one-way ANOVA followed by Tukey's multiple comparisons).

n=30 stomata per treatment	Exact pore depth (Fusicoccin)	GC width center (Fusicoccin)	GC width apex (Fusicoccin)	GC width center (ABA)	GC width apex (ABA)
Mean (μm)	3.37^{A}	3.23^{A}	5.92^{B}	2.48^{C}	3.52^{A}
SD	0.4	0.3	0.4	0.3	0.6

Table 2 – Ratio between stomatal pore length/width and guard cell (GC) length.

Ratio	Pore length/GC length	Pore width/GC length
Mean	0.44	0.13
SD	0.03	0.03
R^2	0.90	0.23

3.3.9 Seasonal variation in anatomical $g_s$max in *Brachypodium distachyon*

Since the adjusted formula accurately predicted physiological $g_s$max, I calculated anatomical $g_s$max for the summer, autumn, and winter individuals in which stomatal anatomical traits were assessed (section 3.3.5). I observed a decrease in average anatomical $g_s$max in autumn/winter, although not statistically significant (Fig. 1.11J). These results suggested that even though variations in SD and SL may influence iWUE and stomatal speed, the trade-off between SD and SL in wild-type *B. distachyon* may help maintaining optimal g_{sw} capacity in different seasons and/or growth environments.

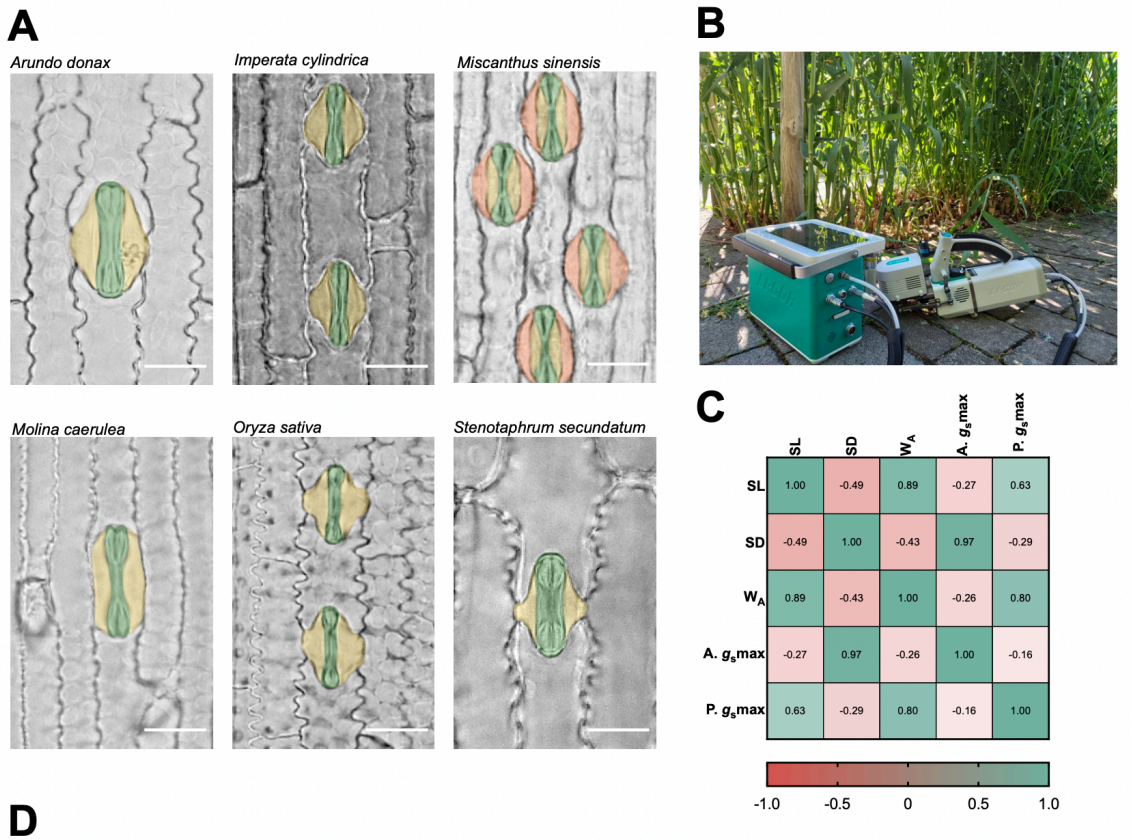
3.3.10 Assessing stomatal anatomy and $g_s$max in other grass species

Finally, Magdalena W. Slawsinka and I took advantage from the diversity of species available in the Botanical Garden at the University of Heidelberg to assess whether the optimized formula for the

estimation of anatomical $g_s$max could be used to accurately predict physiological $g_s$max for other *Poaceae* species. Together, we first performed LI-6800 measurements of physiological $g_s$max for 6 different grass species growing in the botanical garden: *Arundo donax*, *Imperata cylindrica*, *Miscanthus sinensis*, *Molina caerulea*, *Oryza sativa* and *Stenotaphrum secundatum* (Fig. 1.12A, B). Secondly, we collected the section of the leaf measured in the LI-6800 and measured the required stomatal anatomical traits (SL, SD, and W_A) to calculate anatomical $g_s$max. Two limitations of this study must be noted: i) only one individual of each species was assessed and ii) the plants were growing in the botanical garden adapted to conditions different than the ones in the LI-6800 chamber (particularly temperature) to measure physiological $g_s$max. In *B. distachyon*, physiological $g_s$max measurements were performed at 28°C (which is identical to the ambient growing conditions in the glasshouse) and at 1500 PAR (which is a suturing and non-inhibitory light intensity for *B. distachyon* but may differ in other species).

Therefore, it was expected that stomata could not reach a real maximal opening but rather an operational maximum g_{sw} constricted by the conditions the plants are experiencing.

Indeed, for four species, physiological $g_s$max was lower than the anatomical $g_s$max (Fig. 1.12D). Exceptions were *Stenotaphrum secundatum* and *Molina caerulea*, for which the anatomical estimation displayed a significant level of accuracy, representing 75-100 % of the physiological $g_s$max (Fig. 1.12D).



D

Species	ID	SL (µm)	SD (stomata mm^{-2})	W_A (µm)	A. $g_s$max (mol m^{-2} s^{-1})	P. $g_s$max (mol m^{-2} s^{-1})
Arundo donax	101217	38.24	137.70	4.75	0.85	0.39
Imperata cylindrica	5992	26.86	119.71	3.20	0.53	0.14
Miscanthus sinensis	3330	28.35	276.44	3.61	1.25	0.21
Molina caerulea	6523	33.51	36.60	3.86	0.20	0.20
Oryza sativa	50	25.96	184.08	2.78	0.81	0.23
Stenotaphrum secundatum	109325	32.94	77.51	4.87	0.38	0.51

Figure 1.12 – Stomatal anatomy and maximum stomatal conductance in different grass species. (A) Stomatal complexes in *Arundo donax*, *Imperata cylindrica*, *Miscanthus sinensis*, *Molina caerulea*, *Oryza sativa* and *Stenotaphrum secundatum*. Guard cells (GCs) represented in green, subsidiary cells (SCs) represented in yellow. In the case of *Miscanthus sinensis*, the stomatal complexes contain what it seems like a second pair of SCs, represented in orange. **(B)** Set-up of LI-6800 measurements in the botanical garden of the University of Heidelberg. **(C)** Pearson correlation matrix for average stomatal length (SL), stomatal density (SD), average stomatal width at the apex (W_A), anatomical $g_s$max (A. $g_s$max) and physiological $g_s$max (P. $g_s$max). **(D)** Table containing average stomatal length (SL, average of 23-57 stomata per individual), stomatal density (SD), average stomatal width at the apex (W_A, average of 23-57 stomata per individual), anatomical $g_s$max (A. $g_s$max) and physiological $g_s$max (P. $g_s$max) for all six species and their respective identification number (ID) from the botanical garden database. Data produced jointly with Magdalena W. Slawinska.

Additionally, I correlated stomatal anatomical traits (SL, SD, and W_A) with the gas exchange parameters (anatomical and physiological $g_s$max) (Fig. 1.12C).

As previously observed intraspecifically for *B. distachyon*, a negative correlation between SD and SL could be also observed among these six grass species (Fig. 1.12C). Interestingly, while SD seemed to

define the anatomical maximum $g_s$max (strong positive correlation), the (operational) physiological $g_s$max seemed to be rather defined by stomatal size (positive correlation with SL and W_A) (Fig. 1.12C). Finally, the only species which physiological $g_s$max and anatomical $g_s$max were identical (0.20 mol m^{-2} s^{-1}) was *Molina caerulea*, which displayed elongated SCs as observed in *B. distachyon* (Fig. 1.12D). On the other hand, all the other species contained triangular-shaped SCs and displayed a mismatch between anatomical and physiological $g_s$max (Fig. 1.12D).

3.4 Discussion

Stomata in grasses like *B. distachyon* are of the graminoid type, which consists of two dumbbell-shaped guard-cells (GCs) flanked by two lateral subsidiary cells (SCs). SCs contribute to fast stomatal opening and closure by functioning as specialized ion reservoirs and mechanically accommodating GC turgor-driven movements to facilitate stomatal movements. Furthermore, SCs may contribute with improved signalling to accelerate stomatal responsiveness. Additionally, the dumbbell-shaped GCs present a reduced volume-to-surface ration which translates in a lower requirement of ions and water to increase turgor. Thus, fast, and robust stomatal movements are expected in grasses. Indeed, I observed consistent and fast light-response stomatal kinetics in the grass model *B. distachyon*. Fast stomatal opening and closure observed in *B. distachyon* is typical for the family *Poaceae*. Faster stomatal movements in grasses than in non-grass species containing kidney-shaped GCs have been reported in several comparative physiology studies.

One study comparing stomatal closure in *Hordeum vulgare* (monocot, *Poaceae*), *Lepidozamia peroffskyana* (cycad), *Podocarpus macrophyllus* (conifer), *Agathis australis* (conifer), *Solanum Lycopersicon* (eudicot, *Solanaceae*), *Osmunda regalis* (fern) and *Ginkgo biloba* (ginkgophyte) showed that the fastest species closing stomata in response to darkness was the grass *Hordeum vulgare* (Elliott-Kingston et al. 2016).

Faster stomatal movements in response to darkness, light, CO_2 and reduced humidity were also observed in the grasses *Triticum aestivum* and *Hordeum vulgare*, comparatively to non-grass eudicot species (*Arabidopsis thaliana*, *Thellungiella salsuginea*, *Nicotiana tabacum* and *Helianthemum nummularium*) (Merilo et al. 2014). Specifically, *Triticum aestivum* presented

stomatal light-response half-times of approximately 2 minutes for stomatal opening (from 150 to 450 PAR) and approximately 6 minutes for stomatal closure (from 150 to 0 PAR) (Merilo et al. 2014), similarly to the values ranging from 3 to 6 minutes that I observed in *Brachypodium distachyon*. On the other hand, the stomatal half-times observed in the non-grass species ranged between 8 and 14 minutes both for stomatal opening and closure in response to increasing light and to darkness, respectively (Merilo et al. 2014).

Faster stomatal responses to light and VPD changes were also observed in the grass sugarcane in comparison with the eudicot soybean (Grantz and Zeiger 1986). Sugarcane stomatal opening half-time in response to increasing light intensity from 275 to 620 PAR was 1.9±0.5 minutes in contrast to 13.2±2.1 minutes in soybean. Similarly, stomatal closure half-time, in response to decreasing light intensity from 620 to 390 PAR, was 2.3 ± 0.8 minutes in sugarcane in contrast with 9.3±3.3 minutes observed in soybean. An identical 5-fold difference between the two species was observed in stomatal responses to VPD (Grantz and Zeiger 1986), highlighting the faster stomatal movements in grass species.

A study compared stomatal traits including stomatal closure speed in response to darkness in 31 plant species categorized into five groups - ferns, gymnosperms, basal angiosperms, eudicots and monocots (from which 6 out of 7 species belong to the Family *Poaceae* and all 7 species belong to the Order *Poales*) (Haworth et al. 2018). The monocot group significantly showed the highest stomatal closure speed. In *Avena sativa*, *Triticum aestivum* and *Hordeum vulgare*, stomatal closure half-times in response to a decrease in light intensity from 2000 PAR to 0 PAR were 5.0, 5.5 and 4.3 minutes, respectively. Once again, these values are highly comparable to the half-time closure of 3.4 minutes from 1000 to 0 PAR in my study for *B. distachyon*. In contrast, eudicots presented much slower stomatal closure movements. For example, some species of agronomical and forestry interest such as *Populus nigra* (black poplar), *Coffea arabica* (arabian coffee), *Helianthus annus* (common sunflower) and *Solanum lycopersicum* (tomato) showed much slower stomatal closure with half-times of 17.3, 9.0, 18.0 and 9.1 minutes, respectively (Haworth et al. 2018).

In *B. distachyon* I did not find a relevant asymmetry between closure and opening speed which is consistent with the findings from a comparison of stomatal movements among seven grass species

with dumbbell-shaped GCs and eight non-grasses with kidney-shaped GCs. The grass species displayed the higher similarity between stomatal opening and closure speed (McAusland et al. 2016) while the non-grass species displayed great asymmetry between stomatal opening and closure. *Arabidopsis thaliana*, *Solanum lycopersicum* and *Vicia faba* presented a 3-folded faster stomatal closure than opening. This asymmetry in stomatal responses is potentially associated with the mechanical advantage of the neighbouring epidermal cells over the GCs, thus limiting stomatal opening. On the other hand, the symmetry in opening and closure in species containing graminoid stomata supports the hypothesis that graminoid GCs and SCs are more intrinsically inversely coordinated and that graminoid stomatal GCs indeed require less osmotic and turgor exchange to achieve stomatal movements.

Regardless the proximity between stomatal opening and closure speeds in grasses, the fastest stomatal movement in *B. distachyon* was still the stomatal closure in response to darkness (from 1000 to 0 PAR). Faster stomatal closure than opening is considered an advantageous ecological trait as a water conserving strategy (Lawson and Blatt 2014; Eyland et al. 2021; Leakey et al. 2019; McAusland et al. 2016; Lawson and Vialet-Chabrand 2019).

The balance between carbon assimilation (A) and stomatal conductance (g_{sw}) for water vapour loss is characterized by intrinsic water use efficiency (iWUE), which results from the ratio between A and g_{sw}. High g_{sw} allows high rates of A, but at the cost of greater water loss. The maintenance of well-adjusted iWUE levels is conditioned by the speed of stomatal movements, which are generally an order of magnitude slower than the speed of A adjustments. Thus, stomatal kinetics in response to fluctuating light intensity have a major impact on water use efficiency and consequently affect plant productivity, water usage and the tolerance to abiotic stresses. Therefore, stomatal kinetics and water use efficiency are targets to improve plant productivity and fitness.

In my study with *B. distachyon*, iWUE greatly varied between 10 and 100 μmol mol^{-1} under fluctuating light 1000-100-100 PAR. When looking at light-adapted steady-state iWUE, iWUE was in average 50 and 80 μmol mol^{-1} at 100 and 1000 PAR, respectively. These values were consistent with the range of iWUE previously described in other C_3 grasses such as *Triticum aestivum* (25-65

μmol mol^{-1}) and in rice and wild relatives (Genus *Orzya*) (50-80 μmol mol^{-1}) (Jahan et al. 2014; Giuliani et al. 2013).

In *B. distachyon*, I obtained an average g_{sw} of 0.10 and 0.33 mol m^{-2} s^{-1} at 100 and 1000 PAR, respectively. These values are identical to what has been described for other C_3 grass species. In a study on the Genus *Oryza* including rice and wild relatives, g_{sw} ranged from 0.13 and 0.42 mol m^{-2} s^{-1}. In *Oryza sativa* IR64, g_{sw} varied between 0.40 and 0.50 mol m^{-2} s^{-1} at 1000 PAR (Caine et al. 2018). In study on wheat, g_{sw} varied between 0.20 and 0.60 mol m^{-2} s^{-1} at 1500 PAR among *Triticum aestivum* genotypes (Jahan et al. 2014). Average g_{sw} of 0.27 and 0.36 mol m^{-2} s^{-1} were observed in *Hordeum vulgare* and *Triticum aestivum*, respectively, in contrast to 0.13 and 0.12 mol m^{-2} s^{-1} in *Arabidopsis thaliana* and *Nicotiana tabacum* at 450 PAR (Merilo et al. 2014). Average g_{sw} ranging between 0.4 and 0.5 mol m^{-2} s^{-1} at 1000 PAR were observed in *Oryza sativa*, *Avena sativa* and *Triticum aestivum*, in contrast with 0.2 to 0.3 μmol m^{-2} s^{-1} in the eudicots *Arabidopsis thaliana*, *Pisum sativum*, *Nicotiana tabacum* and *Solanum lycopersicum* (McAusland et al. 2016), suggesting higher g_{sw} in grasses. On the other hand, carbon assimilation (*A*) varied between 20 and 30 μmol m^{-2} s^{-1} among *Triticum aestivum* genotypes, and between 10 and 23 μmol m^{-2} s^{-1} in the Genus Oryza. In *Oryza sativa* IR64, *A* reached approximately 30 μmol m^{-2} s^{-1} at 1000 PAR. Average *A* between 20 and 25 μmol m^{-2} s^{-1} at 1000 PAR was observed in the grasses *Oryza sativa*, *Avena sativa* and *Triticum Aestivum*, in contrast with 10 to 15 μmol m^{-2} s^{-1} in the eudicots *Arabidopsis thaliana*, *Pisum sativum*, *Nicotiana tabacum* and *Solanum lycopersicum* (McAusland et al. 2016). In *B. distachyon*, I observed an average *A* of 21 μmol m^{-2} s^{-1} at 1000 PAR. Once again, these observations match the values obtained in the other C_3 grass species.

Overall, this suggests then that *B. distachyon* is a good representative of the faster stomatal movements and higher gas exchange rates in grasses, highlighting the suitability of *B. distachyon* as a model species for C_3 grass stomatal physiology.

Regardless of the consistent leaf-level gas exchange and stomatal responsiveness in *B. distachyon*, I observed a significant diurnal rhythm effect on leaf-level gas exchange measurements. Stomata apertures seem to follow a diurnal rhythm. Stomata start opening in the morning reaching maximum stomatal conductance at noon and afterwards stomata start closing until reaching full

stomatal closure after dusk. This diurnal variation on stomatal functioning has been well observed in C_3 species (Miao et al. 2021; Matthews et al. 2017; Resco de Dios 2017; Vahisalu et al. 2008; Roussel et al. 2009; Stangl et al. 2019).

Still, observing the effect of diurnal rhythms on stomatal speed in artificially and locally induced light transitions performed inside the leaf chamber of the LI-6800 under a fully control environmental conditions was surprising. Stomatal closure speed was highly influenced by the time of the day and the steady state g_{sw} levels before and/or after light intensity transition. Similarly, it was recently shown in *Musa spp.* that stomatal kinetics were influenced by the time of the day and also by the steady-state g_{sw} before the light transitions (Eyland et al. 2021).

Steady state g_{sw} was significantly impacted by the ambient environmental conditions. Increasing temperatures stimulated g_{sw}. The increase in g_{sw} at high temperatures allows for leaf cooling and provides then a mechanism to cope with thermal stress (Urban et al. 2017b; Lamba et al. 2018; Urban et al. 2017a; Sonawane et al. 2021; Gommers 2020). Still, after a certain level of exposure to high temperatures stomatal may close as a stress-induced response (Ikkonen et al. 2015; Zhou et al. 2015; Yamori et al. 2006; Faria et al. 1996).

Ambient light intensity also had a significant effect on leaf-level gas measurements by eliciting increases in both g_{sw} and A. While light is the core signal for stomatal opening, the systemic effect of light on distant stomata has only recently been described. Recent studies have also observed systemic stomatal responses to light in the model eudicot *Arabidopsis thaliana* (Devireddy et al. 2018; Devireddy et al. 2020). Stomata closed in response to light stress in both local leaves (the leaves exposed to the stressor) and in systemic leaves (leaves not directly exposed to the stressor). Stomatal closure was coordinated by the leaves exposed to the stressor perceiving the signal and transmit it for it to be received by distant leaves. Such systemic signalling cascades involved ABA and jasmonic acid triggering ROS waves in *Arabidopsis thaliana* (Devireddy et al. 2018; Devireddy et al. 2020). Furthermore, systemic effects were also reported in the trees *Betula pendula* and *Populus tremula x tremuloides* during stomatal responses to darkness (from 600 to 0 PAR) and elevated CO_2 (400 to 1100 ppm) (Ehonen et al. 2020). Consistently to these results observed in *Arabidopsis thaliana* and in trees, my results suggest that *Brachypodium distachyon* stomata also integrate local signals

perceived in the LI-6800 leaf chamber and systemic signals originated from distal parts of the plant exposed to different environmental conditions. The outcome of the interplay between local and systemic signalling demonstrates that it is imperative to monitor environmental conditions of the place of study and consider their influence on leaf-level gas exchange measurements, specifically in glasshouse or field studies where environmental fluctuations are noteworthy.

Besides the significant effects of ambient environmental conditions on leaf-level gas exchange, different environmental conditions during plant growth significantly impacted stomatal anatomical traits. SL and SD oppositely varied among meteorological seasons because of significantly changes in growth environmental conditions.

While the seasonal trade-off between SL and SD seems to allow a maintenance of the maximum stomatal gas exchange capacity ($g_s$max), stomatal kinetics and operational gas exchange seems to be significantly affected by the anatomical variations. Faster stomatal closure seems to be associated with higher stomatal numbers while variations in stomatal size in the range observed in wild-type *B. distachyon* did not seem to significantly affect stomatal speed. Still, different relationships between stomatal size and stomatal speed have been described in the literature. A study performing an interspecific comparison among 15 different species including 7 grasses, 7 eudicots and *Gingko biloba*, concluded that shorter stomata result in faster stomatal movements (McAusland et al. 2016). Other studies compared a wider range of species belonging to different plant groups. Elliot-Kingston et al compared 7 species representing the major groups of vascular plants (ferns, cycads, ginkgoacae, gymnosperms, eudicots and monocots) (Elliott-Kingston et al. 2016) and observed that stomatal speed was associated with SD but not with SL. Haworth et al compared 31 species (ferns, gymnosperms, basal angiosperms, eudicots and monocots) (Haworth et al. 2018) suggesting that stomatal speed is strongly and positively correlated with SD with a weaker correlation with stomatal size (i.e., stomatal pore area), matching the results I obtained in wild-type *B. distachyon*. Similarly, stomatal speed in response to fluctuating light was also strongly influenced by SD, while a minor effect of SL was observed in a comparison between different *Arabidopsis* genotypes (Sakoda et al. 2020). Likewise, a comparison between two begonia species, showed that *Begonia plebeja* which contains stomatal clusters exhibited faster stomatal kinetics and improved carbon assimilation

resulting in higher water use efficiency, than *Begonia coccinea* which contains larger stomata and no stomatal clustering (Papanatsiou et al. 2017). These observations suggested a positive effect of stomatal proximity on stomatal speediness, potentially associated with shared substomatal cavities. Nevertheless, studies on rice genotypes observed opposite effects of stomatal anatomy on stomatal kinetics. A comparison of stomatal anatomy and gas exchange under fluctuating light between diploid and tetraploid rice plants showed that tetraploid plants displayed larger stomata and lower SD which resulted in slower stomatal opening (Xiong et al. 2022). Oppositely, a study comparing different *Oryza spp.* genotypes suggested that stomatal size negatively correlated with stomatal half-time, suggesting that larger stomata are faster (Zhang et al. 2019).

Therefore, the impact of SL and SD on gas exchange rapidity may vary among species or even genotypes, and so, no general effect of SL and SD on stomatal speediness can be claimed.

Regardless, I speculate that faster stomatal speediness in plants with higher SD can potentially result from proximity effects by increasing Ci (internal CO_2) concentration through diffusion in the sub-stomatal space triggering stomata in close vicinity to react in a coordinated manner.

Besides the positive effect of SD on stomatal closure speed, higher SD was also associated higher iWUE, suggesting that increased stomatal numbers can contribute to improved water-use efficiency both in fluctuating environments and in steady-state conditions.

Increased SD seems to be an anatomical adaptation to the warm season, and therefore improved stomatal responsiveness and water use efficiency may be beneficial for such environments. Increased stomatal densities in warmer environments has been observed and linked as an adaptative response to allow leaf evaporative cooling in the South African shrub *Protea repens* (Carlson et al. 2016) and in the Australian shrub *Dodonaea viscosa subsp. angustissima* (Hill et al. 2014).

On the other hand, cold seasons featuring shorter days and lower light availability can negatively impact photosynthetic rates (Yamasaki et al. 2002; Feng et al. 2018) and therefore a reduction in stomatal numbers may result in increased leaf epidermal area and mesophyll allocated to light capture for the light-dependent photosynthetic reactions. The reduction in SD may be further counteracted by increasing stomatal size and therefore maintain the maximum gas exchange capacity in the cold seasons.

While we observed higher iWUE in wild-type *B. distachyon* with increased stomatal numbers, cereals overexpressing the stomatal development inhibitor *EPIDERMAL PATTERNING FACTOR* 1 (*EPF1*) showed a reduction in SD and enhanced iWUE (Hughes et al. 2017; Caine et al. 2018; Dunn et al. 2019). Consequently, I hypothesize that genetic modifications of stomatal anatomical traits in *B. distachyon* beyond the intraspecific range of variation observed in wild-type plants grown in different environments might allow alternative ways to anatomically improve iWUE. Furthermore, due to the tight coordination between stomatal density and size, it is hard to make strong claims about how single anatomical traits independently influence stomatal kinetics and gas-exchange efficiency. Future genetic modifications of single anatomical traits may provide a tool to better investigate the independent influence of SL and SD on stomatal kinetics and water-use efficiency and thus validate the correlations I observed in this study.

The adjusted equations to calculate maximum stomatal pore area and pore depth in graminoid stomata, and accurately estimate anatomical $g_s$max, provide now a tool to link stomatal form and function in *B. distachyon*. These corrections for the graminoid stomatal type can be a useful tool to estimate the maximum gas exchange capacity of different *B. distachyon* genotypes varying in stomatal anatomical traits. Comparisons between anatomical and physiological $g_s$max may also provide a tool to identify mutant phenotypes with compromised stomatal signalling pathways.

When looking at other grass species, significant diversity in stomatal morphology can be observed. Particularly, SCs significantly vary in shape and even in number. *Molina caerulea* displayed elongated SCs identical to *B. distachyon*, while triangular-shaped SCs were found in the other grass species assessed. Still, even among those morphological variation in the SCs could be observed.

A mismatch between anatomical and physiological $g_s$max could be observed in the species containing triangular-shaped $g_s$max, but not in the species containing SCs identical to *B. distachyon*. Therefore, I hypothesize that SCs morphology may influence stomatal functioning and/or the anatomy of the stomatal pores, potentially deviating from the adjustments done for calculating maximum stomatal pore area in *B. distachyon* stomatal pores, which might better suit only species with elongated shaped SCs. Therefore, anatomical $g_s$max estimations in other grass species may require additional adjustments and morphometric analysis of open stomatal pores.

On the other side, physiological $g_s$max estimations may not reflect real maximums due to the difference between the conditions in the LI-6800 leaf chamber and the growth ambient conditions and may require adapting the light intensity used for each species to make sure light intensity is saturating and not inhibitory for stomatal opening.

On one side anatomical $g_s$max estimations in other grass species may require adjustments to better account for the morphological variations observed in the stomatal complexes of different species. On the other side, physiological $g_s$max estimations may not reflect real maximums due to the difference between the conditions in the LI-6800 leaf chamber and the growth ambient conditions and may require adapting the light intensity used for each species to make sure light intensity is saturating but not inhibitory of stomatal opening.

Overall, the gas exchange efficiency and fast stomatal kinetics observed in *B. distachyon* are typical for C_3 grass species, making *B. distachyon* a good model plant for C_3 grass stomatal physiology studies. Leaf-level gas exchange measurements using IRGAs (e.g., LI-6800) were robust and consistent over 120 measurements performed over the course of two years. Nonetheless, environmental factors such as ambient light intensity and temperature, and the time of the day can systemically influence gas exchange. Consequently, leaf-level gas exchange measurements locally responding to the environmental parameters set in the infra-red gas analyser leaf chamber can be systemically influenced by the conditions the plant is experiencing.

Stomatal anatomical traits were strikingly plastic and dependent on the environmental growth conditions. Stomatal density and stomatal size were negatively correlated. Still, variations in stomatal density had a major impact than stomatal length in stomatal closure speed and gas exchange efficiency in wild-type *B. distachyon*.

Therefore, the effect of the environmental growth conditions (e.g., light availability and temperature) on stomatal anatomical traits, and consequently on gas-exchange and stomatal movements, must be considered in long term leaf-level gas exchange studies.

4. Results and discussion – Chapter II

A reverse genetic screen to identify new graminoid stomatal physiology and morphology factors in *Brachypodium distachyon*

4.1 Introduction

According to the Food and Agriculture Organization (FAO), crop production increased more than 50 % between 2000 and 2019, and cereals were the main group of cultivated crops representing approximately one third of the total production. Following cereals were sugar crops and vegetables/oil crops representing 24 % and 12 %, respectively (Food and Agriculture Organization of the United Nations 2021).

Cereals (e.g., maize, wheat and rice) and sugarcane belong to the grass family *Poaceae* and therefore, together approximately 50 % of the cultivated crops comprise grasses. For example in 2019, four grass crops indeed represented half of the total global crop production: sugar cane (21 %), maize (12 %), rice (8%) and wheat (8%) (Food and Agriculture Organization of the United Nations 2021).

The demands for grass crops which are crucial for food security and bioenergy production are rising while, simultaneously, the land used for agriculture is declining (127 million ha between 2000 and 2019) and water stress levels are increasing. Water stress represents the share of freshwater withdrawal in available freshwater resources, after considering environmental water requirements. Currently, water stress is a severe problem affecting Western Asia, Central Asia and Northern Africa (Food and Agriculture Organization of the United Nations 2021). Due to climate change, the levels of water stress are increasing worldwide.

In fact, 2020 was the warmest year globally (1.7°C above the world average temperature) and Europe was the region where the temperature increase has been the most severe in the period between 2000 to 2020. In 2020, the average temperature in Europe was 3.4°C above the world average, while the average temperature change in the 2010s was still 1.3°C (Food and Agriculture Organization of the United Nations 2021). In the winter of 2022, the Western Mediterranean region (including Portugal and Spain) has been seriously affected by drought, with soil water content below the season average and water reservoirs much below capacity (Toreti et al. 2022). On the other hand, above-average temperatures in Europe may favour the development of insects increasing biotic stress pressures on crops (Grünig et al. 2020).

Therefore, the study of the genomics, development and physiology of grasses is crucial to improve both plant productivity and increase tolerance to biotic and abiotic stress. While the model eudicot

plant *Arabidopsis thaliana* provided significant insights in the molecular machinery and biological processes occurring in plants (Krämer 2015; Koornneef and Meinke 2010), the establishment of grass model plants is necessary for the research of relevant grass crops.

Brachypodium distachyon is a rising model plant for grass species which has a nuclear genome identical in size to the one of *A. thaliana*, making it the simplest genome described in grasses to date. Furthermore, *B. distachyon* is a self-fertile species with a reasonably short life cycle of less than four months. Together with its small size, straightforward growth requirements and established *Agrobacterium*-based transformation, *B. distachyon* is a suitable biological system for genetic studies and mutant screens to study grass-environment interactions (Raissig and Woods 2022; Catalán and Vogel 2020; Vogel 2016; Coomey and Hazen 2015; Higgins et al. 2010; Draper et al. 2001).

A central piece for plant-environment interactions are stomata which are the gateways between plants and the atmosphere and therefore crucial for optimize carbon dioxide uptake for photosynthesis and restrict water loss. Plants perceive and accordingly respond to the environmental conditions to adjust the aperture of the stomatal pore and thus optimize gas exchange in a water-use efficient manner (Lawson and Matthews 2020). Fast and highly responsive stomata are therefore crucial for optimal and water-use efficient carbon sink processes, allowing plants to optimize their physiology to the different environmental scenarios.

Grasses present faster and more water-use efficient stomatal movements which are associated with the graminoid morphology consisting of dumbbell-shaped GCs and flanking SCs (McAusland et al. 2016; Franks and Farquhar 2007; Haworth et al. 2021; Raissig et al. 2017).

Grass SCs are required for the fast stomatal movements and may function as specialized ion reservoirs and mechanically accommodate GCs to facilitate stomatal opening and closure (Gray et al. 2020; Nunes et al. 2020; Franks and Farquhar 2007; Chen et al. 2017).

It has been shown in *B. distachyon* that SCs are established and recruited by the transcription factor BdMUTE (Raissig et al. 2017). *bdmute* mutants lack SCs, show defective dumbbell GCs shape and present dysfunctional stomata with slower stomatal movements and apertures (Raissig et al. 2017). Transcriptome analysis between of mature leaves of *B. distachyon* wild-type 21-3 and *bdmute* plants, may therefore allow identifying new molecular players associated with graminoid stomatal

morphology and functioning and targets to improve stomatal functioning and gas exchange efficiency in grass crops.

4.2 Material and methods

4.2.1 RNA-seq and identification of mutant lines for the candidate genes

The transcriptome of 7-days old mature leaves from wild-type *Brachypodium distachyon* (21-3) and *bdmute* mutant plants was obtained by RNA-sequencing by Michael T. Raissig.
Then, I analysed the differently expressed genes and identified mutant lines for the candidate genes from available mutant collections (NaN lines, chemically mutagenized with sodium azide and T-DNA insertion lines) annotated in *Brachypodium distachyon Bd21-3 v1.1* (https://phytozome-next.jgi.doe.gov/info/BdistachyonBd21_3_v1_1). Available knockout mutants and SNP mutants with nonsynonymous mutations were selected. The putative impact of the aminoacid substitution was considered by identifying the mutation site and by prediction of conserved domains (https://www.ncbi.nlm.nih.gov/Structure/cdd/wrpsb.cgi).

4.2.2 Plant material and growth conditions

I vernalized WT *B. distachyon* (Bd21-3) and mutant seeds in water at 4°C for 2 days in the dark and then transferred them to soil. Plants were grown in a glasshouse with an 18:6 h light-dark cycle, average day temperature = 28°C, average night temperature = 25°C and average relative humidity = 40 %. One pot per plant (6 cm X 6 cm X 8 cm) was filled with 4 parts soil (Einheitserde CL ED73) and 1 part vermiculite.

4.2.3 Leaf-level gas exchange measurements and data analysis

I performed all measurements on the youngest fully expanded leaf of plants 3 weeks after sowing using a LI-6800 Portable Photosynthesis System (Li-COR Biosciences Inc., Lincoln, NE, USA) equipped with a Multiphase Flash Fluorometer (6800-01A) chamber. To evaluate speed of stomatal movements and intrinsic water use efficiency (iWUE) in response to changing light, I performed light-response kinetics (1000-100-1000-0 PAR) using the 2 cm^2 leaf chamber with conditions as follows: flow rate = 500 μmol s^{-1}; fan speed = 10000 rpm; leaf temperature = 28°C; relative humidity = 40 %; [CO_2] = 400 μmol mol^{-1}; 1000,100,1000,0 μmol PAR m^{-2} s^{-1}, 20 minutes each light step.

Both WT and mutant individuals were measured in the same period and in a randomized manner to avoid the potential influence of ambient conditions (*a posteriori* quantified and described in the previous chapter (i.e., diurnal rhythm, temperature, and/or ambient light intensity). Light-response measurements (1000-100-100-0 PAR) of gas exchange (carbon assimilation, A and stomatal conductance to water vapor, g_{sw}) were obtained for 3-5 WT and mutant individuals per comparison group (one mutant line vs WT). Measurements were automatically logged every minute. I calculated the relative g_{sw} by normalizing g_{sw} to the highest g_{sw} value observed to evaluate stomatal kinetics. iWUE was calculated as the A to g_{sw} ratio (A/g_{sw}) and the steady-state iWUE as the average of the last steady sate 3 minutes of light-adapted conditions 100 and 1000 PAR. Exponential regressions were obtained for the light transition I (stomatal closure from 1000 to 100 PAR), light transition II (stomatal opening from 100 to 1000 PAR) and light transition III (stomatal closure from 1000 – 0 PAR) to determine the stomatal opening and closure rate constants (k).

Stomatal speed rate constants (k_I, k_{II} and k_{III}) and steady state iWUE (at 100 and 1000 PAR) were represented as heat maps indicating the genotype mean value of each parameter for each WT/NaN mutant pair.

For certain NaN lines (i.e., NaN1997 and NaN1508), LI-6800 measurements were complemented with SC-1 porometer (Meter, Pullman, Washington, USA) measurements to quickly assess ambient-adapted absolute g_{sw}. SC-1 was calibrated using the calibration plate and moist circular filter paper provided with the SC-1. Each measurement was performed in automode (30 seconds). The relative humidity of the SC-1 porometer was returned to < 10 % after each measurement by shaking the sensor head during 30 to 90 seconds. The number of leaves measured and/or other specifications are described in the respective result sections of NaN1997 and NaN1508.

All statistical analyses were performed on GraphPad Prism version 9.1.0, GraphPad Software, San Diego, California USA, www.graphpad.com.

4.2.4 CRISPR cloning of selected candidate genes

Additionally, I selected three candidate genes to be targeted for mutagenesis with CRISPR/Cas9: BdiBd21-3.2G0326500 (*CST1*), BdiBd21-3.4G0026800 (*RLK1*) and BdiBd21-3.1G0916100 (*SCS/EF-HAND CALCIUM BINDING PROTEIN*). *CST1* has already been described as SC-

specific in maize (Wang et al. 2019). *RLK1* had a significant log2 fold change, no mutant line was available and RLKs have been described as involved in Ca^{2+} and ROS signalling during stomatal closure, therefore *RLK1* may be potentially relevant for grass stomata functioning. Finally, *SCS/EF-HAND CALCIUM BINDING PROTEIN* was selected because a significant stomatal closure and iWUE defects was observed in NaN68 (Fig. 2.53).

The first CRISPR/Cas9 cloning system that I used was the Csy4-type-based system (Čermák et al. 2017) (Supplementary table 6). To generate CRISPR/Cas9 constructs targeting *CST1*, priDZ8, priTN31, priTN32, priTN33, priTN34 and priDZ13 were used to amplify the following inserts: (i) Insert 1: promoter specific primer (priDZ8) + CSY_ gRNA1 (priTN31), (ii) Insert 2: REP_gRNA1 (priTN32) + CSY_ gRNA2 (priTN33) and (iii) reaction 3: REP_gRNA2 (priTN34) + CSY_ term (priDZ13). The three inserts were introduced into empty pMODB2103 to generate pMODB2103_CST11guide1/guide2. Lastly, pMOD_A1510, pMODB2103_CST1guide2/guide8 and pMOD_C000 were reconstituted into empty pTRAN250D via a Golden Gate reaction to generate final CRISPR/Cas 9 construct pTRAN250D_CST1.

To generate CRISPR/Cas9 constructs targeting RLK1, priDZ8, priTN35, priTN36, priTN37, priTN38 and priDZ13 were used to amplify the following inserts: (i) Insert 1: promoter specific primer (priDZ8) + CSY_ gRNA1 (priTN35), (ii) Insert 2: REP_gRNA1 (priTN35) + CSY_ gRNA2 (priTN36) and (iii) reaction 3: REP_gRNA2 (priTN37) + CSY_ term (priDZ13). The three inserts were introduced into empty pMODB2103 to generate pMODB2103_RLK1guide1/guide2. Lastly, pMOD_A1510, pMODB2103_RLK1guide1/guide2 and pMOD_C000 were reconstituted into empty pTRAN250D via a Golden Gate reaction to generate final CRISPR/Cas 9 construct pTRAN250D_RLK1.

The second CRISPR/Cas9 cloning system that I used was the Multiplexed system (Lowder et al. 2015). To generate pMDC32_EF-Hand-guide2/8, EF-HAND-guide2 and guide 8 oligos were phosphorylated and annealed with priMR423 and priMR424 and priMR425 and priMR426,

respectively. Then, the annealed EF-Hand guide 2 and 8 oligos were ligated with T4 ligase (NEB) into previously linearized pYPQ131C and pYPQ132C with BglII and SalI (digestion 1) and Esp3I (digestion 2), respectively. pYPQ131C_EF-hand-guide2 and pYPQ132C_Ef-hand-guide8 were cloned into pYPQ142 via a Golden Gate reaction (Supplementary Table 7). Finally, pYPQ167 and pYPQ142_EF-hand-guide2/8 were inserted into the destination vector pMDC32 via a Gateway reaction (Gateway™ LR Clonase™ II Enzyme mix, Cat. No. 11791020, Thermo Fisher Scientific, Waltham, Massachusetts, USA).

To generate pMDC32_CST2/9, CST1-guide2 and guide 9 oligos were phosphorylated and annealed with priMR441 and priMR442 and priMR443 and priMR444, respectively. Then, the annealed CST1 guide 2 and 9 oligos were ligated into previously linearized pYPQ131C and pYPQ132C with BglII and SalI (digestion 1) and Esp3I (digestion 2), respectively. pYPQ131C_CST1-guide2 and pYPQ132C_CST1-guide8 were cloned into pYPQ142 via a Golden Gate reaction (Supplementary table 7). Finally, pYPQ167 and pYPQ142_CST12/9 were inserted into the destination vector pMDC32 via a Gateway reaction (Gateway™ LR Clonase™ II Enzyme mix, Cat. No. 11791020, Thermo Fisher Scientific, Waltham, Massachusetts, USA).

I transformed all constructs in *E.coli* DH5α and selected positive colonies after Taq colony PCR (supplementary table 4), test digestion with specific restriction enzymes and sequenced (Mix2Seq Kit NightXpress, Eurofins Genomics, Ebersberg, Germany). Subsequently, I transformed all final constructs in *Agrobacterium* AGL1 (bacterial transformation protocols in appendix) for further transformation of *B. distachyon* (described in the next chapter).

4.3 Results

4.3.1 Identification of candidate genes and mutants

In the RNA-seq dataset, 179 genes were significantly downregulated in *bdmute* (Table 3), thus potentially associated with the graminoid morphology, and functioning in wild-type *B. distachyon*.

I used the online tool "ShinyGO v.075: Gene ontology Enrichment Analysis + more" (http://bioinformatics.sdstate.edu/go/) to perform gene ontology enrichment analysis using "Annotated keywords (UniPROT)" for the genes identified in *B. distachyon* and their respective homologues in *Arabidopsis thaliana* and rice (*Oryza sativa Indica group*) (Fig. 2.1). Furthermore, I grouped the *Arabidopsis thaliana* homologues by GO terms "molecular function" and "cellular component", which are better established for the model eudicot plant *Arabidopsis thaliana* but not for *Brachypodium distachyon* (Fig. 2.2)

When grouping genes by annotated keywords, I observed that the *Brachypodium distachyon* genes fall into three major groups: i) membrane/transmembrane-associated, ii) secreted/apoplast-associated and iii) signalling-associated. Similarly, in rice, I observed a major group associated with membrane/transmembrane-related genes in addition to the interconnected signalling-related, apoplastic and cell wall-associated categories. As expected, the complexity increased in *Arabidopsis thaliana*, as more information is available for this model plant. Still, the same three major categories can be observed, and additional functional groups can be inferred: receptors, glycoproteins, and serine/threonine-protein kinases in association with the membrane, cell wall and signalling (Fig. 2.1). The grouping of *Arabidopsis thaliana* homologues by GO cellular component revealed two major categories: cell membrane and cell periphery (i.e., extracellular and cell wall). On the other hand, the grouping by GO molecular function identified one major cluster associated with enzyme activity and protein interactions (transferase activity, kinase activity and carbohydrate binding properties), while the other group seems to be associated with transmembrane transport activity (Fig. 2.2).

Since stomatal movements involve intracellular and apoplastic signalling, transport of water and ions and functional cell walls, this gene ontology analysis gave confidence that significant genes associated with stomatal functioning and morphology could be identified. Hence, I started with the mutant screening to search for phenotypes linked with stomatal movements and gas exchange efficiency.

Sequenced populations of chemically mutagenized plants (NaN_3, sodium azide) were produced as a collaboration with research in France (Richard Sibout, INRA, IJPB) and in the United States of

America (Debbie Laudencia-Chingcuanco, USDA-ARS, WRRC) (https://jgi.doe.gov/our-science/science-programs/plant genomics/brachypodium/). As a result, approximately 2000 lines have been produced containing approximately 2 million mutations, providing a resourceful tool for mutant screening studies. Information about mutant availability for desired genes and the nature of the point mutations (silent, nonsense or missense) and the change on the downstream protein product can be assessed as a jbrowse on the Bd21-3 reference genome on Phytozome (https://phytozome-next.jgi.doe.gov/).

Therefore, I prioritized genes from the lowest to log2 fold change and with higher expression levels in the mature zone than in developmental zone of leaf, therefore potentially associated with mature stomatal function and morphology rather than early developmental processes such as stomatal initiation. Following this priority, I identified mutants for the candidate genes from the available sodium azide mutant collection (NaN lines) and also T-DNA insertion lines (Hsia et al. 2017; Bragg et al. 2012). Furthermore, I compiled information regarding the nature and location of the mutation and performed a conserved domain analysis (https://www.ncbi.nlm.nih.gov/Structure/cdd/wrpsb.cgi) to identify if the mutation occurred in imperative protein domains and therefore infer the putative impact on protein function (Table 4).

To evaluate the putative function of the identified candidate genes on graminoid stomata physiology, I screened 60 mutant lines (corresponding to 53 different candidate genes) for stomatal light-responses (Fig. 2.3, 2.6 – 2.62).

I looked for differences in the rate of stomatal opening and closure (k, rate constant) between WT and mutant lines in the three light transitions (1000-100, 100-1000 and 1000-0 PAR) (Fig. 2.4), as an attempt to identify genes associated with the fast stomatal movements observed in grasses. Furthermore, I also evaluated intrinsic water use efficiency (iWUE, ratio between carbon assimilation (A) and stomatal conductance (g_{sw}) (Fig. 2.5) which allows me to (i) identify steady state iWUE phenotypes associated with defective g_{sw} and/or A, and (ii) assess defects in iWUE derived from impaired stomatal kinetics.

While most of the mutants displayed wild-type-like stomatal behaviour and gas exchange or only potential minor phenotypes (Fig. 2.6-2.39), I still identified some substantial mutant phenotypes associated with stomatal kinetics and/or steady-state iWUE (Fig. 2.40 – 2.63).

Note 1: To facilitate discussion and since most of the genes are not identified/characterized in *B. distachyon*, I will refer to the *B. distachyon* genes as their *Arabidopsis* homologue gene name.

Note 2: I will not refer to the mutants as "*gene name*" mutant (e.g., gene is *SLAC1*, mutant is *slac1*), since the impact of the mutations in these genes is not confirmed and when a phenotype is identified a second allele is required to confirm the gene-phenotype association. Therefore, I will generally refer to the mutants as "Mutant line (Bd21-3 ID, *Arabidopsis* homologue)". E.g., NaN375 (BdiBd21-3.2G0403400, *SLAH3).*

Table 3 – Significantly downregulated genes in *bdmute.*

Bd21_3	Bradi	log2FoldChange	Best.hit.arabi.name
BdiBd21-3.2G0758400	NA	-6.918	NA
BdiBd21-3.3G0211100	Bradi3g15780	-6.514	NA
BdiBd21-3.3G0800000	Bradi3g60740	-6.215	AT1G20925.1
BdiBd21-3.4G0232100	NA	-5.967	NA
BdiBd21-3.2G0248900	Bradi2g18943	-5.862	NA
BdiBd21-3.5G0028100	Bradi5g02231	-5.786	NA
BdiBd21-3.4G0400900	Bradi4g28540	-5.632	NA
BdiBd21-3.5G0246300	Bradi5g18780	-5.316	AT1G12740.1
BdiBd21-3.2G0403400	Bradi2g31957	-5.163	AT5G24030.1
BdiBd21-3.3G0672500	Bradi3g50740	-4.809	AT1G65680.1
BdiBd21-3.1G0774800	Bradi1g57725	-4.756	AT3G53810.1
BdiBd21-3.3G0672600	Bradi3g50750	-4.389	AT2G45110.1
BdiBd21-3.2G0602200	Bradi2g47171	-4.208	AT1G66980.1
BdiBd21-3.2G0231300	Bradi2g17530	-4.110	AT3G18280.1
BdiBd21-3.4G0016700	Bradi4g01480	-4.061	AT2G34610.1
BdiBd21-3.1G0366100	Bradi1g27867	-3.860	AT2G36870.1
BdiBd21-3.4G0188800	Bradi4g12970	-3.840	NA
BdiBd21-3.1G0863400	Bradi1g63980	-3.835	AT3G56880.1
BdiBd21-3.3G0640200	Bradi3g48290	-3.832	AT3G59710.1
BdiBd21-3.1G0336000	Bradi1g25693	-3.825	AT4G23180.1
BdiBd21-3.1G0816600	Bradi1g60340	-3.792	AT1G79570.1

BdiBd21-3.3G0114100	Bradi3g08450	-3.783	AT4G04480.1
BdiBd21-3.5G0267600	Bradi5g20380	-3.759	AT1G21270.1
BdiBd21-3.2G0659800	Bradi2g51570	-3.751	AT4G05200.1
BdiBd21-3.2G0248800	NA	-3.625	NA
BdiBd21-3.2G0541900	Bradi2g42550	-3.598	AT3G24450.1
BdiBd21-3.5G0117500	Bradi5g09610	-3.545	AT5G05960.1
BdiBd21-3.1G0281300	Bradi1g21540	-3.478	AT1G72480.1
BdiBd21-3.2G0704400	Bradi2g55060	-3.384	AT3G09220.1
BdiBd21-3.1G0859300	Bradi1g63671	-3.376	AT2G39050.1
BdiBd21-3.2G0694800	Bradi2g54300	-3.299	AT3G55090.1
BdiBd21-3.1G0549600	Bradi1g42458	-3.289	AT4G21390.1
BdiBd21-3.2G0542100	Bradi2g42570	-3.279	AT3G24420.1
BdiBd21-3.4G0026800	Bradi4g02250	-3.276	AT5G60900.1
BdiBd21-3.3G0524600	Bradi3g39780	-3.194	NA
BdiBd21-3.2G0291900	Bradi2g22241	-3.164	AT2G40750.1
BdiBd21-3.2G0326500	Bradi2g24850	-3.125	AT1G21460.1
BdiBd21-3.2G0231500	Bradi2g17550	-3.122	AT3G18280.1
BdiBd21-3.2G0575100	Bradi2g45143	-3.082	NA
BdiBd21-3.3G0503900	Bradi3g38150	-3.064	AT3G19270.1
BdiBd21-3.2G0569000	Bradi2g44750	-3.044	AT1G60590.1
BdiBd21-3.3G0685100	Bradi3g51707	-2.986	AT2G36026.1
BdiBd21-3.2G0686100	Bradi2g53580	-2.918	AT2G40610.1
BdiBd21-3.1G0933500	Bradi1g69220	-2.906	AT2G22860.1
BdiBd21-3.2G0231400	Bradi2g17540	-2.763	AT3G18280.1
BdiBd21-3.1G0575500	Bradi1g44110	-2.750	AT1G70710.1
BdiBd21-3.2G0149100	Bradi2g11212	-2.748	NA
BdiBd21-3.3G0433700	Bradi3g33150	-2.719	AT1G65680.1
BdiBd21-3.4G0451500	Bradi4g32310	-2.712	AT1G47480.1
BdiBd21-3.4G0097100	Bradi4g07130	-2.684	AT5G45890.1
BdiBd21-3.2G0303800	Bradi2g23060	-2.674	AT3G55240.1
BdiBd21-3.5G0140400	Bradi5g11030	-2.576	NA
BdiBd21-3.2G0292700	Bradi2g22290	-2.555	AT1G69530.1
BdiBd21-3.2G0581700	Bradi2g45610	-2.554	AT5G24090.1
BdiBd21-3.5G0025300	Bradi5g02077	-2.511	AT4G28780.1
BdiBd21-3.4G0230500	Bradi4g16081	-2.479	AT4G36470.1
BdiBd21-3.4G0496900	NA	-2.466	NA
BdiBd21-3.3G0478000	Bradi3g36397	-2.440	AT3G14270.1
BdiBd21-3.1G0029200	Bradi1g02205	-2.436	NA
BdiBd21-3.3G0258100	Bradi3g18630	-2.421	AT5G53390.1
BdiBd21-3.4G0026500	Bradi4g02220	-2.413	AT5G10530.1
BdiBd21-3.1G0366900	Bradi1g27920	-2.399	AT5G06730.1
BdiBd21-3.3G0622800	Bradi3g46930	-2.390	AT1G14870.1

BdiBd21-3.2G0051100	Bradi2g03910	-2.355	AT2G32660.1
BdiBd21-3.5G0021200	Bradi5g01797	-2.340	AT5G23960.1
BdiBd21-3.5G0344600	Bradi5g26230	-2.322	AT5G54190.1
BdiBd21-3.5G0110100	Bradi5g09120	-2.318	AT5G04660.1
BdiBd21-3.1G0161800	Bradi1g12130	-2.310	AT1G29930.1
BdiBd21-3.1G0623500	Bradi1g47480	-2.303	AT5G25190.1
BdiBd21-3.3G0735200	Bradi3g55550	-2.303	AT5G60760.1
BdiBd21-3.3G0167400	Bradi3g12627	-2.295	AT2G36910.1
BdiBd21-3.4G0610700	Bradi4g44027	-2.294	AT5G18280.1
BdiBd21-3.2G0671100	Bradi2g52460	-2.290	AT5G44680.1
BdiBd21-3.5G0157500	NA	-2.273	NA
BdiBd21-3.1G0673500	NA	-2.270	NA
BdiBd21-3.1G0431500	Bradi1g32160	-2.260	AT5G20480.1
BdiBd21-3.1G0774700	Bradi1g57720	-2.257	AT3G53810.1
BdiBd21-3.1G0848400	Bradi1g62810	-2.239	AT3G55090.1
BdiBd21-3.2G0661500	Bradi2g51696	-2.227	AT5G43150.1
BdiBd21-3.1G0521900	Bradi1g38360	-2.214	AT5G41761.1
BdiBd21-3.2G0625900	Bradi2g48950	-2.182	AT5G05830.1
BdiBd21-3.1G1031600	Bradi1g77390	-2.169	AT2G45720.1
BdiBd21-3.1G0849300	Bradi1g62870	-2.144	AT3G16660.1
BdiBd21-3.2G0388000	Bradi2g30490	-2.140	AT3G53980.2
BdiBd21-3.4G0026100	Bradi4g02201	-2.128	AT5G10530.1
BdiBd21-3.2G0626600	Bradi2g49000	-2.112	AT5G25610.1
BdiBd21-3.3G0776300	Bradi3g58915	-2.110	AT2G22170.1
BdiBd21-3.2G0442600	Bradi2g35450	-2.108	AT1G45201.1
BdiBd21-3.2G0050900	Bradi2g03900	-2.080	AT5G20480.1
BdiBd21-3.4G0114000	NA	-2.076	NA
BdiBd21-3.1G0888600	Bradi1g66000	-2.060	AT2G37300.2
BdiBd21-3.4G0555300	Bradi4g39920	-2.059	AT1G73040.1
BdiBd21-3.1G1011100	Bradi1g75730	-2.039	AT4G39490.1
BdiBd21-3.3G0690400	Bradi3g52096	-2.028	AT1G32450.1
BdiBd21-3.1G0662000	Bradi1g49920	-2.010	NA
BdiBd21-3.3G0434100	Bradi3g33200	-1.991	AT3G60530.1
BdiBd21-3.3G0180300	Bradi3g13630	-1.990	AT2G02450.2
BdiBd21-3.4G0523600	Bradi4g37520	-1.978	AT5G17230.2
BdiBd21-3.1G0309800	NA	-1.976	NA
BdiBd21-3.1G0146300	Bradi1g10930	-1.975	AT3G18080.1
BdiBd21-3.1G0644800	Bradi1g48770	-1.954	AT4G23810.1
BdiBd21-3.5G0048300	Bradi5g03530	-1.935	AT1G21230.1
BdiBd21-3.3G0565300	Bradi3g42780	-1.929	AT4G33790.1
BdiBd21-3.1G0462000	Bradi1g34210	-1.928	AT4G10310.1
BdiBd21-3.5G0150900	Bradi5g12020	-1.914	AT1G34580.1

BdiBd21-3.3G0701700	Bradi3g53030	-1.912	AT3G25640.1
BdiBd21-3.1G0518000	Bradi1g38120	-1.877	AT2G42840.1
BdiBd21-3.2G0087900	Bradi2g06790	-1.859	AT3G58120.1
BdiBd21-3.5G0121500	Bradi5g09861	-1.856	AT4G00340.1
BdiBd21-3.4G0025900	NA	-1.853	NA
BdiBd21-3.5G0228400	NA	-1.820	NA
BdiBd21-3.5G0123400	Bradi5g10027	-1.753	NA
BdiBd21-3.4G0337900	Bradi4g24040	-1.744	AT1G65870.1
BdiBd21-3.3G0498700	Bradi3g37810	-1.691	AT5G06710.1
BdiBd21-3.1G0296400	Bradi1g22750	-1.672	AT5G45890.1
BdiBd21-3.2G0796700	NA	-1.668	NA
BdiBd21-3.5G0050100	Bradi5g03632	-1.631	AT1G21240.1
BdiBd21-3.2G0541400	Bradi2g42508	-1.610	NA
BdiBd21-3.1G0817700	Bradi1g60397	-1.607	AT3G14350.1
BdiBd21-3.2G0309400	Bradi2g23460	-1.600	AT2G37790.1
BdiBd21-3.2G0466600	Bradi2g36910	-1.587	AT3G62160.1
BdiBd21-3.1G0722900	Bradi1g54420	-1.587	NA
BdiBd21-3.2G0781100	Bradi2g60870	-1.576	AT1G02335.1
BdiBd21-3.2G0556300	Bradi2g43640	-1.572	AT1G30820.1
BdiBd21-3.4G0032200	Bradi4g02600	-1.526	AT3G04730.1
BdiBd21-3.3G0620900	Bradi3g46760	-1.507	AT5G64550.1
BdiBd21-3.3G0455900	Bradi3g34727	-1.488	AT3G63520.1
BdiBd21-3.3G0403900	Bradi3g30718	-1.487	NA
BdiBd21-3.1G0353100	Bradi1g26900	-1.477	AT4G20140.1
BdiBd21-3.4G0041900	NA	-1.448	NA
BdiBd21-3.3G0075100	Bradi3g05790	-1.440	AT5G57630.1
BdiBd21-3.3G0590200	Bradi3g44485	-1.424	NA
BdiBd21-3.1G0599400	Bradi1g45760	-1.419	NA
BdiBd21-3.2G0262500	Bradi2g19930	-1.369	AT2G34140.1
BdiBd21-3.3G0405100	Bradi3g30770	-1.361	AT2G01610.1
BdiBd21-3.2G0244000	Bradi2g18540	-1.359	AT4G09720.1
BdiBd21-3.2G0683100	Bradi2g53390	-1.359	AT4G35550.1
BdiBd21-3.5G0144800	Bradi5g11350	-1.349	AT3G57040.1
BdiBd21-3.2G0456200	Bradi2g36268	-1.342	NA
BdiBd21-3.1G0816300	Bradi1g60320	-1.336	AT3G43190.1
BdiBd21-3.4G0347500	Bradi4g24650	-1.318	NA
BdiBd21-3.3G0719200	Bradi3g54341	-1.318	AT5G11090.1
BdiBd21-3.1G0522300	Bradi1g38400	-1.303	AT4G23790.1
BdiBd21-3.3G0359800	Bradi3g27800	-1.292	AT1G02260.1
BdiBd21-3.2G0090500	Bradi2g06980	-1.290	AT5G45910.1
BdiBd21-3.4G0380500	Bradi4g27210	-1.252	AT3G14110.2
BdiBd21-3.2G0141900	Bradi2g10740	-1.241	NA

BdiBd21-3.1G0146400	Bradi1g10940	-1.213	AT3G18080.1
BdiBd21-3.4G0131100	Bradi4g09312	-1.199	AT3G14470.1
BdiBd21-3.1G0591400	Bradi1g45200	-1.193	AT4G10380.1
BdiBd21-3.1G1019900	Bradi1g76430	-1.193	AT1G65880.1
BdiBd21-3.3G0568600	Bradi3g43070	-1.148	AT2G28190.1
BdiBd21-3.2G0467800	Bradi2g37000	-1.128	AT5G51890.1
BdiBd21-3.3G0705900	Bradi3g53380	-1.115	AT1G32450.1
BdiBd21-3.2G0738700	Bradi2g57730	-1.102	AT3G59300.1
BdiBd21-3.2G0738800	Bradi2g57732	-1.088	NA
BdiBd21-3.5G0312200	Bradi5g23807	-1.074	AT5G33280.1
BdiBd21-3.1G0188400	Bradi1g14110	-1.072	AT3G22810.1
BdiBd21-3.3G0724700	Bradi3g54730	-1.067	AT5G60700.1
BdiBd21-3.3G0074700	Bradi3g05755	-1.064	AT4G16442.1
BdiBd21-3.5G0278600	Bradi5g21310	-1.061	AT1G03475.1
BdiBd21-3.2G0617100	Bradi2g48267	-1.057	AT1G34060.1
BdiBd21-3.5G0242000	Bradi5g18470	-1.047	AT4G35560.2
BdiBd21-3.4G0280000	Bradi4g20197	-1.018	AT1G78060.1
BdiBd21-3.1G0916100	Bradi1g68010	-1.009	AT4G38810.2
BdiBd21-3.2G0605300	Bradi2g47387	-0.994	AT4G18160.1
BdiBd21-3.1G0904900	Bradi1g67170	-0.989	AT1G07320.1
BdiBd21-3.3G0526400	NA	-0.978	NA
BdiBd21-3.2G0160600	Bradi2g12020	-0.952	AT5G19290.1
BdiBd21-3.1G0257500	Bradi1g19730	-0.946	AT5G23530.1
BdiBd21-3.1G0313900	Bradi1g24010	-0.933	AT1G31710.1
BdiBd21-3.1G0505500	Bradi1g37330	-0.917	AT1G69850.1
BdiBd21-3.1G0958900	Bradi1g71290	-0.908	AT1G47740.2
BdiBd21-3.4G0071400	Bradi4g05271	-0.903	AT5G18980.1
BdiBd21-3.3G0654000	Bradi3g49290	-0.895	AT2G28260.1
BdiBd21-3.2G0708300	Bradi2g55340	-0.833	AT2G38120.1
BdiBd21-3.2G0616400	Bradi2g48210	-0.786	AT1G74690.1
BdiBd21-3.2G0494200	Bradi2g38765	-0.769	NA
BdiBd21-3.2G0673700	Bradi2g52660	-0.581	AT4G32390.1

Table 4 – Candidate genes and respective identified and screened mutant lines, amino acid (AA) change and location of the mutation in the protein (domain accession).

Gene ID	Gene description	Line	Genotype	AA change	Domain Accession
BdiBd21-3.3G0114100	F-box protein	NaN51	Hom	A309T	pfam14476
BdiBd21-3.4G0555300	Mannose-binding lectin	NaN175	Hom	A228V	cd09612
BdiBd21-3.3G0622800	*PCR2, PLANT CADMIUM RESISTANCE 2*	NaN342	Hom	A41V	OUT
BdiBd21-3.2G0626600	*RD22, RESPONSIVE TO DESICCATION 22*	NaN344	Hom	G60E	OUT
BdiBd21-3.1G0366900	*CLASS III PEROXIDASE 19, BdPRX19*	NaN407	Hom	E330K	cd00693
BdiBd21-3.1G0366900	*CLASS III PEROXIDASE 19, BdPRX19*	NaN1459	Hom	S90N	cd00693
BdiBd21-3.3G0776300	*PLAT DOMAIN PROTEIN 2, PLAT2*	NaN326	Hom	W164*	Early Stop
BdiBd21-3.3G0503900	*CYP707A4*, ABA 8'-hydroxylase	NaN358	Hom	SPLICE_SITE_DONOR	NA
BdiBd21-3.3G0139100	*SWEET7, CST1-like*	NaN514	Het	A122V	OUT
BdiBd21-3.3G0139100	*SWEET7, CST1-like*	NaN401	Het	SPLICE_SITE_DONOR	NA
BdiBd21-3.1G0859300	*EULS3, EUONYMUS LECTIN S3*	JJ3084	Hom	NA	NA
BdiBd21-3.2G0291900	*WRKY54*	JJ12454	Hom	NA	NA
BdiBd21-3.4G0016700	Cotton fiber protein	JJ19779	Hom	NA	NA
BdiBd21-3.2G0248900	Ribosome inactivating protein	JJ8807	Hom	NA	NA
BdiBd21-3.1G0848400	*ABCG16, ATP-BINDING CASSETTE G16; JAT1, JASMONATE TRANSPORTER1*	NaN1673	Hom	D165N	cl36780
BdiBd21-3.4G0097100	*SAG12, SENESCENCE-ASSOCIATED GENE 12*	NaN373	Hom	P176S	pfam00112
BdiBd21-3.4G0114000	Anthranilate O-methyltransferase	JJ2380	Hom	G262E	pfam03492
BdiBd21-3.1G0336000	*CYSTEIN-RICH RLK 10, CRK10*	NaN1942	Hom	G391S	cd14066
BdiBd21-3.1G0281300	Lung seven transmembrane protein	NaN1911	Hom	F241L	cl21735
BdiBd21-3.2G0326500	*SWEET1; CST1*	NaN1997	Hom	A79V	pfam03083
BdiBd21-3.2G0248900	F-box protein	NaN1843	Hom	A129V	OUT

BdiBd21-3.1G0591400	*NIP5;1*, aquaporin	NaN218	Hom	A153V	cl00200
BdiBd21-3.5G0312200	*CHLORIDE CHANNEL G, CLCG*	NaN353	Hom	T12I	OUT
BdiBd21-3.2G0605300	*KCO6,TPK3*	NaN86	Hom	P370S	OUT
BdiBd21-3.3G0167400	*ATP-BINDING CASSETTE B1, ATPGP1*	NaN34	Hom	S822F	cl36537
BdiBd21-3.1G0816300	*SUCROSE SYNTHASE 4, SUS4*	NaN1534	Hom	A78T	PLN00142
BdiBd21-3.3G0359800	Divalent anion-sodium symporter (DASS)	NaN69	Hom	L403F	cl21473
BdiBd21-3.3G0359800	Divalent anion-sodium symporter (DASS)	NaN1599	Hom	A187V	cl21473
BdiBd21-3.3G0359800	Divalent anion-sodium symporter (DASS)	NaN319	Hom	G539E	cl21473
BdiBd21-3.1G0816600	Protein kinase	NaN224	Hom	S205N	OUT
BdiBd21-3.1G0848400	ABC-2 type transporter	NaN356	Hom	V263I	cl36780
BdiBd21-3.2G0244000	*RAB GTPASE HOMOLOG G3A, RABG3A*	NaN428	Hom	D115N	cd01862
BdiBd21-3.5G0021200	*TPS21, TERPENE SYNTHASE 21*	NaN379	Hom	A49V	OUT
BdiBd21-3.2G0542100	*DLK2*, alpha/beta-hydrolase	NaN245	Hom	P203S	COG0596
BdiBd21-3.2G0581700	*CHIA, CHITINASE A*	NaN1550	Hom	H73Y	cd02877
BdiBd21-3.1G0188400	*FL2, FORKED-LIKE2*	NaN263	Hom	W33*	NA
BdiBd21-3.1G0296400	*SAG12, SENESCENCE-ASSOCIATED GENE 12*	NaN1588	Hom	V16I; A235T	pfam00112
BdiBd21-3.1G0916100	*SnRK2-Interacting Calcium Sensor, SCS*; EF hand calcium binding protein	NaN68	Hom	G83R	pfam13499
BdiBd21-3.1G0916100	*SnRK2-Interacting Calcium Sensor, SCS*; EF hand calcium binding protein	NaN369	Hom	R143K	OUT
BdiBd21-3.3G0724700	Glycosyltransferase family protein 2	NaN403	Hom	G462D	OUT
BdiBd21-3.4G0610700	*APYRASE 2, APY2*	NaN251	Hom	E313K	cl17037
BdiBd21-3.2G0659800	*CYSTEIN-RICH RLK 25, CRK25*	NaN307	Hom	A201T	OUT
BdiBd21-3.5G0117500	Probable lipid transfer (LTP_2)	NaN255	Hom	Intron	NA
BdiBd21-3.1G0505500	*NITRATE TRANSPORTER 1:2, NRT1:2/NTL1*	NaN1457	Hom	Gcc/Acc	cl28910
BdiBd21-3.2G0442600	*TRIACYLGLYCEROL LIPASE-LIKE 1, TLL1*	NaN1485	Hom	E135*	NA

BdiBd21-3.3G0211100	Aromatic-L-amino-acid decarboxylase / Tryptophan decarboxylase	NaN132	Hom	A102T	NA
BdiBd21-3.3G0705900	*NITRATE TRANSPORTER 1.5, NRT1.5/NPF7.3*	NaN427	Hom	G525V	cd17419
BdiBd21-3.4G0523600	*PHYTOENE SYNTHASE, PSY*	NaN2038	Hom	A91T	PLN02632
BdiBd21-3.4G0347500	ABA/WDS induced protein	NaN1954	Hom	A27V	OUT
BdiBd21-3.1G0431500	*EF-TU receptor, EFR*	NaN2049	Hom	G228R	cl33413
BdiBd21-3.2G0403400	*SLAC1 HOMOLOGUE 3, SLAH3*	NaN375	Hom	P325L	cd09323
BdiBd21-3.4G0114000	Anthranilate O-methyltransferase	NaN2106	Hom	G262E	pfam03492
BdiBd21-3.5G0121500	*RECEPTOR-LIKE PROTEIN KINASE 4, RLK4*	NaN1541	Hom	A173V	cl03036
BdiBd21-3.3G0075100	*CBL-INTERACTING PROTEIN KINASE 21, CIPK21/SnRK3.4*	NaN1963	Hom	E297K	OUT
BdiBd21-3.2G0704400	*LACCASE 7, LAC7*	NaN170	Hom	G204V	cl37260
BdiBd21-3.5G0050100	*WALL-ASSOCIATED KINASE 3, WAK3*	NaN397	Hom	G147D	OUT
BdiBd21-3.2G0467800	*CLASS III PEROXIDASE 76, BdPRX76*	NaN1528	Hom	A197S	cd00693
BdiBd21-3.2G0467800	*CLASS III PEROXIDASE 76, BdPRX76*	NaN1508	Het[1]	E44*	Na
BdiBd21-3.1G0462000	*HIGH-AFFINITY K+ TRANSPORTER 1, HKT1; OsHKT2;4*	NaN570	Het	W482*	NA
BdiBd21-3.1G0462000	*HIGH-AFFINITY K+ TRANSPORTER 1, HKT1; OsHKT2;4*	NaN553	Het	W321*	NA

Note: OUT means “mutation out of the prediction domains”

[1] Homozygous individuals were selected by genotyping and used in the Li-6800 screening (genotyping described in chapter III).

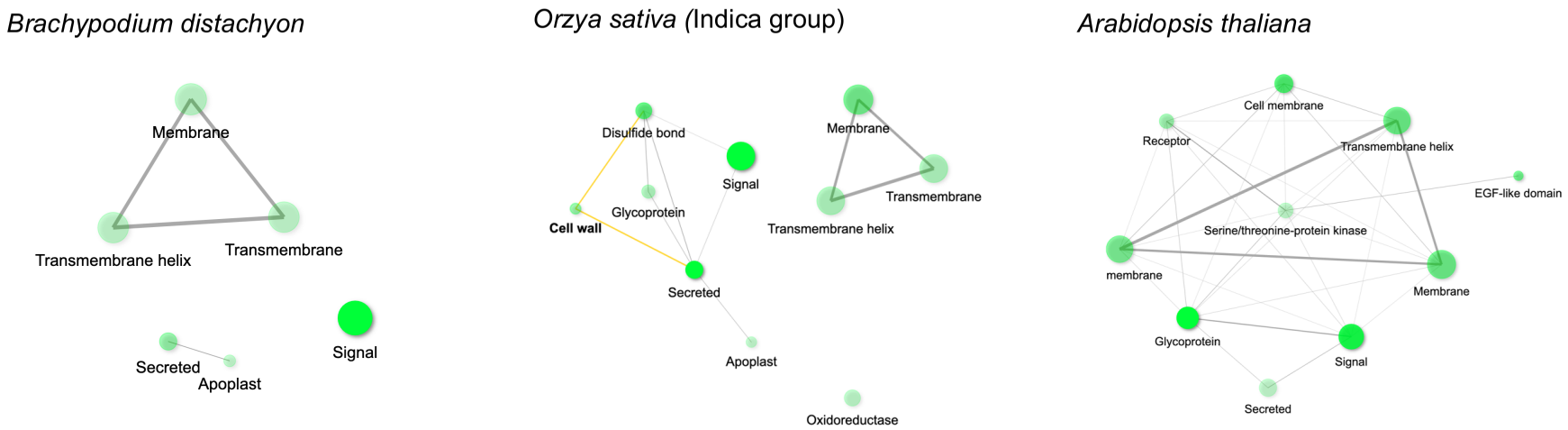
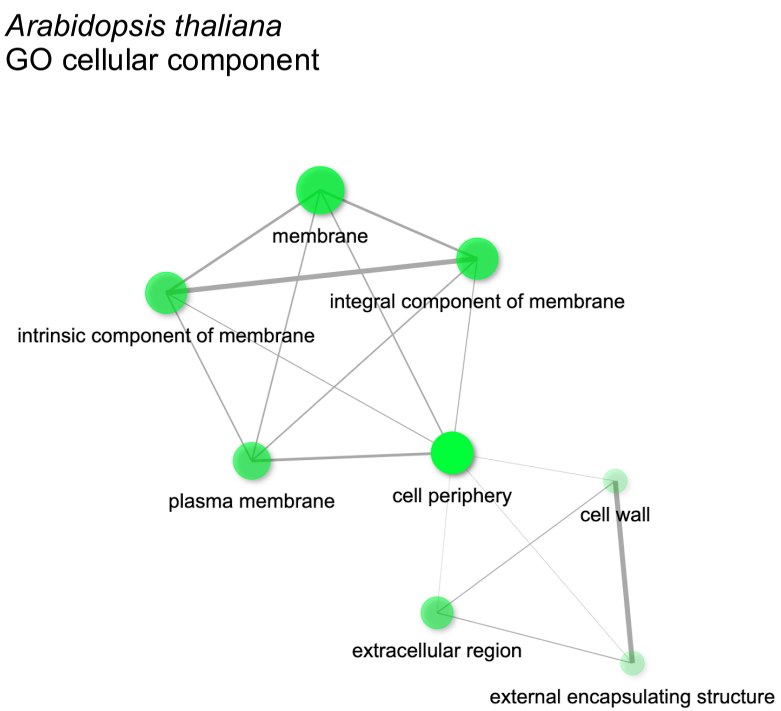


Figure 2.1 – Gene ontology analysis for annotated keywords (UniPROT), using ShinyGO v.075 (http://bioinformatics.sdstate.edu/go/) for the genes identified in *B. distachyon* and their respective homologues in *Oryza sativa (Indica group*) and in *Arabidopsis thaliana*.



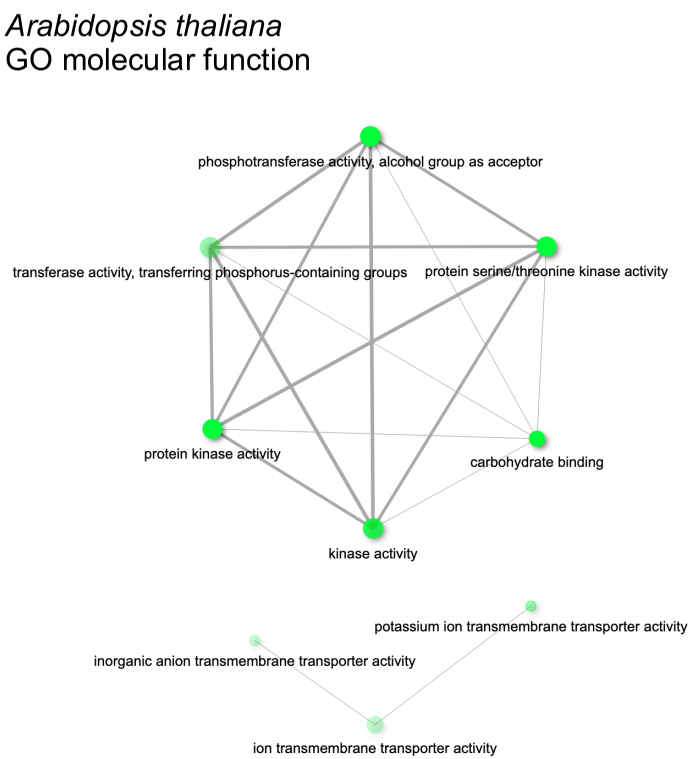


Figure 2.2 – Gene ontology analysis (GO terms for cellular component and molecular function) of *Arabidopsis thaliana* homologues, using ShinyGO v.075 (http://bioinformatics.sdstate.edu/go/)

sporter activity

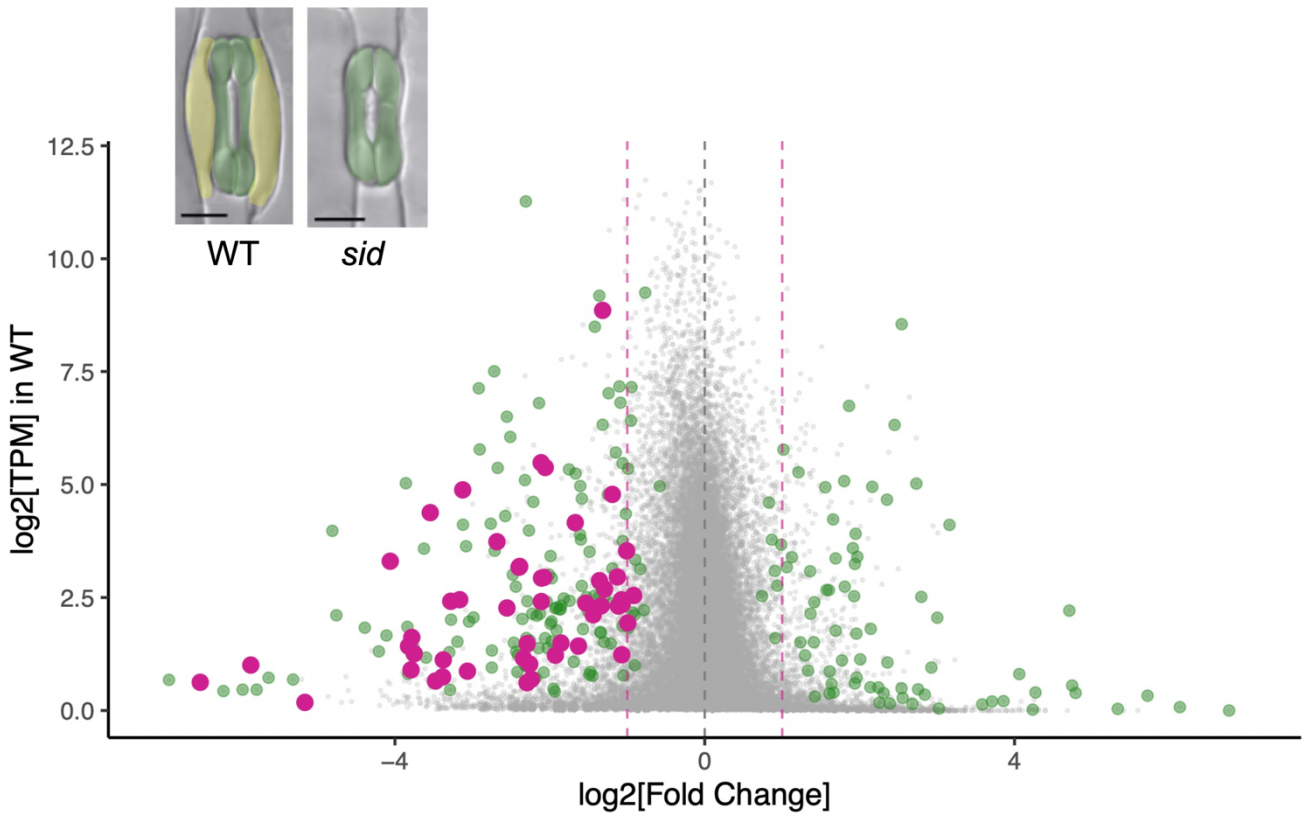


Figure 2.3 – RNA-seq comparison between B21-3 (WT) and *bdmute*. Significantly differentially expressed genes (DEGs) represented in green. Left side represents genes downregulated in *bdmute*. Genes for which mutant lines were identified and screened for leaf-level gas exchange in magenta. Grey dashed line represents log2 fold change = 0 separating downregulated and upregulated genes. Magenta dashed lines rpersents log2 fold change = -1 and 1.

4.3.2 Stomatal kinetics phenotypes

Regarding stomatal kinetics (k), most of the phenotypes that I observed were associated with slower stomatal movements, particularly slower stomatal closure in response to lower light intensity (100 PAR) and/or darkness (0 PAR) (Fig. 2.4).

I found that six mutant lines, NaN375 (BdiBd21-3.2G0403400, *SLAH3*) (Fig. 2.59), NaN1457 (BdiBd21-3.1G0505500, *NRT1.2*) (Fig. 2.56), NaN397 (BdiBd21-3.5G0050100, *WAK3*) (Fig. 2.61), NaN86 (BdiBd21-3.2G0605300, *TK3/KCO6*) (Fig. 2.47), NaN255 (BdiBd21-3.5G0117500, *LTP2*) (Fig. 2.55) and NaN514 (BdiBd21-3.3G0139100, *SWEET7*) (Fig. 2.43) displayed significantly slower stomatal closure in response to decreasing light intensity from 1000 to 100 (k_I) and/or to 0 PAR (k_{III}) ($p<0.05$) (Fig. 2.4).

Furthermore, I found four mutant lines NaN407 (BdiBd21-3.1G0366900, *BdPRX19*) (Fig. 2.41), NaN1550 (BdiBd21-3.2G0581700, *CHIA*) (Fig. 2.52), NaN68 (BdiBd21-3.1G0916100, *SCS/EF-HAND CALCIUM BINDING PROTEIN*) (Fig. 2.53) and NaN1963 (BdiBd21-3.3G0075100, *CPK21*) (Fig. 2.60) showing significant defects ($p<0.05$) not just in stomatal closure (k_I and/or k_{III}) but also in stomatal opening speed (k_{II}) (Fig. 2.4).

Finally, I observed minor stomatal kinetic phenotypes (not statistically significant at 5% of significance, but significant at 10 %, $p<0.10$) in eight other mutant lines (NaN68, NaN34, NaN1599, NaN2049, NaN356, JJ2380 and NaN1508 and NaN379) (Fig. 2.4).

4.3.3 Intrinsic water use efficiency (iWUE) phenotypes

Regarding iWUE, I found iWUE phenotypes in six mutant lines that also contained stomatal kinetics defects, and therefore these iWUE defects may result from the slower stomatal movements (NaN1457, NaN86, NaN1550, NaN255, NaN68 and NaN1963) (Fig. 2.5; section 4.3.2). Nevertheless, I observed that several mutant lines presented iWUE phenotypes but no defects in kinetics, therefore potentially associated with altered g_{sw} and/or A levels (Fig. 2.5). One mutant line presented lower iWUE at both high and low light (1000 and 100 PAR), while 5 and 3 mutant lines showed lower iWUE at only 100 or 1000 PAR, respectively (Fig. 2.5).

NaN397 (BdiBd21-3.5G0050100, *WAK3*) showed lower iWUE at both light-limiting (100 PAR) and non-limiting conditions (1000 PAR) which suggests for lower g_{sw} and constitutively defective stomatal opening (Fig. 2.61). I observed lower iWUE at 100 PAR in NaN69 (BdiBd21-3.3G0359800, *DIVALENT ANION-SODIUM SYMPORTER*) (Fig. 2.49), NaN2049 (BdiBd21-3.1G0431500, *EFR*) (Fig. 2.58), NaN514 (BdiBd21-3.3G0139100, *SWEET7*) (Fig. 2.43), NaN1528 and NaN1508 (BdiBd21-3.2G0467800, *BdPRX76*) (Fig. 2.62), suggesting higher g_{sw} at low light. On the other hand, I observed higher iWUE at 1000 PAR in NaN1485 (BdiBd21-3.2G0442600, *TLL1*) (Fig. 2.57), NaN1459 (BdiBd21-3.1G0366900, *BdPRX19*) (Fig. 2.42) and NaN1997 (BdiBd21-3.2G0326500, *CST1*) (Fig. 2.45), which may reflect either lower g_{sw} or increased A, as photosynthesis is not light-limited in this light step.

4.3.4 *BdPRX19* and *SCS/EF-HAND CALCIUM BINDING PROTEIN*

Since NaN lines contain multiple mutations, no causal relationship can be made between the phenotype observed the mutation in our candidate genes, but only a reported observation of a phenotype in a specific NaN mutant line. For only a few candidate genes multiple NaN lines were phenotyped.

For the *BdPRX19* (BdiBd21-3.1G0366900), I phenotyped two mutant lines (NaN407 and NaN2049). NaN407 showed a statistically significant defect in stomatal movements as described in 4.3.2, while NaN2049 did no display any statistically significant defect at the significance level of 95 % but only at 90 % (Fig. 2.4, 2.41, 2.58). Therefore, the phenotype-gene mutation relationship could not be confirmed.

For the *SCS/EF-HAND CALCIUM BINDING PROTEIN* (BdiBd21-3.1G0916100), a severe defect in stomatal kinetics was observed in NaN68 (Fig. 2.4, 2.53). Still, the second mutant NaN369 displayed a less clear phenotype which was different than what I observed in NaN68 (Fig. 2.4, 2.54). Additionally, I verified that NaN68 also contains another mutation in another candidate gene *RLK4* (BdiBd21-3.5G0121500). To confirm the phenotype in NaN68, I cloned CRIPSR/Cas9 constructs targeting *SCS/EF-HAND CALCIUM BINDING PROTEIN* (BdiBd21-

3.1G0916100), but unfortunately no mutants were obtained due to inefficient CRISPR/Cas9 system and/or calli transformation in *B. distachyon* at this stage of my PhD.

4.3.5 *CST1*

While only one mutant line for BdiBd21-3.2G0326500 (*CST1*) was phenotyped (NaN1997), I observed identical gas exchange phenotypes as described for *zmcst1* maize mutants, which displayed decreased g_{sw} (Wang et al. 2019). I observed that NaN1997 (BdiBd21-3.2G0326500, *CST1*) displayed higher iWUE at 1000 PAR and slightly lower relative g_{sw}, together suggesting potentially lower g_{sw} (Fig. 2.5, 2.45A-D). To further test for absolute g_{sw}, I performed steady-state ambient adapted g_{sw} measurements using the porometer SC-1. I measured five to ten flag leaves per individual. Additionally, I also measured three to six 2nd leaves from the top (mature leaf below flag leaf) per individual. The measurements were performed in randomized manner in two days, equally covering the period from 7:00 to 13:30 h for all individuals and both genotypes, to circumvent the diurnal variation of g_{sw} described in chapter I. I observed a 30 % decrease in steady-state ambient adapted g_{sw} in both flag and 2nd from top mature leaves in NaN1997 than in WT (Fig. 2.45E, F). To confirm that this higher g_{sw} was not caused by anatomical variations, I measured SD and SL from four flag and four 2nd from the top leaves and found no differences between NaN1997 and WT (Fig. 2.45G, H), therefore suggesting a defect in signalling as described in maize *zmcst1* mutants (Wang et al. 2019).

4.3.6 *BdPRX76*

BdiBd21-3.2G0467800 (*BdPRX76*) was the only candidate gene which phenotype was significantly different than WT in one of the targeted gas exchange traits of this study (iWUE) in two independent mutant lines (NaN1528 and NaN1508) (Fig. 2.5, 2.62). Significantly lower iWUE at 100 PAR was observed in both independent screenings of NaN1528 and NaN1508, suggesting that *bdprx76* mutants may present higher g_{sw} and consequently decreased iWUE at the light-limited step (100 PAR) (Fig. 2.5, 2.62B-F). To further assess absolute g_{sw}, I compared steady-state ambient adapted g_{sw} between WT and NaN1508, using the porometer SC-1. I measured twice three to four

leaves per individual and three individuals per genotype. All measurements were performed in randomized manner between 8:00 and 9:30 h, to avoid the effect diurnal rhythms of g_{sw} described in chapter I. NaN1508 mutants showed ~40 % higher ambient-adapted g_{sw} than WT (Fig. 2.62G), corroborating the hypothesis formulated with the LI-6800 results.

Finally, to verify if the higher g_{sw} could be associated with impaired stomatal signalling or with stomatal anatomical defects, I measured SL from the same NaN1508 individuals for which I measured leaf-level gas exchange (but not same leaves, as I performed the leaf collection *a posteriori*). Since the gas exchange phenotype observed in *bdpox* mutants was concordant in both mutant lines NaN1528 and NaN1508, and I observed an anatomical variation in stomatal size, I decided to focus the rest of my PhD project on characterizing *BdPRX76*.

Therefore, I performed further detailed phenotyping studies for this candidate gene to determine its function in the function of grass stomata in the next chapter (Chapter III).

4.3.7 *HKT1/HKT2.4*

After I finish the screening of the described 58 mutant lines and I have chosen *BdPRX76* as the candidate gene to focus the rest of my doctoral research, I received in the laboratory two newly available NaN lines for another candidate gene BdiBd21-3.1G0462000 (*HKT1/HKT2.4*) (Fig. 2.63A). As this gene is a K^+ channel and it has been hypothesized that certain K^+ channels may be specific to SCs while others differently regulated in GCs/SCs, I performed a gas-exchange screening (100-1000-0 PAR) to verify if *hkt2.4* mutants indeed exhibit disturbances in stomatal opening (100-1000 PAR) and/or closure (1000-0 PAR). Both mutants NaN570 and NaN553 contained a heterozygous mutation in the *HKT1/HKT2.4* gene. Therefore, I did plant 10 seeds per line and genotyped the germinating plants (7 to 8 per line). After measuring all individuals for light-responses using the LI-6800, I observed that indeed, NaN553 heterozygous segregants (n=4) and one homozygous individual displayed defective stomatal closure (Fig. 2.63B). On the other hand, I verified that one homozygous NaN570 individual also displayed stomatal closure defects while, in this case, both WT and heterozygous segregants presented wild type-like stomatal responses (Fig. 2.63C). Therefore, I suggest that *hkt2.4* mutants may indeed present significantly impaired

stomatal movements. Further measurements using multiple NaN570 (Hom) and NaN553 (Hom) individuals should be performed to confirm these initial observations.

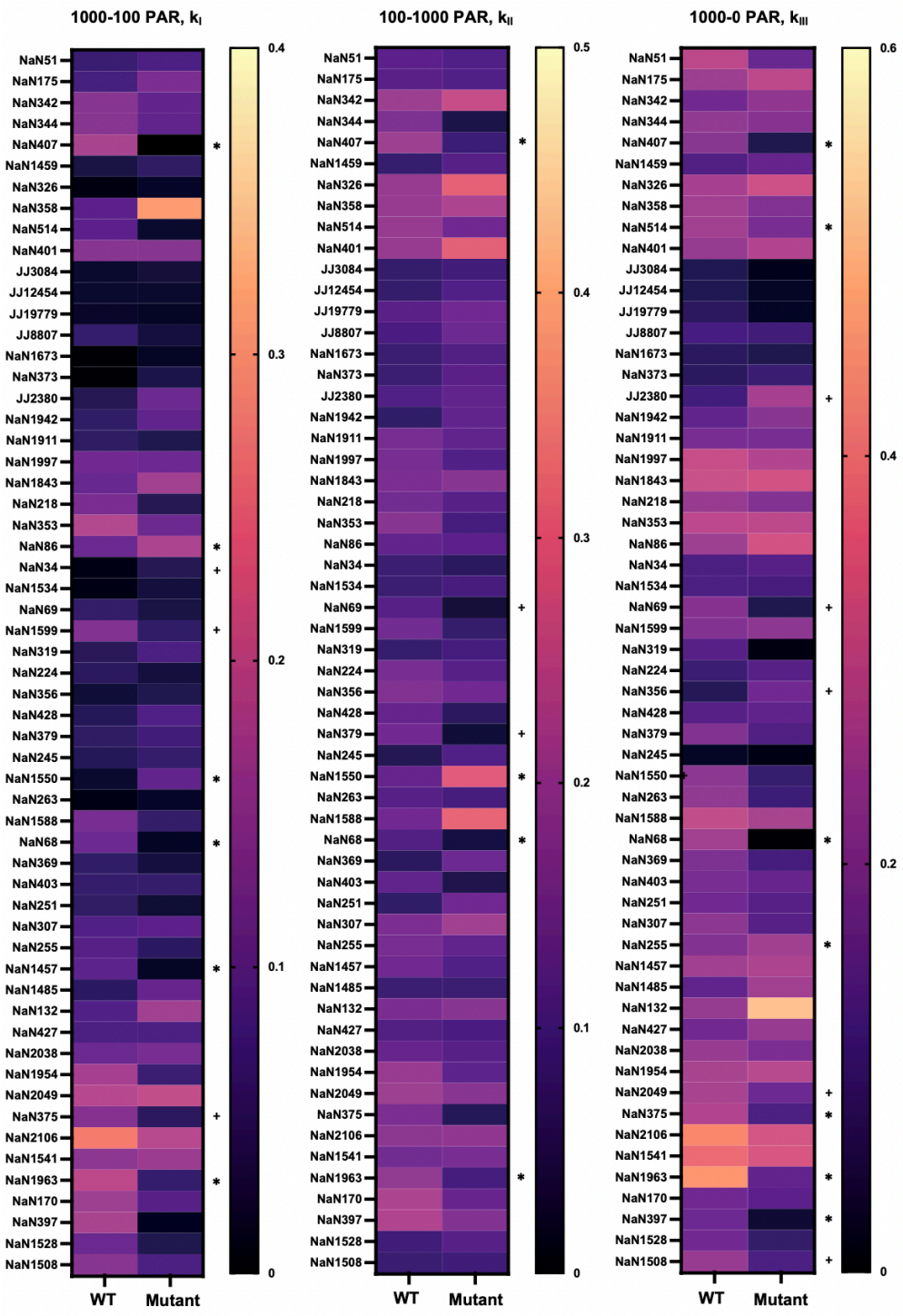


Figure 2.4 – Comparison of stomatal speed (rate constant, k) in the three light transitions (I, 1000-100 PAR; II 100-1000 PAR and III, 1000-0 PAR) between WT and mutant lines. P values obtained from multiple unpaired t-tests. Asterisk (*) represents $p<0.05$; Plus ($^+$) represents $p<0.10$.

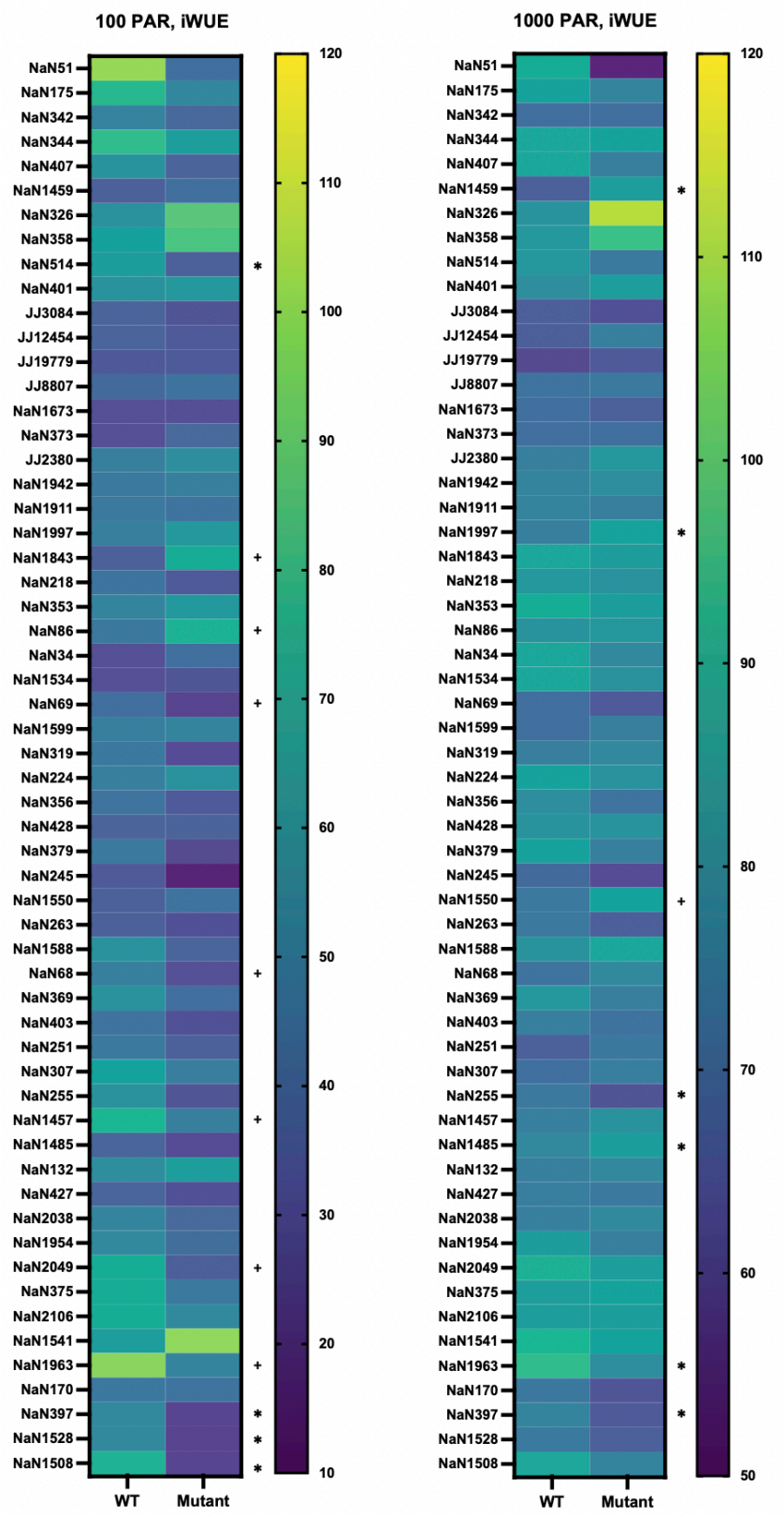
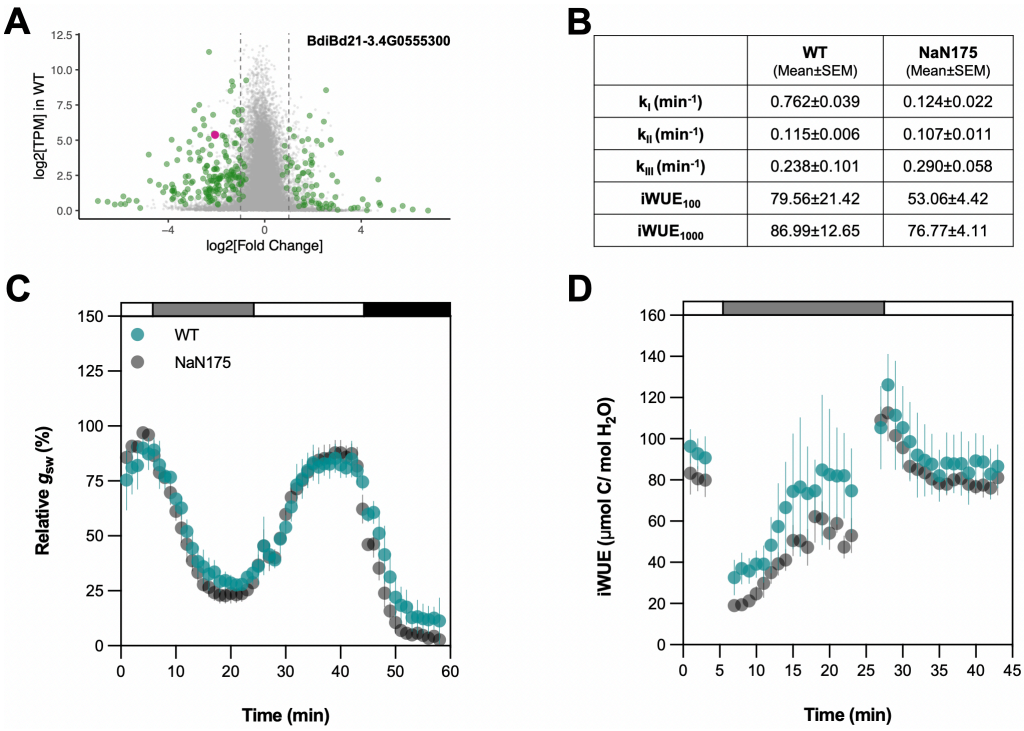


Figure 2.5 – Comparison of iWUE at 100 and 1000 PAR between WT and mutant lines. P values obtained from multiple unpaired t-tests. Asterisk (*) represents $p<0.05$; Plus (+) represents $p<0.10$.

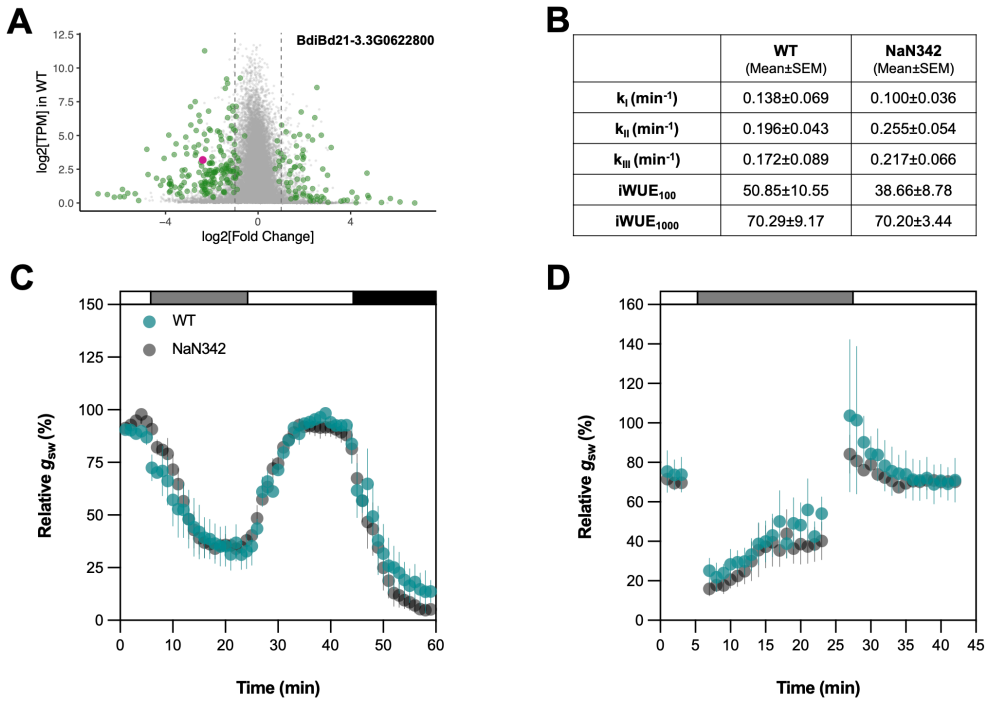
Mutant 2 - NaN175



	WT (Mean±SEM)	NaN175 (Mean±SEM)
k_I (min^{-1})	0.762±0.039	0.124±0.022
k_{II} (min^{-1})	0.115±0.006	0.107±0.011
k_{III} (min^{-1})	0.238±0.101	0.290±0.058
$iWUE_{100}$	79.56±21.42	53.06±4.42
$iWUE_{1000}$	86.99±12.65	76.77±4.11

Figure 2.6– Gas exchange phenotyping of mutant line 2 (NaN175). (A) Identification of the candidate gene in the RNA-seq. **(B)** Average stomatal speed (k) for the three light transitions (k_I, 1000-100 PAR; k_{II}, 100-1000 PAR; k_{III}, 1000-0 PAR) and iWUE at 100 and 1000 PAR in WT and NaN175. **(C)** Relative g_{sw} in WT and NaN175 (n=3). **(D)** iWUE in WT and NaN175 (n=3). Error bars represent SEM.

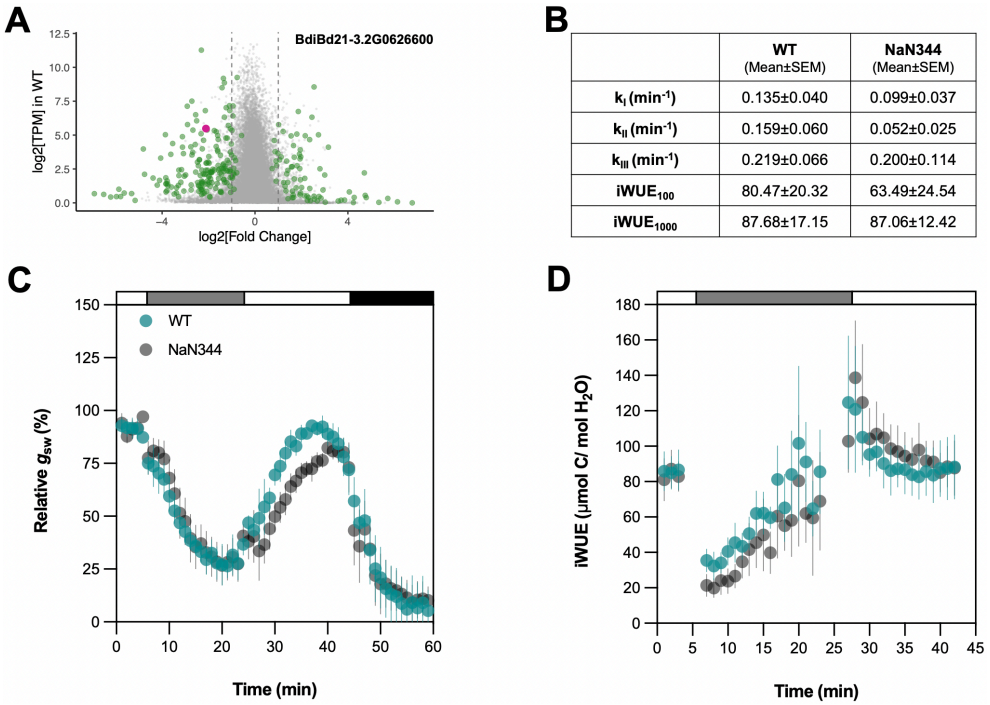
Mutant 3 - NaN342



	WT (Mean±SEM)	NaN342 (Mean±SEM)
k_I (min^{-1})	0.138±0.069	0.100±0.036
k_{II} (min^{-1})	0.196±0.043	0.255±0.054
k_{III} (min^{-1})	0.172±0.089	0.217±0.066
$iWUE_{100}$	50.85±10.55	38.66±8.78
$iWUE_{1000}$	70.29±9.17	70.20±3.44

Figure 2.7 – Gas exchange phenotyping of mutant line 3 (NaN342). (A) Identification of the candidate gene in the RNA-seq. **(B)** Average stomatal speed (k) for the three light transitions (k_I, 1000-100 PAR; k_{II}, 100-1000 PAR; k_{III}, 1000-0 PAR) and iWUE at 100 and 1000 PAR in WT and NaN342. **(C)** Relative g_{sw} in WT and NaN342 (n=3). **(D)** iWUE in WT and NaN342 (n=3). Error bars represent SEM.

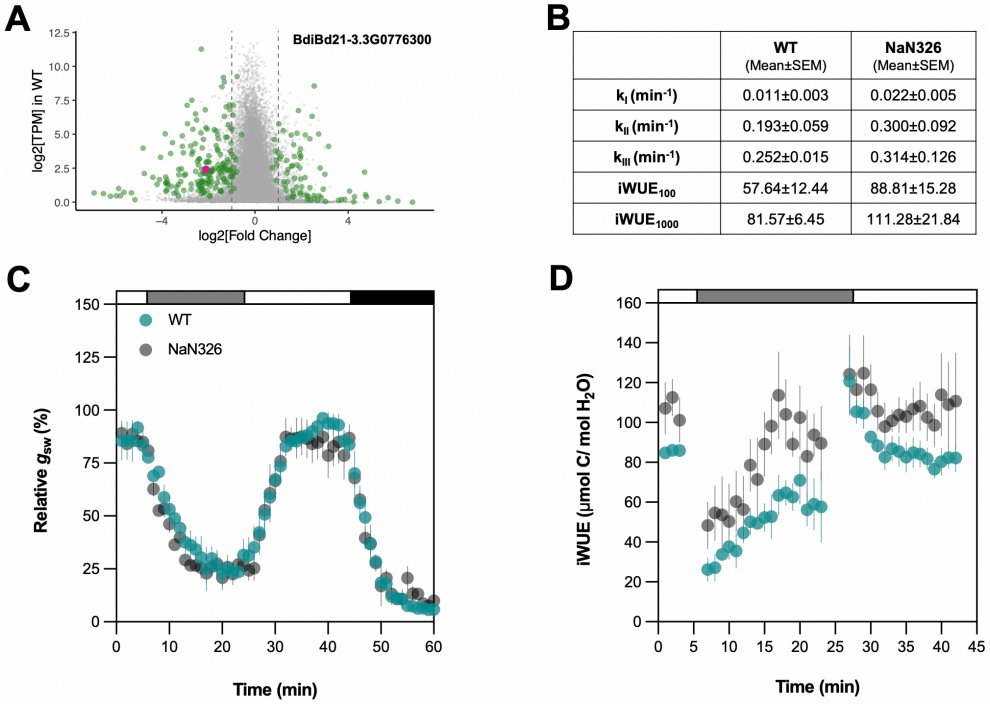
Mutant 4 - NaN344



	WT (Mean±SEM)	NaN344 (Mean±SEM)
k_I (min^{-1})	0.135±0.040	0.099±0.037
k_{II} (min^{-1})	0.159±0.060	0.052±0.025
k_{III} (min^{-1})	0.219±0.066	0.200±0.114
$iWUE_{100}$	80.47±20.32	63.49±24.54
$iWUE_{1000}$	87.68±17.15	87.06±12.42

Figure 2.8 – Gas exchange phenotyping of mutant line 4 (NaN344). (A) Identification of the candidate gene in the RNA-seq. **(B)** Average stomatal speed (k) for the three light transitions (k_I, 1000-100 PAR; k_{II}, 100-1000 PAR; k_{III}, 1000-0 PAR) and iWUE at 100 and 1000 PAR in WT and NaN344. **(C)** Relative g_{sw} in WT and NaN344 (n=3-4). **(D)** iWUE in WT and NaN344 (n=3-4). Error bars represent SEM.

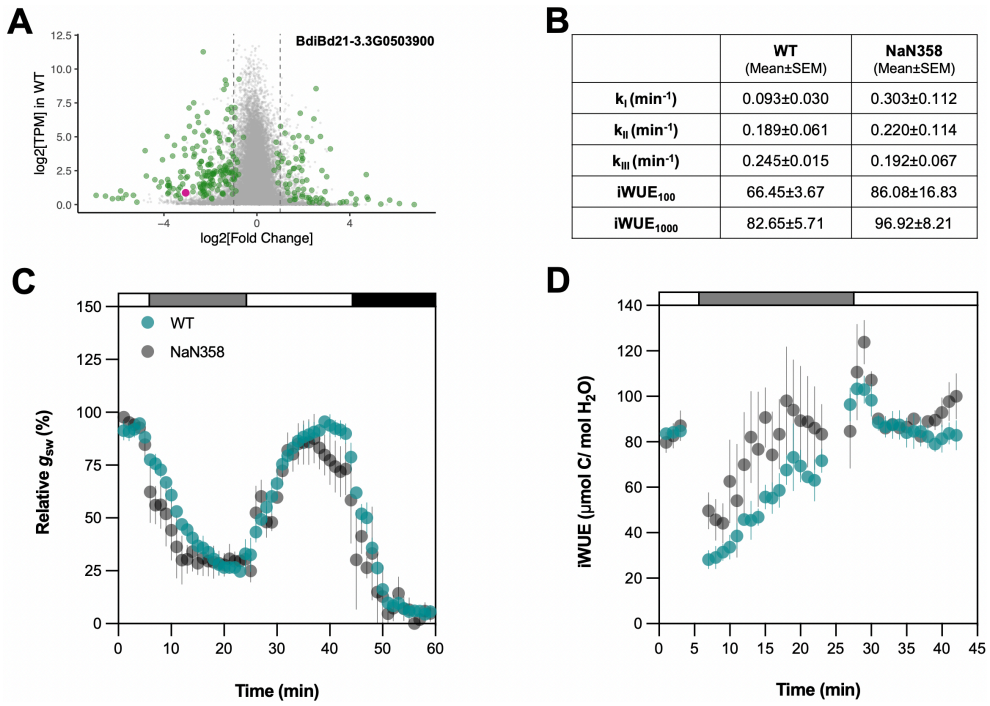
Mutant 7 - NaN326



	WT (Mean±SEM)	NaN326 (Mean±SEM)
k_I (min^{-1})	0.011±0.003	0.022±0.005
k_{II} (min^{-1})	0.193±0.059	0.300±0.092
k_{III} (min^{-1})	0.252±0.015	0.314±0.126
$iWUE_{100}$	57.64±12.44	88.81±15.28
$iWUE_{1000}$	81.57±6.45	111.28±21.84

Figure 2.9 – Gas exchange phenotyping of mutant line 7 (NaN326). (A) Identification of the candidate gene in the RNA-seq. **(B)** Average stomatal speed (k) for the three light transitions (k_I, 1000-100 PAR; k_{II}, 100-1000 PAR; k_{III}, 1000-0 PAR) and iWUE at 100 and 1000 PAR in WT and NaN326. **(C)** Relative g_{sw} in WT and NaN326 (n=3). **(D)** iWUE in WT and NaN326 (n=3). Error bars represent SEM.

Mutant 8 - NaN358



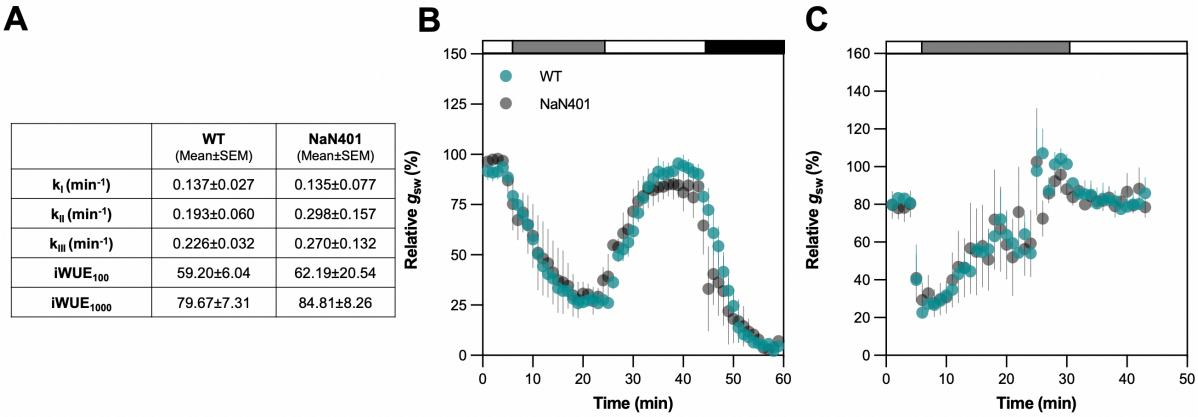
	WT (Mean±SEM)	NaN358 (Mean±SEM)
k_I (min^{-1})	0.093±0.030	0.303±0.112
k_{II} (min^{-1})	0.189±0.061	0.220±0.114
k_{III} (min^{-1})	0.245±0.015	0.192±0.067
$iWUE_{100}$	66.45±3.67	86.08±16.83
$iWUE_{1000}$	82.65±5.71	96.92±8.21

Figure 2.10 – Gas exchange phenotyping of mutant line 8 (NaN358). (A) Identification of the candidate gene in the RNA-seq. **(B)** Average stomatal speed (k) for the three light transitions (k_I, 1000-100 PAR; k_{II}, 100-1000 PAR; k_{III}, 1000-0 PAR) and iWUE at 100 and 1000 PAR in WT and NaN358. **(C)** Relative g_{sw} in WT and NaN358 (n=3). **(D)** iWUE in WT and NaN358 (n=3). Error bars represent SEM.

Mutant 10 - NaN401

BdiBd21-3.3G0139100

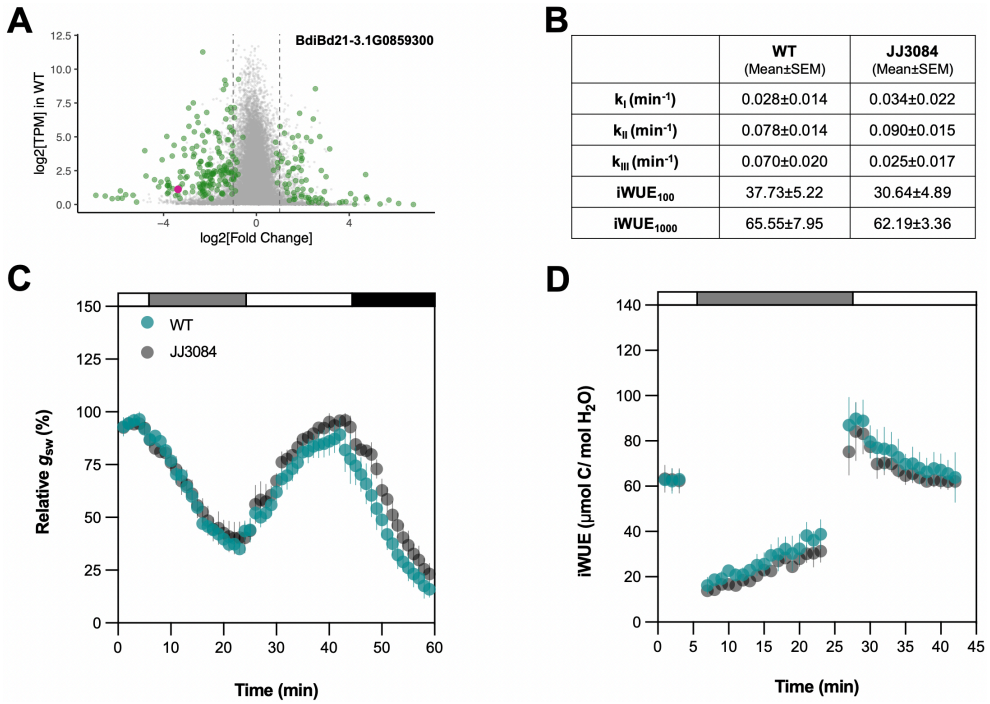
Note: BdiBd21-3.3G0139100 (*SWEET7*) was not found in the RNA-seq comparison between WT and *bdmute*. Although due to its homology to *SWEET1/CST1* (SC-specific gene in maize), I took a quick look at these mutant lines (NaN401 and NaN514).



	WT (Mean±SEM)	NaN401 (Mean±SEM)
k_I (min^{-1})	0.137±0.027	0.135±0.077
k_{II} (min^{-1})	0.193±0.060	0.298±0.157
k_{III} (min^{-1})	0.226±0.032	0.270±0.132
$iWUE_{100}$	59.20±6.04	62.19±20.54
$iWUE_{1000}$	79.67±7.31	84.81±8.26

Figure 2.11 – Gas exchange phenotyping of mutant line 10 (NaN401). (A) Average stomatal speed (k) for the three light transitions (k_I, 1000-100 PAR; k_{II}, 100-1000 PAR; k_{III}, 1000-0 PAR) and iWUE at 100 and 1000 PAR in WT and NaN401. **(B)** Relative g_{sw} in WT and NaN401 (n=3). **(C)** iWUE in WT and NaN401 (n=3). Error bars represent SEM.

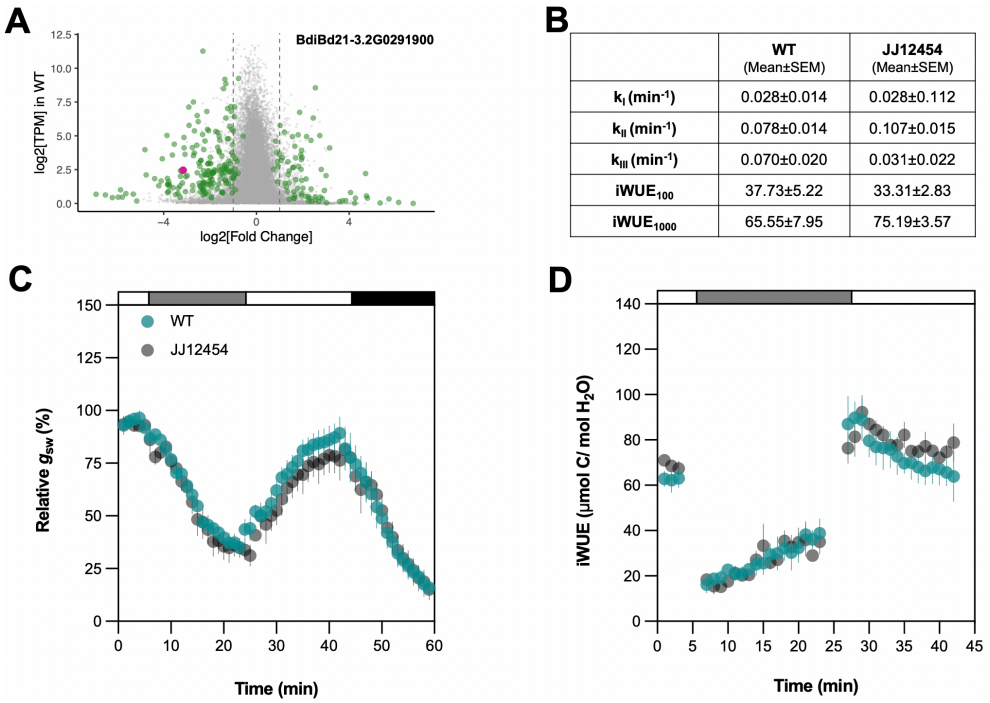
Mutant 11 - JJ3084



	WT (Mean±SEM)	JJ3084 (Mean±SEM)
k_I (min^{-1})	0.028±0.014	0.034±0.022
k_{II} (min^{-1})	0.078±0.014	0.090±0.015
k_{III} (min^{-1})	0.070±0.020	0.025±0.017
$iWUE_{100}$	37.73±5.22	30.64±4.89
$iWUE_{1000}$	65.55±7.95	62.19±3.36

Figure 2.12 – Gas exchange phenotyping of mutant line 11 (JJ3084). (A) Identification of the candidate gene in the RNA-seq. **(B)** Average stomatal speed (k) for the three light transitions (k_I, 1000-100 PAR; k_{II}, 100-1000 PAR; k_{III}, 1000-0 PAR) and iWUE at 100 and 1000 PAR in WT and JJ3084. **(C)** Relative g_{sw} in WT and JJ3084 (n=3). **(D)** iWUE in WT and JJ3084 (n=3). Error bars represent SEM.

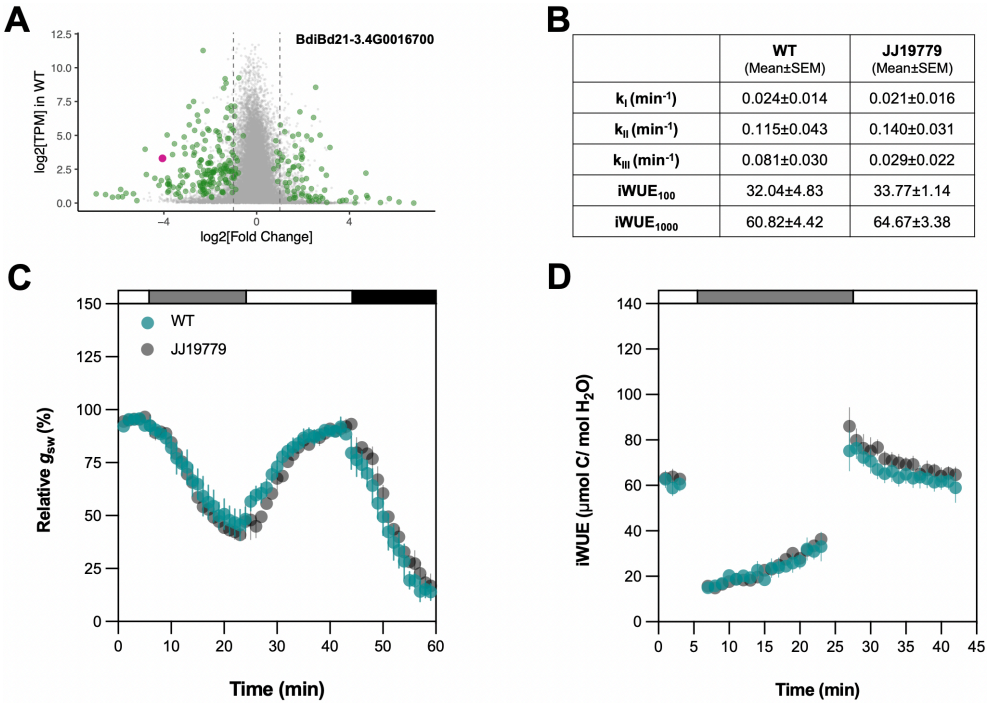
Mutant 12 - JJ12454



	WT (Mean±SEM)	JJ12454 (Mean±SEM)
k_I (min^{-1})	0.028±0.014	0.028±0.112
k_{II} (min^{-1})	0.078±0.014	0.107±0.015
k_{III} (min^{-1})	0.070±0.020	0.031±0.022
$iWUE_{100}$	37.73±5.22	33.31±2.83
$iWUE_{1000}$	65.55±7.95	75.19±3.57

Figure 2.13 – Gas exchange phenotyping of mutant line 12 (JJ12454). (A) Identification of the candidate gene in the RNA-seq. **(B)** Average stomatal speed (k) for the three light transitions (k_I, 1000-100 PAR; k_{II}, 100-1000 PAR; k_{III}, 1000-0 PAR) and iWUE at 100 and 1000 PAR in WT and JJ12454. **(C)** Relative g_{sw} in WT and JJ12454 (n=3-5). **(D)** iWUE in WT and JJ12454 (n=3-5). Error bars represent SEM.

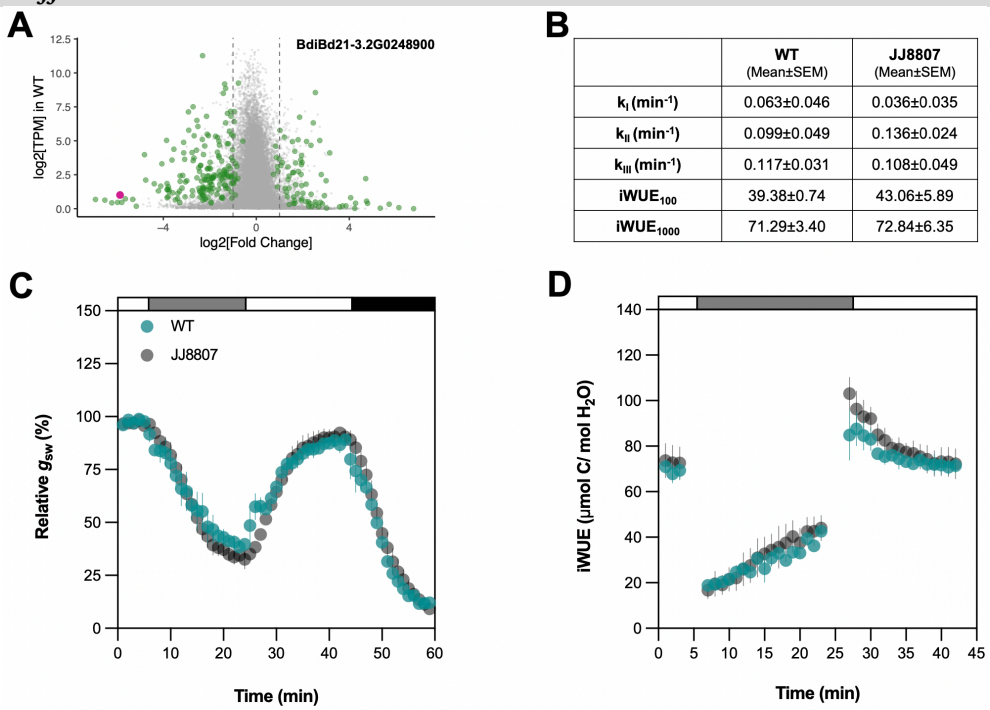
Mutant 13 - JJ19779



	WT (Mean±SEM)	JJ19779 (Mean±SEM)
k_I (min^{-1})	0.024±0.014	0.021±0.016
k_{II} (min^{-1})	0.115±0.043	0.140±0.031
k_{III} (min^{-1})	0.081±0.030	0.029±0.022
$iWUE_{100}$	32.04±4.83	33.77±1.14
$iWUE_{1000}$	60.82±4.42	64.67±3.38

Figure 2.14 – Gas exchange phenotyping of mutant line 13 (JJ19779). (A) Identification of the candidate gene in the RNA-seq. **(B)** Average stomatal speed (k) for the three light transitions (k_I, 1000-100 PAR; k_{II}, 100-1000 PAR; k_{III}, 1000-0 PAR) and iWUE at 100 and 1000 PAR in WT and JJ19779. **(C)** Relative g_{sw} in WT and JJ19779 (n=4). **(D)** iWUE in WT and JJ19779 (n=4). Error bars represent SEM.

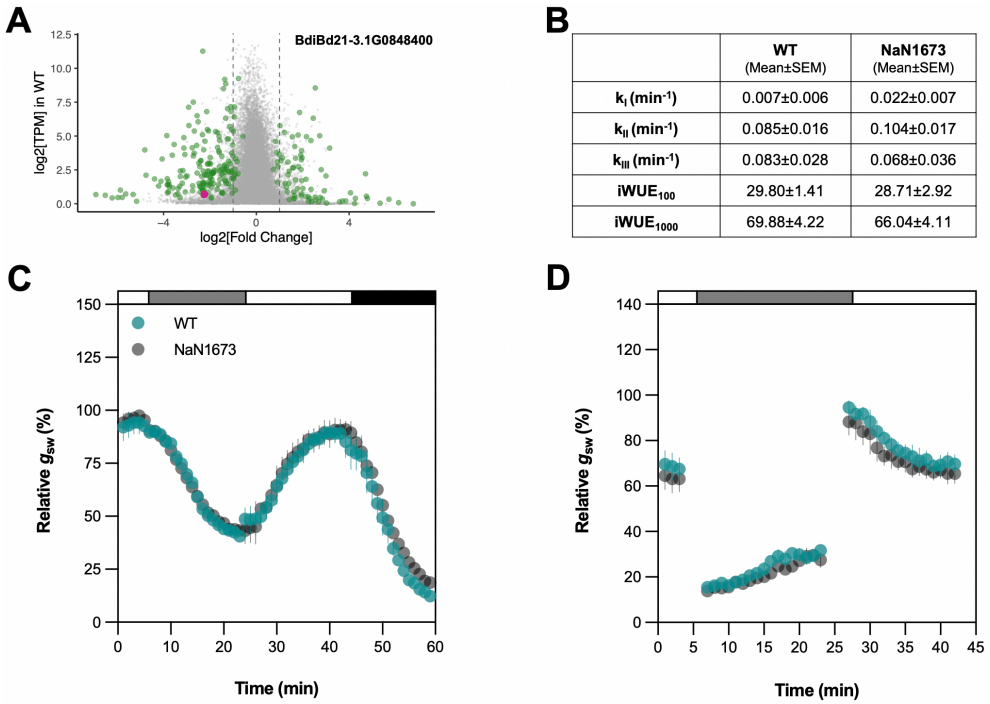
Mutant 14 - JJ8807



	WT (Mean±SEM)	JJ8807 (Mean±SEM)
k_I (min^{-1})	0.063±0.046	0.036±0.035
k_{II} (min^{-1})	0.099±0.049	0.136±0.024
k_{III} (min^{-1})	0.117±0.031	0.108±0.049
$iWUE_{100}$	39.38±0.74	43.06±5.89
$iWUE_{1000}$	71.29±3.40	72.84±6.35

Figure 2.15 – Gas exchange phenotyping of mutant line 14 (JJ8807). (A) Identification of the candidate gene in the RNA-seq. **(B)** Average stomatal speed (k) for the three light transitions (k_I, 1000-100 PAR; k_{II}, 100-1000 PAR; k_{III}, 1000-0 PAR) and iWUE at 100 and 1000 PAR in WT and JJ8807. **(C)** Relative g_{sw} in WT and JJ8807 (n=3). **(D)** iWUE in WT and JJ8807 (n=3). Error bars represent SEM.

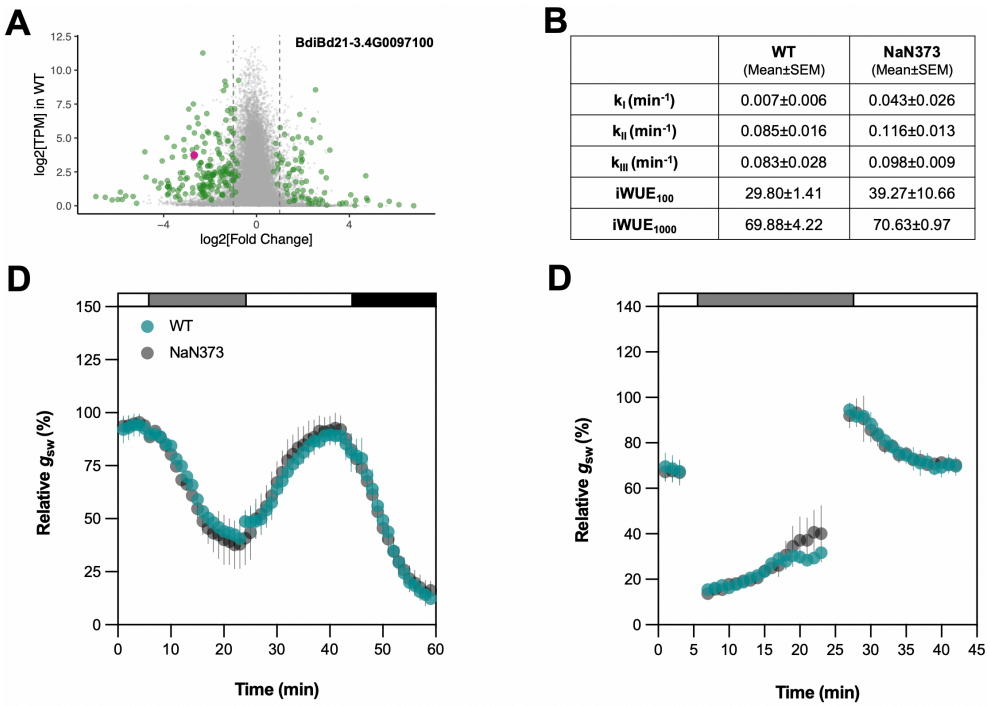
Mutant 15 - NaN1673



	WT (Mean±SEM)	NaN1673 (Mean±SEM)
k_I (min^{-1})	0.007±0.006	0.022±0.007
k_{II} (min^{-1})	0.085±0.016	0.104±0.017
k_{III} (min^{-1})	0.083±0.028	0.068±0.036
$iWUE_{100}$	29.80±1.41	28.71±2.92
$iWUE_{1000}$	69.88±4.22	66.04±4.11

Figure 2.16 – Gas exchange phenotyping of mutant line 15 (NaN1673). (A) Identification of the candidate gene in the RNA-seq. **(B)** Average stomatal speed (k) for the three light transitions (k_I, 1000-100 PAR; k_{II}, 100-1000 PAR; k_{III}, 1000-0 PAR) and iWUE at 100 and 1000 PAR in WT and NaN1673. **(C)** Relative g_{sw} in WT and NaN1673 (n=3). **(D)** iWUE in WT and NaN1673 (n=3). Error bars represent SEM.

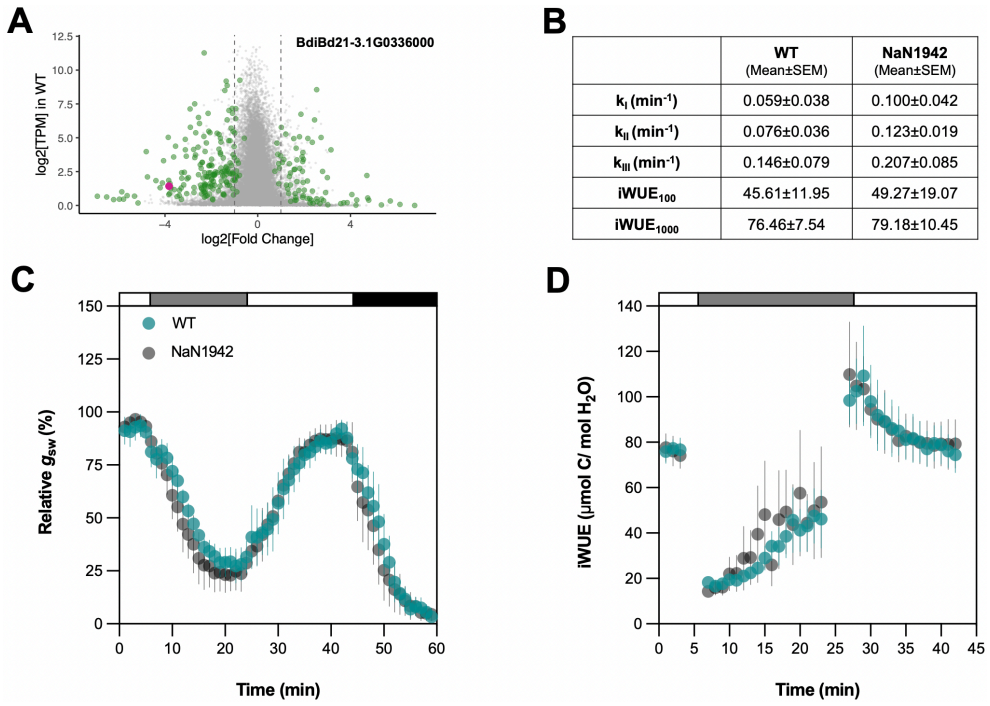
Mutant 16 - NaN373



	WT (Mean±SEM)	NaN373 (Mean±SEM)
k_I (min^{-1})	0.007±0.006	0.043±0.026
k_{II} (min^{-1})	0.085±0.016	0.116±0.013
k_{III} (min^{-1})	0.083±0.028	0.098±0.009
$iWUE_{100}$	29.80±1.41	39.27±10.66
$iWUE_{1000}$	69.88±4.22	70.63±0.97

Figure 2.17 – Gas exchange phenotyping of mutant line 16 (NaN373). (A) Identification of the candidate gene in the RNA-seq. **(B)** Average stomatal speed (k) for the three light transitions (k_I, 1000-100 PAR; k_{II}, 100-1000 PAR; k_{III}, 1000-0 PAR) and iWUE at 100 and 1000 PAR in WT and NaN373. **(C)** Relative g_{sw} in WT and NaN373 (n=3). **(D)** iWUE in WT and NaN373 (n=3). Error bars represent SEM.

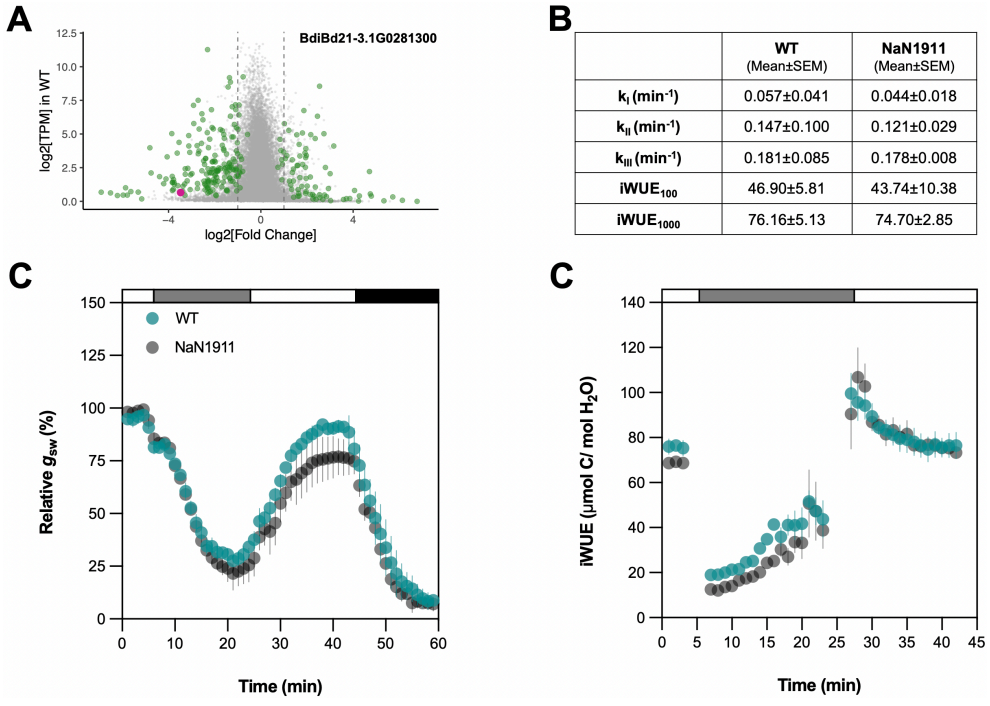
Mutant 18 – NaN1942



	WT (Mean±SEM)	NaN1942 (Mean±SEM)
k_I (min^{-1})	0.059±0.038	0.100±0.042
k_{II} (min^{-1})	0.076±0.036	0.123±0.019
k_{III} (min^{-1})	0.146±0.079	0.207±0.085
$iWUE_{100}$	45.61±11.95	49.27±19.07
$iWUE_{1000}$	76.46±7.54	79.18±10.45

Figure 2.18 – Gas exchange phenotyping of mutant line 18 (NaN1942). (A) Identification of the candidate gene in the RNA-seq. **(B)** Average stomatal speed (k) for the three light transitions (k_I, 1000-100 PAR; k_{II}, 100-1000 PAR; k_{III}, 1000-0 PAR) and iWUE at 100 and 1000 PAR in WT and NaN1942. **(C)** Relative g_{sw} in WT and NaN1942 (n=3). **(D)** iWUE in WT and NaN1942 (n=3). Error bars represent SEM.

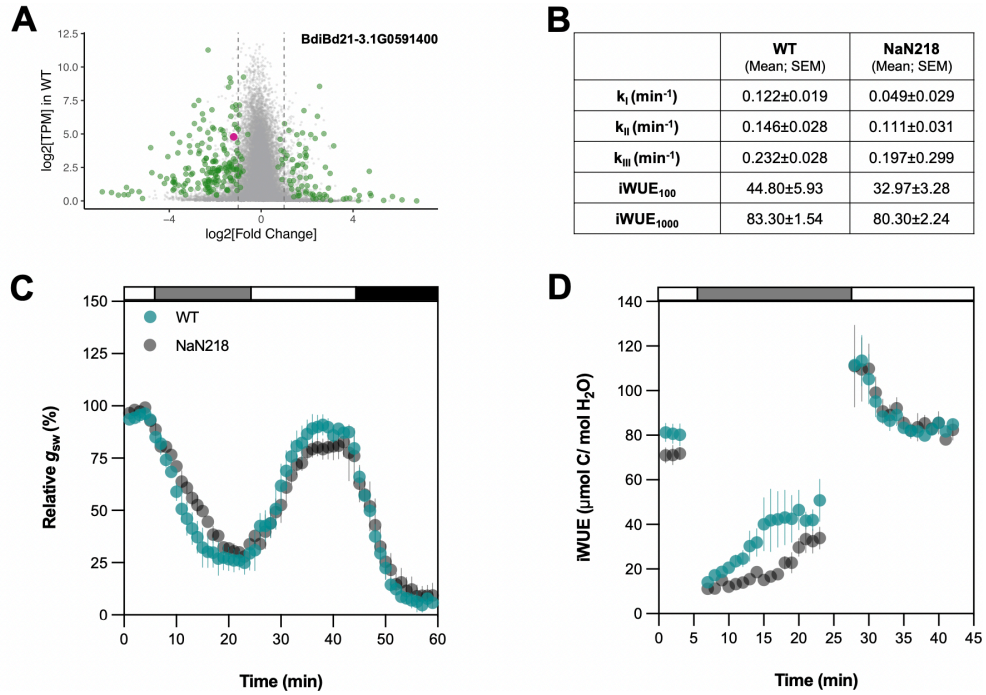
Mutant 19 – NaN1911



	WT (Mean±SEM)	NaN1911 (Mean±SEM)
k_I (min^{-1})	0.057±0.041	0.044±0.018
k_{II} (min^{-1})	0.147±0.100	0.121±0.029
k_{III} (min^{-1})	0.181±0.085	0.178±0.008
$iWUE_{100}$	46.90±5.81	43.74±10.38
$iWUE_{1000}$	76.16±5.13	74.70±2.85

Figure 2.19– Gas exchange phenotyping of mutant line 19 (NaN1911). (A) Identification of the candidate gene in the RNA-seq. **(B)** Average stomatal speed (k) for the three light transitions (k_I, 1000-100 PAR; k_{II}, 100-1000 PAR; k_{III}, 1000-0 PAR) and iWUE at 100 and 1000 PAR in WT and NaN1911. **(C)** Relative g_{sw} in WT and NaN1911 (n=3). **(D)** iWUE in WT and NaN1911 (n=3). Error bars represent SEM.

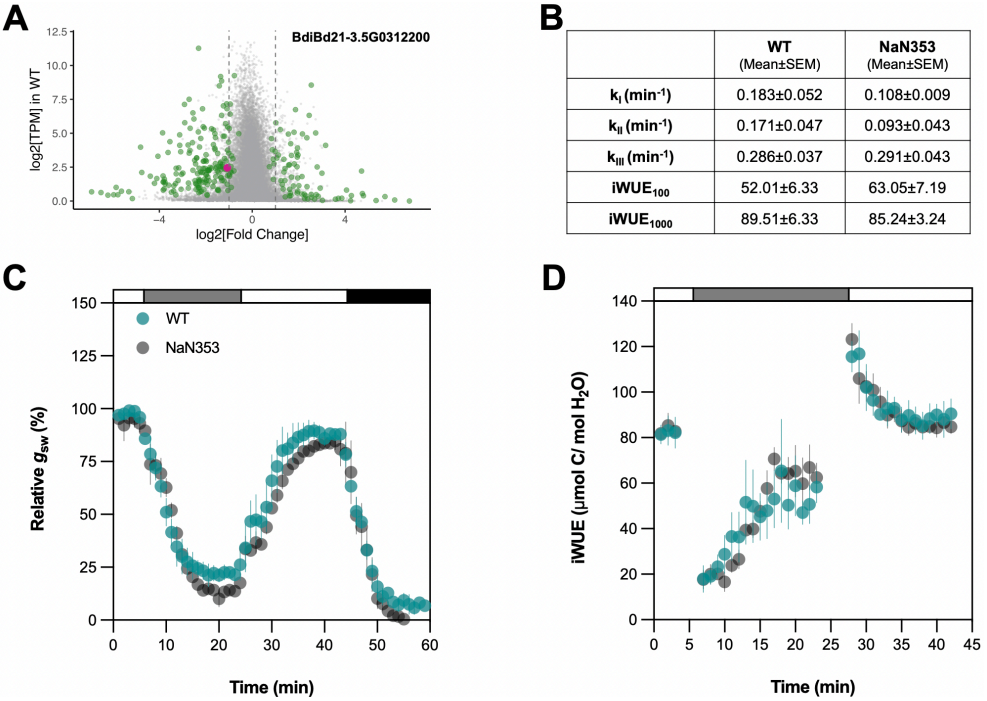
Mutant 22 – NaN218



	WT (Mean; SEM)	NaN218 (Mean; SEM)
k_I (min^{-1})	0.122±0.019	0.049±0.029
k_{II} (min^{-1})	0.146±0.028	0.111±0.031
k_{III} (min^{-1})	0.232±0.028	0.197±0.299
$iWUE_{100}$	44.80±5.93	32.97±3.28
$iWUE_{1000}$	83.30±1.54	80.30±2.24

Figure 2.20 - Gas exchange phenotyping of mutant line 22 (NaN218). (A) Identification of the candidate gene in the RNA-seq. **(B)** Average stomatal speed (k) for the three light transitions (k_I, 1000-100 PAR; k_{II}, 100-1000 PAR; k_{III}, 1000-0 PAR) and iWUE at 100 and 1000 PAR in WT and NaN218. **(C)** Relative g_{sw} in WT and NaN218 (n=3). **(D)** iWUE in WT and NaN218 (n=3). Error bars represent SEM.

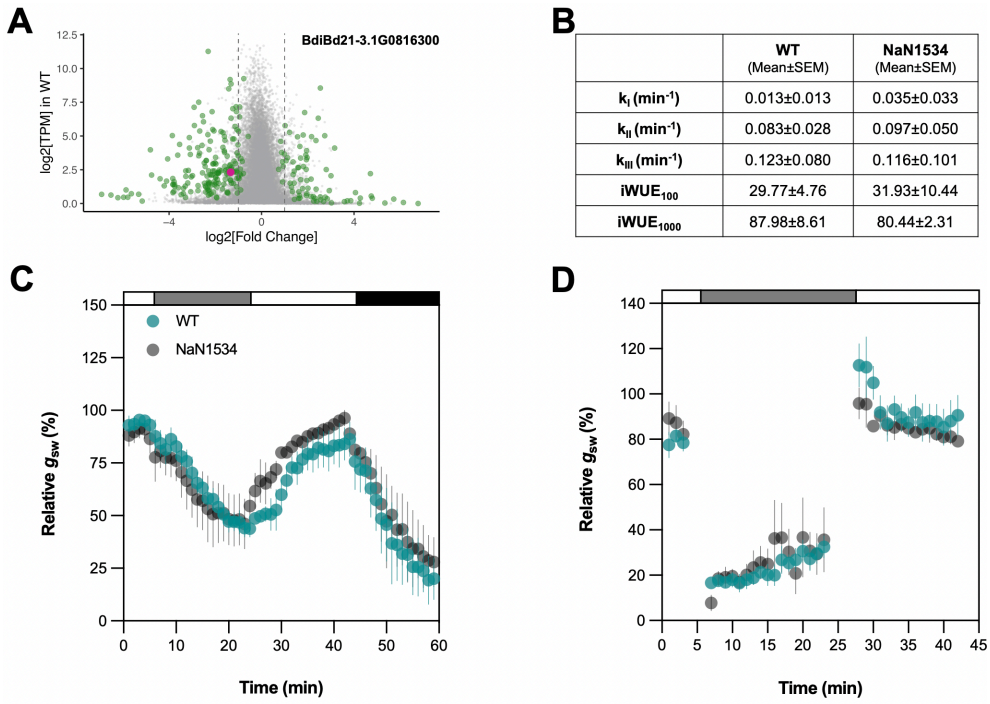
Mutant 23 – NaN353



	WT (Mean±SEM)	NaN353 (Mean±SEM)
k_I (min^{-1})	0.183±0.052	0.108±0.009
k_{II} (min^{-1})	0.171±0.047	0.093±0.043
k_{III} (min^{-1})	0.286±0.037	0.291±0.043
$iWUE_{100}$	52.01±6.33	63.05±7.19
$iWUE_{1000}$	89.51±6.33	85.24±3.24

Figure 2.21 – Gas exchange phenotyping of mutant line 23 (NaN353). (A) Identification of the candidate gene in the RNA-seq. **(B)** Average stomatal speed (k) for the three light transitions (k_I, 1000-100 PAR; k_{II}, 100-1000 PAR; k_{III}, 1000-0 PAR) and iWUE at 100 and 1000 PAR in WT and NaN353. **(C)** Relative g_{sw} in WT and NaN353 (n=3). **(D)** iWUE in WT and NaN353 (n=3). Error bars represent SEM.

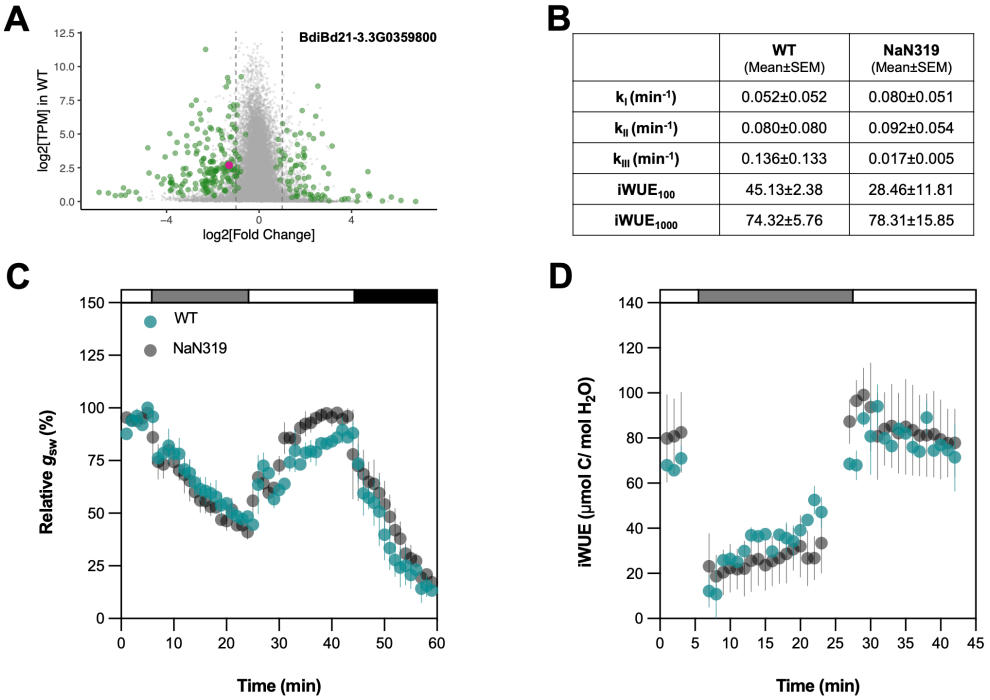
Mutant 26 – NaN1534



	WT (Mean±SEM)	NaN1534 (Mean±SEM)
k_I (min^{-1})	0.013±0.013	0.035±0.033
k_{II} (min^{-1})	0.083±0.028	0.097±0.050
k_{III} (min^{-1})	0.123±0.080	0.116±0.101
$iWUE_{100}$	29.77±4.76	31.93±10.44
$iWUE_{1000}$	87.98±8.61	80.44±2.31

Figure 2.22 – Gas exchange phenotyping of mutant line 26 (NaN1534). (A) Identification of the candidate gene in the RNA-seq. **(B)** Average stomatal speed (k) for the three light transitions (k_I, 1000-100 PAR; k_{II}, 100-1000 PAR; k_{III}, 1000-0 PAR) and iWUE at 100 and 1000 PAR in WT and NaN1534. **(C)** Relative g_{sw} in WT and NaN1534 (n=3). **(D)** iWUE in WT and NaN1534 (n=3). Error bars represent SEM.

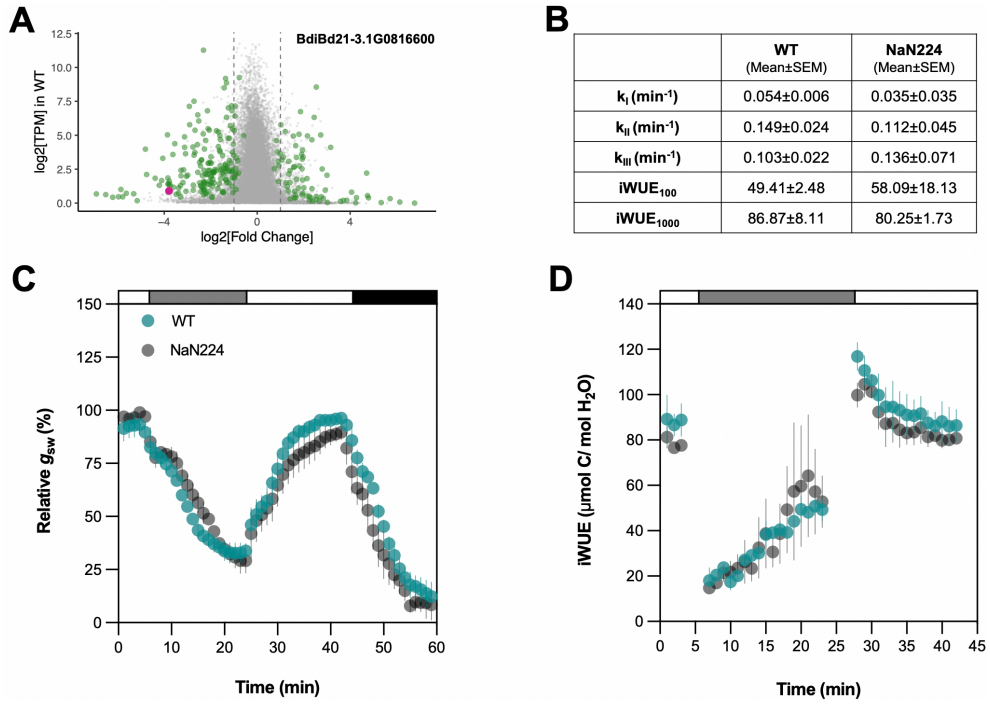
Mutant 29 - NaN319



	WT (Mean±SEM)	NaN319 (Mean±SEM)
k_I (min^{-1})	0.052±0.052	0.080±0.051
k_{II} (min^{-1})	0.080±0.080	0.092±0.054
k_{III} (min^{-1})	0.136±0.133	0.017±0.005
$iWUE_{100}$	45.13±2.38	28.46±11.81
$iWUE_{1000}$	74.32±5.76	78.31±15.85

Figure 2.23 – Gas exchange phenotyping of mutant line 29 (NaN319). (A) Identification of the candidate gene in the RNA-seq. **(B)** Average stomatal speed (k) for the three light transitions (k_I, 1000-100 PAR; k_{II}, 100-1000 PAR; k_{III}, 1000-0 PAR) and iWUE at 100 and 1000 PAR in WT and NaN319. **(C)** Relative g_{sw} in WT and NaN319 (n=2). **(D)** iWUE in WT and NaN319 (n=2). Error bars represent SEM.

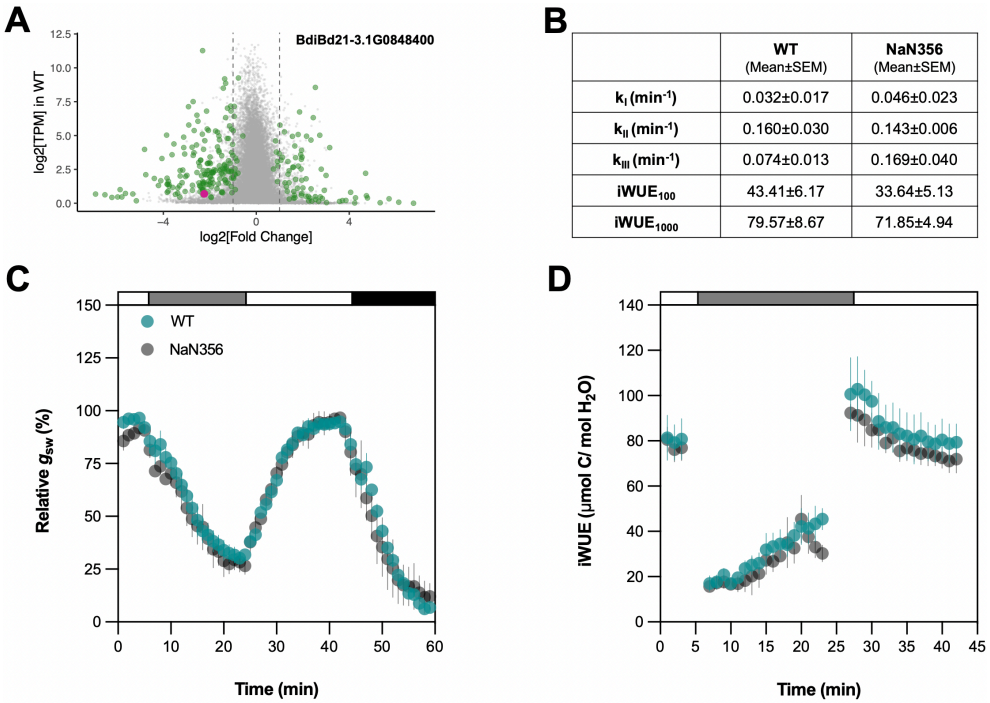
Mutant 30 – NaN224



	WT (Mean±SEM)	NaN224 (Mean±SEM)
k_I (min^{-1})	0.054±0.006	0.035±0.035
k_{II} (min^{-1})	0.149±0.024	0.112±0.045
k_{III} (min^{-1})	0.103±0.022	0.136±0.071
$iWUE_{100}$	49.41±2.48	58.09±18.13
$iWUE_{1000}$	86.87±8.11	80.25±1.73

Figure 2.24 – Gas exchange phenotyping of mutant line 30 (NaN224). (A) Identification of the candidate gene in the RNA-seq. **(B)** Average stomatal speed (k) for the three light transitions (k_I, 1000-100 PAR; k_{II}, 100-1000 PAR; k_{III}, 1000-0 PAR) and iWUE at 100 and 1000 PAR in WT and NaN224. **(C)** Relative g_{sw} in WT and NaN224 (n=3). **(D)** iWUE in WT and NaN224 (n=3). Error bars represent SEM.

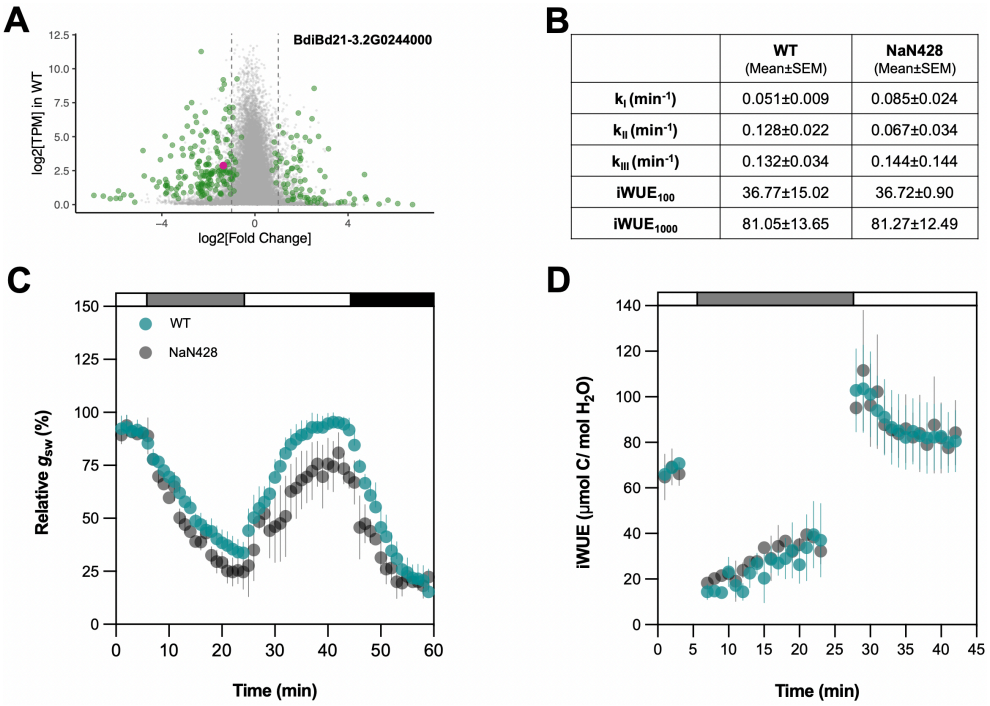
Mutant 31 – NaN356



	WT (Mean±SEM)	NaN356 (Mean±SEM)
k_I (min^{-1})	0.032±0.017	0.046±0.023
k_{II} (min^{-1})	0.160±0.030	0.143±0.006
k_{III} (min^{-1})	0.074±0.013	0.169±0.040
$iWUE_{100}$	43.41±6.17	33.64±5.13
$iWUE_{1000}$	79.57±8.67	71.85±4.94

Figure 2.25 – Gas exchange phenotyping of mutant line 31 (NaN356). (A) Identification of the candidate gene in the RNA-seq. **(B)** Average stomatal speed (k) for the three light transitions (k_I, 1000-100 PAR; k_{II}, 100-1000 PAR; k_{III}, 1000-0 PAR) and iWUE at 100 and 1000 PAR in WT and NaN356. **(C)** Relative g_{sw} in WT and NaN356 (n=3). **(D)** iWUE in WT and NaN356 (n=3). Error bars represent SEM.

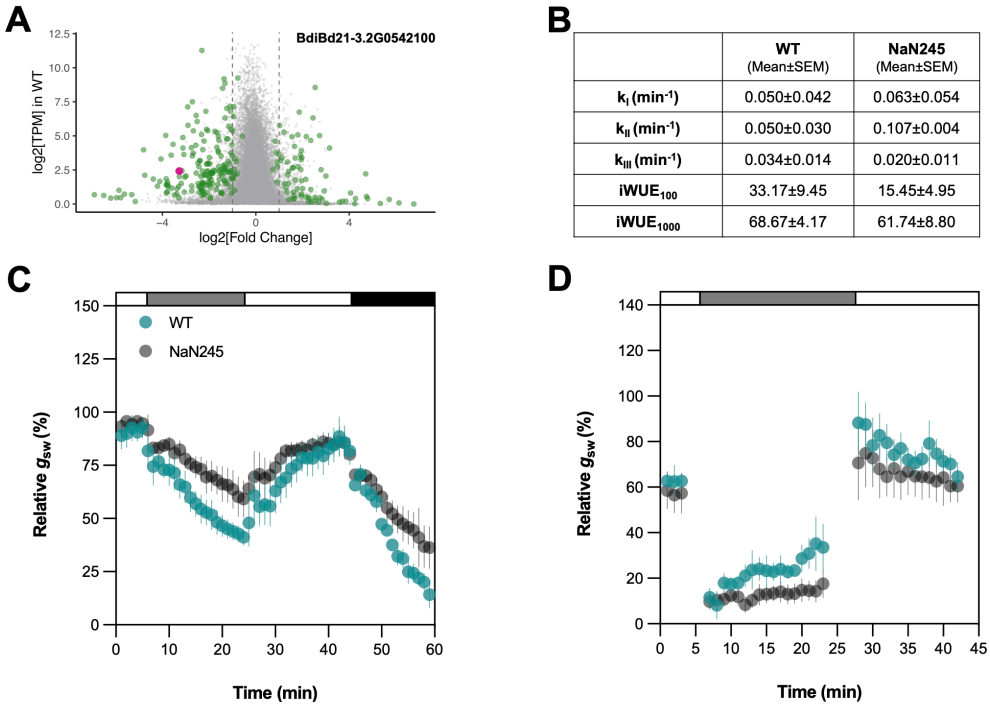
Mutant 32 – NaN428



	WT (Mean±SEM)	NaN428 (Mean±SEM)
k_I (min^{-1})	0.051±0.009	0.085±0.024
k_{II} (min^{-1})	0.128±0.022	0.067±0.034
k_{III} (min^{-1})	0.132±0.034	0.144±0.144
$iWUE_{100}$	36.77±15.02	36.72±0.90
$iWUE_{1000}$	81.05±13.65	81.27±12.49

Figure 2.26 – Gas exchange phenotyping of mutant line 32 (NaN428). (A) Identification of the candidate gene in the RNA-seq. **(B)** Average stomatal speed (k) for the three light transitions (k_I, 1000-100 PAR; k_{II}, 100-1000 PAR; k_{III}, 1000-0 PAR) and iWUE at 100 and 1000 PAR in WT and NaN428. **(C)** Relative g_{sw} in WT and NaN428 (n=3). **(D)** iWUE in WT and NaN428 (n=3). Error bars represent SEM.

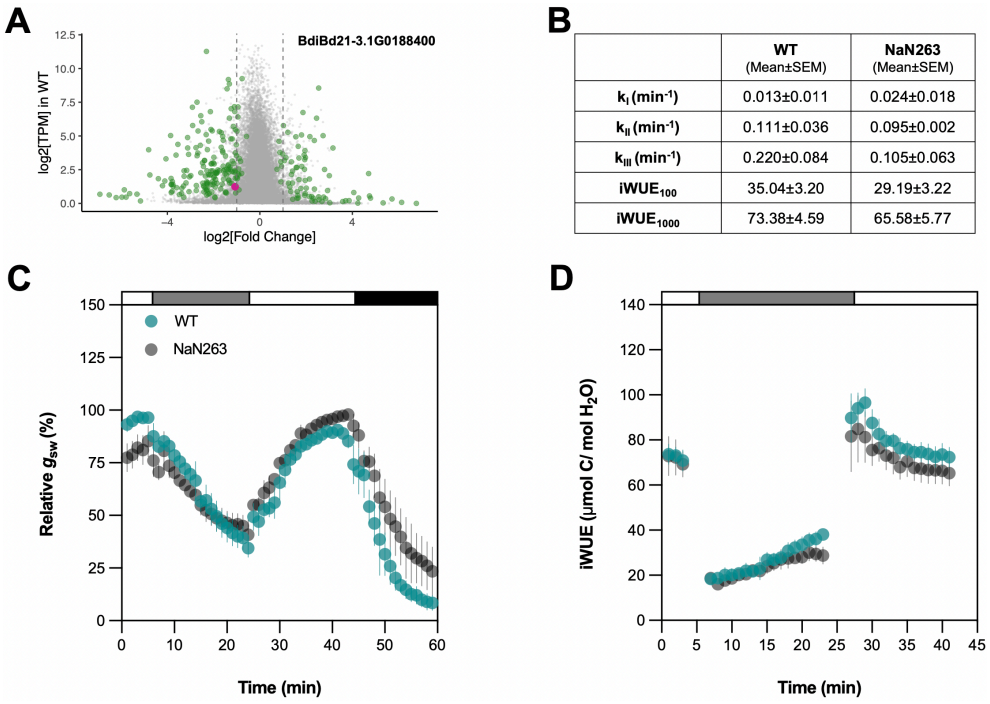
Mutant 34 – NaN245



	WT (Mean±SEM)	NaN245 (Mean±SEM)
k_I (min^{-1})	0.050±0.042	0.063±0.054
k_{II} (min^{-1})	0.050±0.030	0.107±0.004
k_{III} (min^{-1})	0.034±0.014	0.020±0.011
$iWUE_{100}$	33.17±9.45	15.45±4.95
$iWUE_{1000}$	68.67±4.17	61.74±8.80

Figure 2.27 – Gas exchange phenotyping of mutant line 34 (NaN245). (A) Identification of the candidate gene in the RNA-seq. **(B)** Average stomatal speed (k) for the three light transitions (k_I, 1000-100 PAR; k_{II}, 100-1000 PAR; k_{III}, 1000-0 PAR) and iWUE at 100 and 1000 PAR in WT and NaN245. **(C)** Relative g_{sw} in WT and NaN245 (n=3). **(D)** iWUE in WT and NaN245 (n=3). Error bars represent SEM.

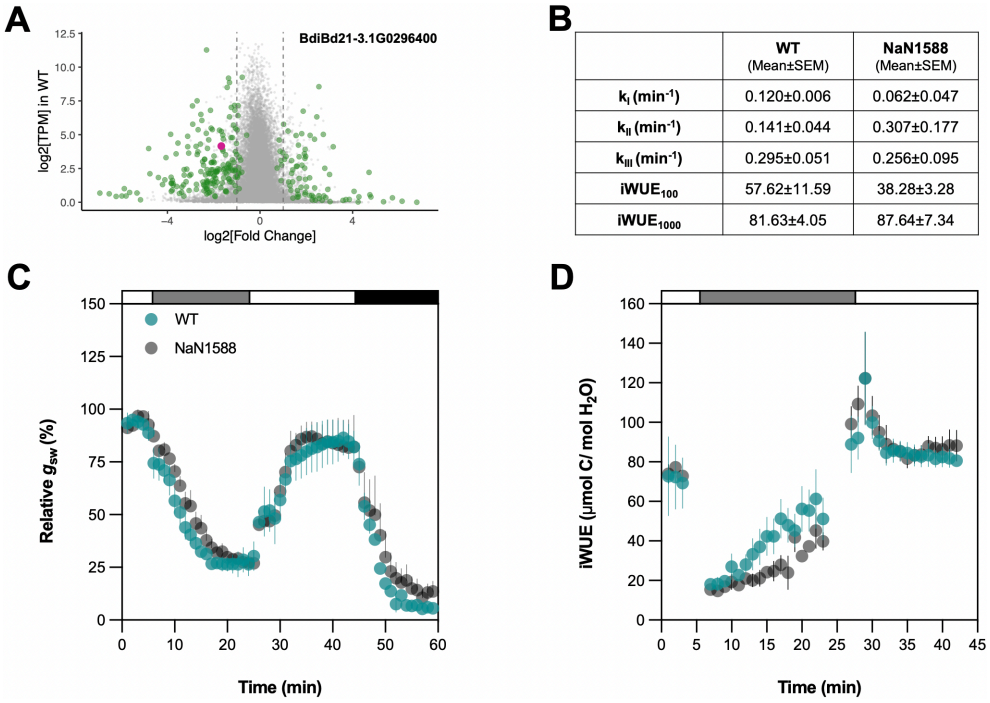
Mutant 36 – NaN263



	WT (Mean±SEM)	NaN263 (Mean±SEM)
k_I (min^{-1})	0.013±0.011	0.024±0.018
k_{II} (min^{-1})	0.111±0.036	0.095±0.002
k_{III} (min^{-1})	0.220±0.084	0.105±0.063
$iWUE_{100}$	35.04±3.20	29.19±3.22
$iWUE_{1000}$	73.38±4.59	65.58±5.77

Figure 2.28 – Gas exchange phenotyping of mutant line 36 (NaN263). (A) Identification of the candidate gene in the RNA-seq. **(B)** Average stomatal speed (k) for the three light transitions (k_I, 1000-100 PAR; k_{II}, 100-1000 PAR; k_{III}, 1000-0 PAR) and iWUE at 100 and 1000 PAR in WT and NaN263. **(C)** Relative g_{sw} in WT and NaN263 (n=3). **(D)** iWUE in WT and NaN263 (n=3). Error bars represent SEM.

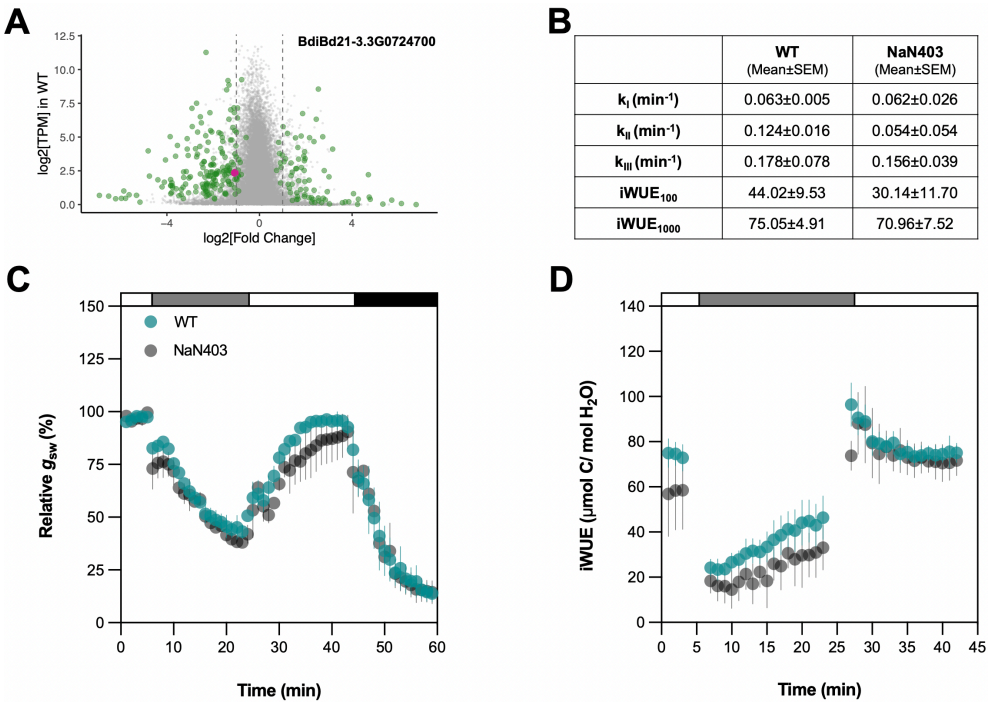
Mutant 37 – NaN1588



	WT (Mean±SEM)	NaN1588 (Mean±SEM)
k_I (min^{-1})	0.120±0.006	0.062±0.047
k_{II} (min^{-1})	0.141±0.044	0.307±0.177
k_{III} (min^{-1})	0.295±0.051	0.256±0.095
$iWUE_{100}$	57.62±11.59	38.28±3.28
$iWUE_{1000}$	81.63±4.05	87.64±7.34

Figure 2.29 – Gas exchange phenotyping of mutant line 37 (NaN1588). (A) Identification of the candidate gene in the RNA-seq. **(B)** Average stomatal speed (k) for the three light transitions (k_I, 1000-100 PAR; k_{II}, 100-1000 PAR; k_{III}, 1000-0 PAR) and iWUE at 100 and 1000 PAR in WT and NaN1588. **(C)** Relative g_{sw} in WT and NaN1588 (n=3). **(D)** iWUE in WT and NaN1588 (n=3). Error bars represent SEM.

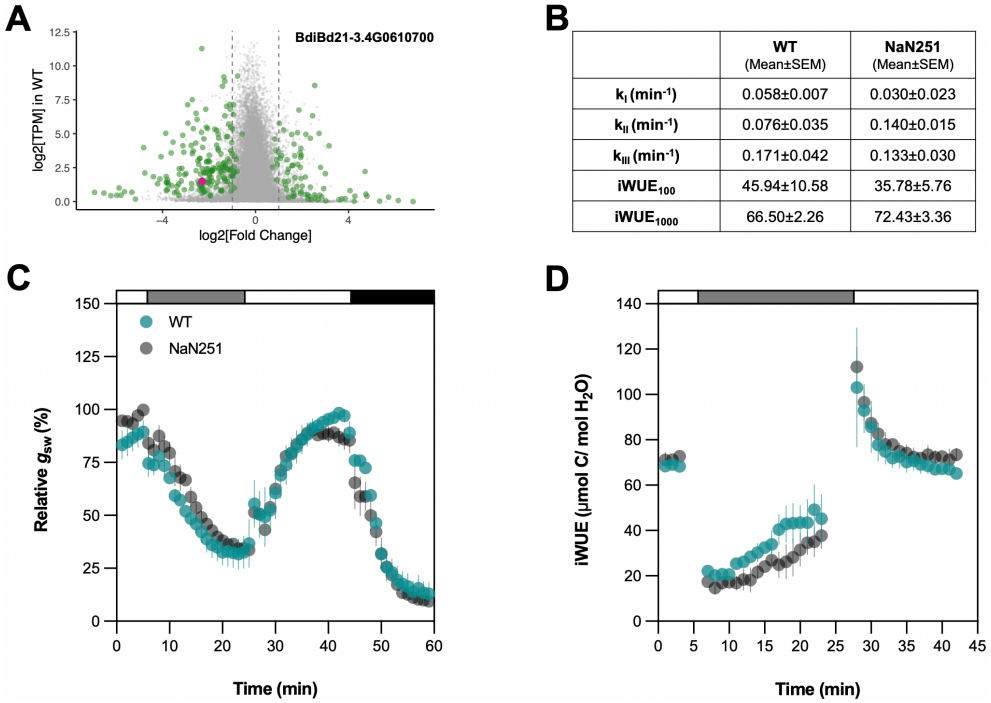
Mutant 40 – NaN403



	WT (Mean±SEM)	NaN403 (Mean±SEM)
k_I (min^{-1})	0.063±0.005	0.062±0.026
k_{II} (min^{-1})	0.124±0.016	0.054±0.054
k_{III} (min^{-1})	0.178±0.078	0.156±0.039
$iWUE_{100}$	44.02±9.53	30.14±11.70
$iWUE_{1000}$	75.05±4.91	70.96±7.52

Figure 2.30 – Gas exchange phenotyping of mutant line 40 (NaN403). (A) Identification of the candidate gene in the RNA-seq. **(B)** Average stomatal speed (k) for the three light transitions (k_I, 1000-100 PAR; k_{II}, 100-1000 PAR; k_{III}, 1000-0 PAR) and iWUE at 100 and 1000 PAR in WT and NaN403. **(C)** Relative g_{sw} in WT and NaN403 (n=2). **(D)** iWUE in WT and NaN403 (n=2). Error bars represent SEM.

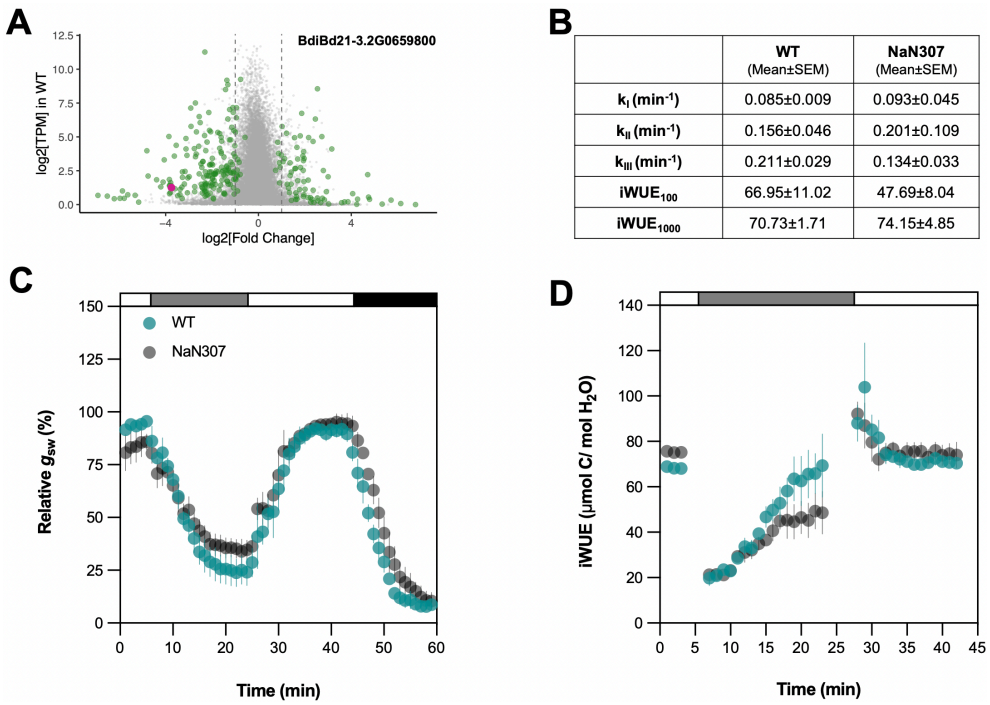
Mutant 41 - NaN251



	WT (Mean±SEM)	NaN251 (Mean±SEM)
k_I (min^{-1})	0.058±0.007	0.030±0.023
k_{II} (min^{-1})	0.076±0.035	0.140±0.015
k_{III} (min^{-1})	0.171±0.042	0.133±0.030
$iWUE_{100}$	45.94±10.58	35.78±5.76
$iWUE_{1000}$	66.50±2.26	72.43±3.36

Figure 2.31 – Gas exchange phenotyping of mutant line 41 (NaN251). (A) Identification of the candidate gene in the RNA-seq. **(B)** Average stomatal speed (k) for the three light transitions (k_I, 1000-100 PAR; k_{II}, 100-1000 PAR; k_{III}, 1000-0 PAR) and iWUE at 100 and 1000 PAR in WT and NaN251. **(C)** Relative g_{sw} in WT and NaN251 (n=3). **(D)** iWUE in WT and NaN251 (n=3). Error bars represent SEM.

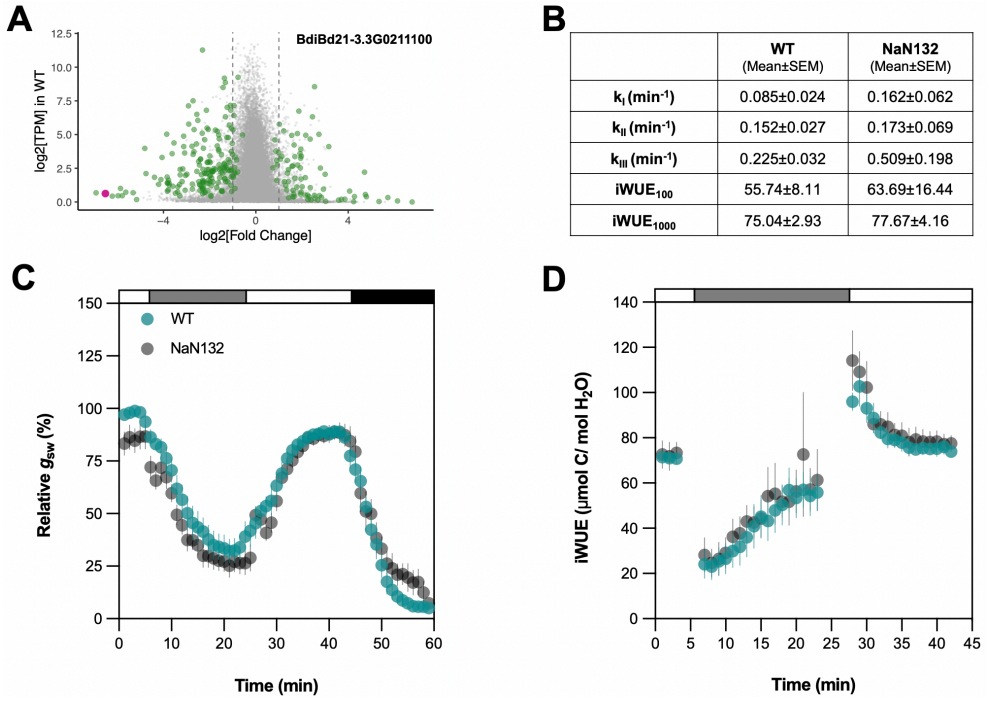
Mutant 42 - NaN307



	WT (Mean±SEM)	NaN307 (Mean±SEM)
k_I (min^{-1})	0.085±0.009	0.093±0.045
k_{II} (min^{-1})	0.156±0.046	0.201±0.109
k_{III} (min^{-1})	0.211±0.029	0.134±0.033
$iWUE_{100}$	66.95±11.02	47.69±8.04
$iWUE_{1000}$	70.73±1.71	74.15±4.85

Figure 2.32 – Gas exchange phenotyping of mutant line 42 (NaN307). (A) Identification of the candidate gene in the RNA-seq. **(B)** Average stomatal speed (k) for the three light transitions (k_I, 1000-100 PAR; k_{II}, 100-1000 PAR; k_{III}, 1000-0 PAR) and iWUE at 100 and 1000 PAR in WT and NaN307. **(C)** Relative g_{sw} in WT and NaN307 (n=3). **(D)** iWUE in WT and NaN307 (n=3). Error bars represent SEM.

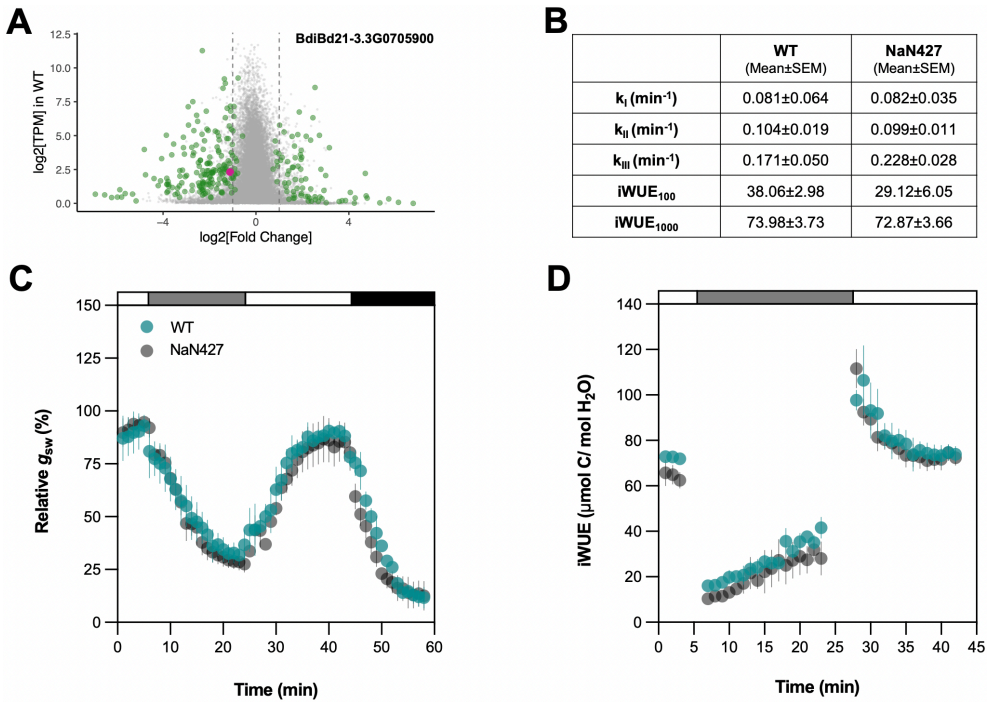
Mutant 46 - NaN132



	WT (Mean±SEM)	NaN132 (Mean±SEM)
k_I (min^{-1})	0.085±0.024	0.162±0.062
k_{II} (min^{-1})	0.152±0.027	0.173±0.069
k_{III} (min^{-1})	0.225±0.032	0.509±0.198
$iWUE_{100}$	55.74±8.11	63.69±16.44
$iWUE_{1000}$	75.04±2.93	77.67±4.16

Figure 2.33 – Gas exchange phenotyping of mutant line 46 (NaN132). (A) Identification of the candidate gene in the RNA-seq. **(B)** Average stomatal speed (k) for the three light transitions (k_I, 1000-100 PAR; k_{II}, 100-1000 PAR; k_{III}, 1000-0 PAR) and iWUE at 100 and 1000 PAR in WT and NaN132. **(C)** Relative g_{sw} in WT and NaN132 (n=6). **(D)** iWUE in WT and NaN132 (n=6). Error bars represent SEM.

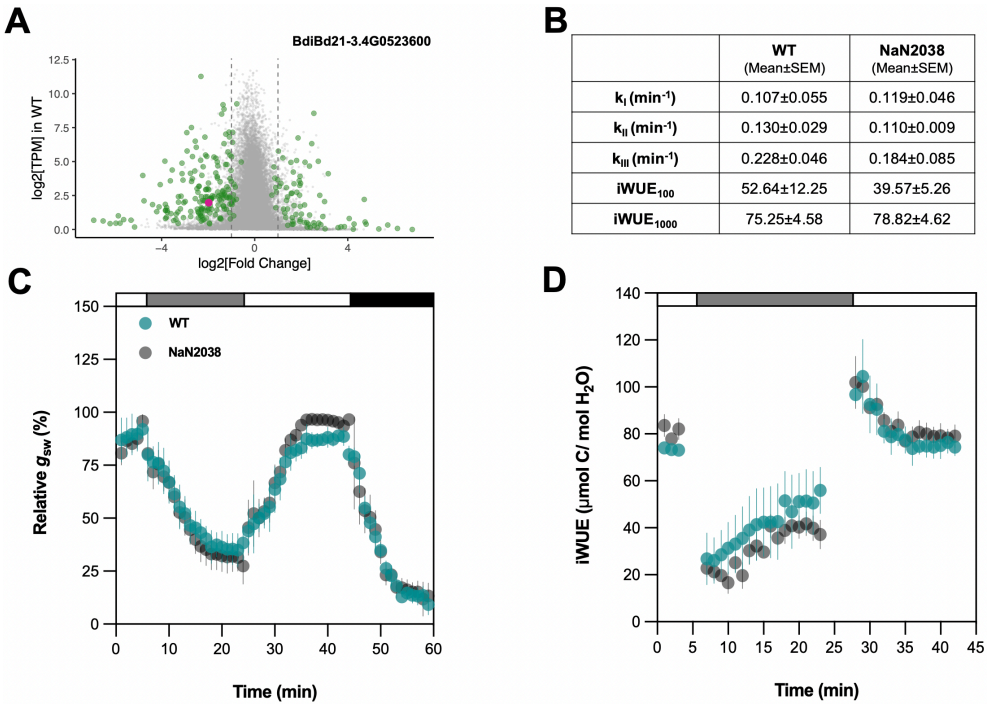
Mutant 47 - NaN427



	WT (Mean±SEM)	NaN427 (Mean±SEM)
k_I (min^{-1})	0.081±0.064	0.082±0.035
k_{II} (min^{-1})	0.104±0.019	0.099±0.011
k_{III} (min^{-1})	0.171±0.050	0.228±0.028
$iWUE_{100}$	38.06±2.98	29.12±6.05
$iWUE_{1000}$	73.98±3.73	72.87±3.66

Figure 2.34 – Gas exchange phenotyping of mutant line 47 (NaN427). (A) Identification of the candidate gene in the RNA-seq. **(B)** Average stomatal speed (k) for the three light transitions (k_I, 1000-100 PAR; k_{II}, 100-1000 PAR; k_{III}, 1000-0 PAR) and iWUE at 100 and 1000 PAR in WT and NaN427. **(C)** Relative g_{sw} in WT and NaN427 (n=3). **(D)** iWUE in WT and NaN427 (n=3). Error bars represent SEM.

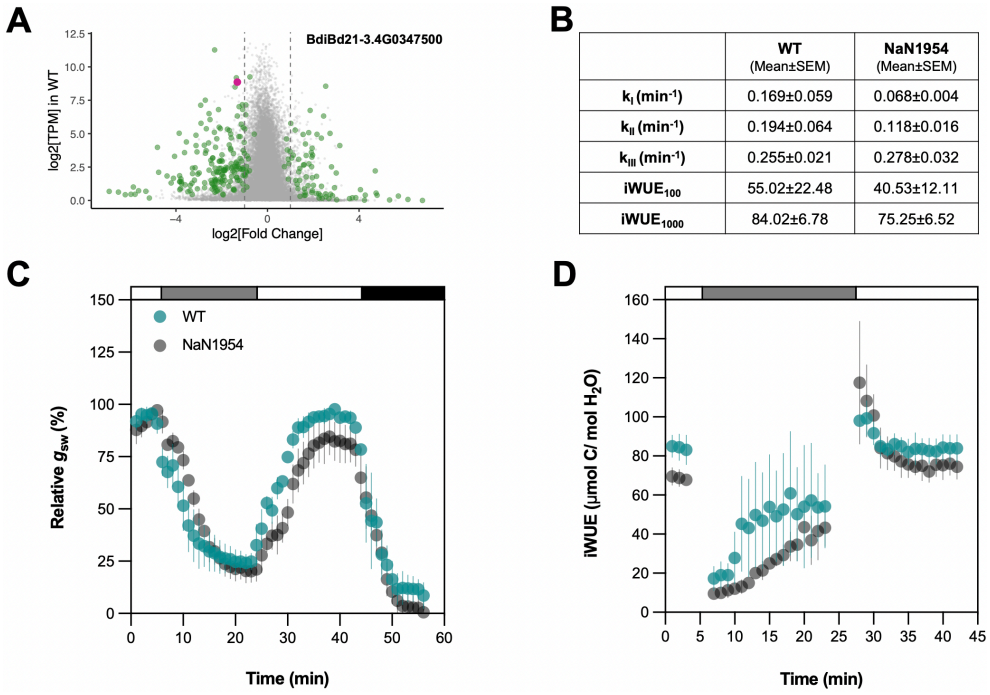
Mutant 48 - NaN2038



	WT (Mean±SEM)	NaN2038 (Mean±SEM)
k_I (min^{-1})	0.107±0.055	0.119±0.046
k_{II} (min^{-1})	0.130±0.029	0.110±0.009
k_{III} (min^{-1})	0.228±0.046	0.184±0.085
$iWUE_{100}$	52.64±12.25	39.57±5.26
$iWUE_{1000}$	75.25±4.58	78.82±4.62

Figure 2.35 – Gas exchange phenotyping of mutant line 48 (NaN2038). (A) Identification of the candidate gene in the RNA-seq. **(B)** Average stomatal speed (k) for the three light transitions (k_I, 1000-100 PAR; k_{II}, 100-1000 PAR; k_{III}, 1000-0 PAR) and iWUE at 100 and 1000 PAR in WT and NaN2038. **(C)** Relative g_{sw} in WT and NaN2038 (n=3). **(D)** iWUE in WT and NaN2038 (n=3). Error bars represent SEM.

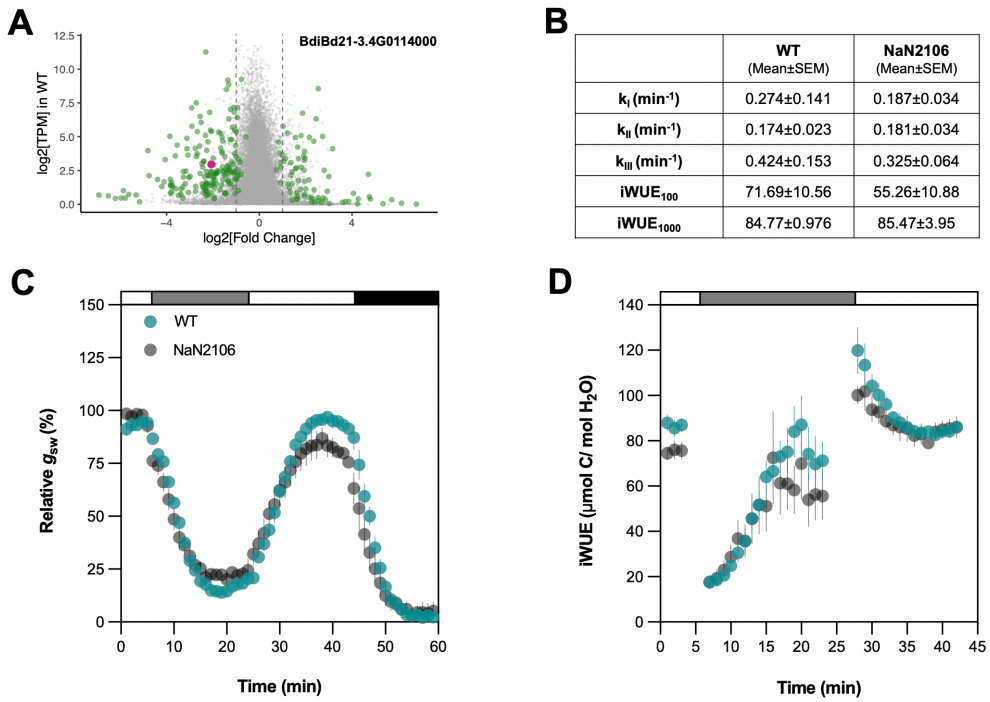
Mutant 49 - NaN1954



	WT (Mean±SEM)	NaN1954 (Mean±SEM)
k_I (min^{-1})	0.169±0.059	0.068±0.004
k_{II} (min^{-1})	0.194±0.064	0.118±0.016
k_{III} (min^{-1})	0.255±0.021	0.278±0.032
$iWUE_{100}$	55.02±22.48	40.53±12.11
$iWUE_{1000}$	84.02±6.78	75.25±6.52

Figure 2.36 – Gas exchange phenotyping of mutant line 49 (NaN1954). (A) Identification of the candidate gene in the RNA-seq. **(B)** Average stomatal speed (k) for the three light transitions (k_I, 1000-100 PAR; k_{II}, 100-1000 PAR; k_{III}, 1000-0 PAR) and iWUE at 100 and 1000 PAR in WT and NaN1954. **(C)** Relative g_{sw} in WT and NaN1954 (n=3). **(D)** iWUE in WT and NaN1954 (n=3). Error bars represent SEM.

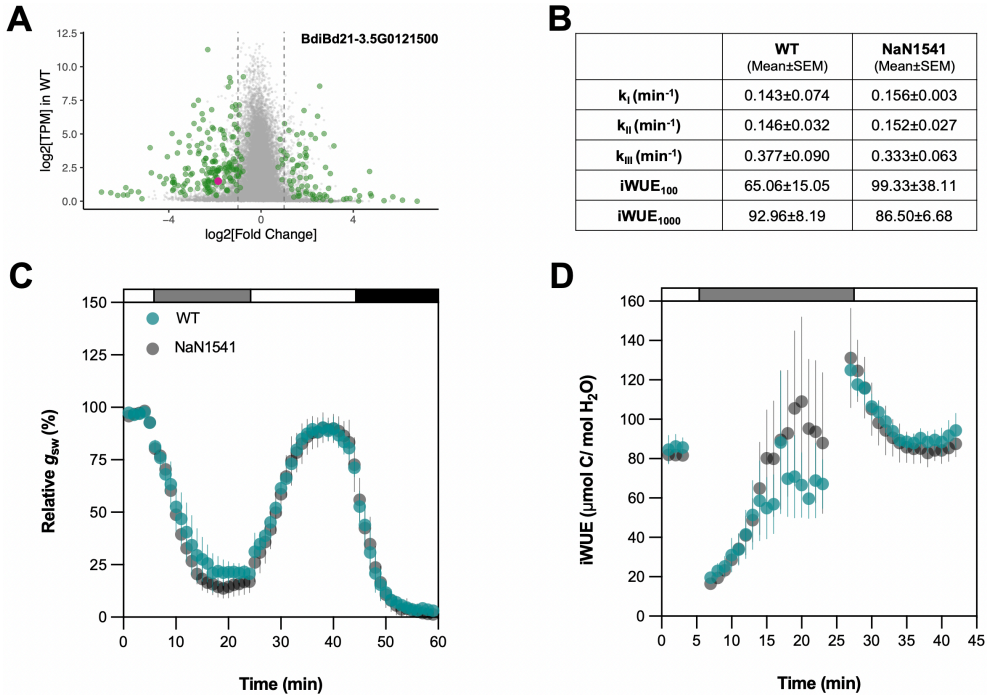
Mutant 52 - NaN2106



	WT (Mean±SEM)	NaN2106 (Mean±SEM)
k_I (min^{-1})	0.274±0.141	0.187±0.034
k_{II} (min^{-1})	0.174±0.023	0.181±0.034
k_{III} (min^{-1})	0.424±0.153	0.325±0.064
$iWUE_{100}$	71.69±10.56	55.26±10.88
$iWUE_{1000}$	84.77±0.976	85.47±3.95

Figure 2.37 – Gas exchange phenotyping of mutant line 52 (NaN2106). (A) Identification of the candidate gene in the RNA-seq. **(B)** Average stomatal speed (k) for the three light transitions (k_I, 1000-100 PAR; k_{II}, 100-1000 PAR; k_{III}, 1000-0 PAR) and iWUE at 100 and 1000 PAR in WT and NaN2106. **(C)** Relative g_{sw} in WT and NaN2106 (n=4). **(D)** iWUE in WT and NaN2106 (n=4). Error bars represent SEM.

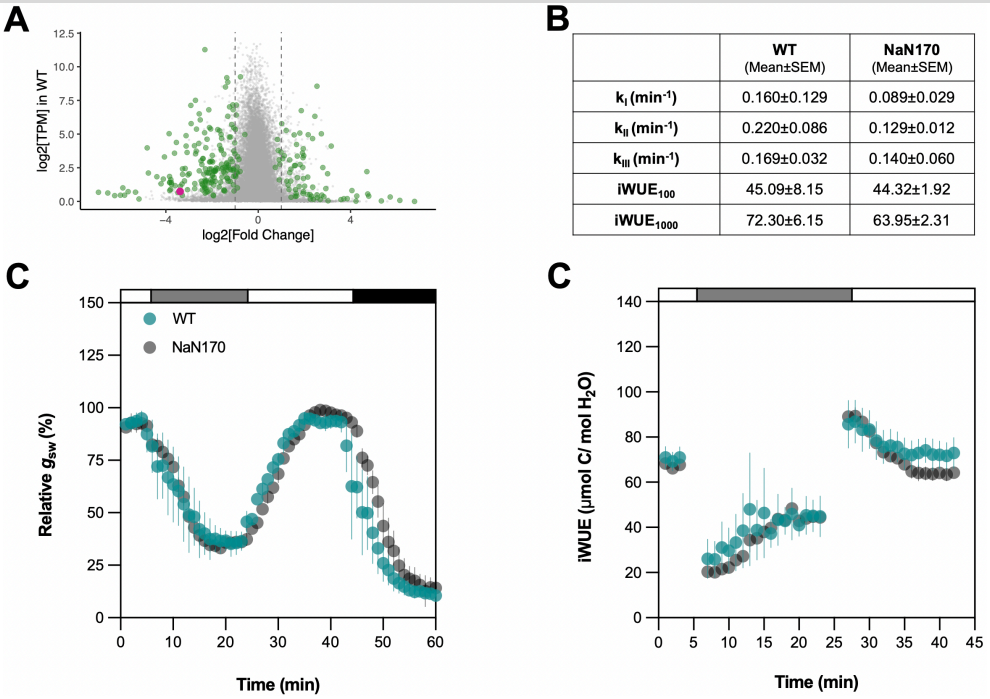
Mutant 53 – NaN1541



	WT (Mean±SEM)	NaN1541 (Mean±SEM)
k_I (min^{-1})	0.143±0.074	0.156±0.003
k_{II} (min^{-1})	0.146±0.032	0.152±0.027
k_{III} (min^{-1})	0.377±0.090	0.333±0.063
$iWUE_{100}$	65.06±15.05	99.33±38.11
$iWUE_{1000}$	92.96±8.19	86.50±6.68

Figure 2.38 – Gas exchange phenotyping of mutant line 53 (NaN1541). (A) Identification of the candidate gene in the RNA-seq. **(B)** Average stomatal speed (k) for the three light transitions (k_I, 1000-100 PAR; k_{II}, 100-1000 PAR; k_{III}, 1000-0 PAR) and iWUE at 100 and 1000 PAR in WT and NaN1541. **(C)** Relative g_{sw} in WT and NaN1541 (n=3). **(D)** iWUE in WT and NaN1541 (n=3). Error bars represent SEM.

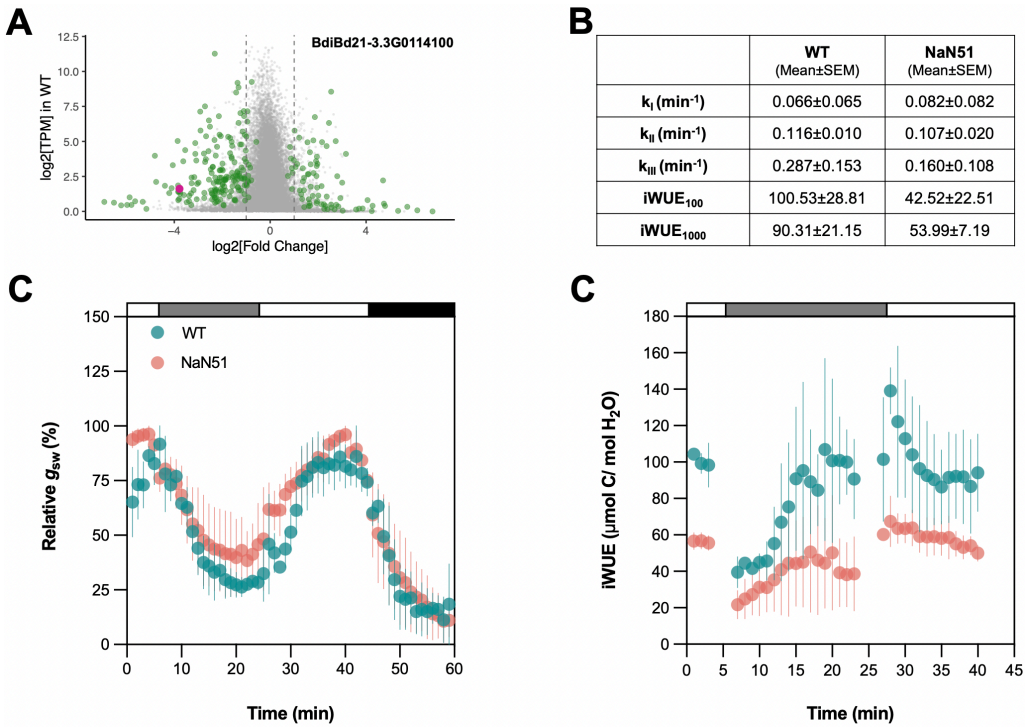
Mutant 55 – NaN170



	WT (Mean±SEM)	NaN170 (Mean±SEM)
k_I (min^{-1})	0.160±0.129	0.089±0.029
k_{II} (min^{-1})	0.220±0.086	0.129±0.012
k_{III} (min^{-1})	0.169±0.032	0.140±0.060
$iWUE_{100}$	45.09±8.15	44.32±1.92
$iWUE_{1000}$	72.30±6.15	63.95±2.31

Figure 2.39 – Gas exchange phenotyping of mutant line 55 (NaN170). (A) Identification of the candidate gene in the RNA-seq. **(B)** Average stomatal speed (k) for the three light transitions (k_I, 1000-100 PAR; k_{II}, 100-1000 PAR; k_{III}, 1000-0 PAR) and iWUE at 100 and 1000 PAR in WT and NaN170. **(C)** Relative g_{sw} in WT and NaN170 (n=3). **(D)** iWUE in WT and NaN170(n=3). Error bars represent SEM. This line was screened by Leonie Redt (master student) under my supervision.

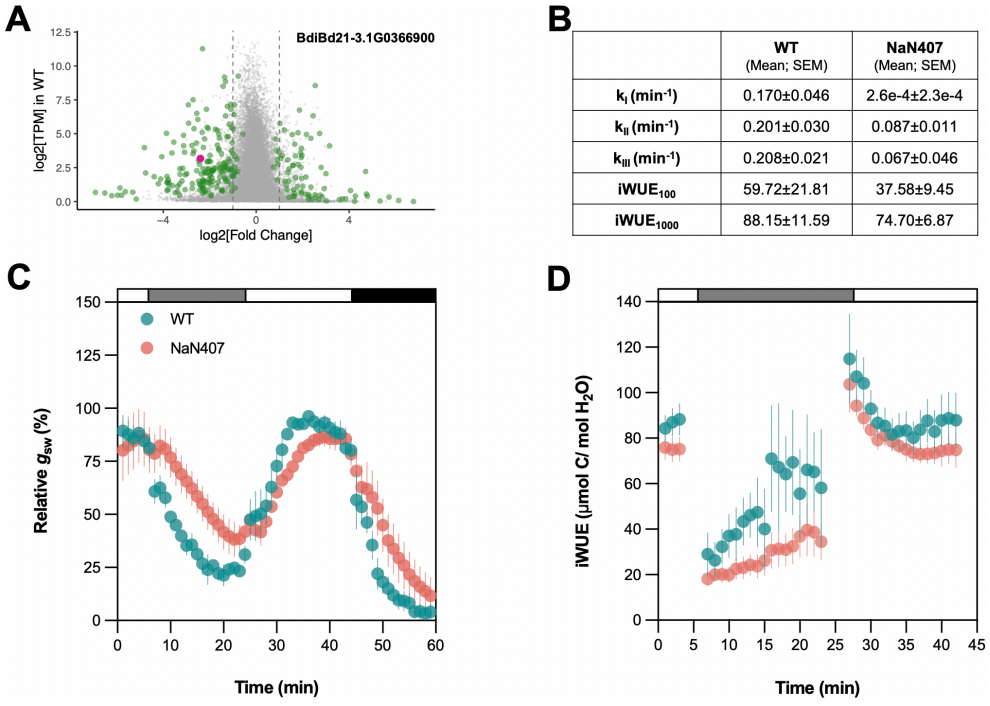
Mutant 1 - NaN51



	WT (Mean±SEM)	NaN51 (Mean±SEM)
k_I (min^{-1})	0.066±0.065	0.082±0.082
k_{II} (min^{-1})	0.116±0.010	0.107±0.020
k_{III} (min^{-1})	0.287±0.153	0.160±0.108
$iWUE_{100}$	100.53±28.81	42.52±22.51
$iWUE_{1000}$	90.31±21.15	53.99±7.19

Figure 2.40 – Gas exchange phenotyping of mutant line 1 (NaN51). (A) Identification of the candidate gene in the RNA-seq. **(B)** Average stomatal speed (k) for the three light transitions (k_I, 1000-100 PAR; k_{II}, 100-1000 PAR; k_{III}, 1000-0 PAR) and iWUE at 100 and 1000 PAR in WT and NaN51. **(C)** Relative g_{sw} in WT and NaN51 (n=2). **(D)** iWUE in WT and NaN51 (n=2). Error bars represent SEM.

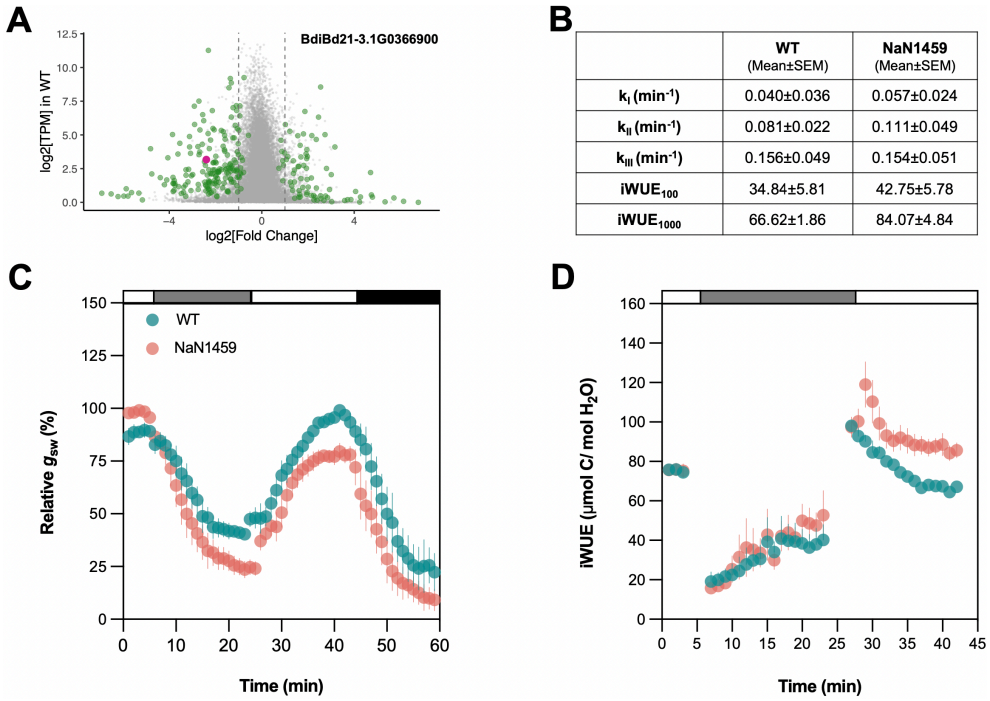
Mutant 5 - NaN407



	WT (Mean; SEM)	NaN407 (Mean; SEM)
k_I (min^{-1})	0.170±0.046	2.6e-4±2.3e-4
k_{II} (min^{-1})	0.201±0.030	0.087±0.011
k_{III} (min^{-1})	0.208±0.021	0.067±0.046
$iWUE_{100}$	59.72±21.81	37.58±9.45
$iWUE_{1000}$	88.15±11.59	74.70±6.87

Figure 2.41– Gas exchange phenotyping of mutant line 5 (NaN407). (A) Identification of the candidate gene in the RNA-seq. **(B)** Average stomatal speed (k) for the three light transitions (k_I, 1000-100 PAR; k_{II}, 100-1000 PAR; k_{III}, 1000-0 PAR) and iWUE at 100 and 1000 PAR in WT and NaN407. **(C)** Relative g_{sw} in WT and NaN407 (n=4). **(D)** iWUE in WT and NaN407 (n=4). Error bars represent SEM.

Mutant 6 - NaN1459

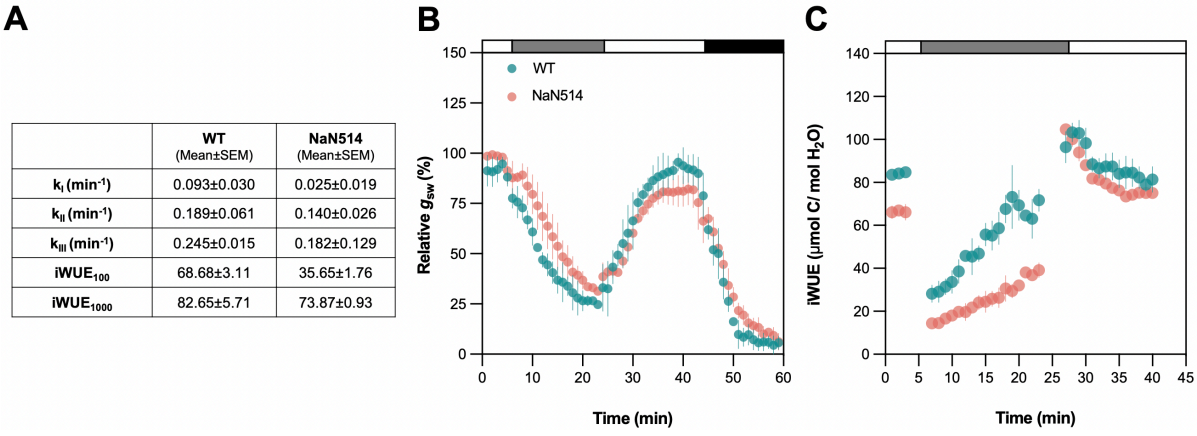


	WT (Mean±SEM)	NaN1459 (Mean±SEM)
k_I (min^{-1})	0.040±0.036	0.057±0.024
k_{II} (min^{-1})	0.081±0.022	0.111±0.049
k_{III} (min^{-1})	0.156±0.049	0.154±0.051
$iWUE_{100}$	34.84±5.81	42.75±5.78
$iWUE_{1000}$	66.62±1.86	84.07±4.84

Figure 2.42 – Gas exchange phenotyping of mutant line 6 (NaN1459). (A) Identification of the candidate gene in the RNA-seq. **(B)** Average stomatal speed (k) for the three light transitions (k_I, 1000-100 PAR; k_{II}, 100-1000 PAR; k_{III}, 1000-0 PAR) and iWUE at 100 and 1000 PAR in WT and NaN1459. **(C)** Relative g_{sw} in WT and NaN1459 (n=4). **(D)** iWUE in WT and NaN1459 (n=4). Error bars represent SEM.

Mutant 9 - NaN514

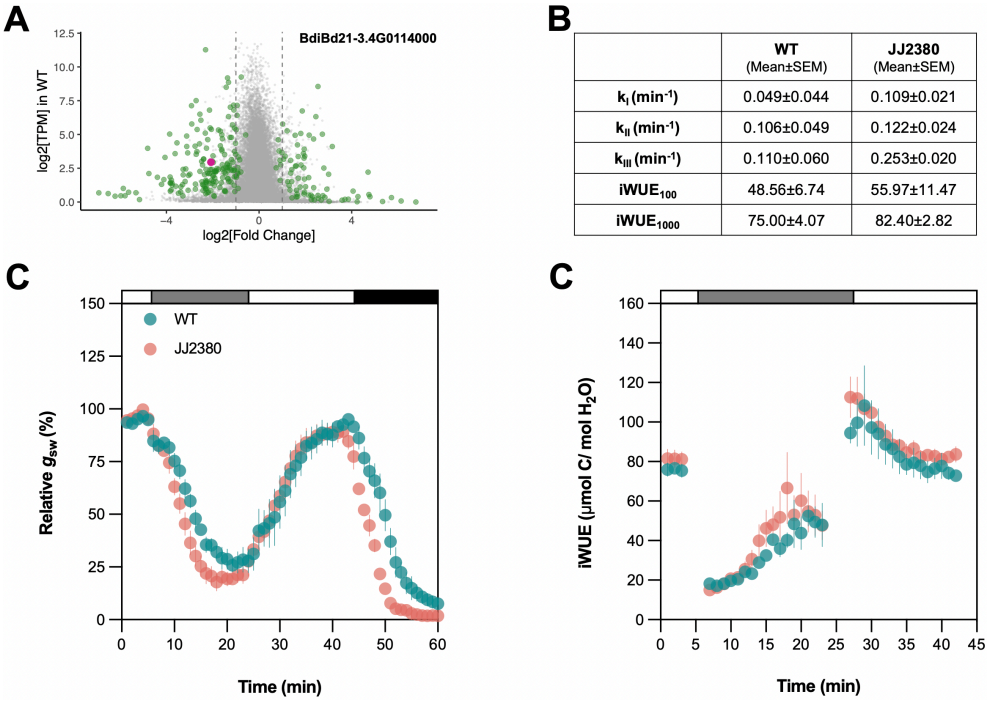
BdiBd21-3.3G0139100



	WT (Mean±SEM)	NaN514 (Mean±SEM)
k_I (min^{-1})	0.093±0.030	0.025±0.019
k_{II} (min^{-1})	0.189±0.061	0.140±0.026
k_{III} (min^{-1})	0.245±0.015	0.182±0.129
$iWUE_{100}$	68.68±3.11	35.65±1.76
$iWUE_{1000}$	82.65±5.71	73.87±0.93

Figure 2.43 – Gas exchange phenotyping of mutant line 9 (NaN514). (A) Average stomatal speed (k) for the three light transitions (k_I, 1000-100 PAR; k_{II}, 100-1000 PAR; k_{III}, 1000-0 PAR) and iWUE at 100 and 1000 PAR in WT and NaN514. **(C)** Relative g_{sw} in WT and NaN514 (n=3). **(D)** iWUE in WT and NaN514 (n=3). Error bars represent SEM.

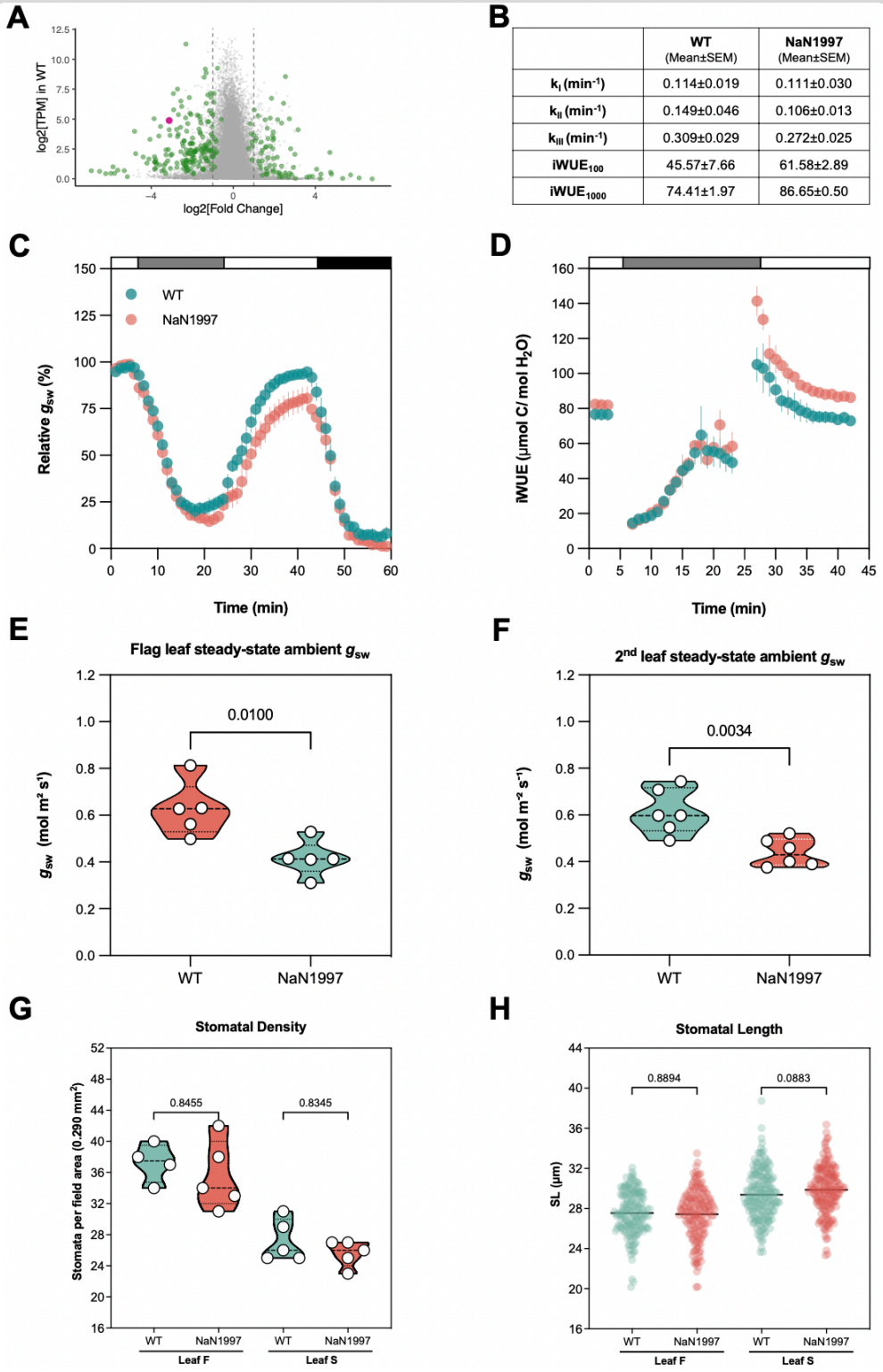
Mutant 17 – JJ2380



	WT (Mean±SEM)	JJ2380 (Mean±SEM)
k_I (min^{-1})	0.049±0.044	0.109±0.021
k_{II} (min^{-1})	0.106±0.049	0.122±0.024
k_{III} (min^{-1})	0.110±0.060	0.253±0.020
$iWUE_{100}$	48.56±6.74	55.97±11.47
$iWUE_{1000}$	75.00±4.07	82.40±2.82

Figure 2.44 – Gas exchange phenotyping of mutant line 17 (JJ2380). (A) Identification of the candidate gene in the RNA-seq. **(B)** Average stomatal speed (k) for the three light transitions (k_I, 1000-100 PAR; k_{II}, 100-1000 PAR; k_{III}, 1000-0 PAR) and iWUE at 100 and 1000 PAR in WT and JJ2380. **(C)** Relative g_{sw} in WT and JJ2380 (n=3). **(D)** iWUE in WT and JJ2380 (n=3). Error bars represent SEM.

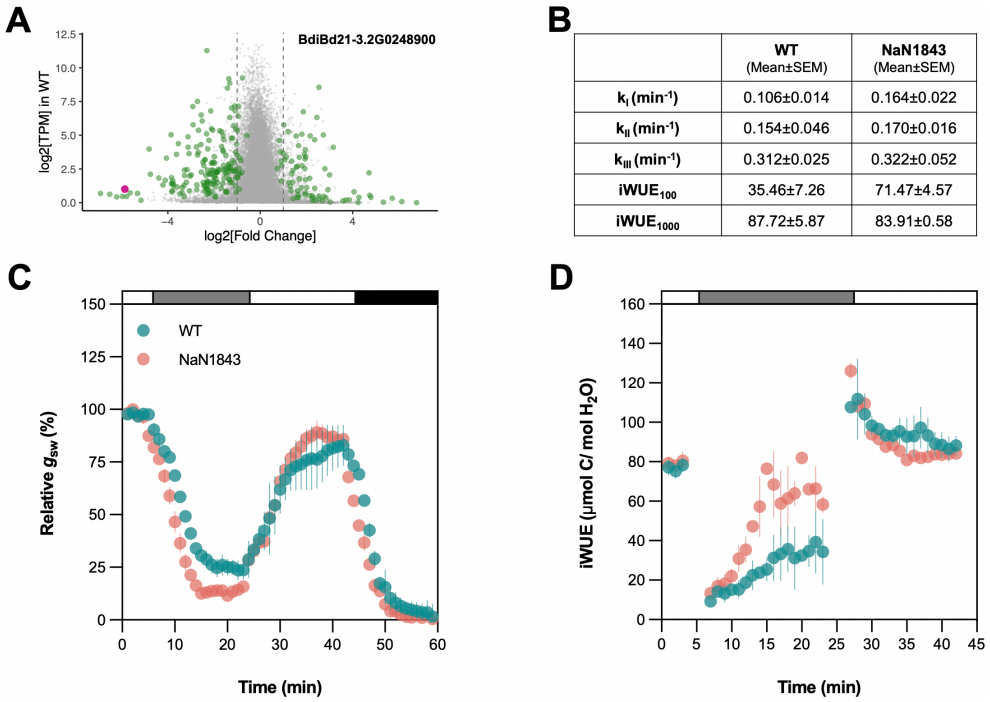
Mutant 20 – NaN1997



	WT (Mean±SEM)	NaN1997 (Mean±SEM)
k_I (min^{-1})	0.114±0.019	0.111±0.030
k_{II} (min^{-1})	0.149±0.046	0.106±0.013
k_{III} (min^{-1})	0.309±0.029	0.272±0.025
$iWUE_{100}$	45.57±7.66	61.58±2.89
$iWUE_{1000}$	74.41±1.97	86.65±0.50

Figure 2.45 – Phenotyping of mutant line 20 (NaN1997). (A) Identification of the candidate gene in the RNA-seq. **(B)** Average stomatal speed (k) for the three light transitions (k_I, 1000-100 PAR; k_{II}, 100-1000 PAR; k_{III}, 1000-0 PAR) and iWUE at 100 and 1000 PAR in WT and NaN1997. **(C)** Relative g_{sw} in WT and NaN1997 (n=3-4). **(D)** iWUE in WT and NaN1997 (n=3-4). Error bars represent SEM. **(E, F)** SC-1 measurements of ambient-adapted g_{sw} in flag leaves (Leaf F) and 2nd leaf from top (Leaf S) (n=5-6 individuals per genotype; each dots represents the average of 5-10 measurements per NaN1997 individual and 3-6 measurements per WT individual). **(G)** Stomatal density in WT and NaN1997 (n=4-5 individuals; each dot represents the average stomatal density from three 0.290 mm^2 fields of view per individual). **(G)** Stomatal length in WT and NaN1997 (n=164-172 stomata in Leaves F, n=188-192 in Leaves S per genotype). P values from unpaired t-tests.

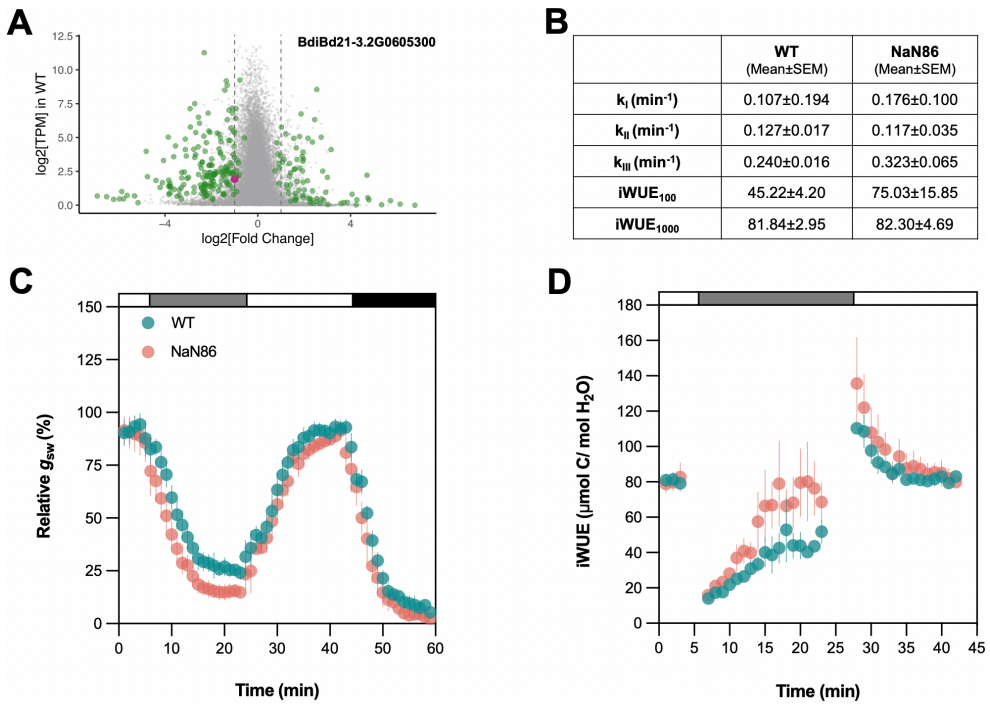
Mutant 21 – NaN1843



	WT (Mean±SEM)	NaN1843 (Mean±SEM)
k_I (min^{-1})	0.106±0.014	0.164±0.022
k_{II} (min^{-1})	0.154±0.046	0.170±0.016
k_{III} (min^{-1})	0.312±0.025	0.322±0.052
$iWUE_{100}$	35.46±7.26	71.47±4.57
$iWUE_{1000}$	87.72±5.87	83.91±0.58

Figure 2.46 – Gas exchange phenotyping of mutant line 21 (NaN1843). (A) Identification of the candidate gene in the RNA-seq. **(B)** Average stomatal speed (k) for the three light transitions (k_I, 1000-100 PAR; k_{II}, 100-1000 PAR; k_{III}, 1000-0 PAR) and iWUE at 100 and 1000 PAR in WT and NaN1843. **(C)** Relative g_{sw} in WT and NaN1843 (n=2). **(D)** iWUE in WT and NaN1843 (n=2). Error bars represent SEM.

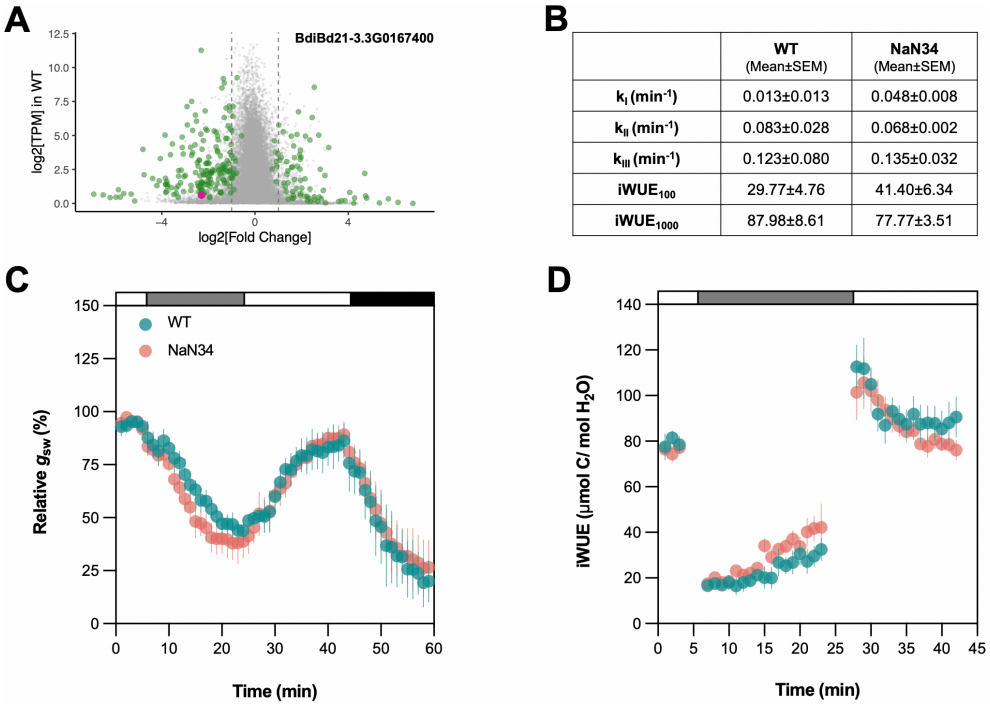
Mutant 24 – NaN86



	WT (Mean±SEM)	NaN86 (Mean±SEM)
k_I (min^{-1})	0.107±0.194	0.176±0.100
k_{II} (min^{-1})	0.127±0.017	0.117±0.035
k_{III} (min^{-1})	0.240±0.016	0.323±0.065
$iWUE_{100}$	45.22±4.20	75.03±15.85
$iWUE_{1000}$	81.84±2.95	82.30±4.69

Figure 2.47 – Gas exchange phenotyping of mutant line 24 (NaN86). (A) Identification of the candidate gene in the RNA-seq. **(B)** Average stomatal speed (k) for the three light transitions (k_I, 1000-100 PAR; k_{II}, 100-1000 PAR; k_{III}, 1000-0 PAR) and iWUE at 100 and 1000 PAR in WT and NaN86. **(C)** Relative g_{sw} in WT and NaN86 (n=3-4). **(D)** iWUE in WT and NaN86 (n=3-4). Error bars represent SEM.

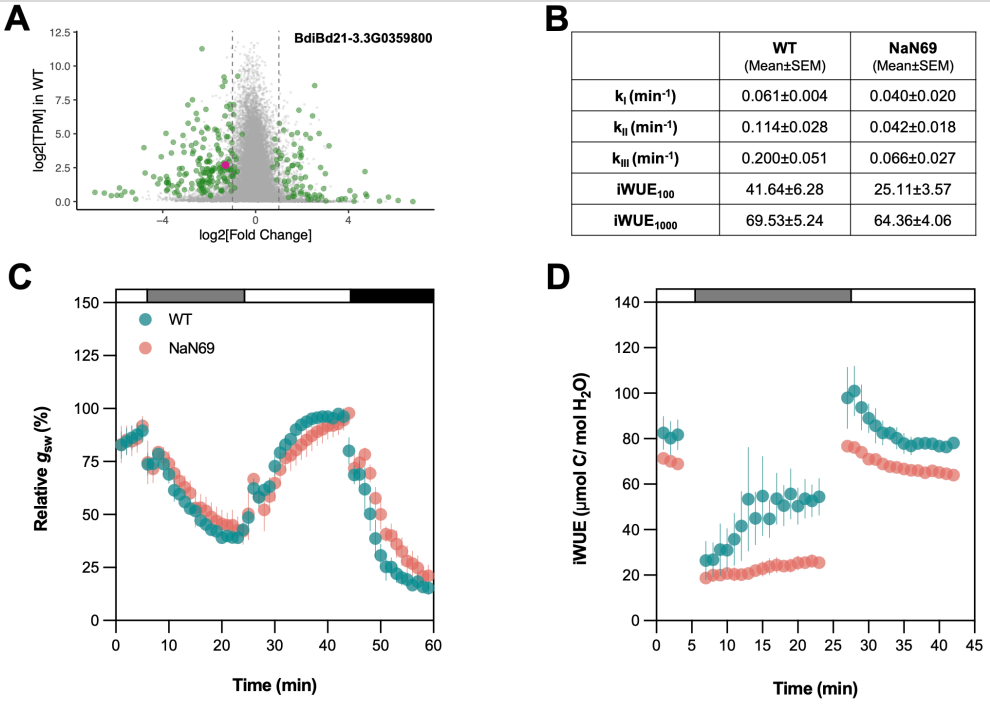
Mutant 25 - NaN34



	WT (Mean±SEM)	NaN34 (Mean±SEM)
k_I (min^{-1})	0.013±0.013	0.048±0.008
k_{II} (min^{-1})	0.083±0.028	0.068±0.002
k_{III} (min^{-1})	0.123±0.080	0.135±0.032
$iWUE_{100}$	29.77±4.76	41.40±6.34
$iWUE_{1000}$	87.98±8.61	77.77±3.51

Figure 2.48 – Gas exchange phenotyping of mutant line 25 (NaN34). (A) Identification of the candidate gene in the RNA-seq. **(B)** Average stomatal speed (k) for the three light transitions (k_I, 1000-100 PAR; k_{II}, 100-1000 PAR; k_{III}, 1000-0 PAR) and iWUE at 100 and 1000 PAR in WT and NaN34. **(C)** Relative g_{sw} in WT and NaN34 (n=3). **(D)** iWUE in WT and NaN34 (n=3). Error bars represent SEM.

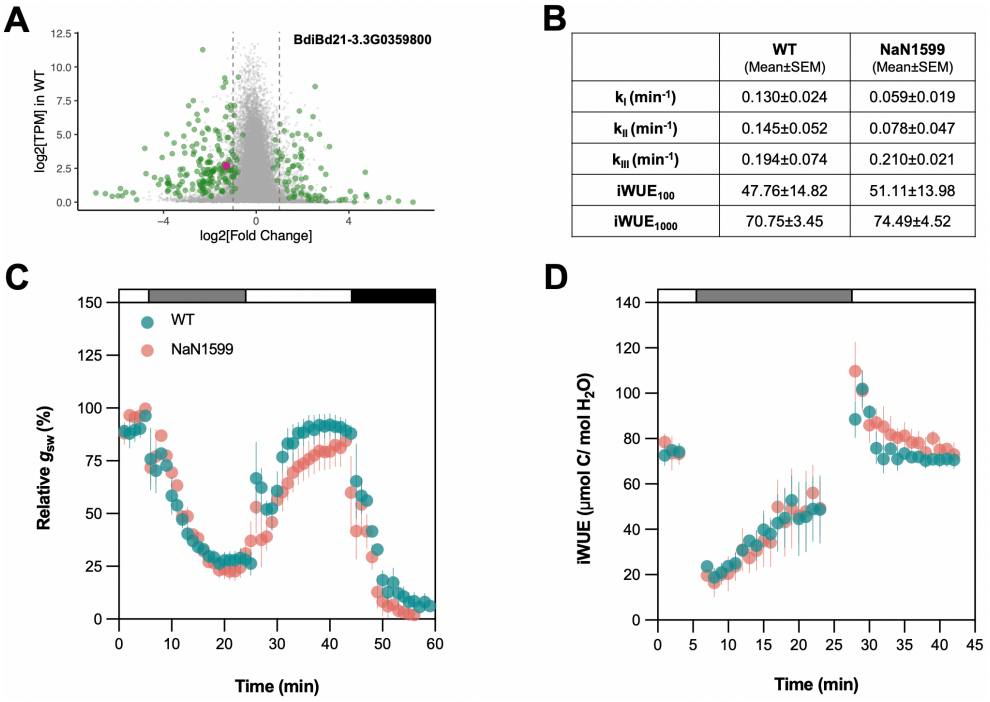
Mutant 27 – NaN69



	WT (Mean±SEM)	NaN69 (Mean±SEM)
k_I (min^{-1})	0.061±0.004	0.040±0.020
k_{II} (min^{-1})	0.114±0.028	0.042±0.018
k_{III} (min^{-1})	0.200±0.051	0.066±0.027
$iWUE_{100}$	41.64±6.28	25.11±3.57
$iWUE_{1000}$	69.53±5.24	64.36±4.06

Figure 2.49 – Gas exchange phenotyping of mutant line 27 (NaN69). (A) Identification of the candidate gene in the RNA-seq. **(B)** Average stomatal speed (k) for the three light transitions (k_I, 1000-100 PAR; k_{II}, 100-1000 PAR; k_{III}, 1000-0 PAR) and iWUE at 100 and 1000 PAR in WT and NaN69. **(C)** Relative g_{sw} in WT and NaN69 (n=3). **(D)** iWUE in WT and NaN69 (n=3). Error bars represent SEM.

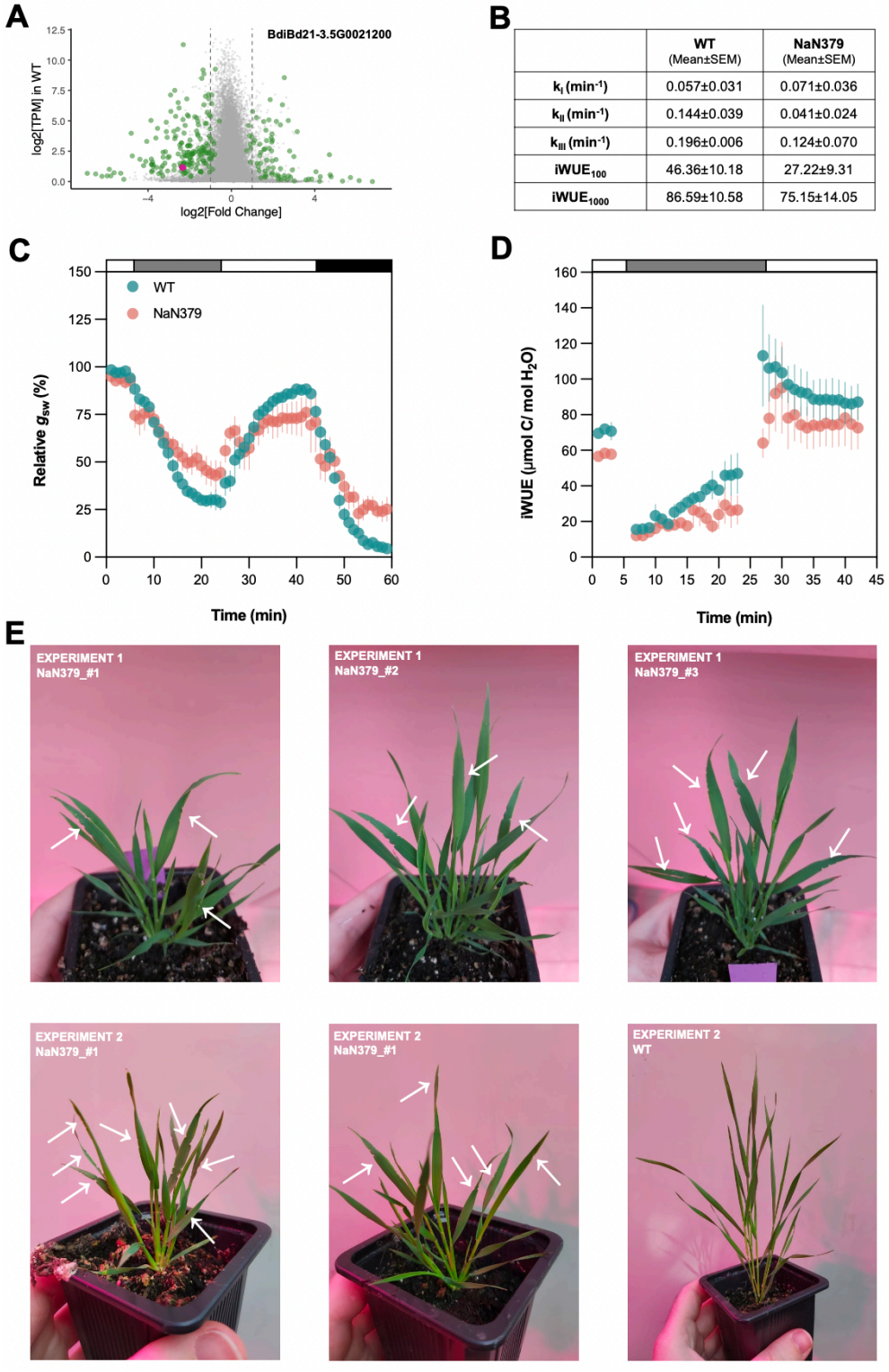
Mutant 28 - NaN1599



	WT (Mean±SEM)	NaN1599 (Mean±SEM)
k_I (min^{-1})	0.130±0.024	0.059±0.019
k_{II} (min^{-1})	0.145±0.052	0.078±0.047
k_{III} (min^{-1})	0.194±0.074	0.210±0.021
$iWUE_{100}$	47.76±14.82	51.11±13.98
$iWUE_{1000}$	70.75±3.45	74.49±4.52

Figure 2.50 – Gas exchange phenotyping of mutant line 28 (NaN1599). (A) Identification of the candidate gene in the RNA-seq. **(B)** Average stomatal speed (k) for the three light transitions (k_I, 1000-100 PAR; k_{II}, 100-1000 PAR; k_{III}, 1000-0 PAR) and iWUE at 100 and 1000 PAR in WT and NaN1599. **(C)** Relative g_{sw} in WT and NaN1599 (n=3). **(D)** iWUE in WT and NaN1599 (n=3). Error bars represent SEM.

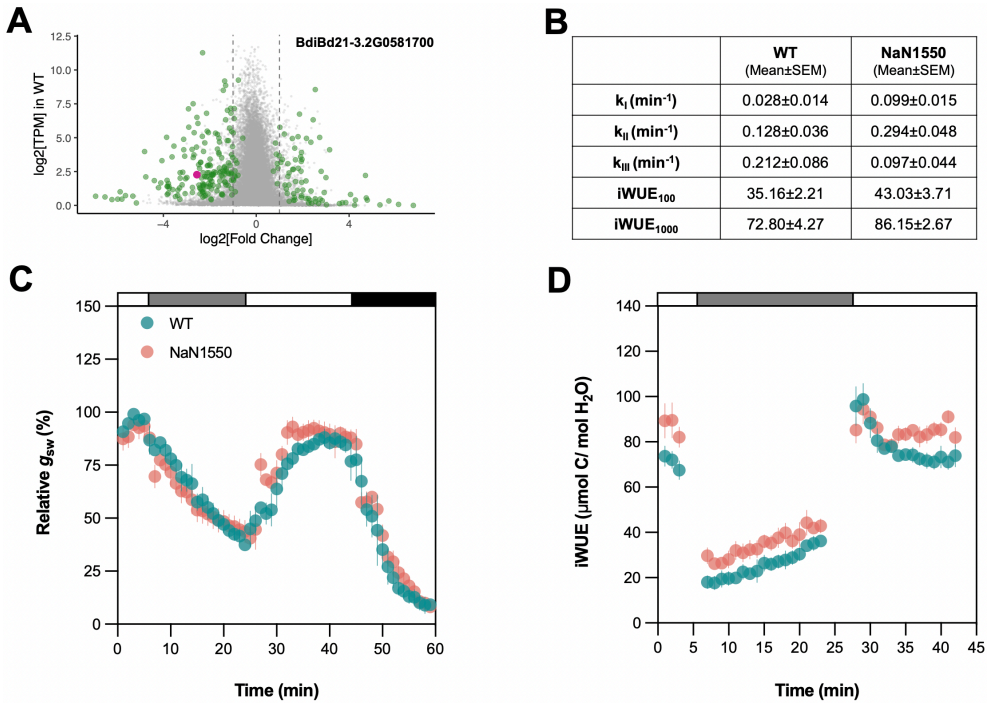
Mutant 33 – NaN379



	WT (Mean±SEM)	NaN379 (Mean±SEM)
k_I (min^{-1})	0.057±0.031	0.071±0.036
k_{II} (min^{-1})	0.144±0.039	0.041±0.024
k_{III} (min^{-1})	0.196±0.006	0.124±0.070
$iWUE_{100}$	46.36±10.18	27.22±9.31
$iWUE_{1000}$	86.59±10.58	75.15±14.05

Figure 2.51 – Gas exchange phenotyping of mutant line 33 (NaN379). (A) Identification of the candidate gene in the RNA-seq. **(B)** Average stomatal speed (k) for the three light transitions (k_I, 1000-100 PAR; k_{II}, 100-1000 PAR; k_{III}, 1000-0 PAR) and iWUE at 100 and 1000 PAR in WT and NaN379. **(C)** Relative g_{sw} in WT and NaN379 (n=3). **(D)** iWUE in WT and NaN379 (n=3). Error bars represent SEM. **(E)** Herbivore-induced leaf damages observed in NaN379 individuals in two independent experiments indicated by white arrows.

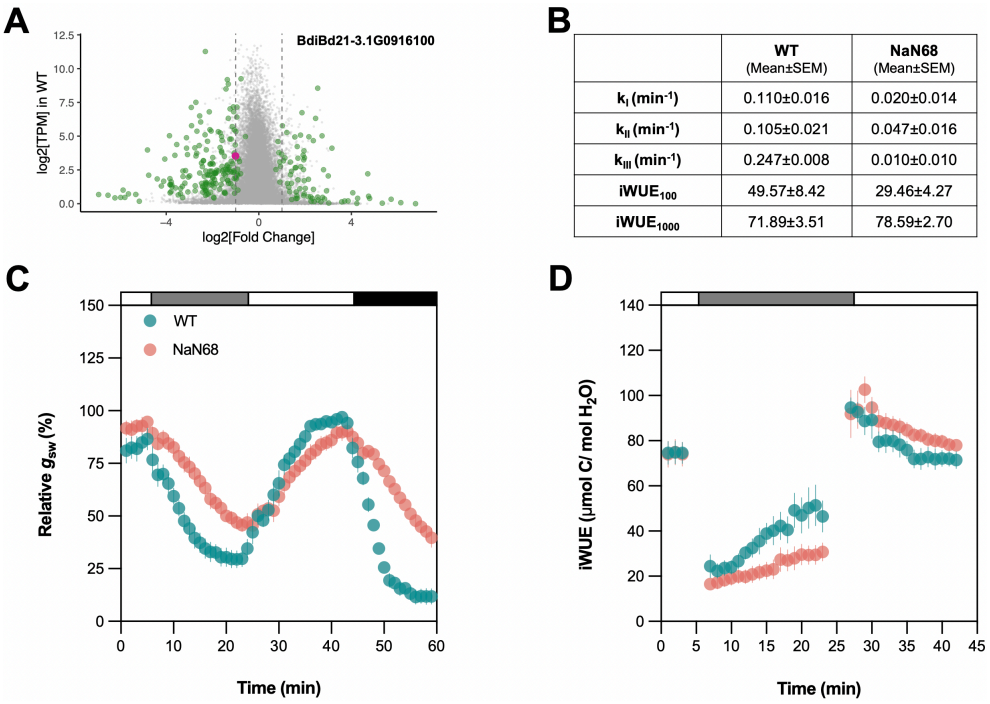
Mutant 35 - NaN1550



	WT (Mean±SEM)	NaN1550 (Mean±SEM)
k_I (min^{-1})	0.028±0.014	0.099±0.015
k_{II} (min^{-1})	0.128±0.036	0.294±0.048
k_{III} (min^{-1})	0.212±0.086	0.097±0.044
$iWUE_{100}$	35.16±2.21	43.03±3.71
$iWUE_{1000}$	72.80±4.27	86.15±2.67

Figure 2.52 – Gas exchange phenotyping of mutant line 35 (NaN1550). (A) Identification of the candidate gene in the RNA-seq. **(B)** Average stomatal speed (k) for the three light transitions (k_I, 1000-100 PAR; k_{II}, 100-1000 PAR; k_{III}, 1000-0 PAR) and iWUE at 100 and 1000 PAR in WT and NaN1550. **(C)** Relative g_{sw} in WT and NaN1550 (n=3). **(D)** iWUE in WT and NaN1550 (n=3). Error bars represent SEM.

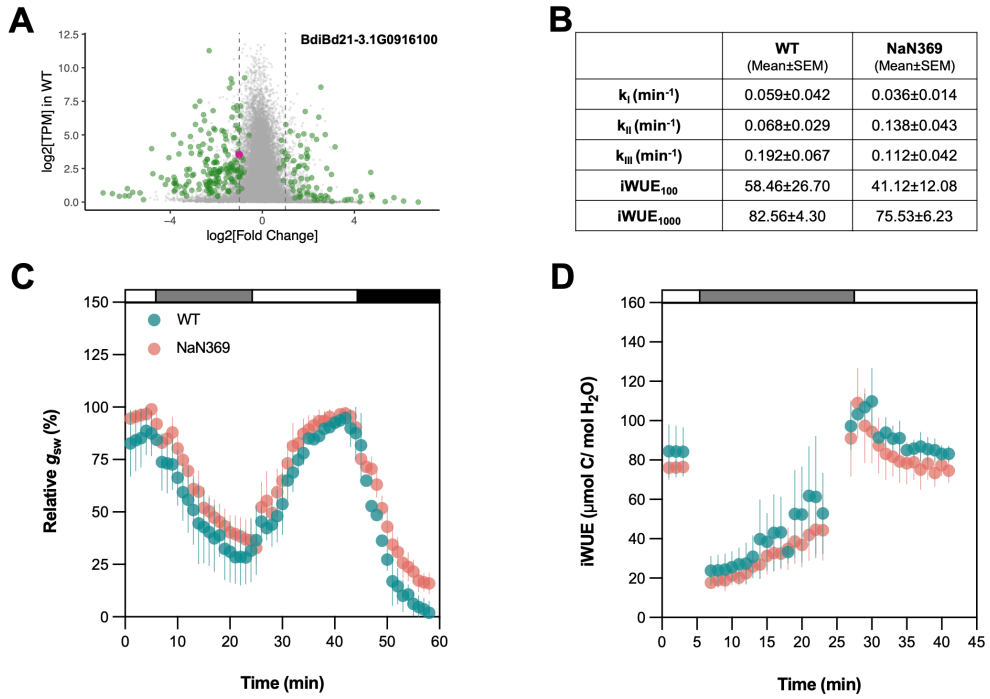
Mutant 38 – NaN68



	WT (Mean±SEM)	NaN68 (Mean±SEM)
k_I (min^{-1})	0.110±0.016	0.020±0.014
k_{II} (min^{-1})	0.105±0.021	0.047±0.016
k_{III} (min^{-1})	0.247±0.008	0.010±0.010
$iWUE_{100}$	49.57±8.42	29.46±4.27
$iWUE_{1000}$	71.89±3.51	78.59±2.70

Figure 2.53 – Gas exchange phenotyping of mutant line 38 (NaN68). (A) Identification of the candidate gene in the RNA-seq. **(B)** Average stomatal speed (k) for the three light transitions (k_I, 1000-100 PAR; k_{II}, 100-1000 PAR; k_{III}, 1000-0 PAR) and iWUE at 100 and 1000 PAR in WT and NaN68. **(C)** Relative g_{sw} in WT and NaN68 (n=6). **(D)** iWUE in WT and NaN68 (n=6). Error bars represent SEM.

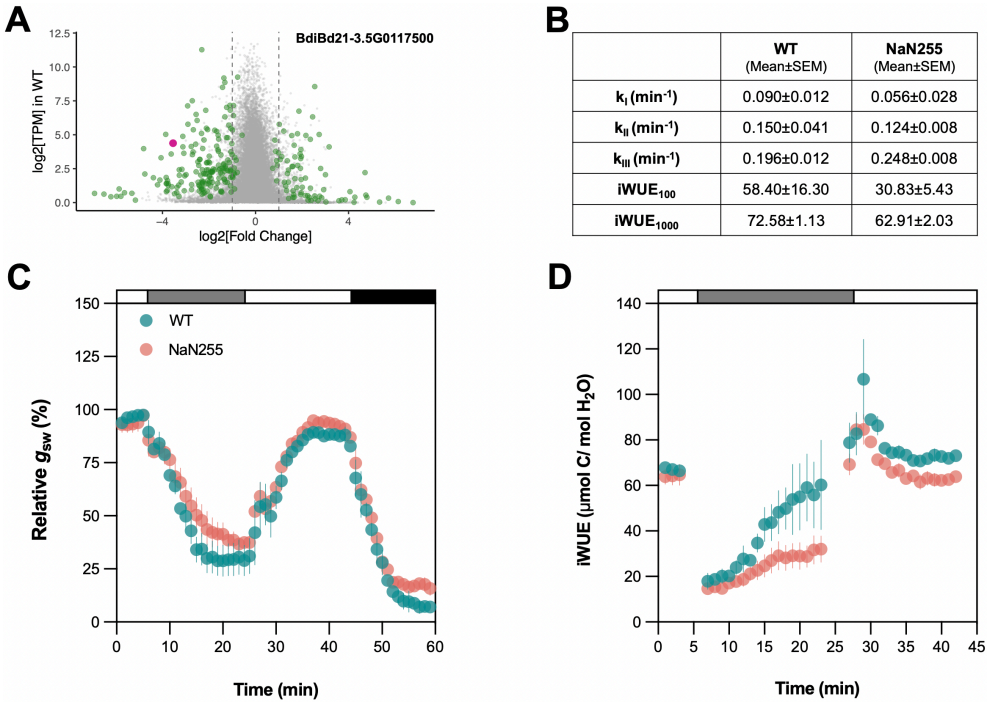
Mutant 39 – NaN369



	WT (Mean±SEM)	NaN369 (Mean±SEM)
k_I (min^{-1})	0.059±0.042	0.036±0.014
k_{II} (min^{-1})	0.068±0.029	0.138±0.043
k_{III} (min^{-1})	0.192±0.067	0.112±0.042
$iWUE_{100}$	58.46±26.70	41.12±12.08
$iWUE_{1000}$	82.56±4.30	75.53±6.23

Figure 2.54 – Gas exchange phenotyping of mutant line 39 (NaN369). (A) Identification of the candidate gene in the RNA-seq. **(B)** Average stomatal speed (k) for the three light transitions (k_I, 1000-100 PAR; k_{II}, 100-1000 PAR; k_{III}, 1000-0 PAR) and iWUE at 100 and 1000 PAR in WT and NaN369. **(C)** Relative g_{sw} in WT and NaN369 (n=2). **(D)** iWUE in WT and NaN369 (n=2). Error bars represent SEM.

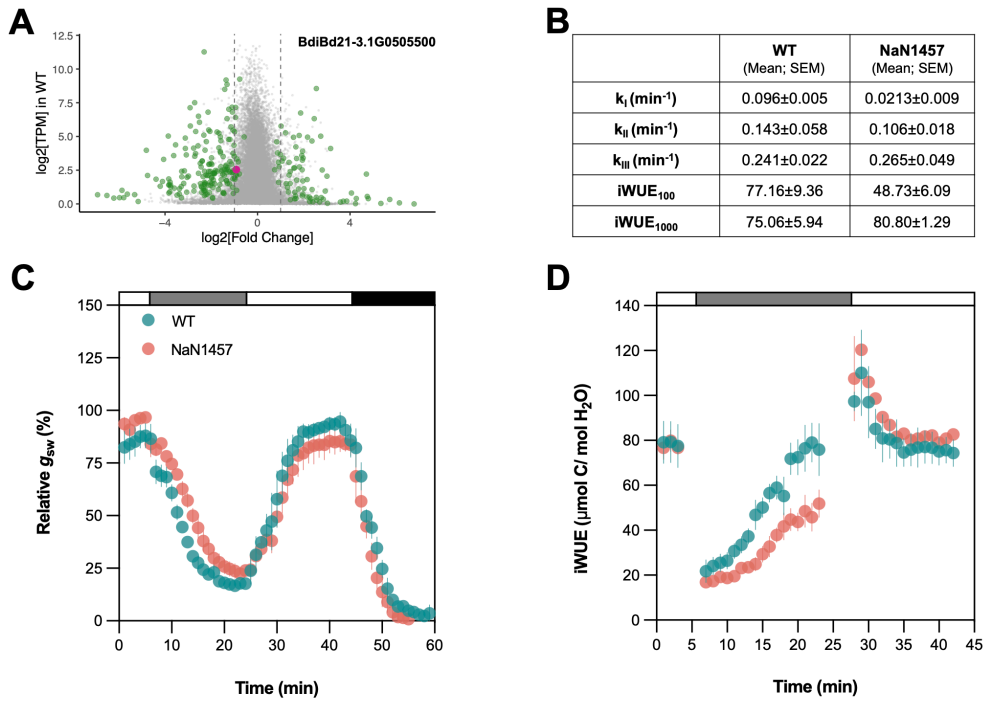
Mutant 43 – NaN255



	WT (Mean±SEM)	NaN255 (Mean±SEM)
k_I (min^{-1})	0.090±0.012	0.056±0.028
k_{II} (min^{-1})	0.150±0.041	0.124±0.008
k_{III} (min^{-1})	0.196±0.012	0.248±0.008
$iWUE_{100}$	58.40±16.30	30.83±5.43
$iWUE_{1000}$	72.58±1.13	62.91±2.03

Figure 2.55 – Gas exchange phenotyping of mutant line 43 (NaN255). (A) Identification of the candidate gene in the RNA-seq. **(B)** Average stomatal speed (k) for the three light transitions (k_I, 1000-100 PAR; k_{II}, 100-1000 PAR; k_{III}, 1000-0 PAR) and iWUE at 100 and 1000 PAR in WT and NaN255. **(C)** Relative g_{sw} in WT and NaN255 (n=3). **(D)** iWUE in WT and NaN255 (n=3). Error bars represent SEM.

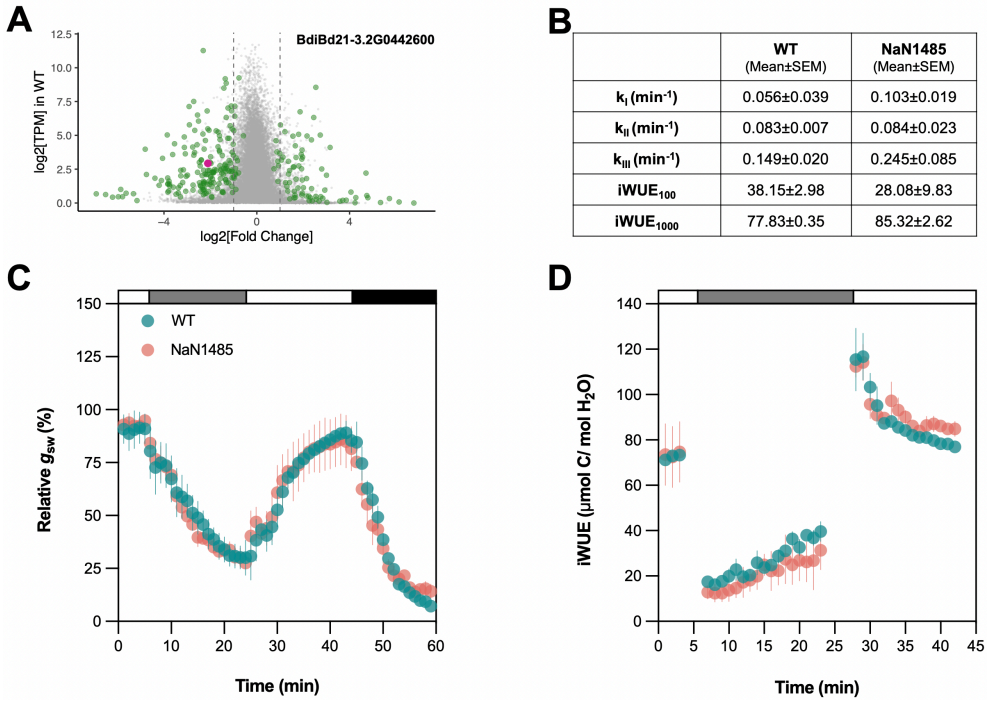
Mutant 44 – NaN1457



	WT (Mean; SEM)	NaN1457 (Mean; SEM)
k_I (min^{-1})	0.096±0.005	0.0213±0.009
k_{II} (min^{-1})	0.143±0.058	0.106±0.018
k_{III} (min^{-1})	0.241±0.022	0.265±0.049
$iWUE_{100}$	77.16±9.36	48.73±6.09
$iWUE_{1000}$	75.06±5.94	80.80±1.29

Figure 2.56 – Gas exchange phenotyping of mutant line 44 (NaN1457). (A) Identification of the candidate gene in the RNA-seq. **(B)** Average stomatal speed (k) for the three light transitions (k_I, 1000-100 PAR; k_{II}, 100-1000 PAR; k_{III}, 1000-0 PAR) and iWUE at 100 and 1000 PAR in WT and NaN1457. **(C)** Relative g_{sw} in WT and NaN1457 (n=3). **(D)** iWUE in WT and NaN1457 (n=3). Error bars represent SEM.

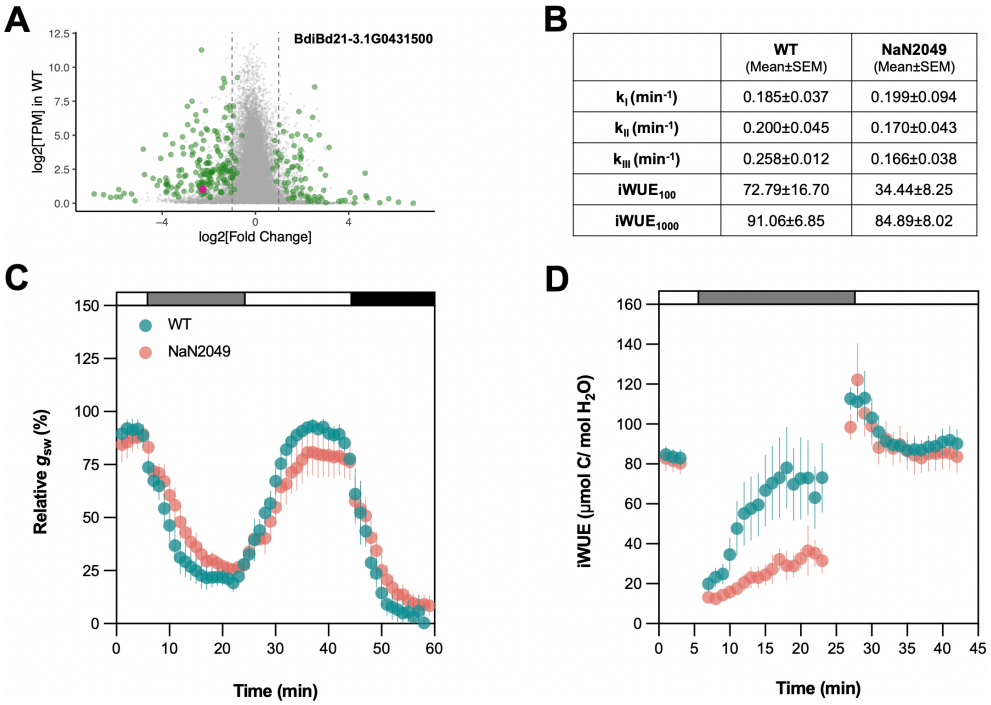
Mutant 45 - NaN1485



	WT (Mean±SEM)	NaN1485 (Mean±SEM)
k_I (min^{-1})	0.056±0.039	0.103±0.019
k_{II} (min^{-1})	0.083±0.007	0.084±0.023
k_{III} (min^{-1})	0.149±0.020	0.245±0.085
$iWUE_{100}$	38.15±2.98	28.08±9.83
$iWUE_{1000}$	77.83±0.35	85.32±2.62

Figure 2.57 – Gas exchange phenotyping of mutant line 45 (NaN1485). (A) Identification of the candidate gene in the RNA-seq. **(B)** Average stomatal speed (k) for the three light transitions (k_I, 1000-100 PAR; k_{II}, 100-1000 PAR; k_{III}, 1000-0 PAR) and iWUE at 100 and 1000 PAR in WT and NaN1485. **(C)** Relative g_{sw} in WT and NaN1485 (n=3). **(D)** iWUE in WT and NaN1485 (n=3). Error bars represent SEM.

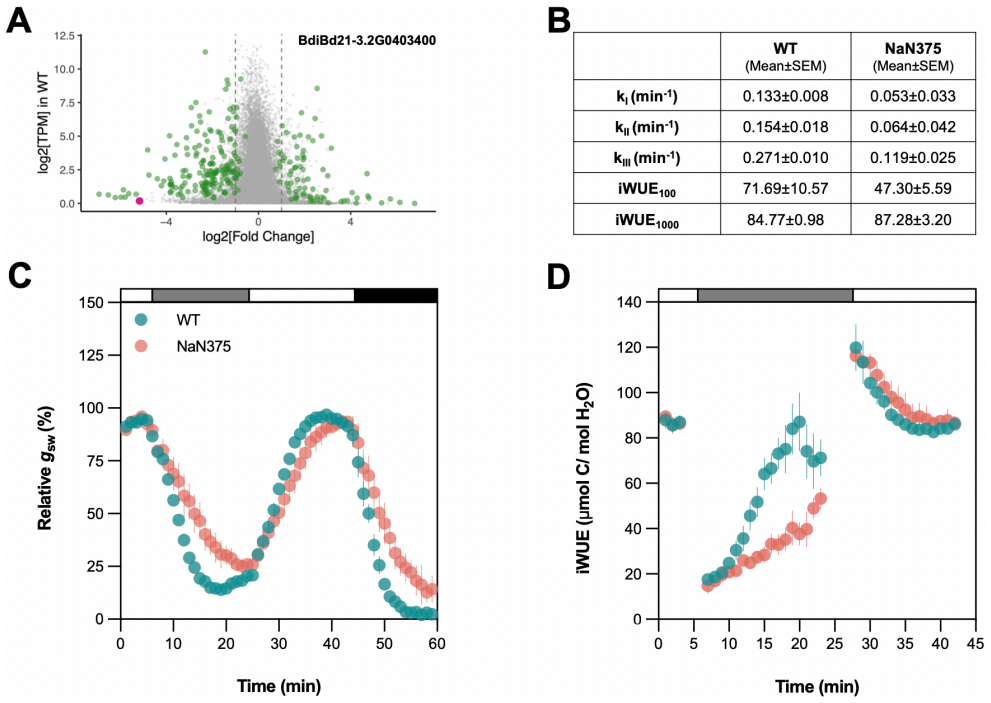
Mutant 50 - NaN2049



	WT (Mean±SEM)	NaN2049 (Mean±SEM)
k_I (min^{-1})	0.185±0.037	0.199±0.094
k_{II} (min^{-1})	0.200±0.045	0.170±0.043
k_{III} (min^{-1})	0.258±0.012	0.166±0.038
$iWUE_{100}$	72.79±16.70	34.44±8.25
$iWUE_{1000}$	91.06±6.85	84.89±8.02

Figure 2.58 – Gas exchange phenotyping of mutant line 50 (NaN2049). (A) Identification of the candidate gene in the RNA-seq. **(B)** Average stomatal speed (k) for the three light transitions (k_I, 1000-100 PAR; k_{II}, 100-1000 PAR; k_{III}, 1000-0 PAR) and iWUE at 100 and 1000 PAR in WT and NaN2049. **(C)** Relative g_{sw} in WT and NaN2049 (n=5-6). **(D)** iWUE in WT and NaN2049 (n=5-6). Error bars represent SEM.

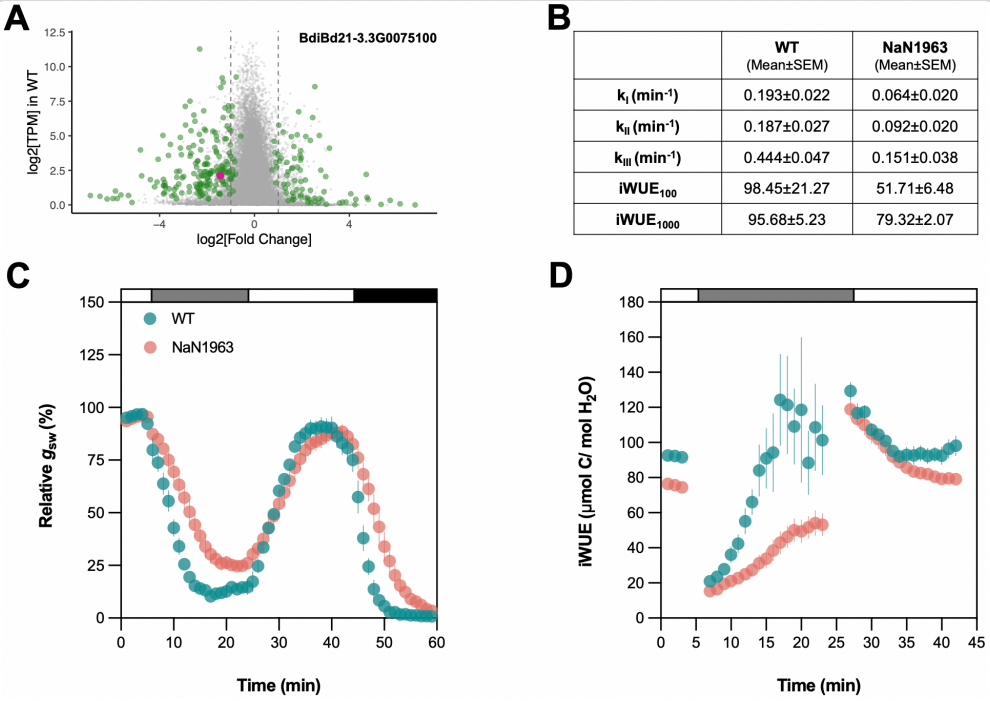
Mutant 51 - NaN375



	WT (Mean±SEM)	NaN375 (Mean±SEM)
k_I (min^{-1})	0.133±0.008	0.053±0.033
k_{II} (min^{-1})	0.154±0.018	0.064±0.042
k_{III} (min^{-1})	0.271±0.010	0.119±0.025
$iWUE_{100}$	71.69±10.57	47.30±5.59
$iWUE_{1000}$	84.77±0.98	87.28±3.20

Figure 2.59 – Gas exchange phenotyping of mutant line 51 (NaN375). (A) Identification of the candidate gene in the RNA-seq. **(B)** Average stomatal speed (k) for the three light transitions (k_I, 1000-100 PAR; k_{II}, 100-1000 PAR; k_{III}, 1000-0 PAR) and iWUE at 100 and 1000 PAR in WT and NaN375. **(C)** Relative g_{sw} in WT and NaN375 (n=3). **(D)** iWUE in WT and NaN375 (n=3). Error bars represent SEM.

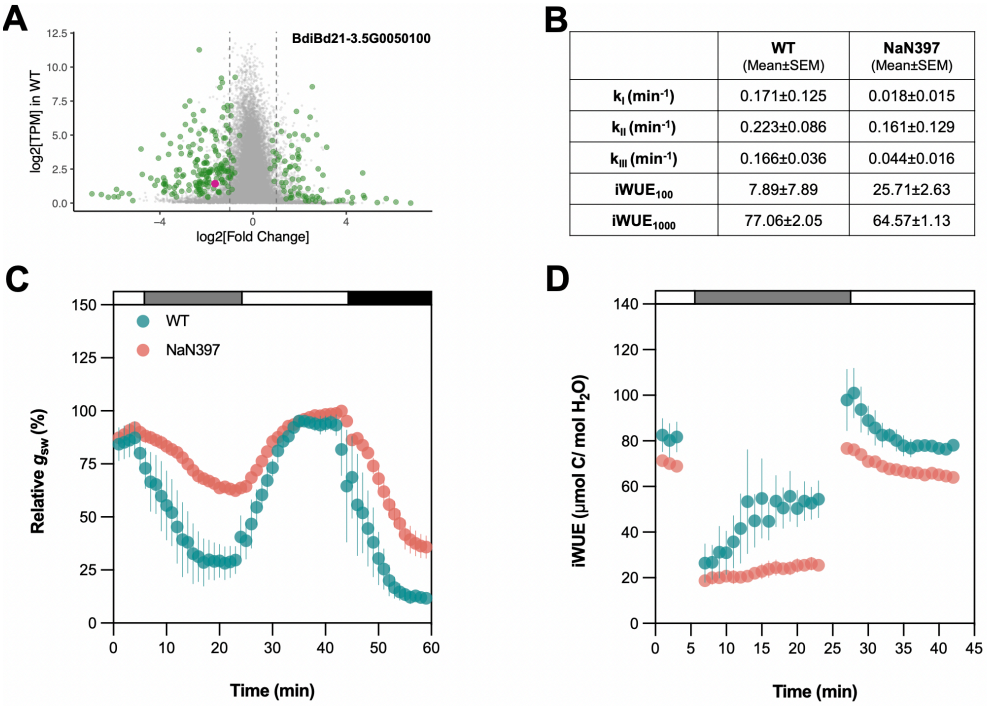
Mutant 54 – NaN1963



	WT (Mean±SEM)	NaN1963 (Mean±SEM)
k_I (min^{-1})	0.193±0.022	0.064±0.020
k_{II} (min^{-1})	0.187±0.027	0.092±0.020
k_{III} (min^{-1})	0.444±0.047	0.151±0.038
$iWUE_{100}$	98.45±21.27	51.71±6.48
$iWUE_{1000}$	95.68±5.23	79.32±2.07

Figure 2.60 – Gas exchange phenotyping of mutant line 54 (NaN1963). (A) Identification of the candidate gene in the RNA-seq. **(B)** Average stomatal speed (k) for the three light transitions (k_I, 1000-100 PAR; k_{II}, 100-1000 PAR; k_{III}, 1000-0 PAR) and iWUE at 100 and 1000 PAR in WT and NaN1963. **(C)** Relative g_{sw} in WT and NaN1963 (n=4-5). **(D)** iWUE in WT and NaN1963 (n=4-5). Error bars represent SEM.

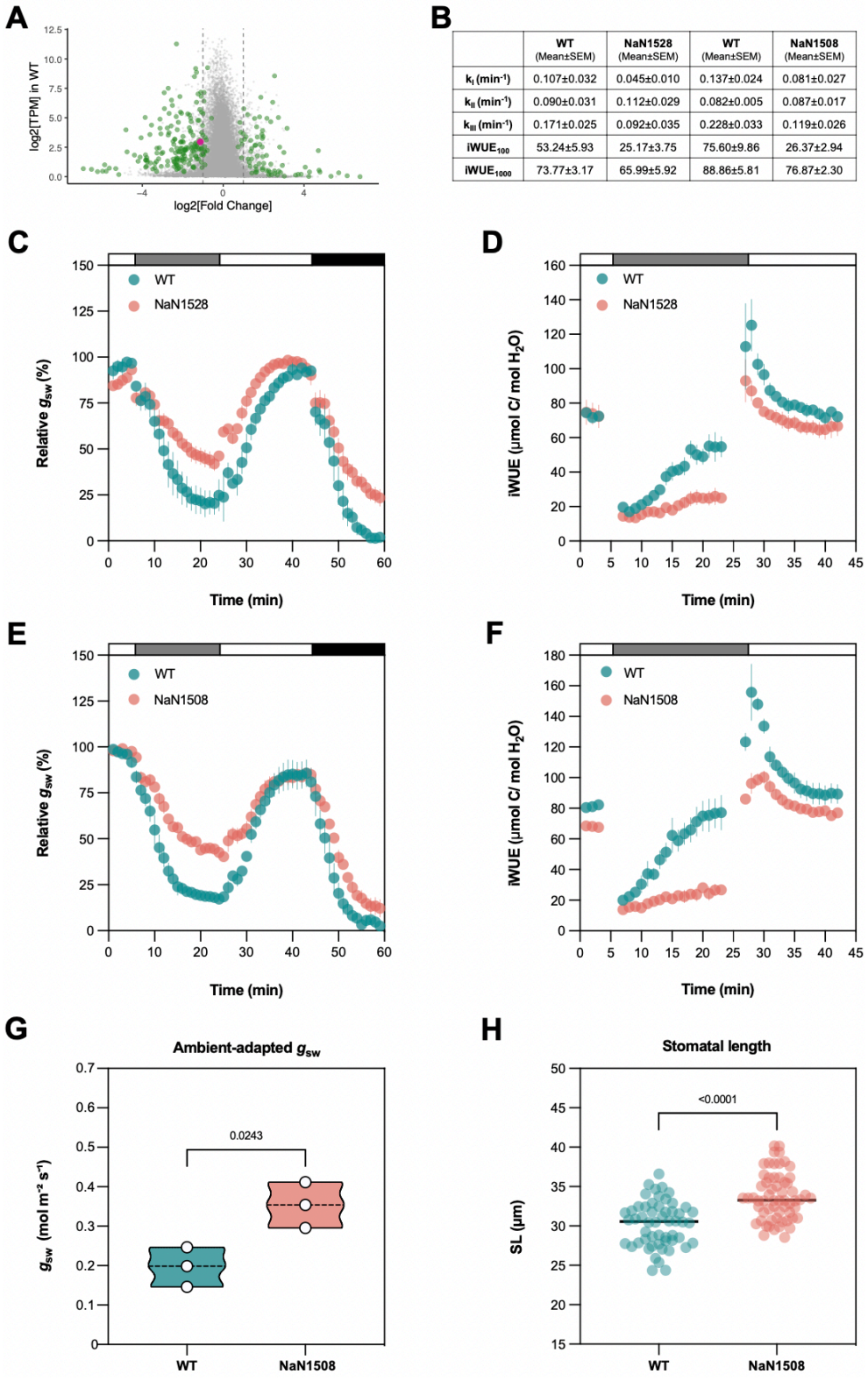
Mutant 56 – NaN397



	WT (Mean±SEM)	NaN397 (Mean±SEM)
k_I (min^{-1})	0.171±0.125	0.018±0.015
k_{II} (min^{-1})	0.223±0.086	0.161±0.129
k_{III} (min^{-1})	0.166±0.036	0.044±0.016
$iWUE_{100}$	7.89±7.89	25.71±2.63
$iWUE_{1000}$	77.06±2.05	64.57±1.13

Figure 2.61 – Gas exchange phenotyping of mutant line 56 (NaN397). (A) Identification of the candidate gene in the RNA-seq. **(B)** Average stomatal speed (k) for the three light transitions (k_I, 1000-100 PAR; k_{II}, 100-1000 PAR; k_{III}, 1000-0 PAR) and iWUE at 100 and 1000 PAR in WT and NaN397. **(C)** Relative g_{sw} in WT and NaN397 (n=3-5). **(D)** iWUE in WT and NaN397 (n=3-5). Error bars represent SEM. This line was screened by Leonie Redt (master student) under my supervision.

Mutants 57 and 58 – NaN1528 and NaN1508



	WT (Mean±SEM)	NaN1528 (Mean±SEM)	WT (Mean±SEM)	NaN1508 (Mean±SEM)
k_I (min^{-1})	0.107±0.032	0.045±0.010	0.137±0.024	0.081±0.027
k_{II} (min^{-1})	0.090±0.031	0.112±0.029	0.082±0.005	0.087±0.017
k_{III} (min^{-1})	0.171±0.025	0.092±0.035	0.228±0.033	0.119±0.026
$iWUE_{100}$	53.24±5.93	25.17±3.75	75.60±9.86	26.37±2.94
$iWUE_{1000}$	73.77±3.17	65.99±5.92	88.86±5.81	76.87±2.30

Figure 2.62 – Gas exchange phenotyping of mutant lines 57 (NaN1528) and 58 (NaN1508). (A) Identification of the candidate gene in the RNA-seq. **(B)** Average stomatal speed (k) for the three light transitions (k_I, 1000-100 PAR; k_{II}, 100-1000 PAR; k_{III}, 1000-0 PAR) and iWUE at 100 and 1000 PAR in WT and NaN1528; and WT and NaN1508. **(C)** Relative g_{sw} in WT and NaN1528 (n=3). **(D)** iWUE in WT and NaN1528 (n=3).

(E) Relative g_{sw} in WT and NaN1508 (n=3). **(F)** iWUE in WT and NaN1508 (n=3). **(G)** Ambient-adapted g_{sw} in WT and NaN1508 (n=3 individuals, each point represents the average of two measurements of 3-4 leaves per individual). (H) Stomatal length in WT and NaN1508 (n=54-60 stomata per genotype, measured from 3 individuals).

Mutants 59 and 60 – NaN570 and NaN553

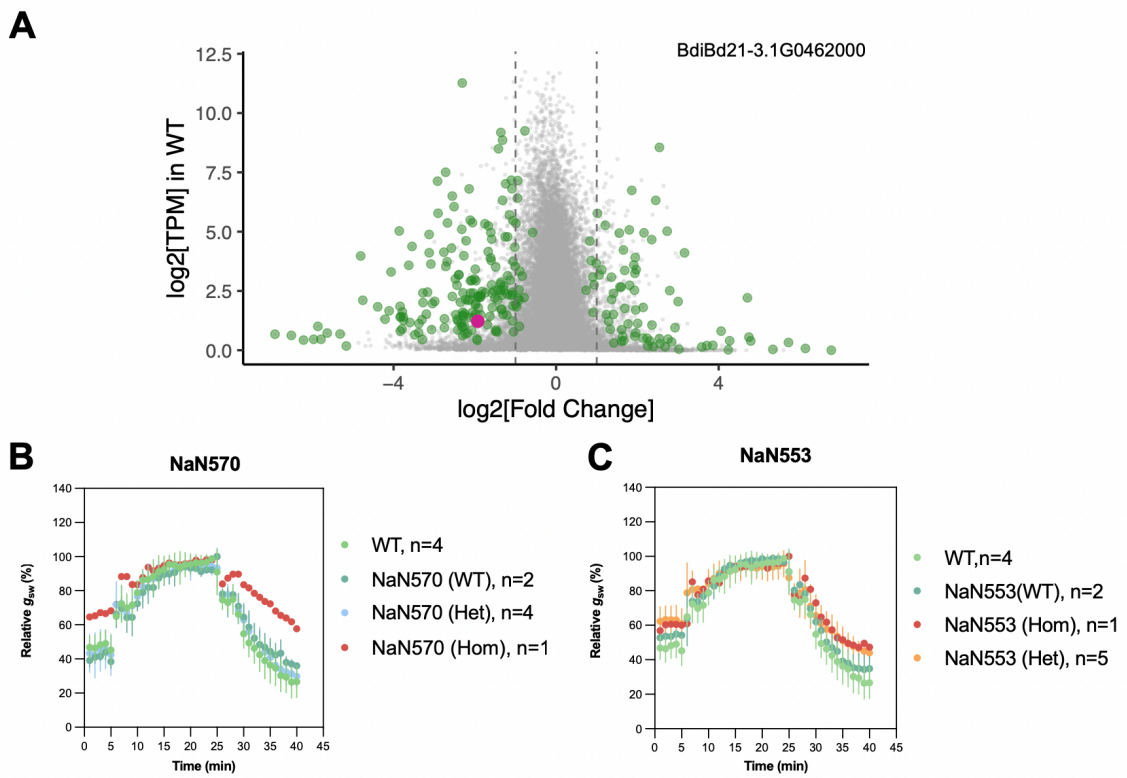


Figure 2.63 – Gas exchange phenotyping of mutant lines 59 (NaN570) and 60 (NaN553). (A) Identification of the candidate gene in the RNA-seq. **(B)** Relative g_{sw} in WT and NaN570. Number of WT, NaN570 (WT), NaN570 (Het) and NaN570 (Hom) individuals indicated. **(B)** Relative g_{sw} in WT and NaN553. Number of WT, NaN553 (WT), NaN553 (Het) and NaN553 (Hom) indicated.

4.4 Discussion

Increasing temperatures, increasing aridity and decreasing water availability in current arable lands are occurring due to climate change (Chai et al. 2021; Takeshima et al. 2020; Greve et al. 2018; Rosenzweig et al. 2014). Consequently, it is crucial to improve crop fitness and resilience to stress. Grasses, such as the major crops wheat, rice and barley, show faster stomatal movements than most plant species (McAusland et al. 2016), a trait that is associated with their unique stomatal morphology – graminoid stomata – consisting of two dumbbell-shaped GCs and two flanking SCs (Franks and Farquhar 2007; Nunes et al. 2020; Raissig et al. 2017; Gray et al. 2020). Stomatal closure

and opening speed and water-use efficiency define how efficiently plants can fix carbon while limiting water loss in changing environments, and thus are important traits for improving plant resilience to stress and plant productivity (Lawson and Vialet-Chabrand 2019; Eyland et al. 2021; Lawson and Blatt 2014).

In order to identify imperative genes for the form and function of graminoid stomata, I explored the leaf transcriptome of WT *B. distachyon* (21-3) and of *bdmute* mutants which lack SCs, contain anomalous GC shape and display aberrant stomatal opening and closure speed (Raissig et al. 2017). On this RNA-seq analysis, I identified 179 significantly differentially expressed genes that were downregulated in *bdmute* and therefore potentially associated with the graminoid stomatal morphology and physiology present in WT.

After performing a gene ontology enrichment analysis, I verified that these 179 candidate genes fell into three major categories: i) membrane/transmembrane-related, ii) apoplastic/cell-wall associated and iii) signalling-related. As stomatal movements result from changes in osmotic and turgor pressure regulated by the transport of solutes and water, the occurrence of transmembrane proteins such as ion channels and/or transporters is crucial and the core of stomatal functioning. Furthermore, membrane-associated proteins are important for signal perception to induce signalling cascades resulting in stomatal movements in response to the different environmental triggers. Cell wall properties are also relevant for both morphogenesis and function of stomata, and thus apoplastic and/or cell-wall associated proteins may be also required for the graminoid stomatal cell wall composition and functional success. Finally, different signalling pathways are fundamental for perceiving and inducing stomatal responses triggered by various environmental stimuli. While stomatal opening is induced by light, high humidity and low CO_2 concentrations, stomatal closure occurs in response to darkness (in C_3/C_4 plants) and biotic/abiotic stresses. Therefore, different environmental cues must be perceived, integrated, and signalled through different molecular routes to induce the turgor-driven stomatal movements.

When it comes to membrane-associated genes, I identified some known players already described in other grass species and in *Arabidopsis thaliana* (Nunes et al. 2020). SLOW ANION CHANNEL-ASSOCIATED 1 (SLAC1) is a channel protein occurring in *Arabidopsis* GCs and essential for

stomatal closure (Vahisalu et al. 2008). In grasses, *SLAC1* expression has also been detected in GCs of *Hordeum vulgare* (Schäfer et al. 2018) and in GCs/SCs of *Oryza sativa* (Kusumi et al. 2017). SLAC1 and SLAH3 (SLAC1 HOMOLOGUE 3) inhibit the inward K^+ channel KAT1 via protein-protein interactions in *Arabidopsis* and therefore impede stomatal opening (Zhang et al. 2016; Geiger et al. 2011). BdiBd21-3.2G0403400 (*SLAH3*) was one of the genes downregulated in *bdmute*. I identified one mutant line NaN375 which showed slower stomatal movements, particularly significantly slower stomatal closure in response to darkness. Therefore, I speculate that in *B. distachyon SLAH3* is either expressed in GCs to inhibit inward K^+ channels and regulate loss of turgor in GCs as described in *Arabidopsis*, or *SLAH3* might display a novel opposite function in grasses to promote K^+ uptake in SCs during stomatal closure (Fig. 2.64). Either of these functions would explain the slower stomatal movements in NaN375, associated with defective loss of turgor in GCs and increase of turgor in SCs.

Another membrane-associated gene identified was a nitrate transporter/ABA importer BdiBd21-3.1G0505500 (*NRT1.2/NPF4.6*) which mutant NaN1457 contains a SNP mutation A301T on the Major Facilitator Superfamily (MFS) domain. I observed slower stomatal closure in NaN1457 compared to WT, particularly in response to decreasing light intensity (1000 - 100 PAR) and lower iWUE at 100 PAR. In *Arabidopsis*, *NRT1.2/NPF4.6* controls stomatal aperture by regulating ABA transport (Shimizu et al. 2021), a core hormone for stomatal closure signalling pathways. Since the ABA signalling machinery has been hypothesized to occur in GCs, I speculate that *NRT1.2/NPF4.6* might be expressed in GCs to regulate ABA import and trigger stomatal closure or alternatively in SCs regulating the import of other solutes (e.g., nitrate) to increase SC turgor during stomatal closure (Fig. 2.64).

Two other membrane-associated genes were the Ca^{2+}-activated outward rectifying K^+ channel BdiBd21-3.2G0605300 (*KCO6/TPK3*, NaN86) and a divalent anion-sodium symporter BdiBd21-3.3G0359800 (NaN69 and NaN1599), with potential mild stomatal closure defects observed in the mutants. In *Arabidopsis*, *KCO6/TPK3* has been described as a vacuolar K^+ channel regulating potassium effluxes (Höhner et al. 2019; Voelker et al. 2006). If *KCO6/TPK3* also functions as a regulator of K^+ efflux in *Brachypodium* stomata, and since NaN86 displayed stomatal closure

defects, *KCO6/TPK3* could be expected to be expressed in GCs (Fig. 2.64). Therefore, loss of function *kco6/tpk3* mutants would display defective loss of turgor in GCs constraining stomatal closure.

The Na^+/K^+ co-transporter BdiBd21-3.1G0462000 (homologue of *AtHKT1* and *OsHTK2;4*) was also one of the differently expressed genes downregulated in *bdmute*. The maize *HKT2* was recently found to be enriched in SCs in maize (Sun et al. 2022). Therefore, I speculate that *HTK2;4* could also be a SC-specific player regulating the transport of cations in the SCs of *B. distachyon* (Fig. 2.64). I performed a quick leaf-level gas exchange screening in the NaN570 and NaN553 (containing mutations in *HKT1/HKT2;4*) and observed potential defective stomatal closure which I hypothesize to be associated with impaired K^+ import in the SCs during stomatal closure (Fig. 2 .64).

BdiBd21-3.1G0848400 is ABC-2 type transporter, which mutant NaN356 displayed potential stomatal closure defects. ABC transporters have been shown to be involved in malate import to modulate stomatal responses to CO_2 in *Arabidopsis* (Lee et al. 2008) and in the modulation of Ca^{2+} and anion channels in *Arabidopsis* GCs (Suh et al. 2007), therefore BdiBd21-3.1G0848400 may also be involved in solute transport in GCs/SCs (Fig. 2.64). Another ABC transporter, *WBC19*, seemed to be up-regulated 4 hours after *FAMA* induction, therefore suggesting a role for these genes in stomatal morphogenesis and maturation (Hachez et al. 2011).

Besides ion channels, aquaporins are also important for the regulation of turgor pressure required for stomatal movements (Heinen et al. 2014; Cui et al. 2021a). While *PIP1* and *PIP2* have already been characterized in the stomatal complexes of rice and maize (Vinnakota et al. 2016; Heinen et al. 2014), the *PUTATIVE NIP-TYPE AQUAPORIN* (BdiBd21-3.1G0591400) was downregulated in *bdmute*. I observed a potential minor phenotype in NaN218, which contains a mutation in this gene. NaN218 displayed slower stomatal movements, although not significantly different than WT in this initial screen. In *Arabidopsis*, PIP2;1 cell-type specific dynamics between GCs and neighbouring cells have been observed (Cui et al. 2021b), suggesting that a tight and cell-type specific regulation of water transport between GCs and SCs in *B. distachyon* may also be required

and mediated by aquaporins such as the identified *PUTATIVE NIP-TYPE AQUAPORIN* (BdiBd21-3.1G0591400) (Fig. 2.64).

Regarding cell wall-associated genes, five expansin genes were identified (BdiBd21-3.3G0672500, BdiBd21-3.3G0672600, BdiBd21-3.2G0686100, BdiBd21-3.3G0433700, BdiBd21-3.2G0292700) (Table 3). Expansins possess cell wall loosening activity and are involved in developmental processes (Muller et al. 2007; Cosgrove 2000). Furthermore, expansins also hold physiological functions in mature cells. In *Arabidopsis, AtEXPA1* has been described as a regulator of stomatal opening by modifying cell wall mechanical properties (Wei et al. 2011; Zhang et al. 2011). An identical role was observed in *Vicia faba*, where the overexpression of *VfEXPA1* accelerated light-induced stomatal opening increasing transpiration rates (Wei et al. 2011). Thus, I hypothesize that these expansin genes may be involved in cell wall momentaneous modifications during stomatal movements or in stomatal maturation.

Another cell wall-associated gene identified was BdiBd21-3.5G0050100 (*WAK3*), a wall-associated receptor kinase galacturonan-binding. Wall-associated kinases (WAKs) are transmembrane proteins that contain a cytoplasmic serine/threonine kinase domain and an extracellular domain binding pectin on the cell wall, functioning as a connector between the intracellular and extracellular environments (Kohorn and Kohorn 2012; Decreux and Messiaen 2005). WAKs are involved both in cell expansion processes and stress responses (Wu et al. 2020). NaN397 (containing a mutation in BdiBd21-3.5G0050100) showed severely impaired stomatal closure in response to decreasing light intensity and to darkness (1000 - 100 and 1000 - 0 PAR, respectively). Additionally, lower iWUE was observed in both limiting (100 PAR) and non-limiting (1000 PAR) light steps, suggesting that the iWUE defect may derive from higher stomatal conductance. Thus, I hypothesize WAK3 may be involved in cell wall composition of grass stomatal complexes by binding pectin. Pectin dynamics have indeed already been shown to be required for stomatal function (Amsbury et al. 2016; Chen et al. 2021; Jones et al. 2005; Kohorn and Kohorn 2012).

Other genes with potential roles associated with cell wall morphogenesis were identified: BdiBd21-3.2G0569000, a pectin lyase-like gene and BdiBd21-3.4G0417700, a xyloglucan:xyloglucosyl transferase *XTH28/XTR2*. In *Arabidopsis*, PECTATE LYASE LIKE12 has been described as a GC

wall component involved in the regulation of turgor pressure and cell wall mechanics in stomata (Chen et al. 2021). Xyloglucan:xyloglucosyl transferases were also identified as cell wall biosynthesis and remodelling genes in the differentiation of *Arabidospis* GCs (Hachez et al. 2011), and so impacting water-use efficiency and drought tolerance (Damerum et al. 2021; Iurlaro et al. 2016; Cal et al. 2013; Wang et al. 2018).

Still regarding apoplast and cell wall, I also identified BdiBd21-3.2G0704400 (*LACCASE-7-RELATED*) and two class III peroxidases *BdPRX19* (BdiBd21-3.1G0366900) and *BdPRX76* (BdiBd21-3.2G0467800). Laccases and class III peroxidases polymerize lignin in the cell wall (Mnich et al. 2020; Shigeto and Tsutsumi 2016), which is an abundant polyphenolic polymer in grass cell walls (Coomey et al. 2020; Vogel 2008) and particularly also in grass stomata (Shtein et al. 2017). Additionally, they are involved in ROS signalling as they can consume H_2O_2 and produce other ROS species (Passardi et al. 2005). I phenotyped two *bdprx19* mutants (NaN407 and NaN1459). I observed slower stomatal closure and lower iWUE in NaN407 and initially hypothesized that *BdPRX19* could be involved in ROS-induced stomatal closure. Still, the second mutant NaN1459 presented rather the opposite phenotype consisting of potentially quicker closure and higher iWUE. Therefore, I cannot conclude if the phenotypes observed relate to the mutations in *BdPRX19*. Regarding *BdPRX76* (BdiBd21-3.2G0467800), both mutants NaN1528 and NaN1508 displayed lower iWUE particularly at low light (100 PAR) which seemed to be caused by higher g_{sw} and potentially associated with stomatal size. So, I speculated that *BdPRX76* could be involved with the regulation of stomatal size.

Another candidate gene which mutants displayed gas exchange phenotypes was BdiBd21-3.5G0117500 (*LIPID TRANSFER 2, LTP2)*. NaN255 displayed significant stomatal closure defects in response to darkness, and consequently lower iWUE. *LTP2* was recently associated with SCs in maize, although no functional studies have been performed. Thus, I hypothesize BdiBd21-3.5G0117500 may also be specific to SCs in *B. distachyon*. In *Arabidopsis*, *LTP2* is involved in lipid transfer between membranes and in maintaining the integrity of the cuticle-cell wall interface (Jacq et al. 2017).

When it comes to signalling, *CST1* was one of the downregulated genes in *bdmute*. *CST1* has been previously characterized in maize as SC-specific glucose transporter that promotes stomatal conductance and photosynthesis (Wang et al. 2019). Therefore, *CST1* may play a similar function in *B. distachyon*. Identifying *CST1* homologue as one of the downregulated genes in *bdmute* also provided a quality control for our study which aimed to identify genes associated with SCs and dumbbell-shaped GCs.

Another identified gene associated with stomatal signalling was an ABA 8′-hydroxylase gene (BdiBd21-3.3G0503900), which mutant NaN358 displayed potentially faster stomatal closure and higher iWUE at 100 PAR, even though not statistically significant differences were observed between NaN358 and WT. Since ABA is a central player in stomatal closure, ABA catabolism may inhibit or limit stomatal closure (Munemasa et al. 2015). Thus, I speculate that a non-functional ABA 8′-hydroxylase could decrease ABA catabolism leading to increased levels of ABA and consequently increase stomatal responsiveness resulting in enhanced stomatal closure. Besides further screenings and phenotype confirmation with additional mutant alleles, the quantification of endogenous ABA dynamics would be required to further test this hypothesis. Regardless, I suggest that ABA catabolism-related genes may be interesting targets for the improvement of stomatal responsiveness in *B. distachyon*. In fact, abscinazole-E3M has been described as inhibitor of ABA 8′-hydroxylases to enhance ABA responses and improve drought tolerance in *Arabidopsis* and maize (Takeuchi et al. 2016). Recently, it was also observed that the expression of the maize homologue *ZmCYP707A4* was specific to SCs (Sun et al. 2022), which suggests that ABA catabolism may occur in SCs while ABA-signalling cascades may proceed in GCs during stomatal closure.

Several kinases which *Arabidopsis* homologues are involved in stomatal movements were also downregulated in *bdmute* leaves. For example, two CRKs BdiBd21-3.1G0336000 (*CRK10*), BdiBd21-3.2G0659800 (*CRK25*) and two RLKs BdiBd21-3.4G0026800 (*RLK1*) and BdiBd21-3.5G0121500 (*RLK4*). In *Arabidopsis*, *crk10* mutants showed defective stomatal closure (Bourdais et al. 2015; Sierla et al. 2018) and *RLK4* was shown to play a role in calcium signalling during ABA perception for stomatal closure responses (Bai et al. 2009). RLKs are also known mediators of ROS

signalling during stomatal closure signalling cascades (Kimura et al. 2017; Sierla et al. 2018, 2016). Another identified kinase was BdiBd21-3.3G0075100 (*CIPK21*), which mutant NaN1963 showed impaired stomatal movements, most significantly impaired stomatal closure. *CIPK* genes are indeed associated with the regulation of stomatal closure. Stomatal closure initiates with the activation of the anion channels SLAC1 and SLAH3 which are regulated by OST1 and CPK21 and 23 (Geiger et al. 2009; Geiger et al. 2010; Geiger et al. 2011). CIPK16 also has a similar function to CIPK21 by regulating AKT1 activity (Lee et al. 2007). CPK6 also positively regulates SLAC1 and inhibits inward-rectifier potassium channels to inhibit stomatal opening (Brandt et al. 2012; Ye et al. 2013). More recently it was shown that *CIPK23* regulates blue light-dependent stomatal opening through the activation of K^+ channels in *Arabidopsis thaliana* GCs (Inoue et al 2020). Still, the function of CIPK23 is not restricted to GCs, as it also regulates K^+ uptake by activation of the high-affinity K^+ transporter 5 (HAK5) in *Arabidopsis* roots (Ragel et al. 2015). Due to these functions in the regulation of K^+ transport, I hypothesize that the *CIPK21* homologue may be involved in the regulation of K^+ import in SCs and/or export from GCs to induce stomatal closure in *B. distachyon* (Fig. 2.64).

Finally, one terpene synthase BdiBd21-3.5G0021200 (*TPS21*) was downregulated in *bdmute* which mutant NaN379 showed an herbivory-related phenotype. Leaves in NaN379 mutants showed physical damages induced by herbivore feeding while WT plants in the same tray and other plants nearby did not suffer any damage and appeared healthy. Furthermore, healthy leaves of NaN379 individuals showed slower stomatal kinetics and disturbed iWUE.

Terpenes are volatile secondary metabolites that play important roles in response to biotic and abiotic stresses (Harley et al. 2014). The function of terpenes in the defence against herbivores is well known (Bustos-Segura and Foley 2018), which easily explains the observed phenotype.

Regarding abiotic stress, terpenes antioxidant activity has been demonstrated *in vitro* in diverse biological systems (Wang et al. 2019; Nunes et al. 2018; Cardoso et al. 2020; Loreto et al. 2004) and variations in terpene biosynthesis and emission in response to abiotic stresses have been observed (Sabillón and Cremades 2001; Kopaczyk et al. 2020; Ormeño et al. 2007; Lee et al. 2015; Haberstroh et al. 2018), so their antioxidant function during abiotic stress has been claimed although their

specific functions remain largely unexplored (Pichersky and Raguso 2018). Some links between terpenes and stomata can also be appreciated. Terpenoid compounds were shown to reduce plant transpiration in barley (Jung and Grossmann 1985) and the herbivory-induced emission of sesquiterpenes has been reported to be regulated by stomatal aperture in maize seedlings (Seidl-Adams et al. 2015). Stomatal closure was also suggested to selectively inhibit the biosynthesis of certain terpenes (Niinemets et al. 2002).

Since stomata are impaired in *bdmute* mutants, a downregulation of this gene may be a consequence of lower stomatal opening/stomatal conductance observed in *bdmute* (Raissig et al. 2017). The gas exchange phenotype observed in the intact leaves of NaN379 mutants may be a direct consequence from lower terpene emissions affecting stomatal functioning or, more likely, a systemic effect triggered by herbivory. Either way, BdiBd21-3.5G0021200 (*TPS21*) may be a suitable candidate to investigate secondary metabolism for herbivore-resistance but also how stomatal functioning is systemically impaired during the attack of herbivores and regulates terpenes emission.

Overall, I identified potential players involved in grass stomata morphology and physiology. Furthermore, the reverse genetic screen allowed me to speculate on the putative function of several candidate genes (Fig. 2.64) by investigating changes in stomatal behaviour in the mutants.

Further characterization of the phenotypes found in the screening may disclose cell-specific regulation between GCs and SCs and unravel molecular mechanisms behind the faster and efficient stomatal movements in grasses.

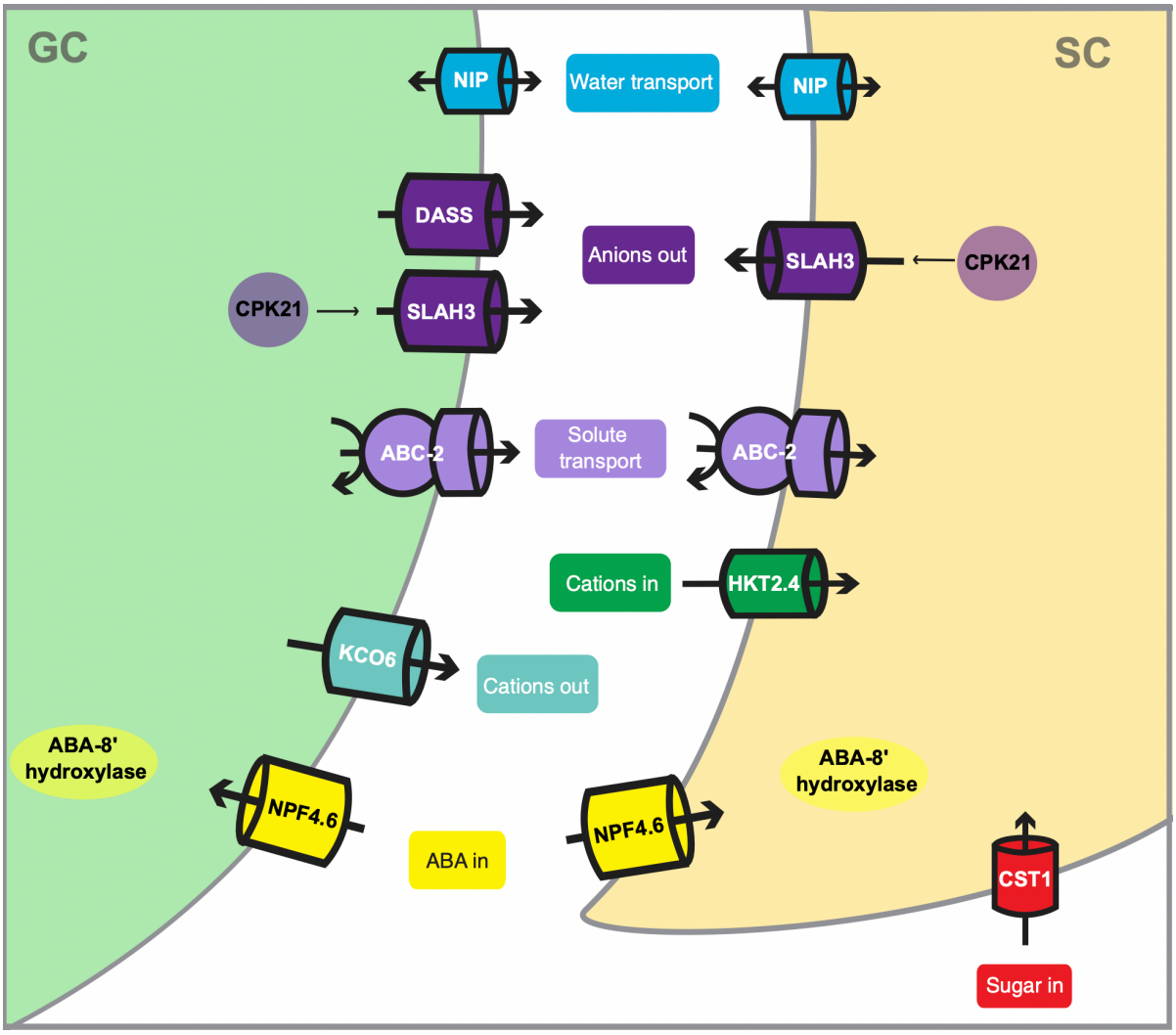


Figure 2.64 - Hypothetical localization and function of genes identified in the RNA-seq which mutants displayed impaired stomatal function. NPF4.6/NRT1.2 (BdiBd21-3.1G0505500) might be associated with the import of ABA in GC and/or SC to induce cellular responses required during stomatal closure. ABA-8' hydroxylase (BdiBd21-3.3G0503900) may be required for ABA catabolism and therefore a negative regulator of ABA-induced signalling preventing ABA-induced signalling. KCO6 (BdiBd21-3.2G0605300) might be a GC-specific potassium channel regulating the export of K^+ from GCs during stomatal closure, while HKT2.4 (BdiBd21-3.1G0462000) might be localized in SCs to regulate the import of K^+ to increase osmotic pressure in SCs during stomatal closure. The ABC-2 type transporter (BdiBd21-3.1G0848400) maybe be required for the regulation of solute export/import between GCs/GCs. The divalent anion-sodium symporter (DASS, BdiBd21-3.3G0359800) and SLAH3 (BdiBd21-3.2G0403400) may regulate anion transport in GCs and/or SCs. The calcium-dependent protein kinase CPK21 (BdiBd21-3.3G0075100) may act as a regulator of ion channels. The NIP-type aquaporin (BdiBd21-3.1G0591400) may be involved in the regulation of water transport within the stomatal complexes to regulate turgor exchange between GCs and SCs. Finally, CST1 (BdiBd21-3.2G0326500) might be a SC-specific sugar transporter and a positive regulator of stomatal opening, as previously described in maize stomatal complexes.

5. Results and discussion – Chapter III

BdPRX76/BdPOX* limits stomatal size to maintain water use efficient gas exchange by regulating prickle hair cell size in *Brachypodium distachyon

5.1 Introduction

From the reverse genetics screen to identify candidate genes involved in the regulation of form and function of grass stomata in *Brachypodium distachyon*, I identified *BdPRX76/BdPOX*, a class III peroxidase (*PRX*), which mutant lines NaN1528 and NaN1508 displayed lower iWUE and higher ambient-adapted g_{sw}. From these initial phenotyping experiments I also observed shorter stomata in NaN1508 than in WT.

Class III peroxidases (PRXs) are secreted peroxidases found in plants which contain many isozymes that allow PRXs to play different functions and act in different cell-types and tissues (Shigeto and Tsutsumi 2016). PRXs are involved in different biological processes such as auxin metabolism, lignification, cell-wall crosslinking of phenolic compounds and modulation of reactive oxygen species (ROS) levels (Shigeto and Tsutsumi 2016; Cosio and Dunand 2009; Francoz et al. 2015). PRXs can display two reaction cycles (Passardi et al. 2004). The hydroxylic cycle generates ROS while the peroxidative cycle can oxidize various substrates (Passardi et al. 2005). The peroxidative cycle is involved in three different processes: auxin catabolism, polymerization/crosslinking of cell wall components and NAD(P)H oxidation that forms superoxide, which is then converted either spontaneously or by superoxide dismutase to H_2O_2 and O_2 (Passardi et al. 2005). Therefore, PRXs are bifunctional enzymes that can either oxidize different substrates in the presence of H_2O_2 or produce ROS (Passardi et al. 2004; Passardi et al. 2005), which allows them to play vital roles in both plant development and stress responses (Francoz et al. 2015; Shigeto and Tsutsumi 2016). One of the peculiarities of PRXs is their involvement in both inducing cell elongation but also restricting growth (Francoz et al. 2015). They can promote cell elongation by locally generating ROS or regulating local H_2O_2 concentrations. On the other hand, they can increase cell wall stiffness and limit elongation by directly polymerizing/cross-linking several phenolic compounds in the cell wall (e.g., lignin, ferulates or glycoproteins) or by indirectly regulating H_2O_2 which can also be a substrate for other cell-wall modifying enzymes such as laccases (Francoz et al. 2015).

Genome-wide identification of the class III peroxidase family has been reported in several species such as *Arabidopsis thaliana* (Tognolli et al. 2002), *Oryza sativa* (Passardi et al. 2004), *Betula*

pendula (Cai et al. 2021), *Solanum tuberosum* (Yang et al. 2020) and also in *B. distachyon* (Zhu et al. 2019) .

A total of 151 *PRXs* genes has been identified in *B. distachyon* (Zhu et al. 2019), which is a higher number of genes than in *A. thaliana* (73), *O. sativa* (138) or *S. tuberosum* (102) (Tognolli et al. 2002; Filippo Passardi et al. 2004; Yang et al. 2020). Furthermore, a phylogenetic analysis of *PRXs* in *B. distachyon*, *A. thaliana* and *O. sativa* arranged *PRX* genes in 15 subfamilies and showed that *BdPRX76* belongs to the subfamily VIII which includes only *B. distachyon* and *O. sativa*, suggesting that only in grasses real orthologues of *BdPRX76* might occur (Zhu et al. 2019).

Still, the *Arabidopsis* closest homologue *AtPRX66* has been associated with lignification of the tracheary elements (Tokunaga et al. 2009). Lignin is a cell wall component found in grass stomata which provides mechanical strength (Shtein et al. 2017; Hatfield et al. 2016). Since stomatal movements are driven by turgor changes that induce severe changes in cell volume, this requires strong and flexible cell walls (Spiegelhalder and Raissig 2021). Therefore, defects in the cell wall composition of stomata may result in impaired stomatal function.

Since *BdPRX76/BdPOX* was one of the significantly differently expressed genes in *bdmute*, which lack SCs, display affected GC dumbbell-shape and impaired stomatal movements, I hypothesized that *BdPRX76/BdPOX* could be involved in the lignification of stomatal cell walls for optimal stomatal function.

5.2 Material and Methods

5.2.1 Plant material and growth conditions

bdpox mutants were selected from the collection of NaN mutant lines. NaN1508 is a knockout mutant containing a heterozygous early STOP mutation (Gag/Tag translating into E44*) in the early first exon of the gene. A homozygous-segregant (NaN1508^{bdpox}, further referred as *bdpox-1*) and a WT-like segregant (NaN1508^{BdPOX}) were selected by genotyping using priTN88/priTN99 by a master student Leonie Redt. NaN1508^{BdPOX} and *bdpox-1* originated from the same mutant original line NaN1508, and so share the same mutational background but differ in the occurrence of the mutation in *BdPOX*. Thus, I used NaN1508^{BdPOX} for the further phenotyping experiments as a WT-like control in addition to WT (Bd21-3). NaN1528 contains a missense mutation (Gca/Tca) resulting in the substitution of an alanine (A) to a serine (S) at the position 197 (A197S) in the active and heme-binding sites of BdPOX and was used as a second mutant allele and referred *bdpox-2* (Fig. 3.1A).

I sterilized seeds with sterilization solution (supplementary table 1) for 15 minutes, washed them four times in sterile deionized water and stratified them on MS plates (½ MS (Caisson Labs), 1% Agar (w/v), pH 5.7) at 4°C for 2 days in darkness. Then, I transferred the plates to a growth chamber with 16h light:8h dark cycle (110 μmol m^{-2} s^{-1}) and temperature of 25°C or transferred to soil. When transferred to soil, plants grew in a glasshouse with 18h light:6h dark cycle (200-400 μmol m^{-2} s^{-1}; average diurnal temperature = 28°C, average nocturnal temperature = 25°C), as described in the previous chapters.

5.2.2 Cloning of reporter lines

I generated reporter and overexpression constructs using the Greengate cloning system (Lampropoulos et al. 2013). In short, 6 different entry modules: A) pGGA_specific promoter; B) pGGB_dummy or N-tag; C) pGGC_gene sequence or tag; D) pGGD_C-tag; E) pGGE_terminator and F) pGGF_Resistance were digested and ligated with the destination vector Z) pGGZ004 during 50 cycles (5 min 37°C followed by 5 min 16°C) followed by 5 min at 50°C and 5 min at 80°C for heat inactivation of the enzymes (Suplementary table 5).

I amplified *BdPOX* sequences by Q5 PCR (supplementary table 3) from wild-type *Brachypodium distachyon* (Bd21-3) genomic DNA previously extracted using the standard CTAB DNA extraction protocol (supplementary table 2) and from cDNA previously synthesized with the RevertAid First Strand cDNA Synthesis Kit (Cat. No.: K1621) (ThermoFisher Scientific, Massachusetts, USA) from RNA extracted with the RNeasy Micro Kit (Cat. No.: 74004) (Qiagen, Hilden, Germany).

To clone *BdPOX* genomic (C module, pGGC_*BdPOX*), I mutagenized a BsaI/Eco31I site (GGTCTC) occurring in the second intron by amplifying *BdPOX* genomic sequence in two separate fragments using priTN99/priTN102 and priTN100/priTN101 (containing the bp substitution **A**GTCTC). Then I purified the two resulting PCR products using the NucleoSpin Gel and PCR Clean-up kit (Ref. 740609.50) (Macherey-Nagel, Düren, Germany), digested them at 37°C overnight using FastDigest Eco31I (Cat. No.: FD0294) (Thermo Fisher Scientific, Waltham, Massachusetts, USA) and ligated them overnight at 16°C using T4 ligase (Cat. No.: EL0014) (NEB, Ipswich, Massachusetts, USA). Afterwards, I ligated the fully reassembled *BdPOX* gene overnight at 16°C with previously digested (using FastDigest Eco31I, Thermo Fisher Scientific) and dephosphorylated (with Antarctic Phosphatase, NEB) pGGC000 entry vector to generate pGGC_*BdPOX*.

To clone *BdPOX* promoter (A module, pGGA_*BdPOXp*), I amplified the upstream adjacent region of the *BdPOX* transcriptional start site (3.5 kb) using priTN95/ priTN97. *BdPOX* promoter was digested and then ligated with previously digested and dephosphorylated entry vector pGGA000 to generate pGGA_*BdPOXp*.

To clone *BdMUTE* promoter (A module, pGGA_*BdMUTEp*), I amplified (Q5 PCR, supplementary table 3) *BdMUTE* promoter from pEX_BdMUTEp:CitYFP-BdMUTE (Raissig et al. 2017) in two fragments with priTN1/priTN28 and priTN2/priTN29 (containing a bp substitution GA**T**ACC to mutate a BsaI site). The two resulting PCR products were purified, digested and ligated as described for *BdPOX* gene. Fully reassembled *BdMUTE* promoter was ligated overnight at 16°C with previously digested (FastDigest Eco31I) and dephosphorylated pGGA000 entry vector (with Antarctic Phosphatase, NEB) to generate pGGA_*BdMUTEp*.

To clone ZmUbi promoter (A module, pGGA_*ZmUbip*), I amplified (Q5 PCR, supplementary table 3) *ZmUbi* promoter from pEX_BdMUTEprom_CitYFP-BdMUTE (Raissig et al. 2017) with priTN3/priTN4 and cloned it into pGGA000, as described for *BdPOX* promoter.

To clone *PvUBip2*-drive hygromycin resistance cassette (F module, pGGF_PvUbi2p:HygRCassette), I amplified (Q5 PCR, supplementary table 3) *PvUbip2*-driven hygromycin resistance cassette pTRANS_250d (Čermák et al. 2017) in two fragments, as described for *BdPOX*, using priTN11/priNT30 and priTN12/priTN29 (containing a bp substitution GATACC to mutate a BsaI site in the *PvUBi2* promoter sequence), and cloned into pGGF000 as described for *BdPOX* gene and *BdMUTE* promoter.

The entry modules pGGA000, pGGB003 (B-dummy), pGGC000, pGGD002(D-dummy), pGGE001 (rbcS terminator), and pGGF000 are described in (Lampropoulos et al. 2013). The entry modules pGGB_3xNLS and pGGC_eGFP were generously provided by Karin Schumacher's group. The pGGD009 (Linker-mCitrine) was generously provided by Jan Lohmann's group. The destination vector pGGZ0004 is described in Lupanga et al. 2020.

The previously described entry modules were used to generate the final constructs *BdPOXp:BdPOX:mCitrine*, *ZmUbip:BdPOX(CDS):mCitrine*, *BdMUTEp:BdPOX(CDS):mCitrine* and *BdPOXp:3xNLS:eGFP* were generated by Green Gate reactions (supplementary table 5).

I transformed all entry modules (pGGA_*BdPOXp*, pGGA_*BdMUTEp*, pGGA_*ZmUbip*, pGGC_*BdPOX*, pGGF_*PvUbi2p:HygRCassette*) in *E.coli* DH5α and selected positive colonies after Taq colony PCR (supplementary table 4), test digestion with specific restriction enzymes and sequenced (Mix2Seq Kit NightXpress, Eurofins Genomics, Ebersberg, Germany). Also, I transformed all final constructs (*BdPOXp:BdPOX:mCitrine*, *ZmUbip:BdPOX(CDS):mCitrine*, *BdMUTEp:BdPOX(CDS):mCitrine* and *BdPOXp:3xNLS:eGFP*) in *E.coli* DH5α, as described before, and then further transformed in *Agrobacterium* AGL1 (bacterial transformation protocols in appendix).

5.2.3 Generation and analysis of transgenic lines

Calli derived from *Brachypodium distachyon* (Bd21-3) and *bdpox-1* parental plants were transformed with the AGL1 *Agrobacterium tumefaciens* strain, selected based on hygromycin resistance, and regenerated according to standard protocols with modifications noted in http://jgi.doe.gov/our-science/science-programs/plant-genomics/brachypodium/.

Embryo isolation, calli induction and calli transformation steps were performed by Dr. Heike Lindner and Barbara Jesenofsky. In summary, young embryos were isolated and grown for three weeks in calli induction media (CIM, appendix). After three weeks of incubation in the dark at 28°C, crisp yellow calli were subcultured to fresh CIM media and incubated for another two weeks. Afterwards, calli were fragmented to 2-5mm pieces and subcultured in CIM for one week under the same conditions. For calli transformation, AGL1 containing the desired constructs were suspended in liquid CIM media (without phytagel) with freshly added 2,4-D (2.5μg/ml), Acetosyringone (200 μM, Sigma/Merck, Cat. No. D134406), and Synperonic PE/F68 (0.1%, Sigma/Merck, Cat. No. 81112). Calli were incubated for a minimum of 10 minutes in the AGL1 solution (OD600 = 0.6). Afterwards, the calli were dried on sterile filter paper and kept in the dark at room temperature for three days.

The following selection and regeneration steps were performed by Dr. Heike Lindner, Barbara Jesenofsky and myself. In summary, transformed calli were moved to selection media (appendix) and incubated for one week in darkness at 28°C (selection 1). Then, calli were moved to fresh selection media and incubated for two more weeks under the same conditions (selection 2). Subsequently, the calli were moved to callus regeneration media (CRM, appendix). Finally, calli were incubated under a 16:8h light:dark cycle (PAR= 70-80 μmol $m^{-2} s^{-1}$) at 28°C for 1 to 6 weeks for shoot formation. Platelets longer than 1 cm displaying minimum two leaves were moved to rooting media (appendix).

Finally, once roots have formed, I moved regenerant plants to soil. I refer to *Brachypodium* regenerants as T0s (which were briefly screened at the confocal microscope) and to the first segregating population as T1. I checked 5-10 independent T0 lines depending on how many independent lines were recovered upon regeneration. Afterwards, I confirmed the initially observed

expression pattern and performed further phenotyping studies in 2 to 3 independent T1 lines, from which their parental T0s were fertile and produced seeds.

5.2.4 Leaf-level gas exchange measurements

I performed light responses on the youngest fully expanded leaf of *Brachypodium distachyon* plants 3 weeks after sowing using a LI-6800 (Li-COR Biosciences Inc.) with LI-6800 leaf chamber conditions as follows: flow rate = 500 μmol s^{-1}; fan speed = 10000 rpm; leaf temperature (T_{leaf}) = 28° C; relative humidity (RH), 40 %; [CO_2] = 400 μmol mol^{-1}; 1000 – 100 – 1000 – 0 μmol PAR m^{-2} s^{-1} (20 min per light step). Gas exchange measurements were automatically logged every minute. I geometrically assessed the leaf area by measuring the leaf width and multiplying this value by the diameter of the leaf chamber 1.59 cm^2) and collected the same leaf section for the microscopic analysis. I performed the maximum stomatal conductance measurements (physiological $g_s$max) on the youngest fully expanded leaf of *Brachypodium distachyon* plants 3 weeks after sowing with the following LI-6800 conditions: flow rate = 500 μmol s^{-1}; fan speed = 10000 rpm; leaf temperature = 28°C; RH= 68-70 %; [CO_2] = 100 μmol mol^{-1}; 1500 μmol PAR m^{-2} s^{-1}. Gas exchange measurements were automatically logged every minute and I calculated $g_s$max as the average of the last steady state 5 minutes.

Finally, I performed steady state g_{sw} measurements as follows: flow rate = 500 μmol s^{-1}; fan speed = 10000 rpm; T_{leaf} = 28° C; RH = 40 %; [CO_2] = 400 μmol mol^{-1}; 1000 PAR m^{-2} s^{-1}, for 20 minutes. Measurements were automatically logged each minute. I assessed the leaf area and collected the same leaf section for further microscopic analysis.

5.2.5 Microscopy analysis of stomatal anatomy

For light microscopy imaging, I fixed the leaf tissue into 7:1 ethanol:acetic acid and incubated the samples at least overnight to clear the tissue. To prepare samples for imaging, I rinsed the tissue twice in water, mounted the samples on slides with Hoyer's medium and imaged the leaf abaxial side using a Leica DM5000B microscope. Generally, I imaged 4-6 (40x objective) and 3-5 (20x objective) fields of view per leaf of each individual. The confocal morphometrical analysis of

stomatal complexes in WT (Bd21-3) and *bdpox* mutants, was performed by Magdalena W. Slawinska as in chapter I. Briefly, leaves were incubated overnight in buffer solution (50mM KCl, 10mM MES-KOH) with fusicoccin (4 mM) in the light to promote full stomatal opening. Leaves were then stained with propidium iodide (10 μg/ml) and z-stacks were taken on the confocal microscope.

For the confocal imaging of reporter lines, I carefully detached the emerging 2nd (6-7 days after germination) or 3rd (11-12 days after germination) leaves and stained them with propidium iodide (10 μg/ml) for 5 min (or imaged the samples together with cell wall autofluorescence and not using propidium iodide), then mounted in water for imaging on a Leica SP8 confocal microscope. Finally, I performed all image analysis using Fiji.

5.2.6 Cell wall phenolics autofluorescence and lignin stainings

Regarding cell wall autofluorescence, I washed twice leaf sections previously fixed and cleared in 7:1 ethanol:acetic acid with 70 % ethanol and then transferred them to distilled water with 0.02 % (v/v) Tween for rehydration for 3 hours and then mounted samples in distilled water for imaging. I imaged the samples on a Leica SP8 confocal microscope. Excitation and detection settings as follows: Ex. 405 nm and Em. 490-550 nm. Laser power set to 10 %. I took z-stacks of 0.33 μm per step to image prickle hair cells (PHCs). For the analysis of PHCs, I used z-projections (sum sliced). Then, I drew a straight line from the base of the PHCs until the tip and obtained plot profiles of gray values. I corrected each measurement by obtaining the mean fluorescence of 9 background readings. To measure the autofluorescence of the PHC base outline, I drew a straight line on the PHC base outline and corrected the mean gray value of this line by obtaining the mean gray value of a straight line on the background below the PHC. Finally, I measured the PHC average fluorescence and calculated it as CTCF (corrected total cell fluorescence) = Integrated Density – (Area of selected cell X Mean fluorescence of 9 background readings).
Regarding stomatal autofluorescence, autofluorescence intensity was measured on the sum slices z-projections (developmental zone) and single images (mature stomata). GCs autofluorescence was calculated as CTCF (corrected total cell fluorescence) = Integrated Density – (Area of selected cell

X Mean fluorescence of background readings). Mean fluorescence of 3-4 background readings surrounding each stoma was obtained to calculate CTCF for each stoma.

Regarding basic fuchsin staining, I transferred small leaf fragments previously fixed and cleared in 7:1 ethanol:acetic acid to distilled water with 0.02 % (v/v) Tween for rehydration for 3 hours. I incubated the samples in 30 µl of 0.01 % Basic Fuchsin for 5 minutes and washed them twice with 30 µl of 50 % glycerol (v/v) for 5 min (2.5 min per wash step) and mounted the samples in 50 % glycerol (v/v). Samples were imaged under Ex. 561 nm and Em. 593/40nm. Laser power set to 1 %. I took z-stacks of 0.33 µm per step to image PHCs. For the analysis of PHCs, I used Z-projections (sum slices). I drew a straight line from the base of the PHCs until the tip and obtained plot profiles of gray values. I obtained the mean fluorescence of 9 background readings to correct each measurement.

Regarding fuchsin fluorescence in stomata, fluorescence intensity was measured from single images of mature stomata. GCs fuchsin fluorescence was calculated as CTCF (corrected total cell fluorescence) = Integrated Density – (Area of selected cell X Mean fluorescence of background readings). Mean fluorescence of 3-4 background readings surrounding each stoma was obtained to calculate CTCF for each stoma.

For safranin-o staining, I transferred small leaf fragments previously fixed and cleared in 7:1 ethanol acetic acid to distilled water for 2 hours. I incubated the samples in 50 µl of 0.2 % Safranin-O (v/v in 50 % EtOH) (Cat. No.: 84120-25G) (Merck, Darmstadt, Germany) for 10 min, washed with 50 % EtOH for 10 min and rehydrated them in distilled water for 15 min. Finally, I mounted the samples in distilled water and imaged under Ex. 488 and Em. 530-560 (Channel 1) and Ex. 561 and Em. 570- 600 (Channel 2). Laser power set to 1 %. I took z-stacks of 0.33 µm per step to image PHCs. I analysed the images obtained using the Fiji macro developed by Baldacci-Cresp et al. 2020 for calculating a ratio from a generated ratiometric image (C2/C1) (Baldacci-Cresp et al. 2020). Additionally, also analysed the z-projection (sum slices) images by drawing a straight line from the base of the PHCs until the tip and obtaining plot profiles of gray values independently for Channel 1 and Channel 2 (using the same defined ROI). Finally, I calculated the ratio between the plot profiles from Channel 2 and Channel 1 (C2/C1).

5.3 Results

5.3.1 *bdpox* mutants show higher stomatal conductance and lower intrinsic water use efficiency

In the previous chapter II, I observed that two NaN mutant lines containing mutations in one of the candidate genes significantly downregulated in *bdmute* (*BdPRX76/BdPOX*, BdiBd21-3.2G0467800) presented defects in iWUE and g_{sw} (Fig. 2.62). Furthermore, from additional observations during the screening, I detected longer stomatal occurring in NaN1508 (Fig. 2.62).

To further confirm the phenotypes observed during the screening in the previous chapter, I performed additional leaf-level gas exchange experiments comparing WT, NaN1508^{BdPOX} (WT-like), *bdpox-1* and *bdpox-2* (Fig. 3.1A). I measured leaf-level gas exchange (g_{sw}, A and iWUE) responses to fluctuating light intensity (1000-100-100-0 PAR) (Fig. 3.1B-D), as described in the previous chapters.

I observed overall higher g_{sw} throughout the different light steps in *bdpox* mutants (Fig. 3.1B), but I observed no significant variation in A, particularly at low light intensity (100 PAR) (Fig. 3.1C). Thus, this resulted in a significant decrease in iWUE ($=A/g_{sw}$) in *bdpox* mutants, particularly at 100 PAR (light-limited step) (Fig. 3.1D), corroborating my initial observations from the screening in chapter II.

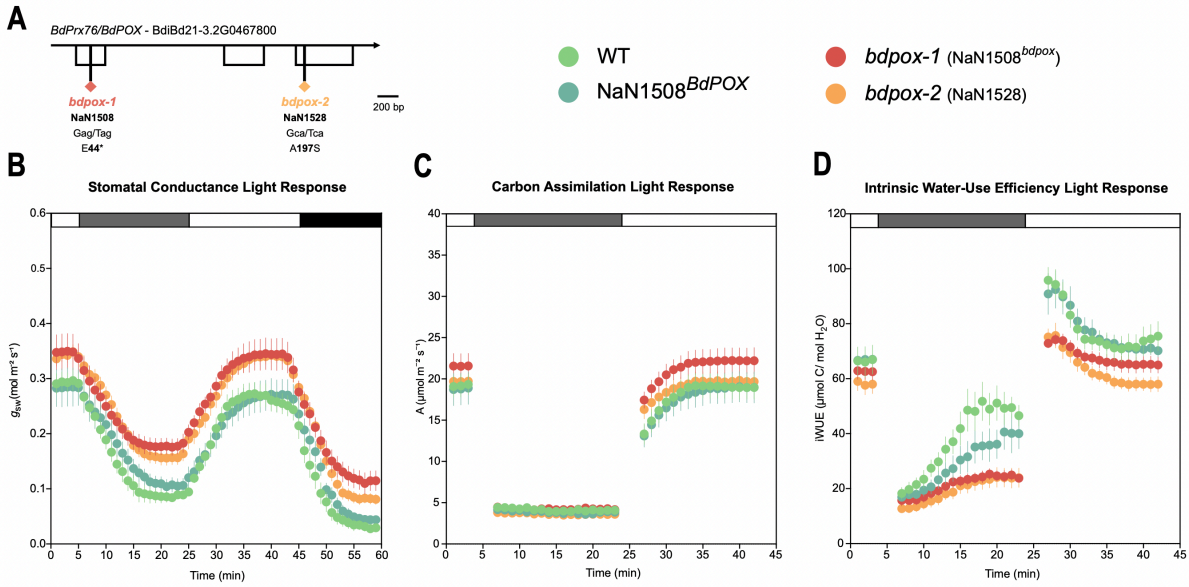


Figure 3.1 – Identification of *bdpox* mutants and leaf-level gas exchange. (A) *BdPRX76/BdPOX* gene model and localization of the mutations in the gene occurring in NaN1508 (*bdpox-1*) and NaN1528 (*bdpox-2*). **(B)** Stomatal conductance (g_{sw}) light responses (1000-100-1000-0 PAR) in WT, NaN1508^{BdPOX}, *bdpox-1* and *bdpox-2* (n=6 individuals per genotype). **(C)** Carbon

assimilation (*A*) light responses (1000-100-1000 PAR) in WT, NaN1508^{BdPOX}, *bdpox-1* and *bdpox-2* (n=6 individuals per genotype). **(D)** Intrinsic water-use efficiency (iWUE) light responses (1000-100-1000 PAR) in WT, NaN1508^{BdPOX}, *bdpox-1* and *bdpox-2* (n=6 individuals per genotype). Error bars represent SEM.

Regarding stomatal kinetics, I found no significant differences in the speed of stomatal opening and closure (i.e., rate constant k) between wild-type and *bdpox* mutant individuals (Fig. 3.2A-C).

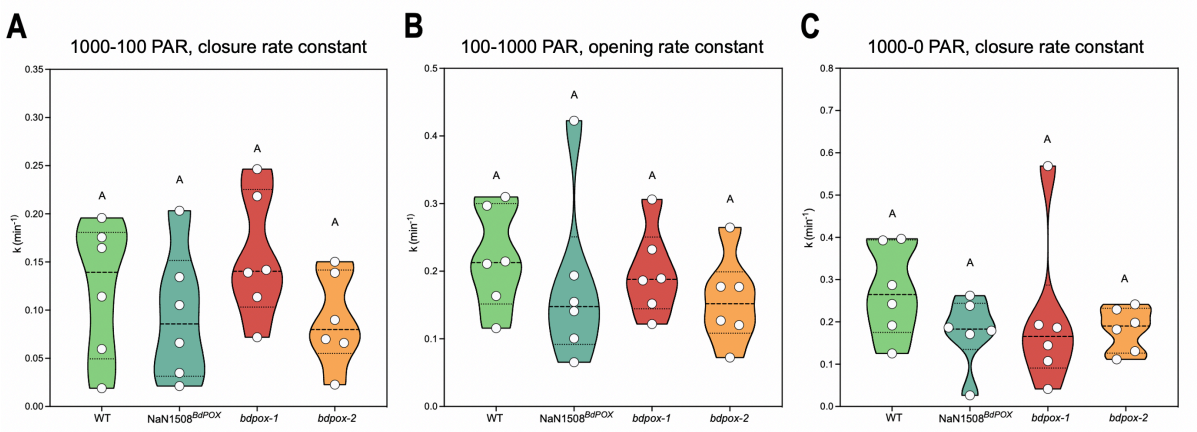


Figure 3.2 – Stomatal closure and opening speed (k) in WT, NaN1508^{BdPOX}, *bdpox-1* and *bdpox-2*. (A) Stomatal closure rate constant (1000-100 PAR) in WT, NaN1508^{BdPOX}, *bdpox-1* and *bdpox-2* (n=6 individuals per genotype). **(B)** Stomatal opening rate constant (100-1000 PAR) in WT, NaN1508^{BdPOX}, *bdpox-1* and *bdpox-2* (n=6 individuals per genotype). **(C)** Stomatal closure rate constant (1000-0 PAR) in WT, NaN1508^{BdPOX}, *bdpox-1* and *bdpox-2* (n=6 individuals per genotype). Different letters represent significant differences ($p<0.05$ obtained from Tukey's multiple comparisons following one-way ANOVA.

Overall, I confirmed the iWUE defect observed in *bdpox* mutants in the original screening and confirmed that the lower iWUE derives indeed from enhanced g_{sw}.

5.3.2 The negative correlation between stomatal size and density is disrupted in *bdpox*

Higher g_{sw} could be a result of: (i) longer stomata, (ii) increased stomatal numbers or (iii) defective stomatal signalling. In the original screening, I quantified the stomatal length (SL) of NaN1508, and verified that NaN1508 displayed longer stomata than WT. Therefore, I quantified stomatal anatomy in the samples where gas exchange was assessed (Fig. 3.1, 3.2) to confirm these observations. Indeed, *bdpox* mutants presented increased SL (Fig. 3.3A, F). However, to my surprise, I found no significant difference in stomatal density (SD) between wild-type and *bdpox*

mutants individuals (Fig. 3.3B). Since SD and SL are negatively correlated both intraspecifically and interspecifically (as shown and discussed in chapter I), this result suggested that this generally observed negative correlation was disrupted in *bdpox* (Fig. 3.3C).

Additionally, I measured SL in other leaf types: juvenile leaves (2nd leaves) and in the glumes (specialized/modified leaves found below the spikelet in the grass inflorescence) and verified that the defect in stomatal size occurred broadly in *bdpox* plants and was not exclusive to 3-week-old mature leaves (Fig. 3.3D, E).

Furthermore, together with Magdalena W. Slawinska, we characterized the stomatal pores in WT, NaN1508^{BdPOX} and *bdpox-1*. After treating the leaf samples with fusicoccin to trigger full stomatal opening, we verified that not just the GCs are longer, but also stomatal pores are longer in *bdpox* which results in larger stomatal pore areas (Fig. 3.4A-C).

To mathematically verify if the increase in g_{sw} could result from the longer stomata and larger stomatal pores, I calculated anatomical $g_s$max (theoretical $g_s$max based on gas diffusion physical constants and stomatal anatomical traits: SD and SL (Fig. 3.3A, B) and pore depth (based on stomatal width at the apex, which was decreased in *bdpox* mutants (Fig. 3.4F)), using the equation optimised for graminoid stomata in chapter I. Additionally, I performed LI-6800-based measurements of maximum stomatal conductance (physiological $g_s$max, maximal conductance when stomata reach their putative maximum stomatal pore areas in response to high relative humidity, high light intensity and lower CO_2 concentrations) and consistently observed increased gas exchange capacity (i.e., $g_s$max) in *bdpox* mutants in both approaches (Fig. 3.4D, E).

Overall, this supported a causal relationship between the anatomical defects and higher gas exchange in *bdpox*.

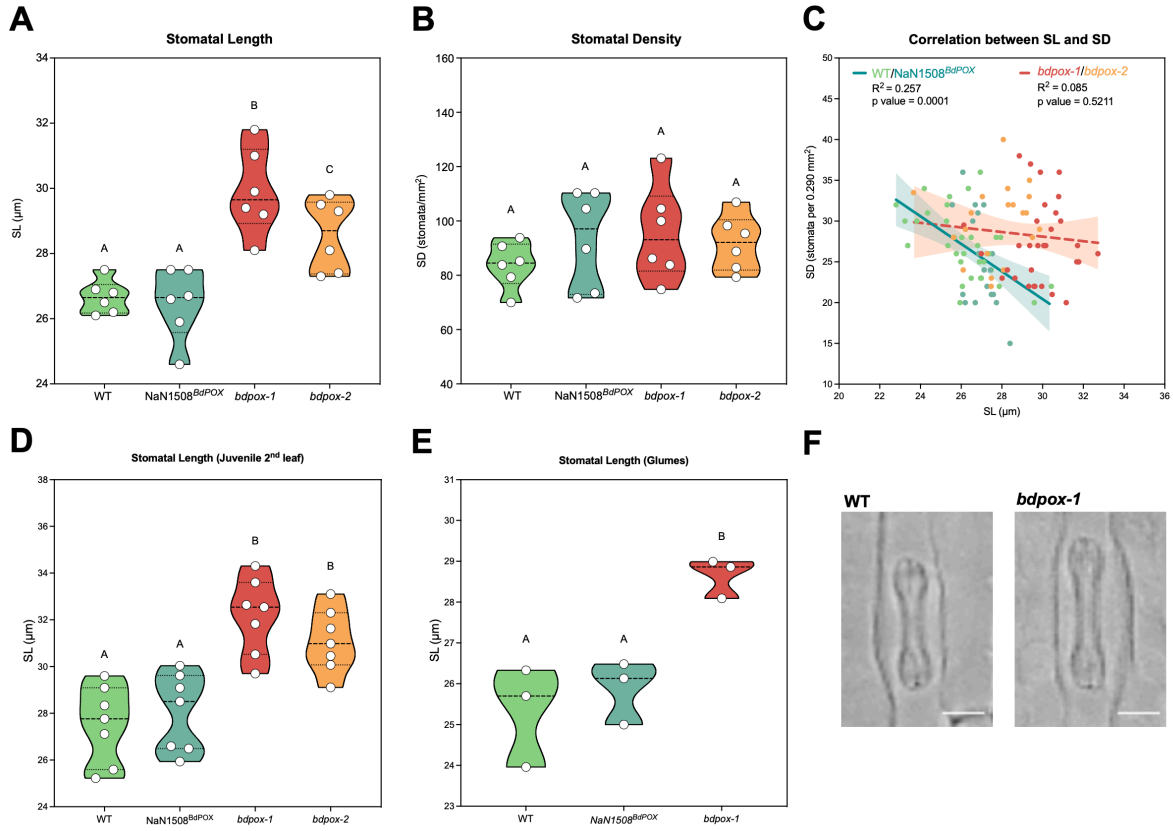


Figure 3.3 – Stomatal anatomical traits in WT, NaN1508^{BdPOX}, *bdpox-1* and *bdpox-2*. (A) Stomatal length (SL) in WT, NaN1508^{BdPOX}, *bdpox-1* and *bdpox-2* (n=6 individuals per genotype, 193-287 stomata per genotype). **(B)** Stomatal density (SD) in WT, NaN1508^{BdPOX}, *bdpox-1* and *bdpox-2* (n=6 individuals per genotype, 548-619 stomata counted per genotype). **(C)** Correlation between SL and SD in WT/NaN1508^{BdPOX} and *bdpox* mutants (n=33-34 individuals per genotype, each dot represents the average anatomical traits of one individual). **(D)** Stomatal length (SL) in 2nd leaves (juvenile leaves) of WT, NaN1508^{BdPOX}, *bdpox-1* and *bdpox-2* (n=7 individuals per genotype, n=169-272 stomata per genotype). **(E)** Stomatal length (SL) in the glumes of WT, NaN1508^{BdPOX}and *bdpox-1* (n=3 individuals per genotype, n=246-296 stomata per genotype). (F) Stomata in WT and *bdpox-1* plants. Scale bar, 10 µm.

5.3.3 Cell size defects in *bdpox* are not exclusive to stomata but also found in prickle hair cells

To verify if stomatal size was the only cell size defect in the epidermis of *bdpox* mutants, I measured the length of the other two dominant cellular features in the leaf epidermis of *B. distachyon*: pavement cells (PCs) and prickle hair cells (PHCs) (Fig. 3.5A).

While I did not observe any differences in the length of PCs among genotypes (Fig. 3.5B), I observed a decrease in the length of the base of PHCs in *bdpox* mutants (Fig. 3.5C).

bdpox mutants seemed to present opposite cell size phenotypes: longer stomata and smaller PHCs. Therefore, I hypothesized that *BdPOX* could be involved in the coordination of cell size across epidermal cell-types.

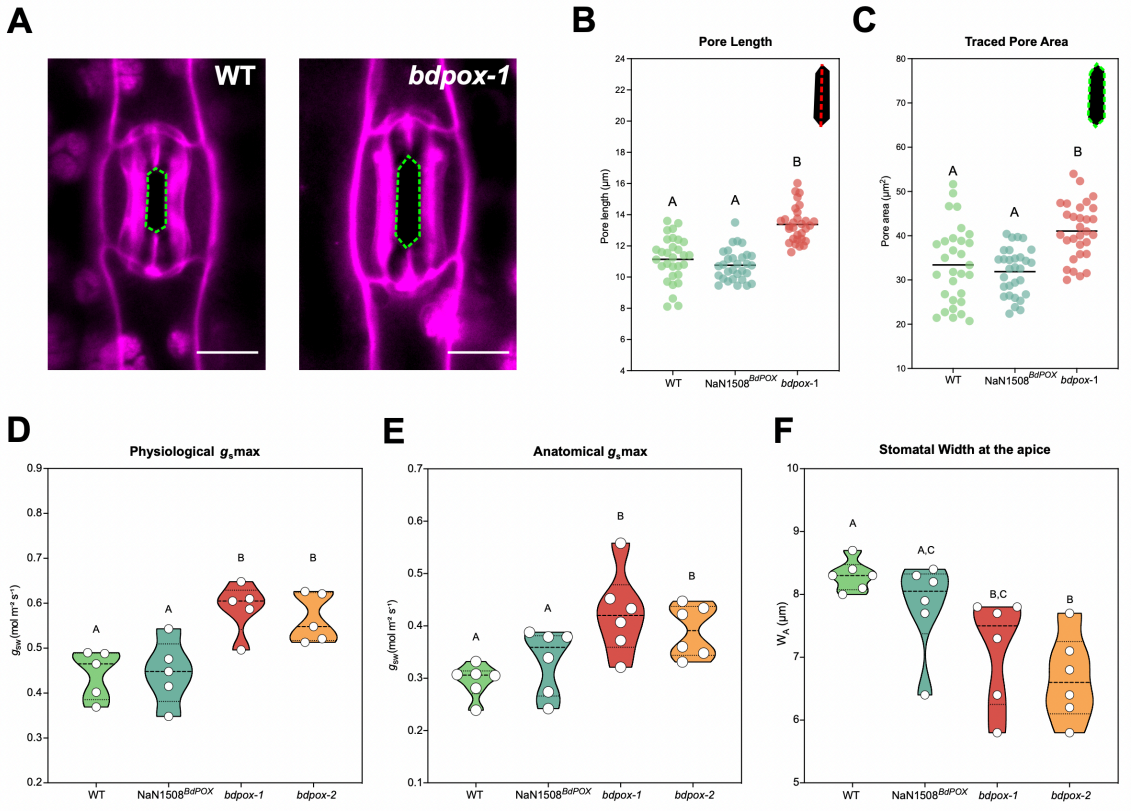


Figure 3.4 – Stomatal morphometry and maximum stomatal conductance in WT, NaN1508^{BdPOX} and *bdpox* mutants. **(A)** Fully open stomata in WT and *bdpox-1* leaves treated with fusicoccin. Scale bars, 10 µm. **(B)** Stomatal pore length in WT, NaN1508^{BdPOX} and *bdpox-1* mutants (n=30 stomata per genotype). **(B)** Stomatal pore area (hand-traced) in WT, NaN1508^{BdPOX} and *bdpox-1* mutants (n=30 stomata per genotype). **(D)** Physiological $g_s$max in WT, NaN1508^{BdPOX}, *bdpox-1* and *bdpox-2* (n=5 individuals per genotype). **(E)** Anatomical $g_s$max in WT, NaN1508^{BdPOX}, *bdpox-1* and *bdpox-2* (n=6 individuals per genotype). (F) Stomatal width at the apex in WT, NaN1508^{BdPOX}, *bdpox-1* and *bdpox-2* (n=6 individuals per genotype, 180 stomata counted per genotype).

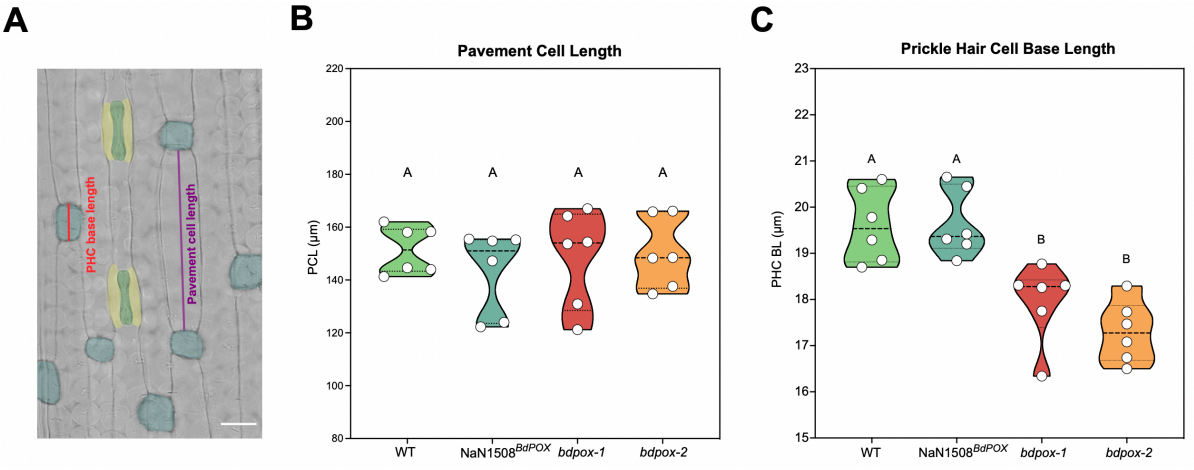


Figure 3.5 – Pavement cells and prickle hair cells in WT, NaN1508^{BdPOX}, *bdpox-1* and *bdpox-2*. (A) Visual representation of prickle hair cell (PHC) base length and pavement cell (PC) length. Base of PHCs represented in blue, stomatal GCs in green, SCs in yellow and PCs in grey. Scale bar, 20 µm. **(B)** Pavement cell length (PCL) in WT, NaN1508^{BdPOX}, *bdpox-1* and *bdpox-2* (n=6 individuals, 272-301 PCs per genotype). **(C)** Prickle hair cell base length (PHC BL) in WT, NaN1508^{BdPOX}, *bdpox-1* and *bdpox-2* (n=6 individuals, 656-691 PHCs per genotype). Different letters represent significant differences ($p<0.05$, obtained from Tukey's multiple comparisons following a One-way ANOVA).

5.3.4 *BdPOX* was specifically expressed in hair cells and its expression occurs before stomatal elongation

To investigate how *BdPOX* could regulate cell-size of both stomata and PHCs, I generated reporter lines to analyse the expression pattern of *BdPOX*.

Surprisingly, I observed that *BdPOX* was expressed exclusively in the hair cells (PHCs (Fig. 3.6A-G, S2, S3) and macrohairs (Fig. S1A)), but not in stomata.

Since *bdpox* mutants did not only contain defects in PHCs, but also significant defects in stomatal length and in gas exchange, I attempted to investigate how could *BdPOX* expression affect stomatal elongation by imaging *BdPOX* expression in coordination with stomatal development.

I imaged reporter lines together with cell wall autofluorescence (to observe the cell outlines and mCitrine signal without interference of propidium iodide stain which also emits fluorescence in the same range as mCitrine therefore making it difficult to observe the signal from BdPOX-mCitrine).

I observed that both *BdPOX* transcription (*BdPOXp:3xNLS-eGFP*) and translation (*BdPOXp:BdPOX-mCitrine*), which occurred specifically in PHCs, started before stomatal elongation and maturation (stage 5-6i of stomatal development) (Fig. 3.6D-G, S0).

Additionally, I used propidium iodide stain to image the leaf developmental zone in WT and described the stages of PHC development in relation to stomatal development (Fig. 3.6H). I verified that PHC bud formation and outgrowth initiation (stage 1 and 2 of PHC development) occurred during early stages of stomata formation (stage 4, when SCs were recruitment). Then, PHCs elongation and maturation (stage 3 and 4) coincide with *BdPOX* expression and occur before stomatal elongation.

Since *BdPOX* expression in PHCs occurs before stomatal elongation and since PHCs elongate and mature before stomatal elongation, I hypothesized that *BdPOX* could cell autonomously regulate PHC size and non-cell autonomously influence stomatal length.

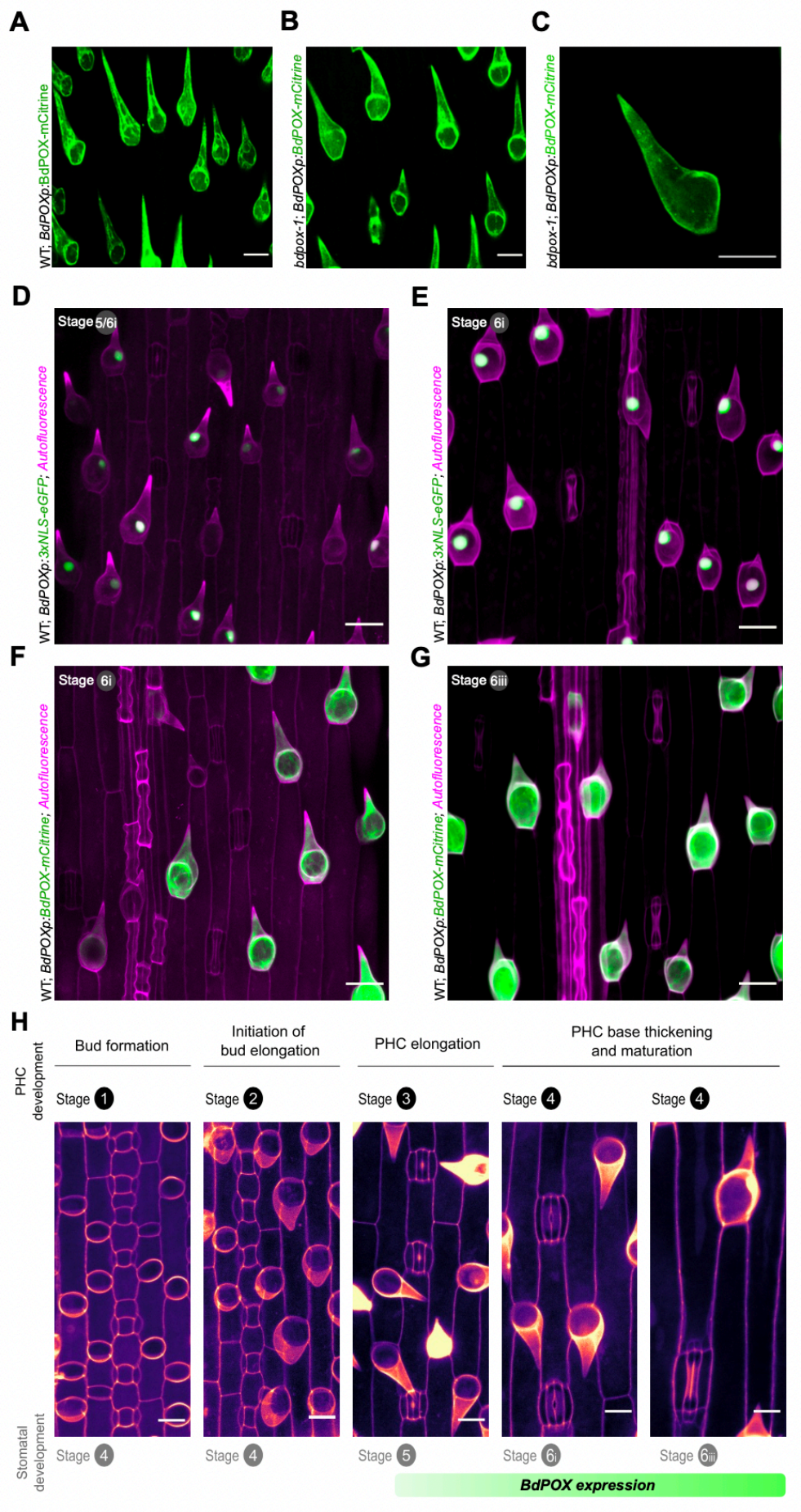

A
B
C
WT; BdPOXp:BdPOX-mCitrine
bdpox-1; BdPOXp:BdPOX-mCitrine
bdpox-1; BdPOXp:BdPOX-mCitrine
D
E
Stage 5/6i
Stage 6i
WT; BdPOXp:3xNLS-eGFP; Autofluorescence
WT; BdPOXp:3xNLS-eGFP; Autofluorescence
F
G
Stage 6i
Stage 6iii
WT; BdPOXp:BdPOX-mCitrine; Autofluorescence
WT; BdPOXp:BdPOX-mCitrine; Autofluorescence
H
PHC development
Bud formation
Initiation of bud elongation
PHC elongation
PHC base thickening and maturation
Stage 1
Stage 2
Stage 3
Stage 4
Stage 4
Stomatal development
Stage 4
Stage 4
Stage 5
Stage 6i
Stage 6iii
BdPOX expression

Figure 3.6 – *BdPOX* expression pattern (A) Translational reporter *BdPOXp:BdPOX-mCitrine* expression in WT in PHCs in mature epidermis. **(B,C)** Translational reporter *BdPOXp:BdPOX-mCitrine* expression in *bdpox-1* in PHCs in mature epidermis. **(D)** Transcriptional reporter *BdPOXp:3xNLS-eGFP* expression in the developing epidermis before stomatal elongation/maturation; cell wall autofluorescence indicates cell outlines (magenta); asterisks (*) indicate immature stomata (early stage 6i). **(E)** Transcriptional reporter *BdPOXp:3xNLS-eGFP* expression in the late developing epidermis; cell wall autofluorescence indicates cell outlines (magenta); plus symbols (+) indicate mature stomata (late stage 6iii). **(F)** Transcriptional reporter *BdPOXp:BdPOX-mCitrine* expression in the developing epidermis before stomatal elongation/maturation; cell wall autofluorescence indicates cell outlines (magenta); asterisks (*) indicate immature stomata (early stage 6i). **(G)** Transcriptional reporter *BdPOXp:BdPOX-mCitrine* expression in the late developing epidermis; cell wall autofluorescence indicates cell outlines (magenta); asterisks (*) indicate mature stomata (late stage 6iii). **(H)** Stages of PHC development on top in black (1-4) and stages of stomatal development below in grey (4-6iii). PHC elongation and maturation (stage 3-4) occur before stomatal elongation and maturation (stage 6).

5.3.5 Mutant complementation with *BdPOXp:BdPOX:mCitrine* rescued cell-size and gas exchange phenotypes

To confirm *BdPOX* role in determining cell size of stomata and PHCs, I complemented *bdpox-1* with *BdPOXp:BdPOX:mCitrine* and confirmed that *BdPOX* is indeed required for the proper regulation of cell size in PHCs and stomata.

Since *BdPOX* was expressed in PHCs, I performed a more detailed phenotyping of this cell-type by measuring PHC base length, base area and outgrowth (Fig. 3.7A-C).

I observed that all PHC size-related parameters which were reduced in *bdpox-1*, were rescued to wild-type levels in the three independent complementation lines (*BdPOXp:BdPOX:mCitrine* expressed in *bdpox-1*) (Fig. 3.7A-C). Interestingly, I also observed a significant positive correlation between PHC base area and outgrowth (Fig. 3.7D), suggesting that PHCs outgrowth requires larger PHC bases.

Regarding stomata, I verified that SL was successfully rescued to wild-type levels in the three complementation lines (Fig. 3.7E), while SD remained unaffected (Fig. S1B). Consequently, steady state g_{sw} was also decreased to wild-type levels in the complementation lines (Fig. 3.7F).

Based on these findings, *BdPOX* seems to play a cell autonomous role in positively regulating PHC size and inducing a non-cell autonomous effect to restrict stomatal elongation.

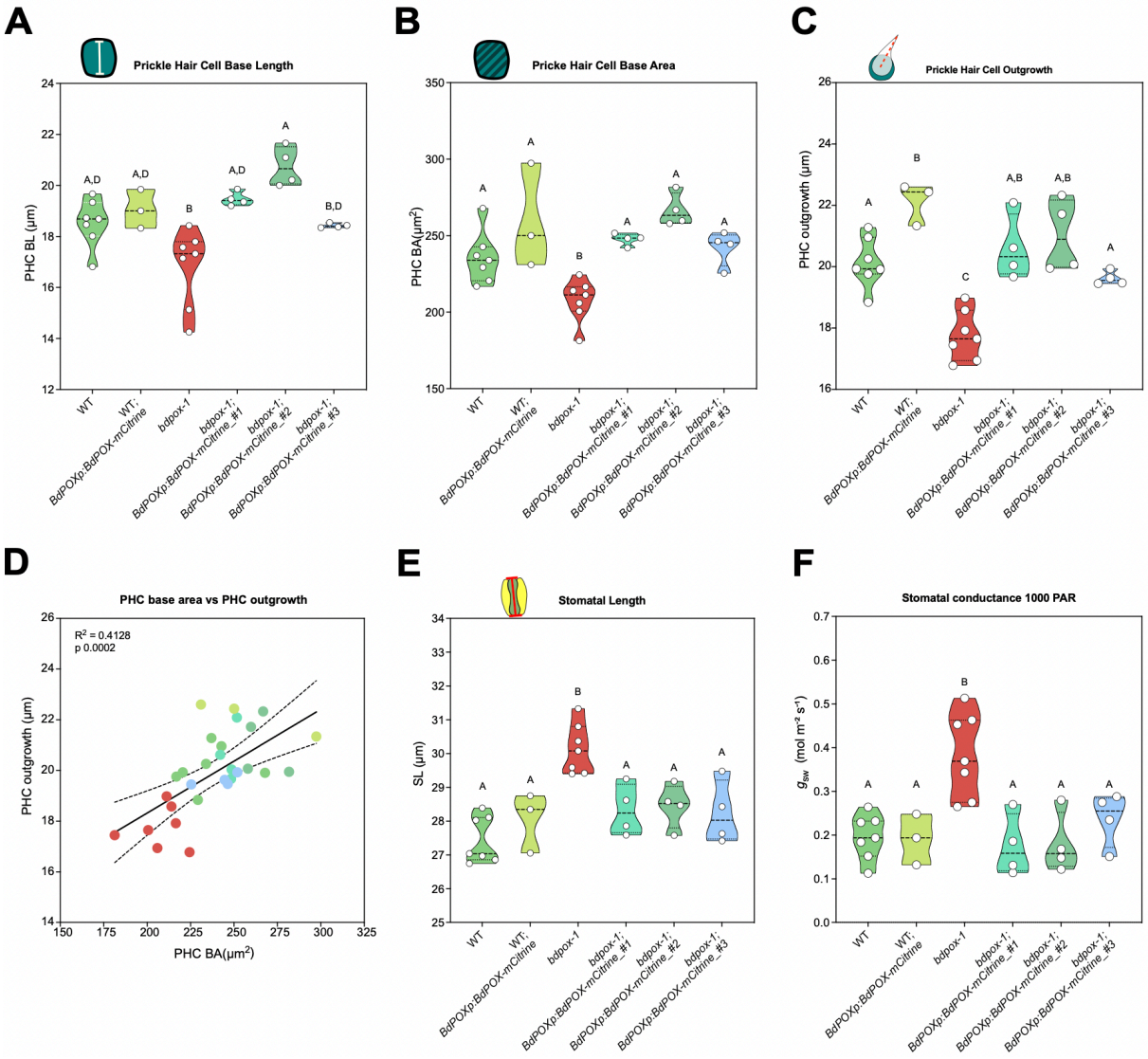


Figure 3.7 – *BdPOX* complementation experiments. (A) PHC base length (PHC BL) in WT, *BdPOXp:BdPOX-mCitrine* (in WT), *bdpox-1* and in three independent complementation lines (*bdpox-1; BdPOXp:BdPOX-mCitrine #1, #2, #3*) (n=3-7 individuals per genotype; each dot represents the average of one individual, n=160-340 PHCs per genotype/line) **(B)** PHC base area (PHC BA) in WT, *BdPOXp:BdPOX-mCitrine* (in WT), *bdpox-1* and in three independent complementation lines (*bdpox-1; BdPOXp:BdPOX-mCitrine #1, #2, #3*) (n=3-7 individuals per genotype; each dot represents the average of one individual, n=128-358 PHCs per genotype/line). **(C)** PHC outgrowth in WT, *BdPOXp:BdPOX-mCitrine* (in WT), *bdpox-1* and in three independent complementation lines (*bdpox-1; BdPOXp:BdPOX-mCitrine #1, #2, #3*) (n=3-7 individuals per genotype; each dot represents the average of one individual, n= 228-639 PHCs per genotype/line). (D) Correlation between PHC base area and PHC outgrowth (n=3-7 individuals per genotype; each dot presents the average traits of one individual). Colors represent the same genotypes as in the other subpanels. **(E)** Stomatal length (SL) in WT, *BdPOXp:BdPOX-mCitrine* (in WT), *bdpox-1* and in three independent complementation lines (*bdpox-1; BdPOXp:BdPOX-mCitrine #1, #2, #3*) (n=3-7 individuals per genotype; each dot represents the average of one individual, n=156-355 stomata per genotype/line). **(F)** Steady-state stomatal conductance (g_{sw}) at 1000 PAR in WT, *BdPOXp:BdPOX-mCitrine* (in WT), *bdpox-1* and in three independent complementation lines (*bdpox-1; BdPOXp:BdPOX-mCitrine #1, #2, #3*) (n=3-7 individuals per genotype/line). Different letters represent significant differences ($p<0.05$) obtained from one-way ANOVA followed by Tukey's multiple comparisons.

5.3.6 *BdPOX* positively regulates prickle hair cell outgrowth by cell wall phenolic modifications at the base of PHCs

Since class III peroxidases are involved in cell-wall phenolic modifications to modulate cell elongation processes and *BdPOX Arabidopsis* closest homologue *AtPRX66* participates in lignification processes (Tokunaga et al. 2009), I hypothesized that BdPOX cell-autonomously regulates PHC size by modifying cell wall properties through polymerization/cross-linking of phenolic compounds.

To test this hypothesis, I assessed UV-induced autofluorescence of total phenolics in the cell wall (Shtein et al. 2017; García-Plazaola et al. 2015; Donaldson 2020) and observed that PHCs in *bdpox-1* appeared shorter and displayed lower cell wall autofluorescence (Fig. 3.8A). To quantify these observations, I measured i) PHC outgrowth average fluorescence, ii) plot profiles, to measure PHC full length and evaluate autofluorescence intensity along a line from the basal section until the tip of the PHC and iii) PHC base outline autofluorescence, to evaluate the autofluorescence intensity at the interface with neighbouring pavement cells. Besides confirming that *bdpox-1* indeed have shorter PHCs than WT or *bdpox-1* complemented with *BdPOXp:BdPOX:mCitrine* (Fig. 3.8B,C), I verified that *bdpox-1* display a lower PHC autofluorescence, specifically at the basal section of the PHCs (approximately the initial 12 μm) than WT or complemented *bdpox-1* (Fig. 3.8B, D-F). Additionally, I also observed lower autofluorescence at the PHC base outline (Fig. 3.8G) and lower average PHCs outgrowth autofluorescence (Fig. 3.8H). Interestingly, I also verified that the average PHC autofluorescence at the initial 12 μm significantly correlated with PHC length (Fig. 3.8I).

Overall, these results suggest that BdPOX is involved in a phenolic enrichment at the basal section of PHCs to provide mechanical support for PHCs outgrowth.

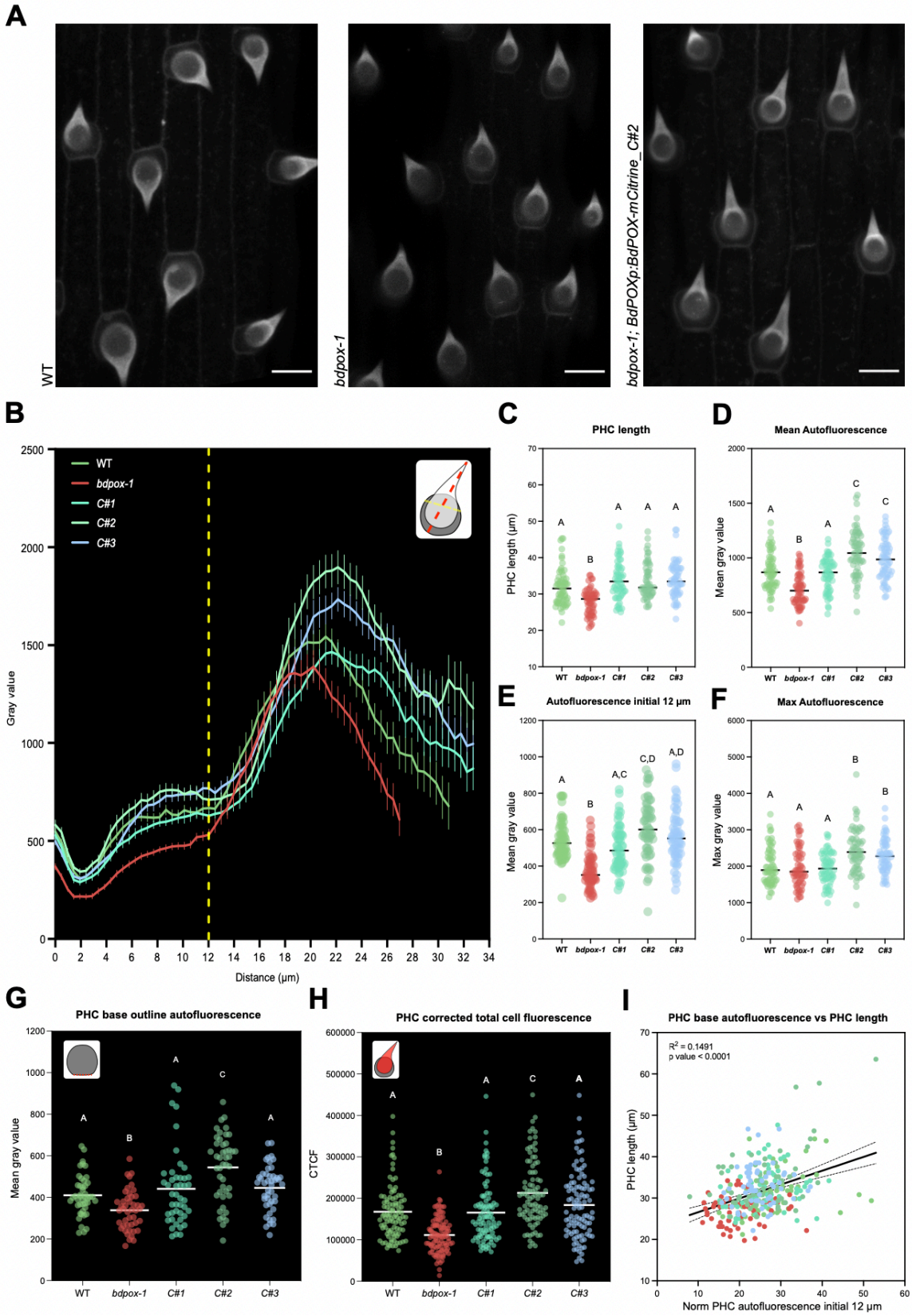


Figure 3.8 – PHC cell wall autofluorescence in WT, *bdpox-1* and complementation lines. (A) Cell wall autofluorescence of the mature epidermis in WT, *bdpox-1* and in *bdpox-1; BdPOXp:BdPOX-mCitrine #2*. Scale bar, 20 µm. **(B)** Average plot profiles of

cell wall autofluorescence in PHCs in WT, *bdpox-1* and three complementation lines (*bdpox-1; BdPOXp:BdPOX-mCitrine #1, #2, #3)* (n=60 PHCs per genotype). Error bars represent SEM. Scale bar, 5 μm. **(C)** PHC length obtained from the plot profile measurements in WT, *bdpox-1* and three complementation lines (*bdpox-1; BdPOXp:BdPOX-mCitrine #1, #2, #3)* (n=60 PHCs per genotype). **(D)** Mean autofluorescence obtained from the plot profile measurements in WT, *bdpox-1* and three complementation lines (*bdpox-1; BdPOXp:BdPOX-mCitrine #1, #2, #3)* (n=60 PHCs per genotype). **(E)** Average cell wall autofluorescence of the initial 12 micrometers of the PHCs in WT, *bdpox-1* and three complementation lines (*bdpox-1; BdPOXp:BdPOX-mCitrine #1, #2, #3)* (n=60 PHCs per genotype. **(F)** Maximum autofluorescence obtained from the plot profile measurements in WT, *bdpox-1* and three complementation lines (*bdpox-1; BdPOXp:BdPOX-mCitrine #1, #2, #3)* (n=60 PHCs per genotype). **(G)** Prickle hair cells base outline autofluorescence in WT, *bdpox-1* and three *bdpox-1; BdPOXp:BdPOX-mCitrine* complementation lines #1, #2 and #3 (n=45 PHCs per genotype/line). **(H)** Prickle hair cells outgrowth autofluorescence (corrected total cell fluorescence) in WT, *bdpox-1* and three *bdpox-1; BdPOXp:BdPOX-mCitrine* complementation lines #1, #2 and #3 (n=91-109 PHCs per genotype/line). **(I)** Correlation between normalized PHC autofluorescence from the initial 12 microns with PHC length. Different letters represent significant differences ($p<0.05$) obtained from one-way ANOVA followed by Tukey's multiple comparisons.

5.3.7 BdPOX plays a lignification or hydroxycinnamates crosslinking function in prickle hair cells

In grasses, an distinctive feature of cell walls is the significant content of phenolics compounds, specifically lignin and cross-linked hydroxycinnamates (ferulic acid and ρ-coumaric acid), which varies among cell types and tissues and which are catalysed by laccases and class III peroxidases (Vogel 2008; Coomey et al. 2020; Hatfield et al. 2016; Rancour et al. 2012; Mnich et al. 2020; Francoz et al. 2015). To confirm if the cell wall autofluorescence defect in *bdpox-1* was due to a deficiency in lignin/hydroxycinnamates, I performed different histochemical staining approaches.

The first stain I used was basic fuchsin, a standard lignin stain (Sexauer et al. 2021; Holzwart et al. 2018; Ursache et al. 2018) which also shown to have high affinity for hydroxycinnamates in the cell walls of *B. distachyon* (Kapp et al. 2015). When I simultaneously imaged cell wall phenolics autofluorescence and fuchsin-stained lignin/hydroxycinammates, I verified that basic fuchsin preferentially stained the lower section of PHCs while total phenolics autofluorescence was still relatively higher until the tip of the PHCs (Fig. 3.9A). Similarly to the results from PHC autofluorescence, I verified that *bdpox-1* mutants presented lower fuchsin fluorescence intensity at the basal section of PHCs (initial 12 μm starting from the PHC base outline) (Fig. 3.9B, C, S7) than WT or *bdpox-1* complemented with *BdPOXp:BdPOX:mCitrine*, indicating reduced lignin/hydroxycinnamates content.

Additionally, I performed safranin-o staining of lignified cell walls. Safranin-o is a basic azo dye that binds to the acidic lignin polymer and which emission spectrum depends on lignin content (Bond

et al. 2008). Increased red fluorescence is observed in safranin-o stained lignified cells, whereas non-lignified cell walls preferentially fluoresce in green (Bond et al. 2008). Therefore, a red/green ratiometric analysis allows for a semi-quantitative evaluation of cell wall lignification (Baldacci-Cresp et al. 2020) (Fig. S9). Safranin-o analysis indicated lower lignin content at the basal section PHCs in *bdpox-1* (initial 12 μm) (Fig. 3.10A-D), corroborating my findings from basic fuchsin stainings.

Regarding stomata, I found no differences in phenolics autofluorescence nor in fuchsin-stained lignin between WT and *bdpox-1* in mature stomata (Fig. S8A-B). Still, when looking at developing stomata, we can observe that cell wall autofluorescence increased in GCs during stomatal elongation/maturation (Fig. S8C). This increased seems to start earlier in *bdpox-1*, which may be related with an enhanced stomatal elongation occurring in *bdpox* mutants that results in longer stomata (Fig. S8C).

Overall, combining the cell wall autofluorescence results with the analysis of two independent histochemical lignin stainings, I suggest that BdPOX participates in lignification/hydroxycinnamates cross-linking at the base of PHCs to support PHC elongation and maturation, and consequently impairing stomatal elongation.

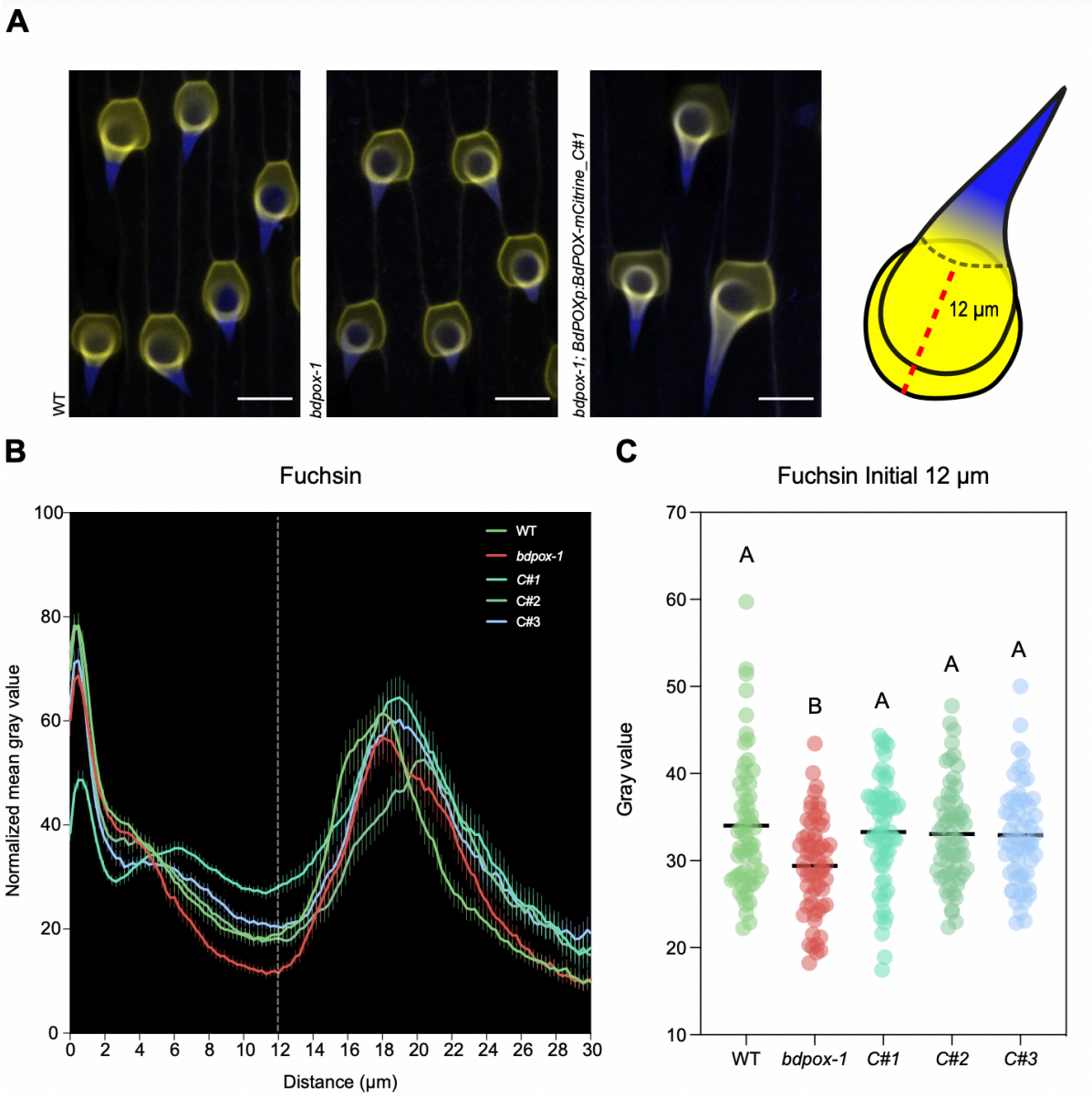


Figure 3.9 – Basic-fuchsin lignin staining in WT, *bdpox-1* and complementation lines. (A) Simultaneous imaging of phenolics autofluorescence (blue) and fuchsin-stained lignin (yellow) in WT, *bdpox-1* and *bdpox-1*; *BdPOXp:BdPOX-mCitrine #1.* Scale bars, 10 µm. **(B)** Average plot profiles of fuchsin-stained lignin in PHCs of WT, *bdpox-1* and three complementation lines (*bdpox-1; BdPOXp:BdPOX-mCitrine #1, #2, #3)* (n=60 PHCs per genotype). Error bars represent SEM. **(C)** Fuchsin stain fluorescence in the initial 12 µm of the PHCs in WT, *bdpox-1* and three complementation lines (*bdpox-1; BdPOXp:BdPOX-mCitrine #1, #2, #3)* (n=60 PHCs per genotype). Different letters represent significant differences ($p<0.05$) from one-way ANOVA followed by Tukey's multiple comparisons.

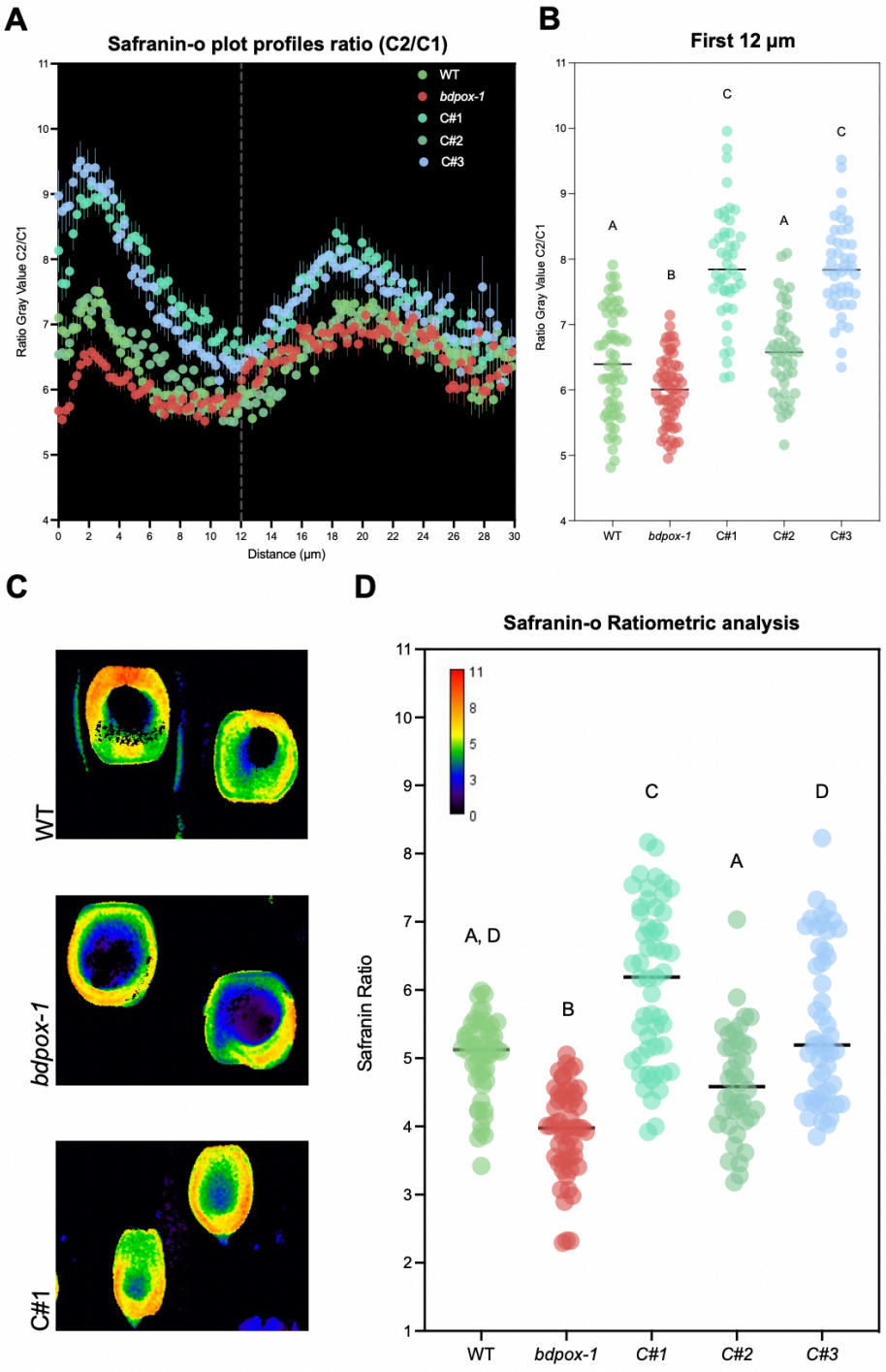


Figure 3.10 – Safranin-o lignin staining in WT, *bdpox-1* and complementation lines. (A) Average safranin-o ratio plot profiles in WT, *bdpox-1* and *bdpox-1*; *BdPOXp:BdPOX:mCitrine* lines #1, #2 and #3 (n=45 PHCs per genotype/line) **(B)** Safranin-o ratio the initial 12 µm of the PHCs in WT, *bdpox-1* and three complementation lines (*bdpox-1; BdPOXp:BdPOX-mCitrine #1, #2, #3)* (n=45 PHCs per genotype). **(C)** Ratiometric images of PHCs in WT, *bdpox-1* and C#1 (*bdpox-1; BdPOXp:BdPOX-mCitrine_#1).* **(D)** Safranin-o ratiometric mean in WT, *bdpox-1* and three *bdpox-1;BdPOXp:BdPOX-mCitrine* complementation lines #1, #2 and #3 (n = 40-53 PHCs per genotype/line). Different letters represent significant differences ($p<0.05$) from one-way ANOVA followed by Tukey's multiple comparisons.

5.3.8 *BdPOX* overexpression driven by maize ubiquitin promoter does not rescue phenotypes in *bdpox-1*

To further test *BdPOX* function, I overexpressed *BdPOX* under the constitutive maize ubiquitin promoter (*ZmUbip*). *ZmUbip:BdPOX-mCitrine* was indeed ubiquitously expressed (Fig. 3.11A, S6), although weakly expressed in the PHCs or GCs (Fig. 3.11A, S6). Curiously, a stronger mCitrine signal could be observed in SCs (Fig. 3.11A). Still, *BdPOX* overexpression (*ZmUbip:BdPOX-mCitrine*) in *bdpox-1* did not rescue gas exchange, stomatal or PHC size defects (Fig. 3.11B), suggesting that a cell-type specific expression is required for *BdPOX* function in coordinating stomata and PHC cell size, and subsequently gas exchange.

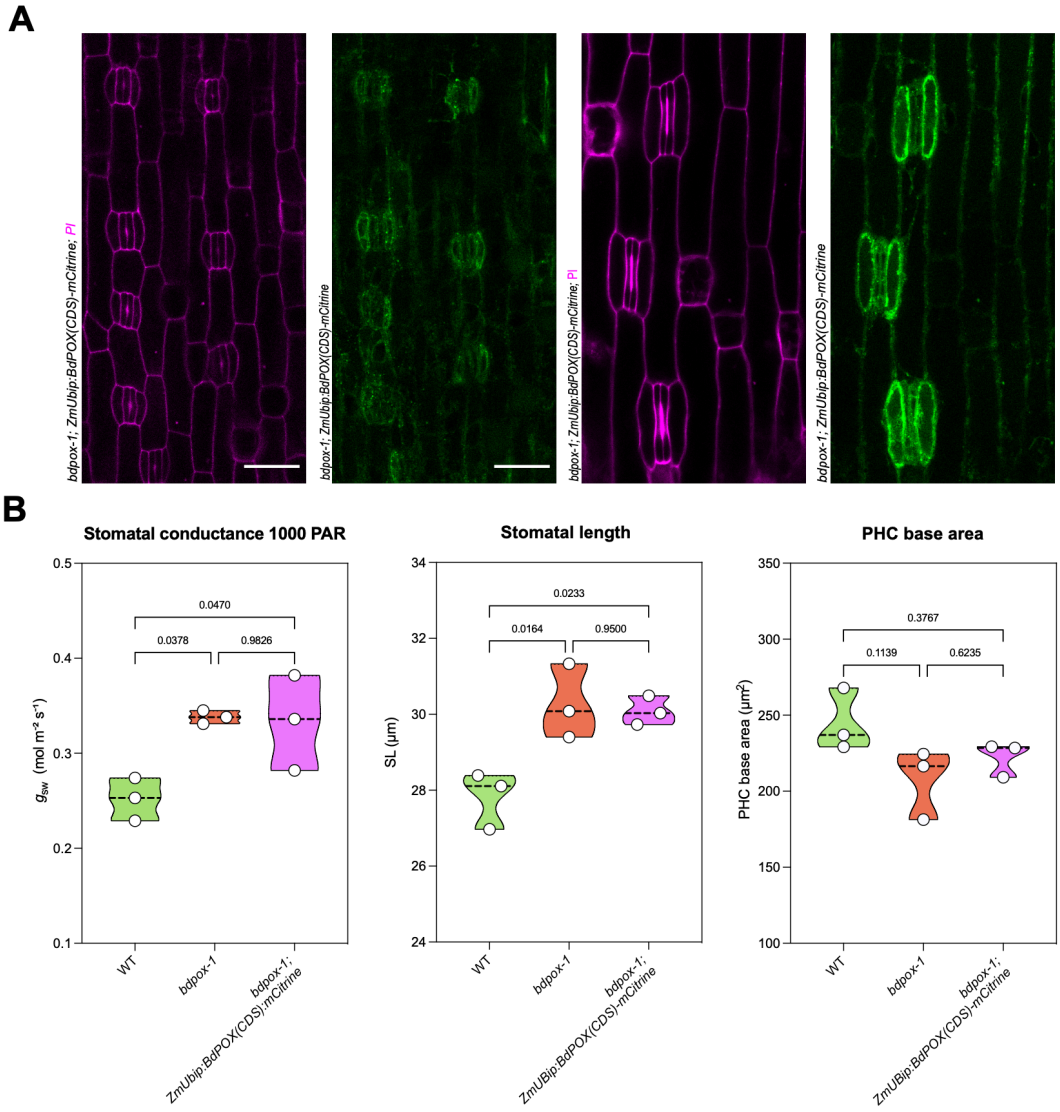


Figure 3.11 – Phenotyping of ubiquitin promoter-driven *BdPOX* overexpression (*ZmUBip:BdPOX(CDS)-mCitrine*). **(A)** *ZmUbip:BdPOX(CDS)-mCitrine* overexpression at the developmental stages of immature stomata and at the mature stages of stomatal development (PI stain in magenta and mCitrine signal in green). **(B)** Steady-state stomatal conductance at 1000 PAR (n=3

individuals per genotype), stomatal length (n= 3 individuals; 133-168 stomata per genotype) and prickle hair cell basal area (n=3 individuals, 129-261 PHCs per genotype) in WT, *bdpox-1* and *bdpox-1; ZmUbip:BdPOX(CDS)-mCitrine.* Significant differences represented by p values ($p<0.05$) obtained from One-way ANOVAs followed by Tukey's multiple comparisons.

5.3.9 *BdPOX* specific expression in the stomatal lineage rescues stomatal phenotype

Since *BdPOX* appears to be involved in phenolic modifications in the cell wall to increase rigidity at the base of PHCs to promote cell outgrowth (Fig. 3.8-10) and a cell-type specific expression seems to be required for *BdPOX* function in regulating cell size (Fig. 3.11), I hypothesized that specifically expressing *BdPOX* in the stomatal lineage before stomatal elongation/maturation steps in *bdpox-1* could increase the phenolic content in cell walls of the GCs, rigidify the cell walls and potentially arrest stomatal elongation. *BdMUTEp:BdPOX(CDS)-mCitrine* was successfully expressed in the GC lineage from stage 3 to 6i of stomatal development (Fig. 3.12A, S4, S5).

Furthermore, *BdPOX* expression driven by a stomatal-lineage specific promoter (*BdMUTEp:BdPOX(CDS)-mCitrine)* in *bdpox-1* indeed increased cell wall phenolic autofluorescence in the GCs and limited stomatal size (Fig. 3.12B, C). I also verified that, *BdMUTEp:BdPOX(CDS)-mCitrine* expression in WT seemed to slightly reduce stomatal length (Fig. 3.12C). Interestingly, PHC size defects remained unaltered (Fig. 3.12D) which can be explained by the fact that PHC size is determined before stomatal elongation. Therefore, modifications in stomatal elongation (stage 6) do not modify PHC size.

Furthermore, I observed aberrant cell divisions nearby the stomatal complexes when *BdMUTEp:BdPOX(CDS)-mCitrine* was expressed in *bdpox-1*, but not in WT (Fig. 3.13A, B).

Therefore, I speculate that GC lignification in *bdpox-1* which contains defective PHCs may cause an imbalance in cellular tension resulting in additional divisions. On the other hand, in WT background the lignin enriched PHCs may support the tissue-wide effect of the increased stomatal lignification.

Overall, *BdPOX* can modify phenolic cell wall content in different cell types to confer structural strength and rigidity to the cell wall and consequently modulates cell growth. Furthermore, I propose that stomatal and PHC are developmentally coordinated for optimal epidermal functionality and disturbing this coordination results in compensatory cell divisions.

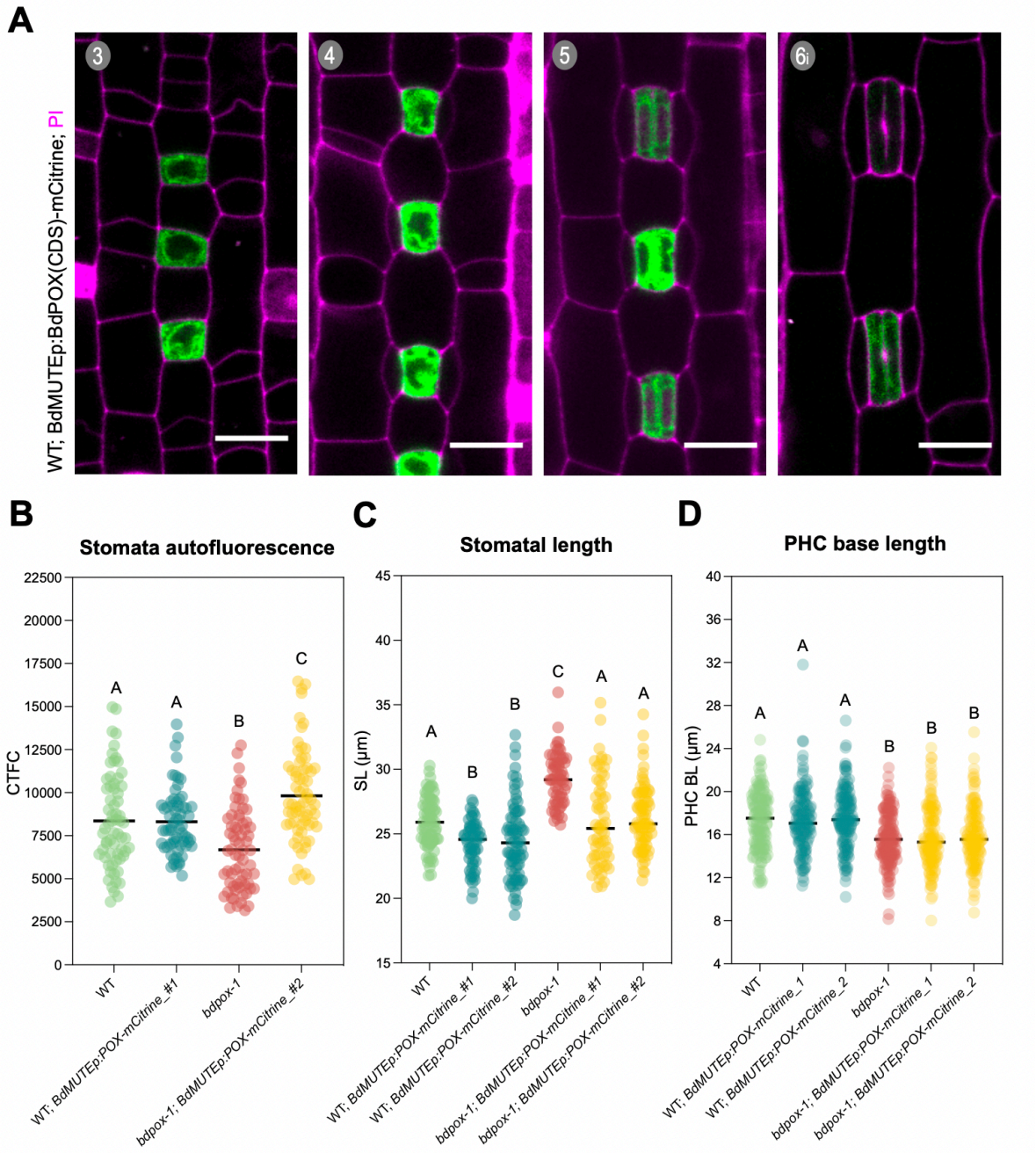


Figure 3.12 - Effect of *BdPOX* expression in stomatal lineage (*BdMUTEp:BdPOX(CDS)-mCitrine*) in GC autofluorescence and stomatal size. (A) *BdMUTEp:BdPOX(CDS)-mCitrine* expression in the developing GC lineage. *BdPOX(CDS)-mCitrine* expression in GMCs (stage 3), GMCs after SC recruitment (stage 4), early developing GCs (stage 5) and later developing GCs (early stage 6 i; from left to right). Scale bar, 20 µm. **(B)** Cell wall autofluorescence of GCs (corrected total cell fluorescence) in WT, *bdpox-1* and *BdMUTEp:BdPOX(CDS)-mCitrine* lines expressed in WT and *bdpox-1* (n=65-67 stomata per genotype). **(C)** Quantification of stomatal length (SL) in WT, *bdpox-1* and *BdMUTEp:BdPOX(CDS)-mCitrine* lines expressed in WT and *bdpox-1* (n=61-81 stomata per genotype). **(D)** Quantification of PHC base length in WT, *bdpox-1* and *BdMUTEp:BdPOX(CDS)-mCitrine* lines expressed in WT and *bdpox-1* (n=140-152 PHCs per genotype). Significant differences represented by different letters ($p<0.05$) obtained from One-way ANOVAs followed by Tukey's multiple comparisons.

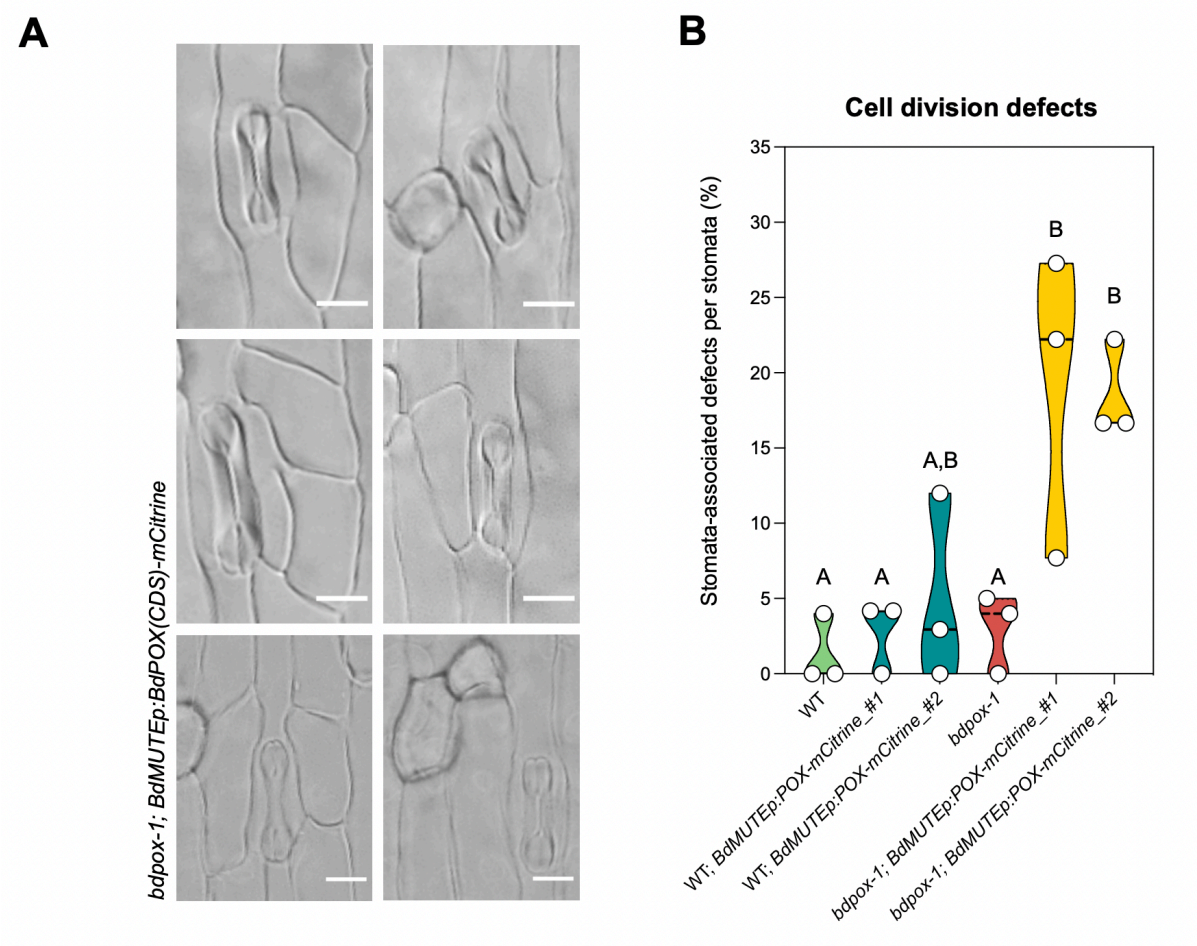


Figure 3.13 – Cell division defects in *BdMUTEp:BdPOX-mCitrine* expressed in *bdpox-1*. (A,B) Stomatal-associated epidermal cell division defects in WT, *bdpox-1* and *BdMUTEp:BdPOX(CDS)-mCitrine* expressed in WT and *bdpox-1* (n=3 individuals per genotype/line; 66-88 stomata per genotype/line). Scale bars, 10 μm. Different letters represent significant differences ($p<0.05$) obtained from one-way ANOVAs followed by Tukey's multiple comparisons.

5.3.10 Supplementary figures

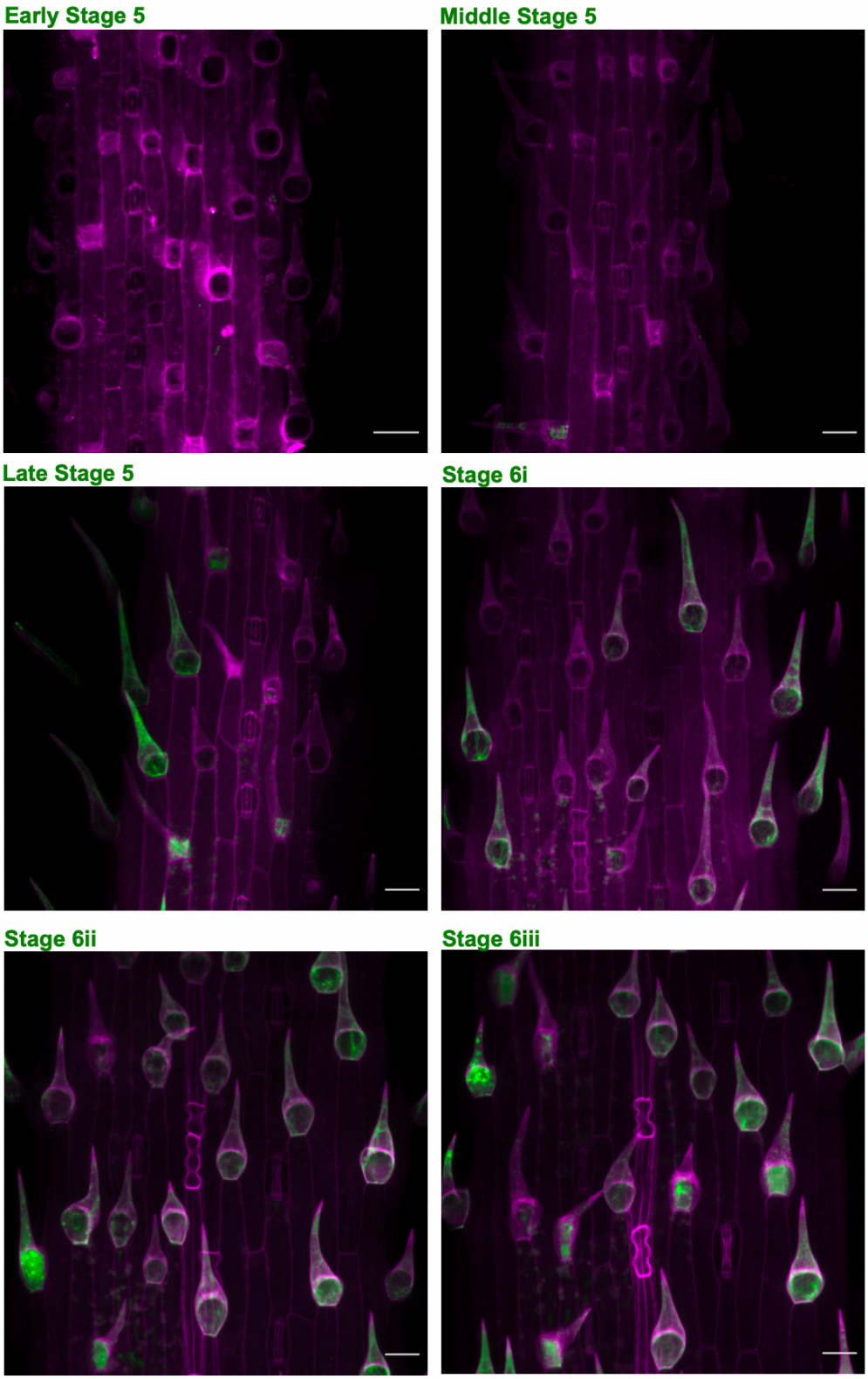


Figure S0 – Stages of *BdPOX* expression in relation with stomatal development. *BdPOX* expression can start to be observed in PHCs when stomata are in middle/late stage 5 of stomatal development (stages labelled in green). Scale bars 20 μm.

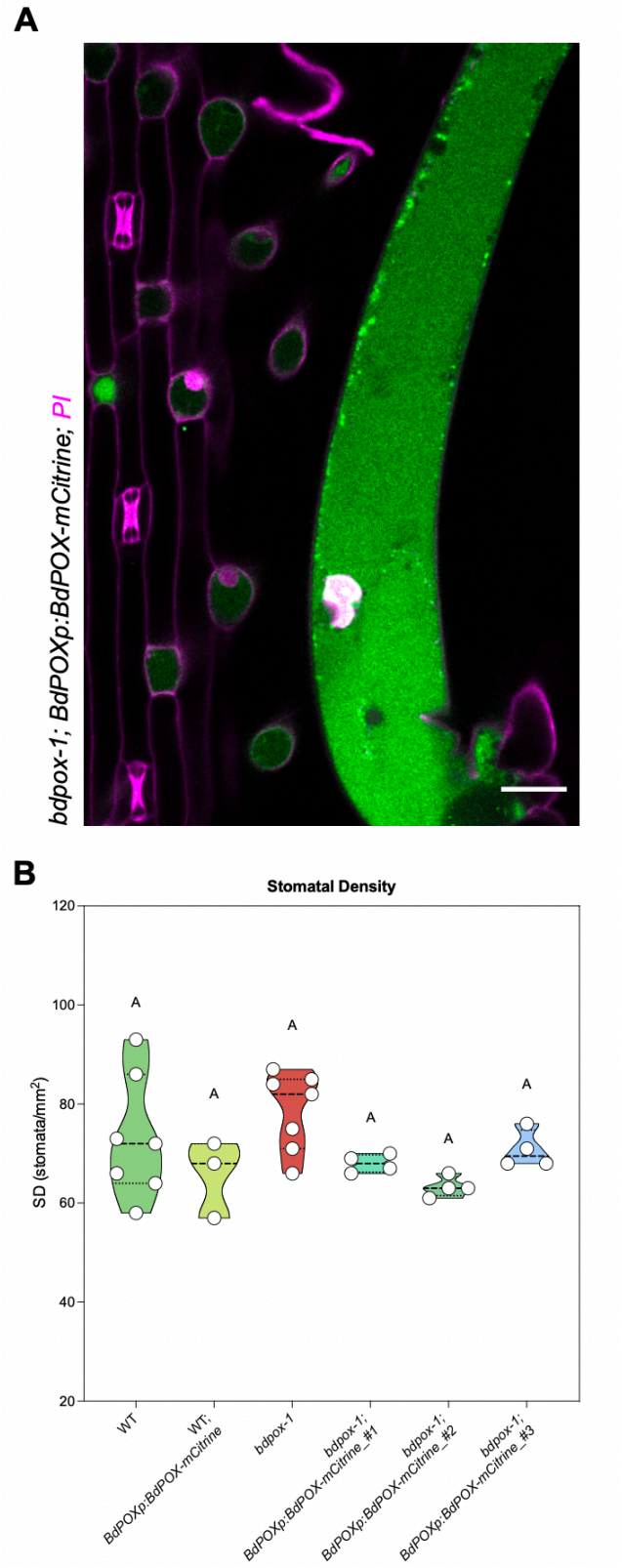


Figure S1 – *BdPOX* expression and stomatal density in complementation experiments. (A) Exclusive *BdPOX* expression in a PHCs and in a macrohair. Scale bar 20 μm. **(B)** Stomatal density (SD) in WT, *BdPOXp:BdPOX-mCitrine* (in WT), *bdpox-1* and in three complementation lines (*bdpox-1; BdPOXp:BdPOX-mCitrine* #1, #2, #3) (n=3-7 individuals per genotype; 228-639 stomata counted per genotype). Different letters present significant differences ($p<0.05$ from one-way ANOVA followed by Tukey's multiple comparisons.

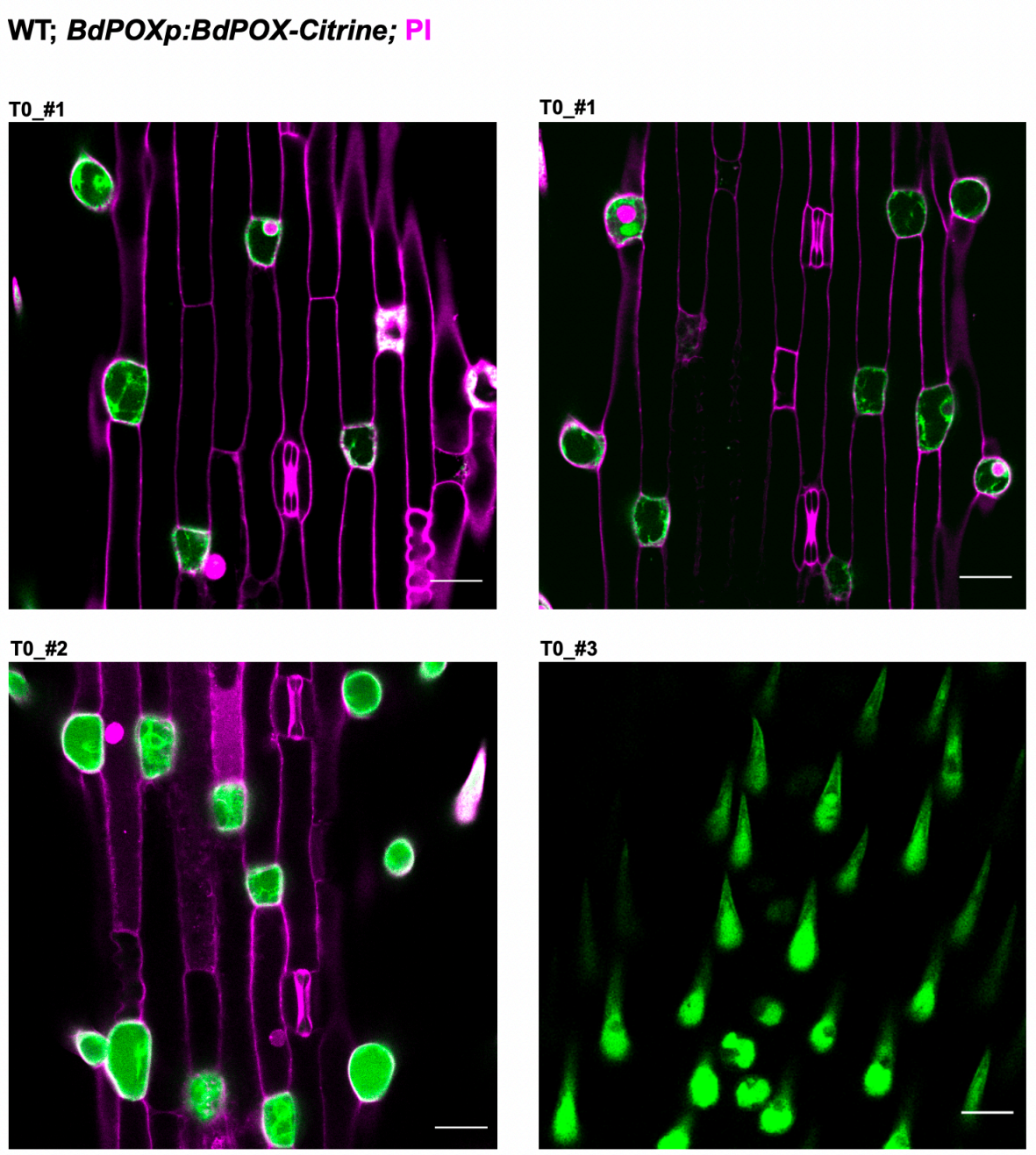


Figure S2 – Additional confocal imaging of three T0 reporter lines (*BdPOXp:BdPOX-mCitrine* in WT). BdPOX-mCitrine signal in green and propidium iodide (PI) in magenta. *BdPOX* expression can be observed exclusively in the PHCs. Scale bars 20 μm.

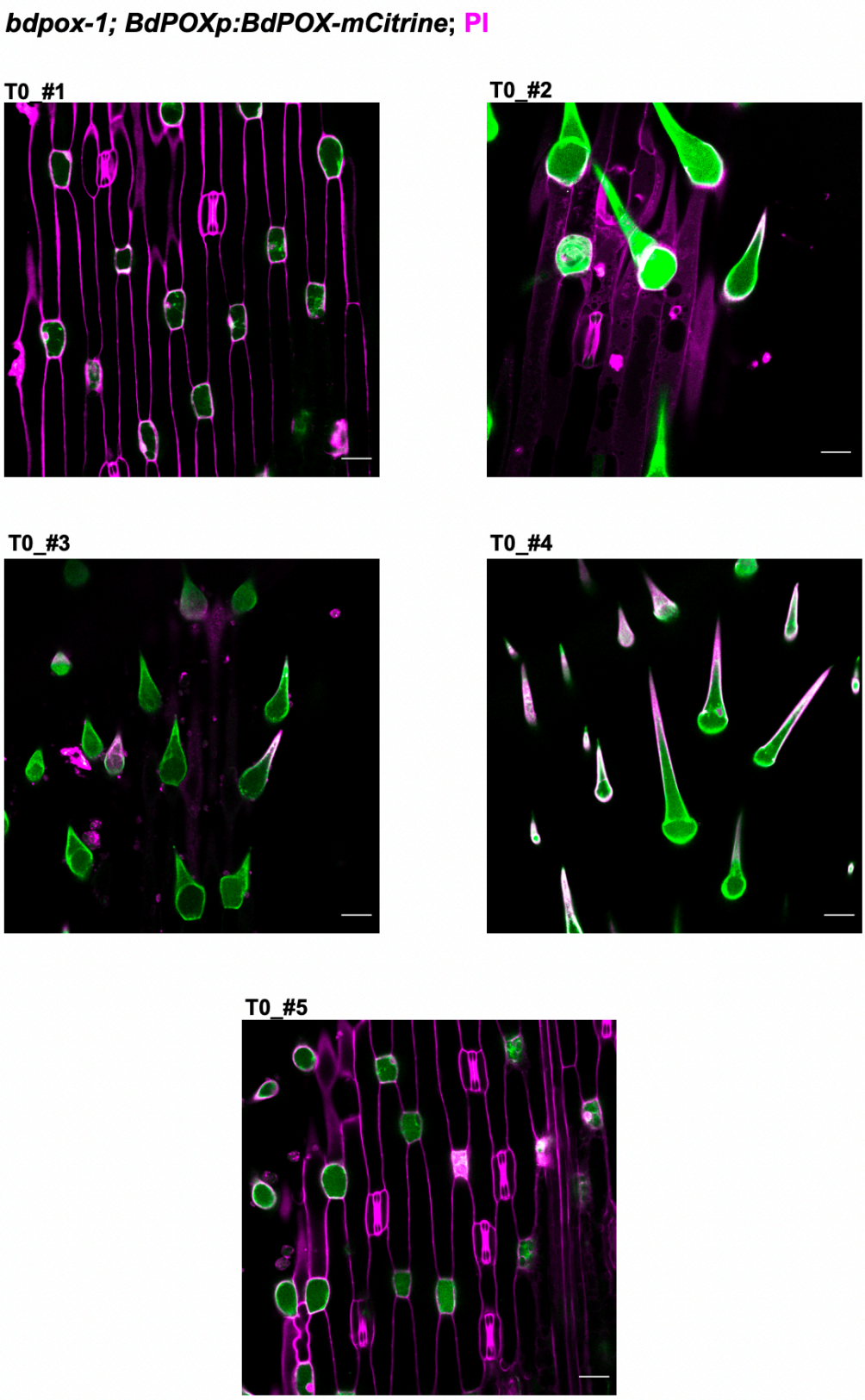


Figure S3 – Additional confocal imaging from T0 complementation lines (*BdPOXp:BdPOX-mCitrine* in *bdpox-1*). BdPOX-mCitrine signal in green and propidium iodide (PI) in magenta. *BdPOX* expression can be observed exclusively in the PHCs. Scale bars 20 μm.

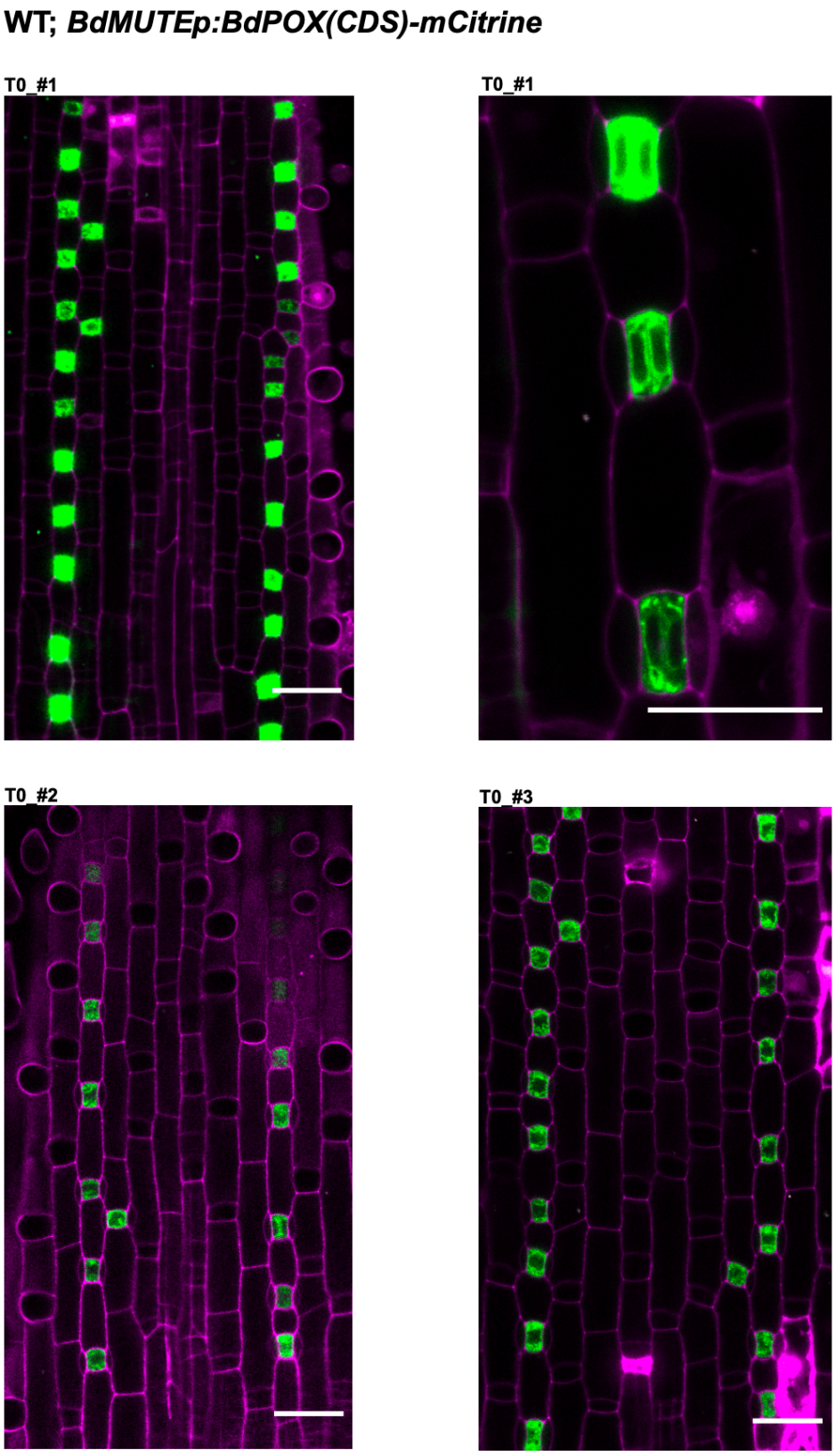


Figure S4 – Additional confocal imaging from T0 WT; *BdMUTEp:BdPOX(CDS)-mCitrine* lines. BdPOX-mCitrine signal in green and propidium iodide (PI) in magenta. *BdPOX* expression driven by *BdMUTE* promoter can be observed exclusively in the the GC lineage. Scale bars 20 μm.

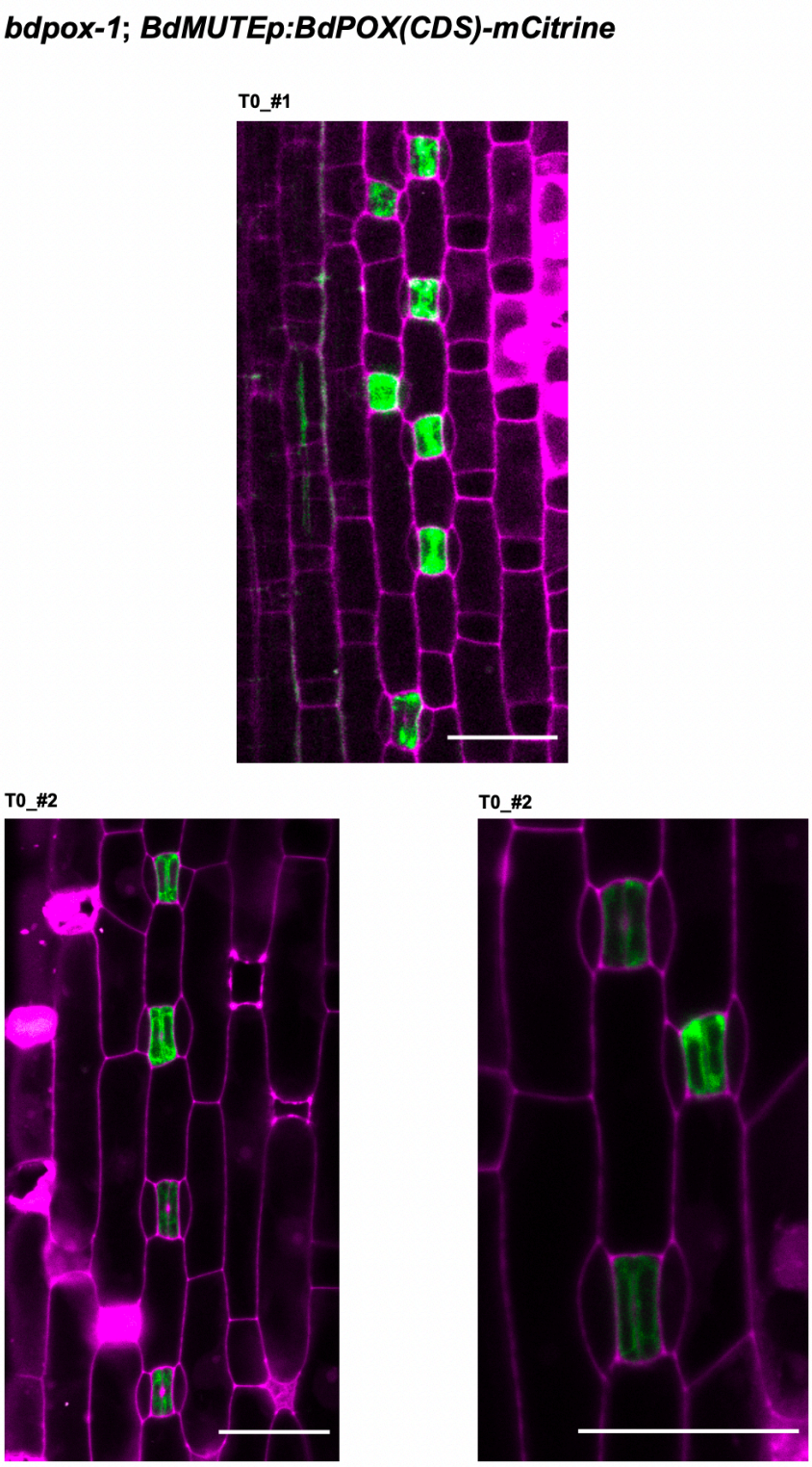


Figure S5 – Additional confocal imaging of two independent T0 *bdpox-1*; *BdMUTEp:BdPOX(CDS)-mCitrine* lines. BdPOX(CDS)-mCitrine signal in green and propidium iodide (PI) in magenta. *BdPOX* expression driven by *BdMUTE* promoter can be observed exclusively in the GC lineage. *BdMUTEp:BdPOX(CDS)-mCitrine* expression in *bdpox-1* results in defective cellular divisions surrounding the stomatal complexes (quantified in the mature leaves of T1 lines) which can already be observed in the developmental zone in these pictures (e.g., bottom stoma in T0_#1 and top two stomatal complexes in the left T0_#2). Scale bars 20 μm.

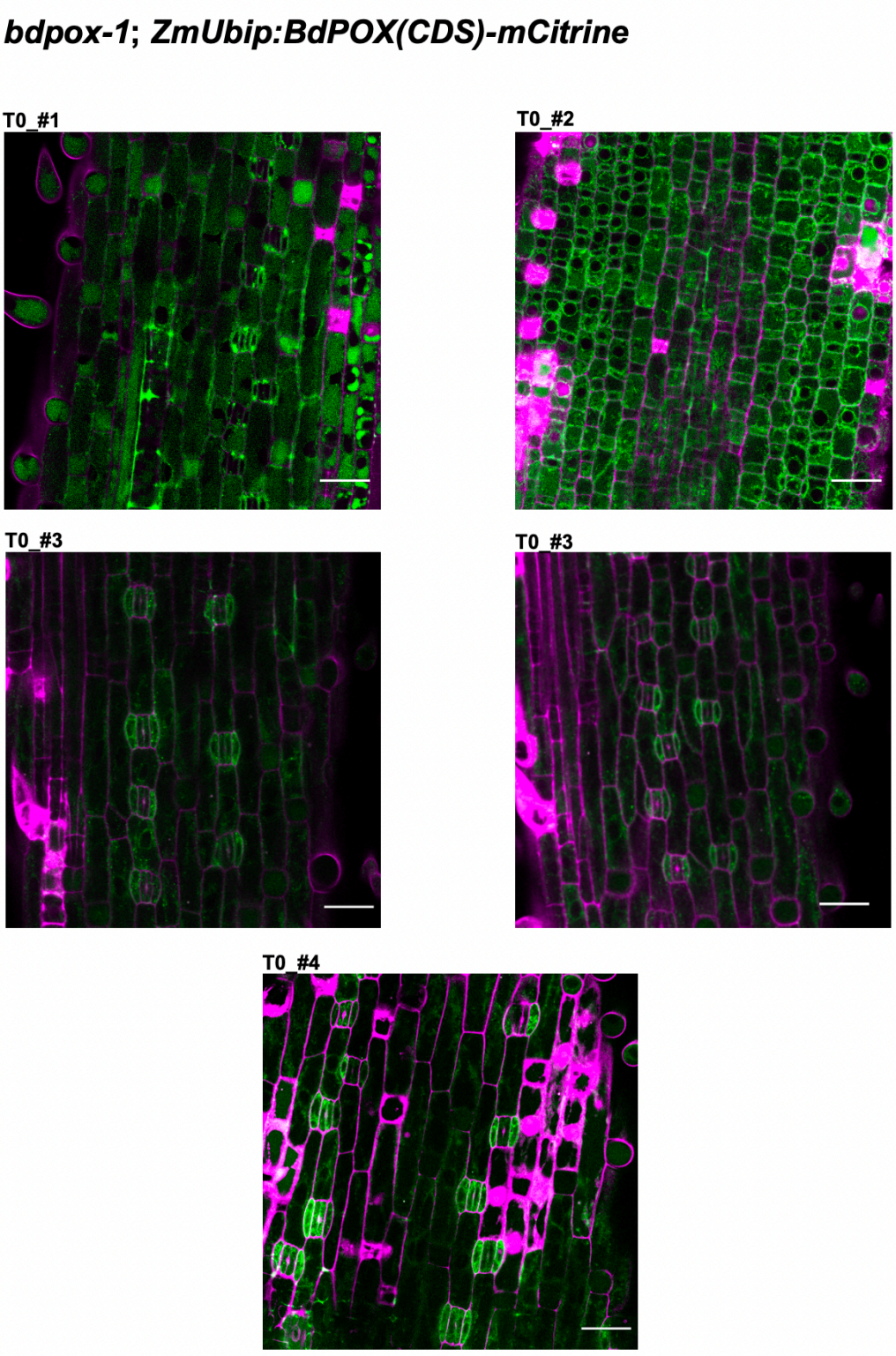


Figure S6 – Additional confocal imaging of four independent T0 *bdpox-1*; *ZmUbip:BdPOX(CDS)-mCitrine* lines. BdPOX(CDS)-mCitrine signal in green and propidium iodide (PI) in magenta. *BdPOX* expression driven by *ZmUbi* promoter can be ubiquitously observed. Scale bars 20 μm.

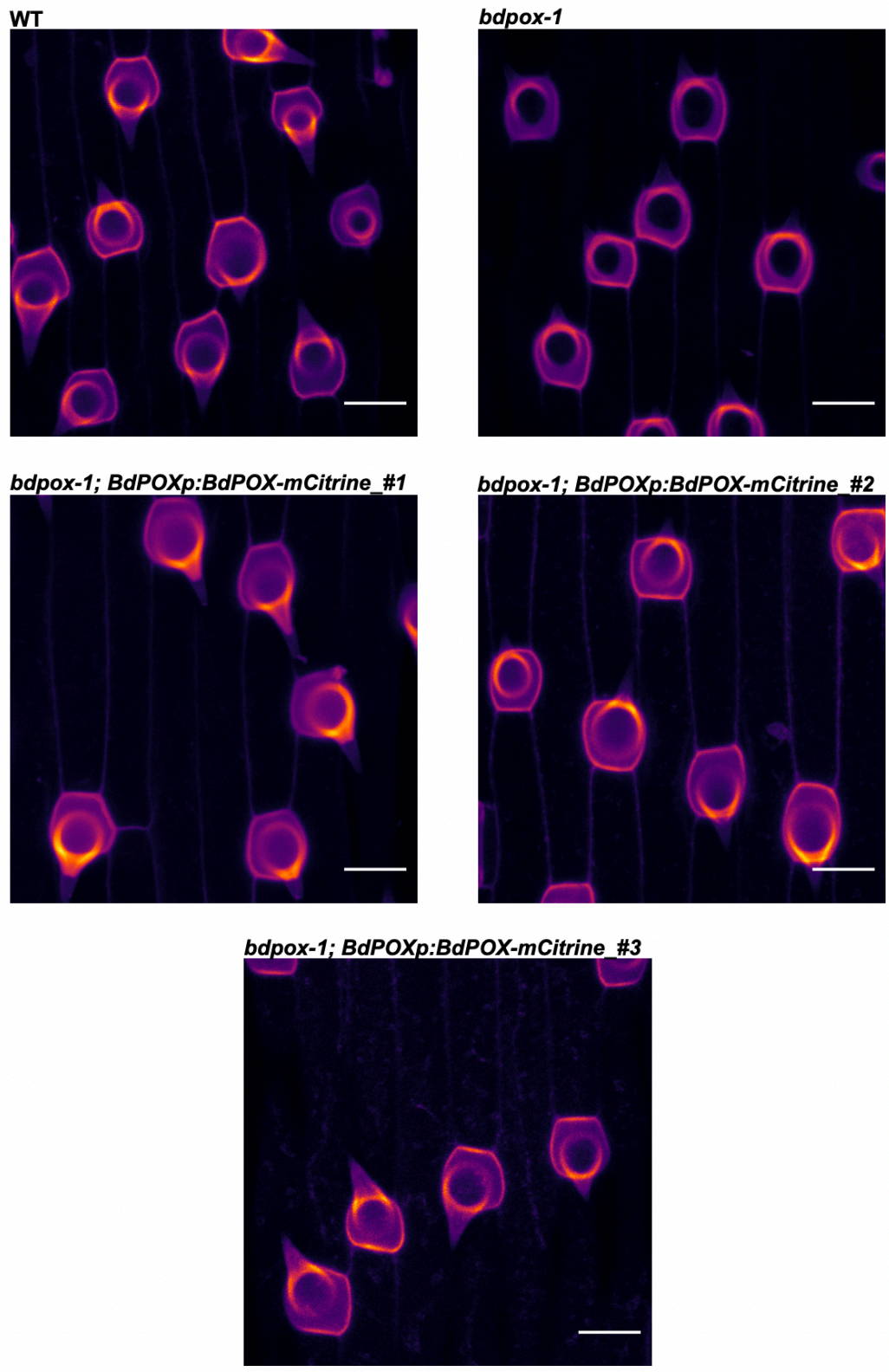


Figure S7 – Example of PHCs of WT, *bdpox-1* and in three complementation lines (*bdpox-1; BdPOXp:BdPOX-mCitrine*_#1, #2 and #3) stained by basic fuchsin (lignin stain). Images are z-projections (sum slices, mpl-magma lookup table applied). Scale bars 10 μm.

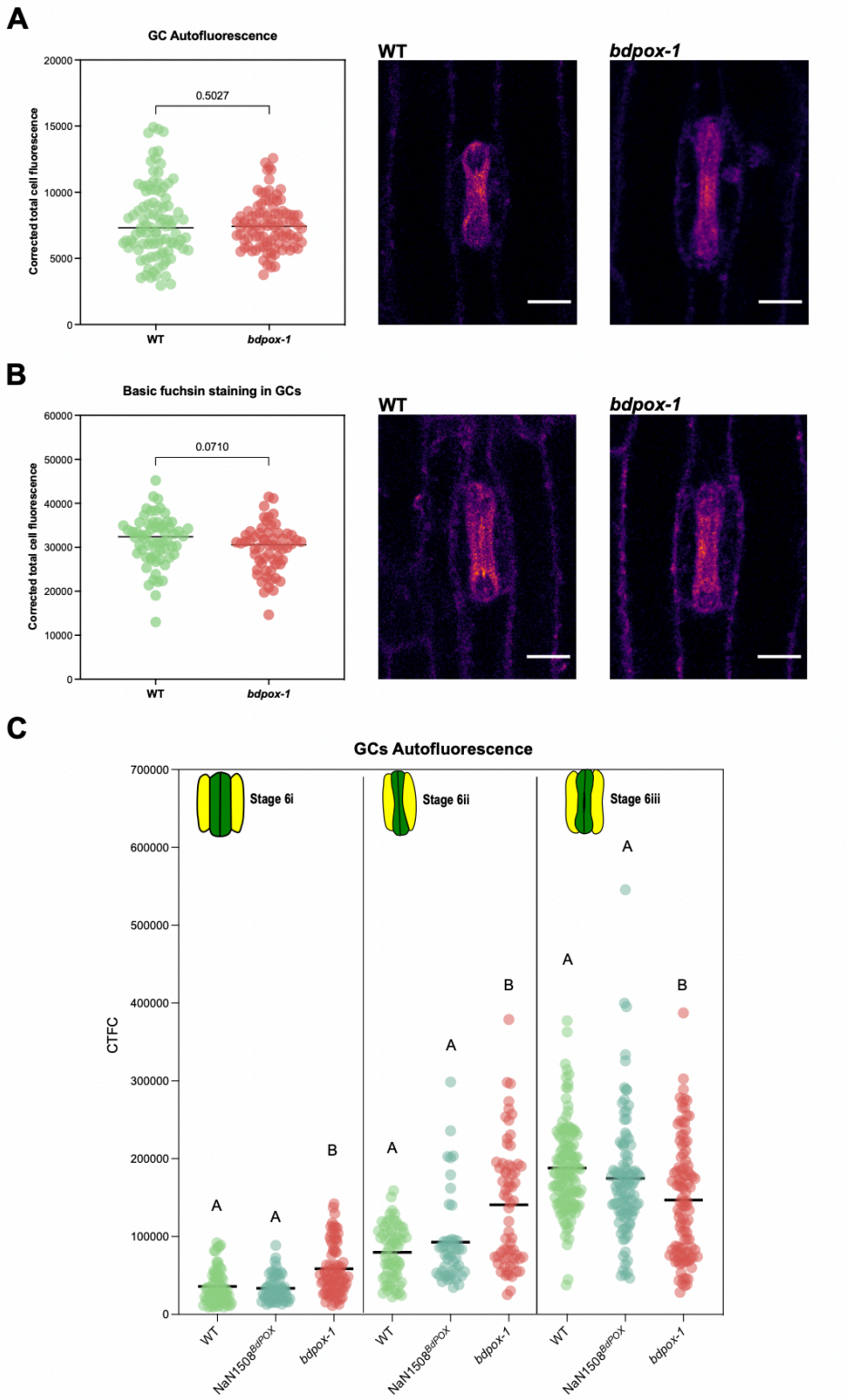


Figure S8 – Cell wall autofluorescence and lignin staining of mature stomata in WT and *bdpox-1,* and cell wall autofluorescence in elongating stomata (step 6i, 6ii and 6iii) in WT, NaN1508^{BdPOX} and *bdpox-1.* (A) Cell wall autofluorescence in mature GCs of WT and *bdpox-1* (n=94-96 stomata per genotype). **(B)** Basic fuchsin fluorescence (lignin staining) in mature GCs of WT and *bdpox-1* (n=59-62 stomata per genotype). Scale bars, 10 μm. **(C)** Stomatal autofluorescence during stomatal elongation/maturation in early stage 6i (n=55-78 stomata per genotype/line), middle stage 6ii (n=47-66 stomata per genotype) and late stage 6iii (n=98-129 stomata per genotype) in WT, NaN1508^{BdPOX} and *bdpox-1*. Data in (C) obtained by Magdalena W. Slawinska.

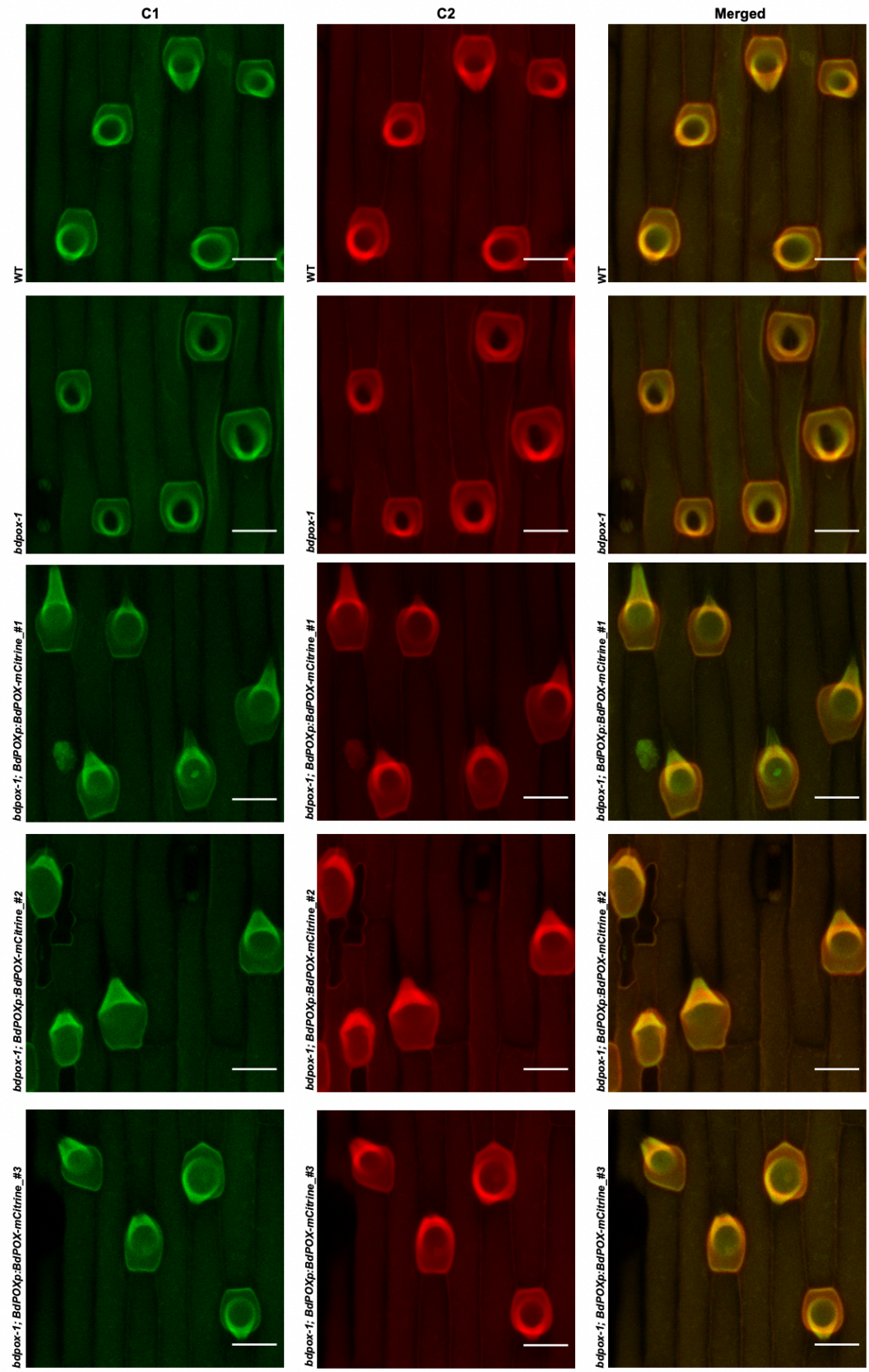


Figure S9 – Example of PHCs of WT, *bdpox-1* and in three complementation lines (*bdpox-1; BdPOXp:BdPOX-mCitrine*_#1, #2 and #3) stained with safranin-o (lignin stain). Emission in the green spectrum (C1), red (C2) and merged. An increase in red fluorescence intensity occurs in lignified cells/tissues. Scale bars 10 μm.

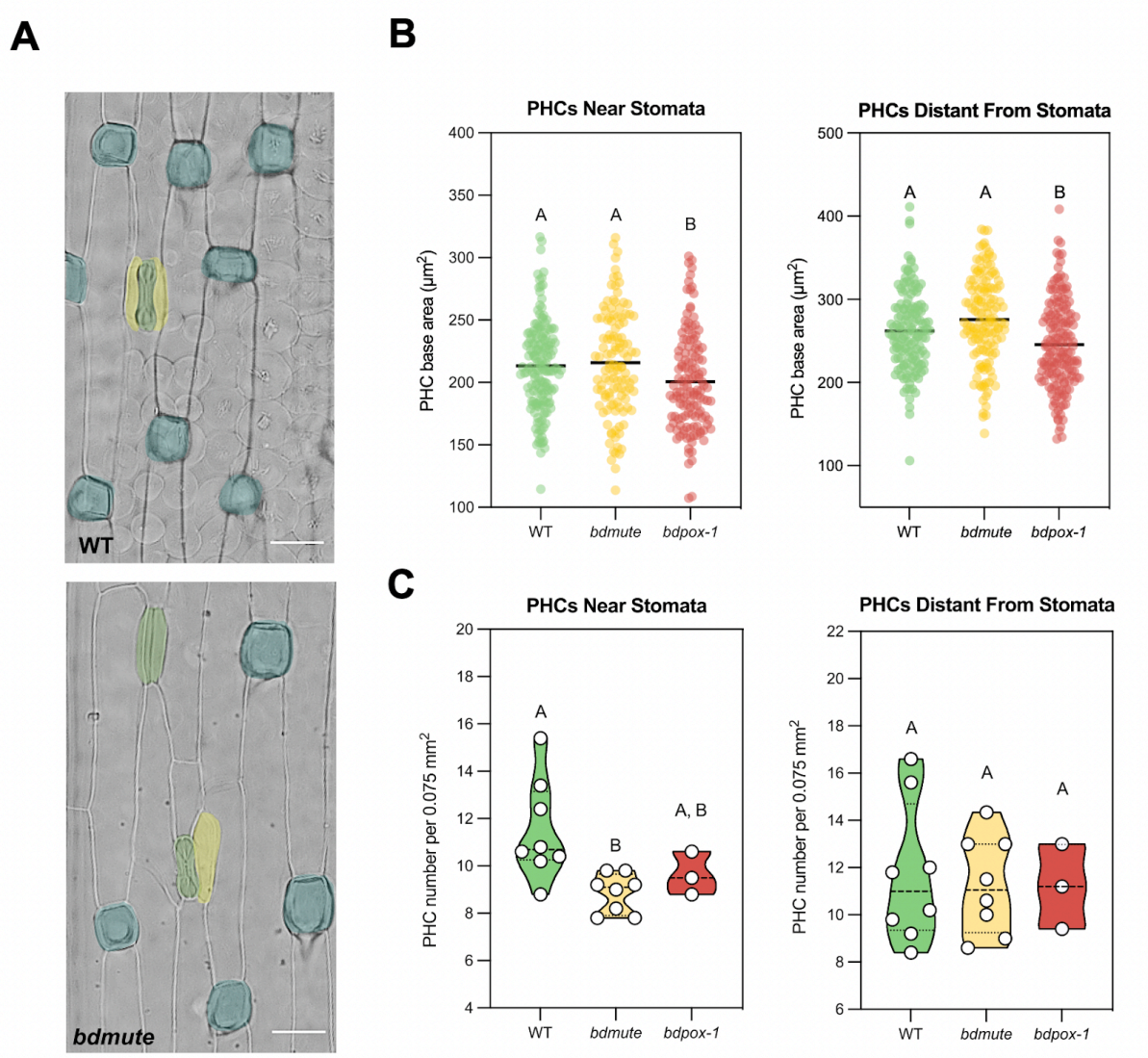


Figure S10 – Prickle hair cell size and numbers in *bdpox*-1 and *bdmute* mutants. (A) Leaf epidermis of *B. distachyon* (21-3) and *bdmute* (representing areas of lower PHC density near some of the epidermal defects described in Raissig et al., 2017, such as stomatal abortions and stomata with defective SC recruitment). **(B)** PHC basal area in WT, *bdmute* and *bdpox-1* of PHCs found in the 2 rows next to stomata (Near stomata, n=3 individuals, 118-159 PHCs per genotype) and in distant rows (Distant from stomata, n=3 individuals, 139-168 PHCs per genotype). **(C)** PHCs numbers in WT, *bdmute* and *bdpox-1* in the 2 rows next to stomata (Near stomata, n=3-8 individuals per genotype, each point represents the average of 4-5 0.075 mm^2 fields of view from one individual, 135-460 PHCs counted per genotype) and in distant rows (Distant from stomata, n=3-8 individuals per genotype, each point represents the average of 4-5 0.075 mm^2 fields of view from one individual, 168-476 PHCs counted per genotype). Different letters indicate significant differences ($p<0.05$ from Tukey's multiple comparisons following One-way ANOVA).

5.4 Discussion

The leaf epidermis is the outermost cell layer forming the interface between plants and the atmosphere that must accomplish two opposite roles: provide a robust barrier against biotic and abiotic stressors while providing an efficient interface regulating the exchange of CO_2 and water. To achieve these contrasting requirements, the plant epidermis developed a wide range of singular cell types (Javelle et al. 2011).

In grasses, besides stomata, another protuberant leaf epidermal feature are the trichomes (from the Greek τρίχωμα, trichōma, meaning "hair"; also referred as hair cells in grasses) which are highly lignified and silicified to provide protection against herbivory, high sun irradiance and desiccation in arid environments (Karabourniotis et al. 2020; Andama et al. 2020; Hall et al. 2020). *B. distachyon* contains two types of trichomes: abundant prickle hair cells (PHCs) and fewer occurring macrohairs (Hall et al. 2020; Głazowska et al. 2018). A third cellular feature are silica cells, also known as phytoliths ("plant stones" from the Greek λίθος, líthos, meaning "stone" and φυτόν, phutón, meaning "plant"), which consist of silicified cells providing additional and energetically inexpensive structural support (as silica is transported to leaves in solution in water across the vascular system, promoted by leaf transpiration). Besides the structural support, silica cells also provide protection against herbivory by reducing the digestibility of plant tissues just like the trichomes (Strömberg et al. 2016; Hall et al. 2020).

Finally, the pavement cells are the ground cell type in the leaf epidermis providing a protection layer separating functionally important cells (e.g., mesophyll cells where photosynthetic reactions take place) from the outside environment. Furthermore, the pavement cells allow the allocating all the above cell types and the proper spacing among stomatal complexes, trichomes and between stomata and trichomes for efficient functionality.

Several studies suggest that trichome initial patterning intersects with the core stomatal developmental programmes in *Arabidopsis* (Kong et al. 2021; Kanaoka et al. 2008; Yan et al. 2014; Adrian et al. 2015; Raissig et al. 2016; Torii 2021).

While many core players guiding grass stomatal development were characterized (Liu et al. 2009; Cartwright et al. 2009; Humphries et al. 2011; Facette et al. 2015; Raissig et al. 2016; Raissig et al.

2017; Abrash et al. 2018; Wu et al. 2019; Wang et al. 2019; Jangra et al. 2021; Nunes et al. 2020), grass trichome formation remains poorly explored (Torii 2021).

Few grass trichome initiation factors have been identified, but morphogenesis and size regulation players remain mostly unknown. HL6 is a AP2/ERF transcription factor that interacts with OsWOX3B to determine the formation of macrohairs in rice (Fei et al. 2020; Sun et al. 2017). Both *hl6* and *oswox3B* mutants displayed glabrous leaves and glumes (Angeles-Shim et al. 2012; Sun et al. 2017). *HL6* overexpression lines presented longer macrohairs (Sun et al. 2017). OCL4 is a D-ZIP IV transcription factor needed for patterning of macrohairs in maize (Vernoud et al. 2009). *ocl4* mutants developed macrohairs ectopically at the leaf margins. ZmSPL10/14/26 are transcription factors inducing epidermal hair fate on maize leaves (Kong et al. 2021). Maize trichomes were completely absent on the leaf surface of *slp10/14/26* triple mutants. Similarly, *OsSPL10* positively controls trichome initiation in rice (Li et al. 2021; Lan et al. 2019). Rice *spl10* mutants presented glabrous leaves and glumes with absent or highly reduced trichome number. Oppositely, *OsSPL10* overexpression lines displayed higher trichome density. Maize *mhl1* locus regulates macrohair initiation in leaves. *mhl1* mutant alleles significantly reduced or eliminated macrohairs (Moose et al. 2004). Rice type-B response regulators (RRs) are transcriptional factors involved in the development of different plant tissues. *rr21/22/23* mutants showed reduced trichome number and shorter macrohairs, besides defects in panicle, shoot, stigma and anthers development (Worthen et al. 2019).

Furthermore, stomatal density and trichome density have been described as being negatively correlated in *Solanum lycopersicum*, and their ratio determines water use efficiency (Galdon-Armero et al. 2018), suggesting a physiological relevance for the coordination between the two cellular features. Still, the developmental and functional coordination between stomata and trichomes remains mostly unexplored.

Here, I report *BdPOX* as a grass trichome marker and first player characterized in the coordination of cell size of multiple epidermal cell-types in *B. distachyon*.

BdPOX was expressed in the hair cells to positively regulate PHC size cell-autonomously, while non-cell-autonomously role constricting stomatal elongation.

BdPOX seems to participate in cell-wall modifications such as lignin polymerisation or cell wall cross-linking of hydroxycinnamates to regulate PHC cell elongation/maturation. Lignin is a cell wall polymer that provides mechanical support to the plant cells (Rogers and Campbell 2004; Zhao et al. 2020; Li et al. 2009). Since *bdpox* mutants displayed lower basal PHCs lignification/hydroxycinammates cross-linking and shorter PHCs, this suggests that a cell wall chemical enrichment in lignin/hydroxycinammates at the basal section of the PHCs is required to provide mechanical support for PHC elongation.

Interestingly, an analysis of gene expression of 19 randomly selected *BdPRX* genes showed that *BdPRX76/BdPOX* expression was induced by H_2O_2, ABA and gibberellic acid (GA) treatments (Zhu et al. 2019). While ABA and H_2O_2 are involved in signaling in response to abiotic stresses, GA is a plant hormone that stimulates cell division and elongation in different organs such as leaves and stems. This finding suggests that *BdPOX* expression to promote PHC growth may be induced by GA and therefore developmentally coordinated with GA-induced leaf elongation. Therefore, BdPOX may provide a mechanism to increase PHC size and limit stomatal elongation to maintain a water-use efficient stomatal size during leaf expansion. Additionally, *BdPOX* expression might also be modulated by environmental factors via ABA and H_2O_2, to regulate PHC size, phenolic content, and putative stiffness to improve tolerance against (a)biotic stresses.

PHC growth via cell wall modifications seems to induce a constriction in stomatal elongation independent of the genetic pathways that directly regulate stomatal formation.

Stomatal numbers are established early in development and seem to condition stomatal size *a posteriori*. Potentially, increases in stomatal numbers may induce a downstream regulation in the cell-wall machinery modelling stomatal elongation and maintaining a negative correlation between stomatal density and size.

PHCs elongation occurs after the establishment of stomatal numbers but before stomatal elongation (Fig. 3.14, 3.15). Consequently, knocking out *BdPOX*, which reduced lignin content and decreased PHC size, may have led to a reduction in mechanical and geometrical constraints allowing for further stomatal elongation (Fig. 3.15). The increase in stomatal length observed in

bdpox mutants (~9%) was quantitatively identical to the decrease in PHC size (~10%) supporting the hypothesis of geometrical compensation on cell size.

In addition, specifically expressing *BdPOX* in the stomatal lineage increased GCs phenolic content and restricted stomatal elongation. In *bdpox-1*, this resulted in a leaf epidermis containing both shorter stomata and shorter PHCs which induced aberrant additional cell divisions potentially due to an imbalance in cellular tension. Therefore, the longer stomata observed in *bdpox-1* seem to result from a compensatory effect due to shorter PHCs to maintain tensile balance in the epidermis. Alternatively, since class III peroxidases consume H_2O_2 during lignification reactions, H_2O_2 levels may be elevated in the PHC apoplast of *bdpox-1* which might have changed ROS homeostasis and non-cell-autonomously affect stomatal length.

Regardless, these observations support a developmental dependence and coordination between stomata and PHCs which has previously been suggested in grasses (Raissig et al. 2016; Kong et al. 2021). Furthermore, another evidence for this dependence is the disturbed PHC patterning in the proximity of the aberrant stomata in *bdmute* mutants (Fig. S10), which may also explain why *BdPOX* was downregulated in *bdmute*.

The indirect modification of stomatal size in *bdpox-1* due to defective PHCs, created a disruption in the negative correlation between stomatal size and density. Such unique disruption allowed me to investigate how modifying a single stomatal anatomical trait (i.e., stomatal size) can affect gas exchange. I verified that an increase in stomatal size increased stomatal conductance rates (both g_{sw} and $g_s$max) while not significantly affecting stomatal speed. This result corroborates my previous results from chapter I, where I verified that stomatal speed significantly correlated with stomatal density but not with stomatal size in wildtype *B. distachyon*.

Besides the reported interaction between PHC and stomatal size, and its impact on abiotic interactions, namely gas exchange and water use efficiency, PHC size is also of major relevance for biotic interactions. Longer PHCs have been negatively correlated with the reproduction rate of herbivores in *B. distachyon* (Hall et al. 2020). Silica supplemented plants showed reduced PHC density, increased PHC size and herbivores (caterpillars and crickets) were negatively affected (Hall et al. 2020), highlighting the relevance of PHCs for abiotic stress resistance. Since *bdpox* mutants

present a change in PHCs length, putative stiffness and/or cell-wall phenolic composition, *BdPOX* may be used as a target to engineer herbivore-deterring crops and also improve resistance against abiotic stress such as sun irradiance (Hall et al. 2020; Karabourniotis et al. 2020; Andama et al. 2020; González Moreno et al. 2022)

Overall, I identified *BdPOX*, a hair cell marker that coordinates stomata and PHC development for optimal leaf functionality. *BdPOX* provides a tool to explore the molecular identity of grass hair cells and, shed light on the importance of this cell type in both biotic and abiotic interactions and further elucidate the developmental and functional interaction between PHCs and stomata for efficient gas exchange.

Finally, I highlight an unexpected indirect route to engineer stomatal size and overcome the negative correlation between stomatal density and side by engineering PHC size and cell wall properties.

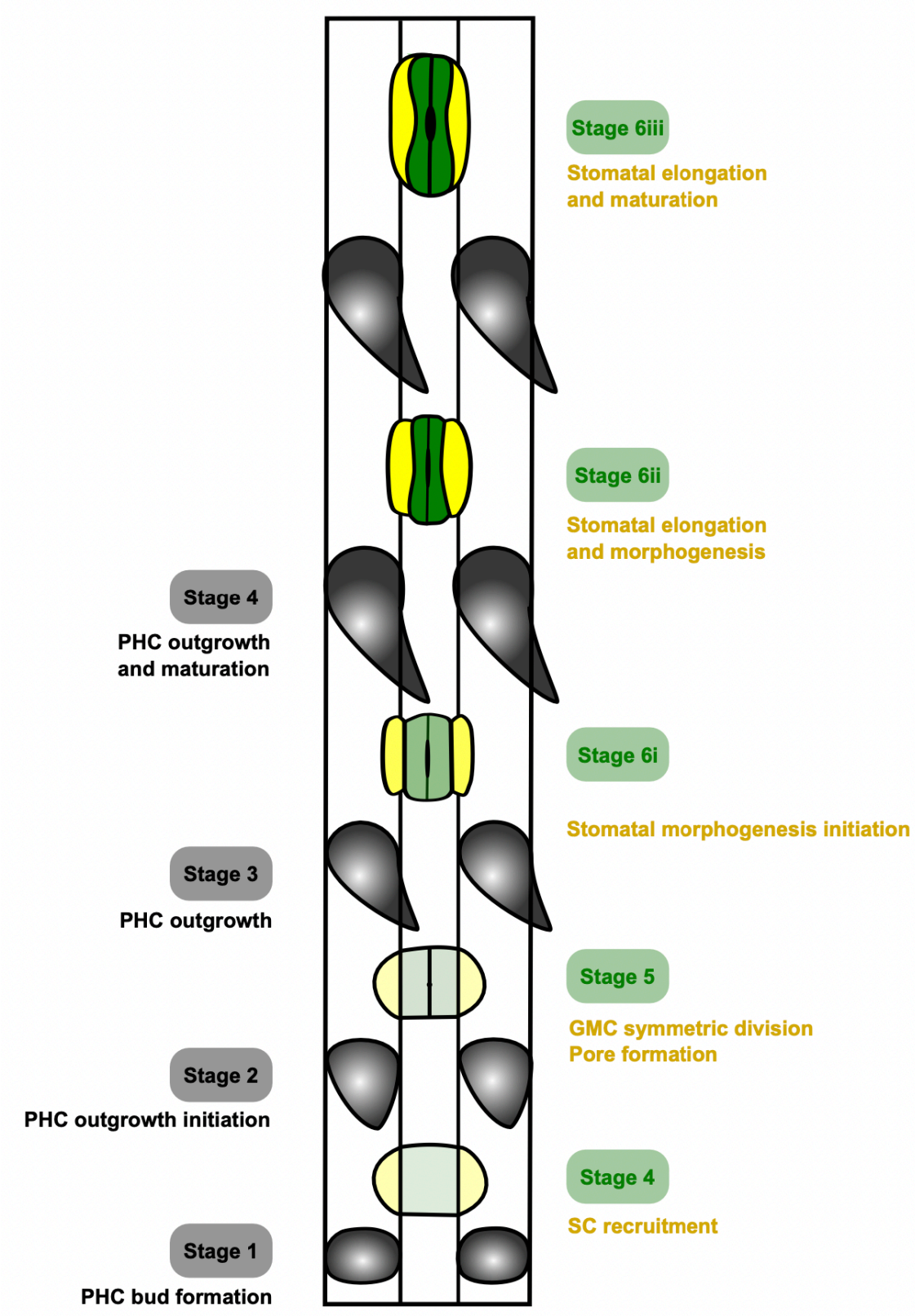


Figure 3.14 – Model for the coordination between PHC and stomatal development. PHC developmental stages represented in grey, stomatal development stages in green. In PHC stage 1, a PHC bud is formed. In PHC stage 2, PHC outgrowth initiates. In PHC stages 3 and 4, PHCs elongate and the PHC base enlarges and the PHC matures. PHC development occurs when stomatal development is on stage 4, when SCs are recruited. PHCs fully mature before stomatal elongation initiates (stage 6i).

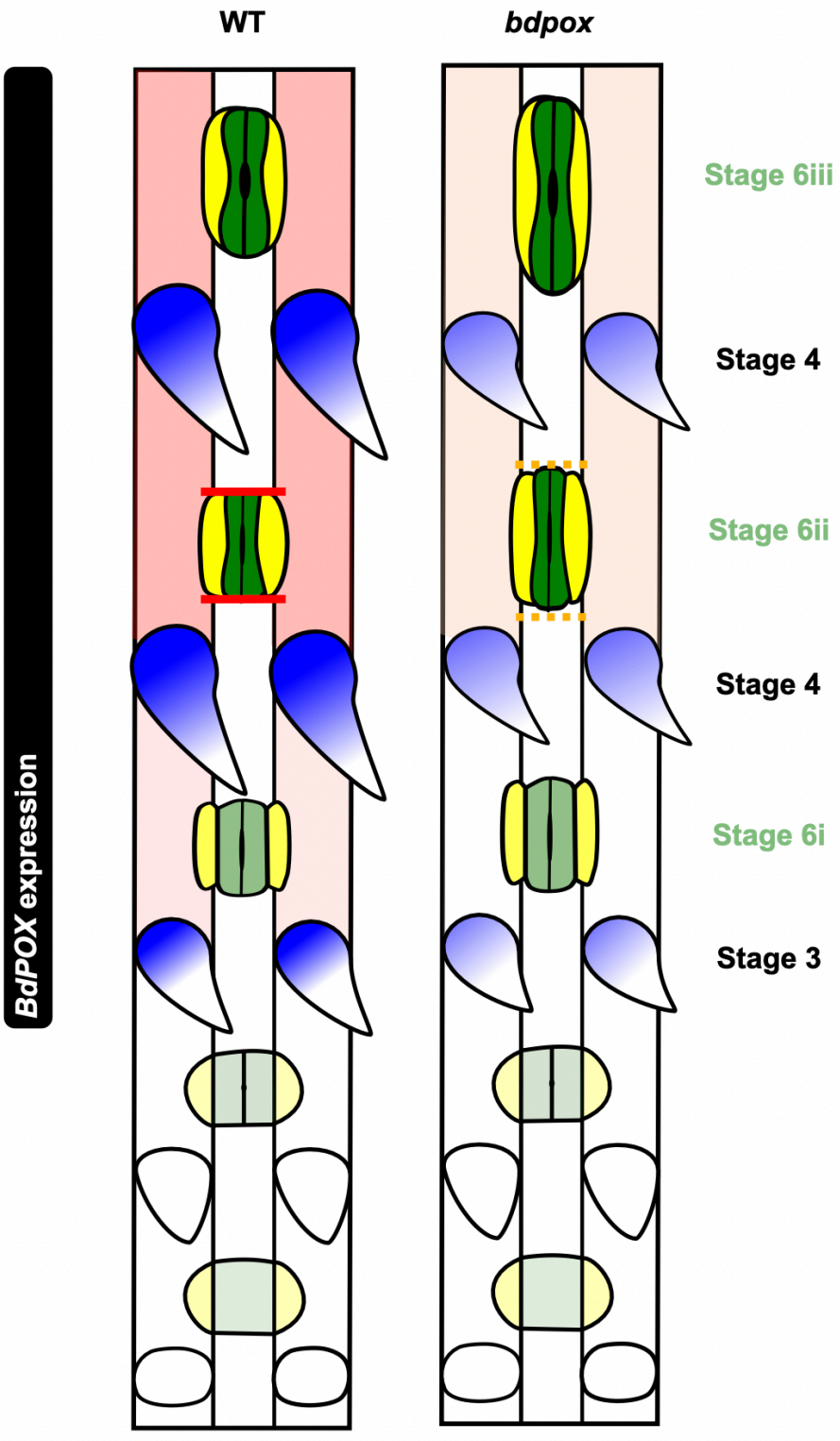


Figure 3.15 – Suggested mechanism for *BdPOX* on promoting PHC growth and limiting stomatal size. *BdPOX* is expressed at stage 3 of PHC development (black) when PHC elongation and enlargement is occurring. BdPOX seems to induce cell wall lignification/cross-linking of hydroxycinammates (represented in blue), which may lead to an increase in mechanical tension in the leaf tissue (represented in faded red) and consequently restrict stomatal elongation (stage 6ii-6iii). In *bdpox* mutants, the lack of *BdPOX* expression results in a reduction of lignification and decrease in PHC size, putatively alleviating the mechanical constrain on the leaf tissue and allowing for further stomatal elongation.

6. Conclusions

This thesis allowed to establish links between stomatal anatomy and function in the model grass *Brachypodium distachyon* and resulted in the characterization of a novel player participating in the coordination between stomatal and prickle hair cell development in grasses for efficient gas exchange.

In chapter I, I quantified how variations in the environment affected stomatal anatomy and gas exchange. Over the course of 2 years, I measured stomatal light-responses in 120 individuals and verified that *B. distachyon* displays fast stomatal movements typical for C_3 grasses and robust stomatal responses. Still, I verified that variations in the ambient light intensity and/or temperature could systemically influence leaf-level gas exchange parameters (A, g_{sw} and/or iWUE). Furthermore, I verified that intrinsic diurnal rhythms could influence the outcome of leaf-level gas exchange measurements and stomatal kinetics. I also verified that stomatal anatomy is significantly plastic, varies seasonally and may significantly impact the outcome of long-term gas exchange studies performed in glasshouses and/or in the field, where environmental conditions fluctuate and follow climacteric trends. While in wild-type *B. distachyon*, stomatal density (SD) and stomatal length (SL) are negatively correlated, SD seems to be the anatomical trait that may impact the most seasonal variations in stomatal kinetics and iWUE. Overall, I observed that daily variations in the environmental conditions may systemically affect leaf-level gas exchange and that seasonal variations may affect stomatal anatomy and consequently alter stomatal kinetics and leaf-level gas exchange.

In chapter II, I explored the leaf transcriptome downregulated in *bdmute* mutants which lack SCs and display defective stomatal movements and performed a reverse genetics screen to identify candidate genes associated with the grass stomatal morphology and physiology. I screened 60 mutant lines for 53 different candidate genes and identified several phenotypes associated with defective stomatal kinetics and/or defective iWUE. This screen allowed me to speculate on the putative function and location of candidate genes in the grass stomatal complexes. Most

importantly, this screen yielded the identification of *BdPRX76/BdPOX* as a gene associated with iWUE in *B. distachyon*.

In chapter III, I characterized *BdPRX76/BdPOX* and verified that this gene is expressed in the prickle hair cells (PHCs) to lignify/crosslink the base of the PHCs to provide mechanical support to promote their outgrowth. This PHC basal lignification and growth seems to limit stomatal elongation. Therefore, *bdpox* mutants displayed shorter PHCs, which may have disrupted the mechanical/geometric constriction on stomatal elongation, resulting in longer stomata. This indirect modification of stomatal size resulted in a unique disruption in the negative correlation between stomatal size and density, and consequently increased g_{sw} and negatively impacted iWUE. Overall, I highlight the importance of the coordination between stomatal and PHC formation for optimal leaf-level gas exchange.

7. Study limitations and outlook

While in chapter I, I observed significant correlations between environmental factors and stomatal traits, I cannot infer causal relationships. While being a limitation of the study, these results open the door for further investigation on the effect of single or combined environmental factors (e.g., light availability, temperature) on stomatal formation and gas exchange, which will require targeted experiments under tight environmental control. Also, regarding the influence of stomatal density on stomatal speed and iWUE, the analysis of mutants displaying increased and decreased stomatal density (e.g., *EPF1* overexpression lines and *epf1* mutants) may provide a suitable tool to confirm the correlations observed in my study. Additionally, live imaging of stomatal opening and closure in response to changes in light intensity, may unravel how the speed of stomatal movements varies between dispersed and clustered stomata.

Regarding chapter II, the mutant lines screening was targeted on light responses to evaluate iWUE and stomatal kinetics. Still, not only light is a trigger of stomatal movements but also other

environmental factors such as vapor pressure deficit (VPD), CO_2 concentrations or biotic factors. Therefore, while many mutant lines did not present any significant phenotype in my screening, stomatal-related phenotypes may have been missed. Screenings for VPD responses may be particularly relevant since not only light is a highly fluctuating factor impacting plant water use efficiency, but also changes in relative humidity and temperature (both affecting VPD).

Regarding chapter III, while I provide histochemical and microscopic data supporting a decrease in lignin/hydroxycinnamates in the prickle hair cells, future research may allow determining the molecular nature of this defect. For example, Raman spectroscopy could be a suitable technique to evaluate the chemical composition of the cell wall of the PHCs and help reveal the product of BdPOX. Raman spectroscopy has been shown to be a useful tool to characterize the cell wall chemotypes between different cells in plant tissues (Zhang et al. 2020). Furthermore, while lignin has been broadly associated with enhanced tensile strength, the establishment of cellular force microscopy on the grass leaf tissue may allow to measure mechanical forces involved in the interaction between PHCs and stomatal development. The observation of cell division defects when *BdPOX* was expressed in the stomatal lineage in *bdpox* mutants that contained defective PHCs, highlights the significance of optimal mechanical forces during leaf development. In the future, further research on the mechanical coordination between PHCs and stomata may provide valuable knowledge for engineering plants for improved plant-environment interactions. Finally, *BdPOX* may provide a tool to further investigate the molecular profile of PHCs (e.g., single cell profiling of PHC transcriptome) and their function on (a)biotic interactions.

8. Appendix

Supplementary Table 1 - Seed sterilization solution

Component	Work concentration	For 25 ml
Bleach 20 %	5.25 %	5 ml
Triton-100	0.1 %	25 µl
Water	NA	20 ml

Supplementary Table 2 – 2x CTAB solution for DNA extraction

Component	Stock concentration	Work concentration	For 100 ml
CTAB	NA	NA	2 g
NaCl	5 M	1.4 M	28 ml
Tris-HCl	1 M (pH = 8.0)	100 mM	10 ml
EDTA	0.5 M (pH = 8.0)	20 mM	4 ml
Water	NA	NA	Up to 100 ml

Protocol

1. Small amount of plant tissue grinded in a 1.5 ml Eppendorf tube;
2. Add 300 µl of 2xCTAB buffer and incubate for min 30 min at 65°C;
3. Add 300 µl of chloroform, vortex and spin the tubes briefly in a microfuge;
4. Transfer the upper aqueous phase to a new tube;
5. Add 300 µl of isopropanol, mix and spin down in a microfuge for 10 min to pellet the DNA;
6. Remove supernatant, wash the pellet with 500 µl of 70 % ethanol and spin tubes in a microfuge;
7. Remove ethanol and dry pellet at 65°C for approximately 15 min;
8. Add 100 µl of water to dissolve the pellet and use 1-2 µl in a PCR reaction.

Supplementary Table 3 - Q5 PCR reaction setup and thermocycler conditions

Component	50 µl reaction	Temperature	Time	Number of cycles
5x Q5 Reaction Buffer	10 µl	98°C	30 s	1
10 mM dNTPs	1 µl	98°C	10 s	
10 µM Forward primer	2.5 µl	58°C	20 s	
10 µM reverse primer	2.5 µl	72°C	20-30 s/kb	x35
DNA Template	Variable	72°C	2 min	1
Q5 high-fidelity DNA Polymerase	0.5 µl	16°C		END
Nuclease-free water	To 50 µl			

Supplementary Table 4 - Taq PCR reaction setup and thermocycler conditions

Component	25 µl reaction	Temperature	Time	Number of cycles
10x Standard Taq reaction buffer	2.5 µl	95°C	30 s	1
10 mM dNTPs	0.5 µl	95°C	30 s	
10 µM Forward primer	0.5 µl	58°C	30 s	
10 µM Reverse primer	0.5 µl	68°C	1 min/kb	x35
DNA Template/Colony	Variable	68°C	5 min	1
Taq DNA Polymerase	0.125 µl	16°C		END
Nuclease-free water	To 25 µl			

Supplementary Table 5 - GreenGate reaction set up

Component	20 µl reaction	Temperature	Time	Number of cycles
Entry module A (Promoter)	1.5 µl	37°C	5 min	
Entry module B (N-tag)	1.5 µl	16°C	2 min	30
Entry module C (Genomic/CDS)	1.5 µl	50°C	5 min	1
Entry module D (C-tag)	1.5 µl	80°C	5 min	1
Entry module E (Terminator)	1.5 µl			
Entry module F (Resistance)	1.5 µl			
Destination vector Z (pGGZ004)	1 µl			
10x Fast Digest buffer	2 µl			
ATP (10 mM)	2 µl			
T4 DNA ligase	0.5 µl			
Eco31I	0.5 µl			
Nuclease-free water	5 µl			

Supplementary Table 6 – Golden gate reaction setup used for CRISPR/Cas9 cloning

Component	20 µl reaction	Temperature	Time	Number of cycles
Reaction 1 (1-5ng)	Variable	37°C	5 min	10
Reaction 2 (1-5ng)	Variable	25°C	10min	
Reaction 3 (1-5ng)	Variable	16°C	END	
pMODB2103(~50ng)	1.5 µl			
SapI	0.5 µl			
Eco31I	0.5 µl			
T4 DNA ligase	1 µl			
10X T4 DNA ligase buffer	2 µl			
Nuclease-free water	To 20 µl			

Supplementary Table 7 – Golden gate reaction setup used for CRISPR/Cas9 Multiplexed cloning protocol

Component	20 µl reaction	Temperature	Time	Number of cycles
pYPQ142 (100 ng/ µl)	1 µl	37°C	5 min	10
pYPQ131--gRNA1 (100 ng/ µl)	1 µl	25°C	10min	
pYPQ132-gRNA2 (100 ng/ µl)	1 µl	50°C	5 mim	
BsaI	0.5 µl	80°C	5 min	
T4 DNA ligase	0.5 µl	16°C	END	
ATP (10mM)	1 µl			
10x Cutsmart buffer	1 µl			
Nuclease-free water	5 µl			

Supplementary Table 8 - List of antibiotics.

Antibiotic	Work concentration	Solvent	Catalogue
Ampicillin (Amp)	100 µg/ml	Water	Sigma-Aldrich, Cat. Nr. 69-52-3
Carbenicillin (Carb)	50 µg/ml	Water	Roth, Cat. Nr. 6344.2
Chloramphenicol (Chl)	25 µg/ml	EtOH	Roth, Cat. Nr.3886.2
Gentamicin (Gent)	100 µg/ml	Water	Roth, Cat. Nr.0233.3
Hygromycin B (Hyg)	40 µg/ml	Water	Roth, Cat. Nr.10843555001
Kanamycin (Kan)	50 µg/ml	Water	Roth, Cat. Nr. T832.4
Spectinomycin (Spec)	50 µg/ml	Water	Sigma-Aldrich, Cat. Nr. 22189-32-8
Tetracycline (Tet)	10 µg/ml	Water	Roth, Cat. Nr.0237.1

Supplementary Table 9 - List of organisms used for molecular studies

Organism	Strain/Line
Escherichia coli	DH5α
Agrobacterium tumefaciens	AGL1
Agrobacterium tumefaciens	GV3101
Brachypodium distachyon	Bd21-3

Supplementary Table 10 – List of primers used for this study

Primer	Sequence
priTN1	AACAGGTCTCAACCTCAGGCTAGCAGCACTATT
priTN2	AACAGGTCTCATGTTGATCGTGTCGTTCTTC
priTN3	AACAGGTCTCAACCTGAAACTTCACGATCGGCTCT
priTN4	AACAGGTCTCATGTTGACCTGCAGAAGTAACACCA
priTN11	AACAGGTCTCAACTAAGAAGCCAACTAAACAAGACCA
priTN12	AACAGGTCTCAATACTTAATTCGGGGGATCTGGATTT
priTN27	AACAGGTCTCACGAGCCAGAGGATACCAAC
priTN28	AACAGGTCTCACTCGCCCCGTACCCGTTG
priTN29	AACAGGTCTCATATCATTTCGGATACCA
priTN30	AACAGGTCTCAGATAGTGCTCAC
priTN31	TGGTCTCCATCGTCGACACCCTGCCTATACGGCAGTGAACCTG
priTN32	TGGTCTCACGATCAACGGCGGTTTTAGAGCTAGAAATAGC
priTN33	TGGTCTCATTCCGGATGATCCTGCCTATACGGCAGTGAAC
priTN34	TGGTCTCAGGAAGAAATCGAGTTTTAGAGCTAGAAATAGC
priTN35	GGTCTCCCGTGAGGTGGTACTGCCTATACGGCAGTGAACCTG
priTN36	TGGTCTCACACGAAAACCAGGTTTTAGAGCTAGAAATAGC
priTN37	TGGTCTCAGTCTCATCCAGGCTGCCTATACGGCAGTGAAC
priTN38	TGGTCTCAAGACATCAGCAGGTTTTAGAGCTAGAAATAGC
priTN88	AAGCAGCTCCAAGGATGAAC
priTN89	GGGGTTCTACAGGGAGTCAT
priTN95	AACAGGTCTCAACCTGCGACCAGATCATACAGCTC
priTN96	AACAGGTCTCATGTTTTAAGTTGGCCAGTGTGCTT
priTN99	AACAGGTCTCAGGCTCTAAGCACACTGGCCAACTT
priTN100	AACAGGTCTCACTGAGTTCACCTTGGAGCAGTTGA
priTN101	AACAGGTCTCAATGGCCCGCCAGTCTC
priTN102	AACAGGTCTCACCATCTCTTTCCAGTTCCACG
priTN119	TAGAAAGGCCTGGATTGATAATTTC
priTN120	TTGGACTAGATTTTGCTTGTGTACT
priTN121	TTGTGGACGTGTTCATGGCAATT
priTN122	ACTTGTGCTTTGGAGACTGTAAATAT
priTN123	GTATATACGAATCATGGATGCTTGT
priTN126	GTGACAACTTTGCCCCATCTCTCA

priTN133	AGAAAAAGTGTCCACCCGTG
priTN134	TCTTCTGACCACCTTCTCCG
priTN135	GGTCAGATTCTTGCAGGGAG
priTN136	TACACCATGAAAACAGGGCC
priDZ8	TGCTCTTCGCGCTGGCAGACATACTGTCCCAC
priDZ13	TGCTCTTCTGACCTGCCTATACGGCAGTGAAC
priMR423	GTGTGCTATGAGCGAGGTCACGCAA
priMR424	AAACTTGCGTGACCTCGCTCATAGC
priMR425	GTGTGAGCAGGGCAGAGTTCCAAG
priMR426	AAACCTTGGAACTCTGCCCTGCTC
priMR441	GTGTGGTGTCGACGATCAACGGCG
priMR442	AAACCGCCGTTGATCGTCGACACC
priMR443	GTGTGAGAGGTTAATTTCACCATG
priMR444	AAACCATGGTGAAATTAACCTCTC

Supplementary Table 11 – List of plasmids that I produced for this study

Plasmid name	Construct
pTN1	pGGA_BdMUTE promoter
pTN2	pGGA_ZmUBi promoter
pTN5	pGGF_PvUBip Hyg R cassete (wo/ BsaI r.site)
pTN7	pGGA_BdMUTE promoter (wo/BsaI r.site)
pTN12	pMOD_B2103_RLK1 guide 1,2
pTN13	pMOD_B2103_CST 1 guide 2,8
pTN14	pTRANS_250_RLK1
pTN15	pTRANS_250_CST1
pTN25	pYPQ131C_EF-hand Ca-binding protein - guide 2
pTN26	pYPQ132C_EF-hand Ca-binding protein - guide 8
pTN27	pYPQ131C_BdCST1 - guide 2
pTN28	pYPQ132C_BdCST1 - guide 9
pTN29	pYFQ142_EF-hand Ca-binding protein -guide 2/8
pTN30	pYFQ142_BdCST1 - guide 2/9
pTN31	pMDC32_EF-hand Ca-binding protein -guide 2/8
pTN32	pMDC32_BdCST1 - guide 2/9
pTN35	pGGA_BdPOXp
pTN41	pGGC_BdPOX(CDS)
pTN43	pGGZ004_BdMUTEp:BdPOX(CDS)-mCitrine
pTN44	pGGZ004_ZmUBip:BdPOX(CDS)-mCitrine
pTN45	pGGC_BdPOX
pTN46	pGGZ004_BdPOXp:BdPOX-mCitrine
pTN48	pGGZ004_BdPOXp:3xNLS-eGFP

Supplementary Table 12 - Hoyer's solution for sample mounting (light microscopy)

Component	Work concentration	For 100 ml
Gum arabic	NA	15 g
Chloral hydrate	20 mM	200 g
Glycerol	100 mM	20 ml
Water	NA	Up to 100 ml
Preparation: Add 15 g of gum arabic to 25 mL of water, heat up to 60 ℃ and stir overnight. Next day, add 200 g of chloral hydrate and 20 mL glycerol.		

Supplementary Table 13 - Emission and excitation wavelength (confocal microscopy)

Fluorescence	Ex (nm)	Em (nm)
mCitrine	514	520-570
eGFP	488	510-560
PI	561	600-650
Cell wall autofluorescence	405	490-550
Basic fuchsin	561	573-613
Safranin-o	488/561	530-560/570-600

Protocol 1: Heat-shock *E.coli* transformation

1. Remove competent cells from -80° and thaw on ice
2. Mix 50µl of competent cells with DNA (for plasmid retransformation, use 1-2 µl; for cloning/ligation, use 10-20µl)
3. Gently mix by tapping the tube and incubate on ice for 20min
4. Heat-shock at 42° for 1 min
5. Put back on ice for 2 min
6. Add 1 mL of LB (without antibiotics) and incubate shaking at 37° for 45-60 min.
7. Plate the bacteria on LB plates with respective antibiotic selection (for plasmid retransformation plate 100 µl ; for ligation, pellet cells (30 sec at 8000 rcf), remove most of supernatant (~900 µl) and resuspend pellet in remaining 100 µl, plate whole suspension)
8. Incubate plates overnight at 37°C

Protocol 2: Heat-shock *Agrobacterium* transformation

1. Remove competent cells from -80°C
2. Add 2-5 µl of plasmid to the frozen cells
3. Thaw cells+plasmid at 37°C for 5 min
4. Gently tap the tube to mix DNA
5. Shock-freeze tubes in liquid nitrogen for 1 min
6. Heat-shock tubes again at 37°C for 5 min
7. Add 1mL of LB and grow cells for 2-4h at 28°C shaking
8. Pellet cells for 30sec at 8000 rcf, remove most of supernatant (~900ul) and resuspend pellet in remaining 100ul
9. Plate resuspended cells on LB with respective antibiotics

Tissue culture media (per liter)

CIM: 4.43 g of Linsmaier & Skoog basal media (LS; Duchefa Cat. No. L0230), 30 g sucrose, 600 µl CuSO4 (1mg/ml, Sigma/Merck, Cat.No. C3036), 50 0µl 2,4-D (5mg/ml in 1M KOH, Sigma/Merck, Cat. No. D7299). pH=5.8, add 2. 1g of Phytagel (Sigma/Merck, Cat. No. P8169).

Selection media: CIM + Hygromycin (40µg/ml, Roche, Cat. No. 10843555001) + Timentin (200µg/ml, Ticarcillin 2NA & Clavulanate Potassium from Duchefa, Cat. No. T0190).

CRM: 4.43 g of Linsmaier & Skoog basal media, 30 g maltose (Sigma/Merck, Cat. No. M5885), 600 µl CuSO4 (1mg/ml). pH adjusted to 5.8, add 2.1 g of Phytagel, autoclave, cool down and add timentin, hygromycin, and sterile kinetin solution (Sigma/Merck, Cat. No. K3253).

Rooting media: 4.3 g Murashige & Skoog including vitamins (Duchefa, Cat. No. M0222), 30 g sucrose. pH adjusted to 5.8, add 2.1g Phytagel, autoclave, cool down and add timentin (200 µg/ml final concentration).

9. Bibliography

Abrash, Emily, M. Ximena Anleu Gil, Juliana L. Matos, and Dominique C. Bergmann. 2018. "Conservation and Divergence of YODA MAPKKK Function in Regulation of Grass Epidermal Patterning." *Development* 145 (14):dev.165860.

Acharya, Biswa R., Byeong Wook Jeon, Wei Zhang, and Sarah M. Assmann. 2013. "Open Stomata 1 (OST1) Is Limiting in Abscisic Acid Responses of Arabidopsis Guard Cells." *New Phytologist*. 200 (4):1049-1063.

Adrian, Jessika, Jessica Chang, Catherine E. Ballenger, Bastiaan O. R. Bargmann, Julien Alassimone, Kelli A. Davies, On Sun Lau, et al. 2015. "Transcriptome Dynamics of the Stomatal Lineage: Birth, Amplification, and Termination of a Self-Renewing Population." *Developmental Cell* 33 (1): 107–18.

Ahmad, Khwaja J. 1964. "Cuticular Studies in Solanaceae." *Canadian Journal of Botany. Journal Canadien de Botanique* 42 (7): 793–803.

Amsbury, Sam, Lee Hunt, Nagat Elhaddad, Alice Baillie, Marjorie Lundgren, Yves Verhertbruggen, Henrik V. Scheller, J. Paul Knox, Andrew J. Fleming, and Julie E. Gray. 2016. "Stomatal Function Requires Pectin De-Methyl-Esterification of the Guard Cell Wall." *Current Biology: CB* 26 (21): 2899–2906.

Andama, Joackin B., Kadis Mujiono, Yuko Hojo, Tomonori Shinya, and Ivan Galis. 2020. "Nonglandular Silicified Trichomes Are Essential for Rice Defense against Chewing Herbivores." *Plant, Cell and Environment* 43 (9): 2019–32.

Ando, Eigo, and Toshinori Kinoshita. 2018. "Red Light-Induced Phosphorylation of Plasma Membrane H+-ATPase in Stomatal Guard Cells." *Plant Physiology* 178 (2): 838–49.

Andrés, Zaida, Javier Pérez-Hormaeche, Eduardo O. Leidi, Kathrin Schlücking, Leonie Steinhorst, Deirdre H. McLachlan, Karin Schumacher, et al. 2014. "Control of Vacuolar Dynamics and Regulation of Stomatal Aperture by Tonoplast Potassium Uptake." *Proceedings of the National Academy of Sciences of the United States of America* 111 (17): E1806-14.

Angeles-Shim, Rosalyn B., Kenji Asano, Tomonori Takashi, Junghyun Shim, Takeshi Kuroha, Madoka Ayano, and Motoyuki Ashikari. 2012. "A WUSCHEL-Related Homeobox 3B Gene, Depilous (Dep), Confers Glabrousness of Rice Leaves and Glumes." *Rice* 5 (1): 28.

Avila, R. T., A. A. Cardoso, W. L. de Almeida, and L. C. Costa. 2020. "Coffee Plants Respond to Drought and Elevated [CO2] through Changes in Stomatal Function, Plant Hydraulic Conductance, and Aquaporin Expression." *Environmental And*. 177 (2020): 104148.

Bachle, Seton, and Jesse B. Nippert. 2022. "Climate Variability Supersedes Grazing to Determine the Anatomy and Physiology of a Dominant Grassland Species." *Oecologia* 198 (2): 345–55.

Bai, Jiaqi, Xuan Wang, Xiaohui Yao, Xiaochen Chen, Kai Lu, Yiqun Hu, Zuodong Wang, Yanjie Mu, Liyuan Zhang, and Hansong Dong. 2021. "Rice Aquaporin OsPIP2;2 Is a Water-Transporting Facilitator in Relevance to Drought-Tolerant Responses." *Plant Direct* 5 (8): e338.

Bai, Ling, Guozeng Zhang, Yun Zhou, Zhaopei Zhang, Wei Wang, Yanyan Du, Zhongyi Wu, and Chun-Peng Song. 2009. "Plasma Membrane-Associated Proline-Rich Extensin-like Receptor Kinase 4, a Novel Regulator of Ca2 Signalling, Is Required for Abscisic Acid Responses InArabidopsis Thaliana." *The Plant Journal* 60 (2): 314-327.

Baldacci-Cresp, Fabien, Corentin Spriet, Laure Twyffels, Anne-Sophie Blervacq, Godfrey Neutelings, Marie Baucher, and Simon Hawkins. 2020. "A Rapid and Quantitative Safranin-Based Fluorescent Microscopy Method to Evaluate Cell Wall Lignification." *The Plant Journal: For Cell and Molecular Biology* 102 (5): 1074–89.

Batool, Sundas, Veli Vural Uslu, Hala Rajab, Nisar Ahmad, Rainer Waadt, Dietmar Geiger, Mario Malagoli, et al. 2018. "Sulfate Is Incorporated into Cysteine to Trigger ABA Production and Stomatal Closure." *The Plant Cell* 30 (12): 2973–87.

Bertolino, Lígia T., Robert S. Caine, and Julie E. Gray. 2019. "Impact of Stomatal Density and Morphology on Water-Use Efficiency in a Changing World." *Frontiers in Plant Science* 10: 225.

Bond, J., L. Donaldson, S. Hill, and K. Hitchcock. 2008. "Safranine Fluorescent Staining of Wood Cell Walls." *Biotechnic and Histochemistry: Official Publication of the Biological Stain Commission* 83 (3–4): 161–71.

Bourdais, Gildas, Paweł Burdiak, Adrien Gauthier, Lisette Nitsch, Jarkko Salojärvi, Channabasavangowda Rayapuram, Niina Idänheimo, et al. 2015. "Large-Scale Phenomics Identifies Primary and Fine-Tuning Roles for CRKs in Responses Related to Oxidative Stress." *PLoS Genetics* 11 (7): e1005373.

Bragg, Jennifer N., Jiajie Wu, Sean P. Gordon, Mara E. Guttman, Roger Thilmony, Gerard R. Lazo, Yong Q. Gu, and John P. Vogel. 2012. "Generation and Characterization of the Western Regional Research Center Brachypodium T-DNA Insertional Mutant Collection." *PloS One* 7 (9): e41916.

Brandt, Benjamin, Dennis E. Brodsky, Shaowu Xue, Juntaro Negi, Koh Iba, Jaakko Kangasjärvi, Majid Ghassemian, Aaron B. Stephan, Honghong Hu, and Julian I. Schroeder. 2012. "Reconstitution of Abscisic Acid Activation of SLAC1 Anion Channel by CPK6 and OST1 Kinases and Branched ABI1 PP2C Phosphatase Action." *Proceedings of the National Academy of Sciences of the United States of America* 109 (26): 10593–98.

Brett, S., and C. K. Y. Ng. 2022. "A Simple Method for the Isolation of Leaf Epidermis from Graminaceous Species for Studying Stomatal Physiology." *Cereal Research Communications* 50 (1): 53–58.

Brodribb, Timothy J., and Scott A. M. McAdam. 2017. "Evolution of the Stomatal Regulation of Plant Water Content." *Plant Physiology* 174 (2): 639–49.

Büchsenschütz, Kai, Irene Marten, Dirk Becker, Katrin Philippar, Peter Ache, and Rainer Hedrich. 2005. "Differential Expression of K+ Channels between Guard Cells and Subsidiary Cells within the Maize Stomatal Complex." *Planta* 222 (6): 968–76.

Bustos-Segura, Carlos, and William J. Foley. 2018. "Foliar Terpene Chemotypes and Herbivory Determine Variation in Plant Volatile Emissions." *Journal of Chemical Ecology* 44 (1): 51–61.

Cai, Kewei, Huixin Liu, Song Chen, Yi Liu, Xiyang Zhao, and Su Chen. 2021. "Genome-Wide Identification and Analysis of Class III Peroxidases in Betula Pendula." *BMC Genomics* 22 (1): 314.

Caine, Robert S., Xiaojia Yin, Jennifer Sloan, Emily L. Harrison, Umar Mohammed, Timothy Fulton, Akshaya K. Biswal, et al. 2018. "Rice with Reduced Stomatal Density Conserves Water and Has Improved Drought Tolerance under Future Climate Conditions." *The New Phytologist*, 221 (1): 371-384.

Cal, Andrew J., Dongcheng Liu, Ramil Mauleon, Yue-Ie Caroline Hsing, and Rachid Serraj. 2013. "Transcriptome Profiling of Leaf Elongation Zone under Drought in Contrasting Rice Cultivars." *PloS One* 8 (1): e54537.

Cardoso, Paulo, Tiago Nunes, Ricardo Pinto, Carina Sá, Diana Matos, and Etelvina Figueira. 2020. "Rhizobium Response to Sole and Combined Exposure to Cadmium and the Phytocompounds Alpha-Pinene and Quercetin." *Ecotoxicology* 29 (4): 444–58.

Carlson, Jane E., Christopher A. Adams, and Kent E. Holsinger. 2016. "Intraspecific Variation in Stomatal Traits, Leaf Traits and Physiology Reflects Adaptation along Aridity Gradients in a South African Shrub." *Annals of Botany* 117 (1): 195–207.

Cartwright, Heather N., John A. Humphries, and Laurie G. Smith. 2009. "PAN1: A Receptor-like Protein That Promotes Polarization of an Asymmetric Cell Division in Maize." *Science* 323 (5914): 649–51.

Catalán, Pilar, and John P. Vogel. 2020. "Advances on Genomics, Biology, Ecology and Evolution of Brachypodium, a Bridging Model Grass System for Cereals and Biofuel Grasses." *The New Phytologist* 227 (6): 1587–90.

Čermák, Tomáš, Shaun J. Curtin, Javier Gil-Humanes, Radim Čegan, Thomas J. Y. Kono, Eva Konečná, Joseph J. Belanto, et al. 2017. "A Multipurpose Toolkit to Enable Advanced Genome Engineering in Plants." *The Plant Cell* 29 (6): 1196–1217.

Chai, Rongfan, Jiafu Mao, Haishan Chen, Yaoping Wang, Xiaoying Shi, Mingzhou Jin, Tianbao Zhao, Forrest M. Hoffman, Daniel M. Ricciuto, and Stan D. Wullschleger. 2021. "Human-

Caused Long-Term Changes in Global Aridity." *Npj Climate and Atmospheric Science* 4 (1): 1–8.

Chater, Caspar C. C., Robert S. Caine, Andrew J. Fleming, and Julie E. Gray. 2017. "Origins and Evolution of Stomatal Development." *Plant Physiology* 174 (2): 624–38.

Chater, Caspar C., Robert S. Caine, Marta Tomek, Simon Wallace, Yasuko Kamisugi, Andrew C. Cuming, Daniel Lang, et al. 2016. "Origin and Function of Stomata in the Moss Physcomitrella Patens." *Nature Plants* 2 (November): 16179.

Chen, Dong-Hua, Hui-Ping Liu, and Chun-Long Li. 2019. "Calcium-Dependent Protein Kinase CPK9 Negatively Functions in Stomatal Abscisic Acid Signaling by Regulating Ion Channel Activity in Arabidopsis." *Plant Molecular Biology* 99 (1–2): 113–22.

Chen, Taiyu, Huan Wu, Jiemin Wu, Xiaolei Fan, Xianghua Li, and Yongjun Lin. 2017. "Absence of OsβCA1 Causes a CO2 Deficit and Affects Leaf Photosynthesis and the Stomatal Response to CO2 in Rice." *The Plant Journal: For Cell and Molecular Biology* 90 (2): 344–57.

Chen, Yintong, Wenlong Li, Joseph A. Turner, and Charles T. Anderson. 2021. "PECTATE LYASE LIKE12 Patterns the Guard Cell Wall to Coordinate Turgor Pressure and Wall Mechanics for Proper Stomatal Function in Arabidopsis." *The Plant Cell*, 33 (9): 3134-3150.

Chen, Zhong-Hua, Guang Chen, Fei Dai, Yizhou Wang, Adrian Hills, Yong-Ling Ruan, Guoping Zhang, Peter J. Franks, Eviatar Nevo, and Michael R. Blatt. 2017. "Molecular Evolution of Grass Stomata." *Trends in Plant Science* 22 (2): 124–39.

Clifton, Olivia E., Danica L. Lombardozzi, Arlene M. Fiore, Fabien Paulot, and Larry W. Horowitz. 2020. "Stomatal Conductance Influences Interannual Variability and Long-Term Changes in Regional Cumulative Plant Uptake of Ozone." *Environmental Research Letters: ERL [Web Site]* 15 (11): 114059.

Coomey, Joshua H., and Samuel P. Hazen. 2015. "Brachypodium Distachyon as a Model Species to Understand Grass Cell Walls." *Genetics and Genomics of Brachypodium*. Plant Genetics and Genomics: Crops and Models, v 18. Springer, Cham.

Coomey, Joshua H., Richard Sibout, and Samuel P. Hazen. 2020. “Grass Secondary Cell Walls, Brachypodium Distachyon as a Model for Discovery.” *The New Phytologist* 227 (6): 1649–67.

Cosgrove, D. J. 2000. “Loosening of Plant Cell Walls by Expansins.” *Nature* 407 (6802): 321–26.

Cosio, Claudia, and Christophe Dunand. 2009. “Specific Functions of Individual Class III Peroxidase Genes.” *Journal of Experimental Botany* 60 (2): 391–408.

Cui, Long-Gang, Jun-Xiang Shan, Min Shi, Ji-Ping Gao, and Hong-Xuan Lin. 2015. “DCA1 Acts as a Transcriptional Co-Activator of DST and Contributes to Drought and Salt Tolerance in Rice.” *PLoS Genetics* 11 (10): e1005617.

Cui, Yaning, Yanxia Zhao, Yuqing Lu, Xiao Su, Yingying Chen, Yingbai Shen, Jinxing Lin, and Xiaojuan Li. 2021a. “In Vivo Single-Particle Tracking of the Aquaporin AtPIP2;1 in Stomata Reveals Cell Type-Specific Dynamics.” *Plant Physiology* 185 (4): 1666–81.

———. 2021b. “In Vivo Single-Particle Tracking of the Aquaporin AtPIP2;1 in Stomata Reveals Cell Type-Specific Dynamics.” *Plant Physiology* 185 (4): 1666–81.

Daloso, Danilo M., David B. Medeiros, Letícia Dos Anjos, Takuya Yoshida, Wagner L. Araújo, and Alisdair R. Fernie. 2017. “Metabolism within the Specialized Guard Cells of Plants.” *The New Phytologist* 216 (4): 1018–33.

Damerum, Annabelle, Hazel K. Smith, G. J. J. Clarkson, Maria José Truco, Richard W. Michelmore, and Gail Taylor. 2021. “The Genetic Basis of Water-use Efficiency and Yield in Lettuce.” *BMC Plant Biology* 21 (1): 1–14.

Decreux, Annabelle, and Johan Messiaen. 2005. “Wall-Associated Kinase WAK1 Interacts with Cell Wall Pectins in a Calcium-Induced Conformation.” *Plant and Cell Physiology* 46 (2): 268–78.

Devireddy, Amith R., Jimmie Arbogast, and Ron Mittler. 2020. “Coordinated and Rapid Whole-Plant Systemic Stomatal Responses.” *The New Phytologist* 225 (1): 21–25.

Devireddy, Amith R., Sara I. Zandalinas, Aurelio Gómez-Cadenas, Eduardo Blumwald, and Ron Mittler. 2018. “Coordinating the Overall Stomatal Response of Plants: Rapid Leaf-to-Leaf Communication during Light Stress.” *Science Signaling* 11 (518): eaam9514.

Ding, Lei, Thomas Milhiet, Boris Parent, Adel Meziane, François Tardieu, and François Chaumont. 2022. "The Plasma Membrane Aquaporin ZmPIP2;5 Enhances the Sensitivity of Stomatal Closure to Water Deficit." *Plant, Cell and Environment* 45 (4): 1146–56.

Donaldson, Lloyd. 2020. "Autofluorescence in Plants." *Molecules* 25 (10):2393.

Dow, Graham J., Joseph A. Berry, and Dominique C. Bergmann. 2014. "The Physiological Importance of Developmental Mechanisms That Enforce Proper Stomatal Spacing in Arabidopsis Thaliana." *The New Phytologist* 201 (4): 1205–17.

Draper, J., L. A. Mur, G. Jenkins, G. C. Ghosh-Biswas, P. Bablak, R. Hasterok, and A. P. Routledge. 2001. "Brachypodium Distachyon. A New Model System for Functional Genomics in Grasses." *Plant Physiology* 127 (4): 1539–55.

Dreyer, L., Rainer Hedrich, Monica Bregante, Ingo Dreyer, and Franco Gambale. 1995. "The Voltage-Dependent Potassium-Uptake Channel of Corn Coleoptiles Has Permeation Properties Different from Other K^+ Channels." *Planta* 197 (1): 193–99.

Dunn, Jessica, Lee Hunt, Mana Afsharinafar, Moaed Al Meselmani, Alice Mitchell, Rhian Howells, Emma Wallington, Andrew J. Fleming, and Julie E. Gray. 2019. "Reduced Stomatal Density in Bread Wheat Leads to Increased Water-Use Efficiency." *Journal of Experimental Botany* 70 (18): 4737-4748.

Ehonen, Sanna, Teemu Holtta, and Jaakko Kangasjärvi. 2020. "Systemic Signaling in the Regulation of Stomatal Conductance." *Plant Physiology* 182 (4): 1829-1832.

Elliott-Kingston, Caroline, Matthew Haworth, Jon M. Yearsley, Sven P. Batke, Tracy Lawson, and Jennifer C. McElwain. 2016. "Does Size Matter? Atmospheric CO2 May Be a Stronger Driver of Stomatal Closing Rate Than Stomatal Size in Taxa That Diversified under Low CO2." *Frontiers in Plant Science* 7 (August): 1253.

Engineer, Cawas B., Mimi Hashimoto-Sugimoto, Juntaro Negi, Maria Israelsson-Nordström, Tamar Azoulay-Shemer, Wouter-Jan Rappel, Koh Iba, and Julian I. Schroeder. 2016. "CO2 Sensing and CO2 Regulation of Stomatal Conductance: Advances and Open Questions." *Trends in Plant Science* 21 (1): 16–30.

Eyland, David, Jelle van Wesemael, Tracy Lawson, and Sebastien Carpentier. 2021. "The Impact of Slow Stomatal Kinetics on Photosynthesis and Water Use Efficiency under Fluctuating Light." *Plant Physiology*, 186 (2): 998-1012.

Facette, Michelle R., Yeri Park, Dena Sutimantanapi, Anding Luo, Heather N. Cartwright, Bing Yang, Eric J. Bennett, Anne W. Sylvester, and Laurie G. Smith. 2015. "The SCAR/WAVE Complex Polarizes PAN Receptors and Promotes Division Asymmetry in Maize." *Nature Plants* 1 (2): 14024.

Fairley-Grenot, K. A., and S. M. Assmann. 1992. "Whole-Cell K+ Current across the Plasma Membrane of Guard Cells from a Grass: Zea Mays." *Planta* 186 (2): 282–93.

Faralli, Michele, Jack Matthews, and Tracy Lawson. 2019. "Exploiting Natural Variation and Genetic Manipulation of Stomatal Conductance for Crop Improvement." *Current Opinion in Plant Biology* 49 (June): 1–7.

Faria, T., J. I. García-Plazaola, A. Abadía, S. Cerasoli, J. S. Pereira, and M. M. Chaves. 1996. "Diurnal Changes in Photoprotective Mechanisms in Leaves of Cork Oak (Quercus Suber) during Summer." *Tree Physiology* 16 (1_2): 115–23.

Fei, Shang, Mou Wenbin, Wu Hao, Xu Furong, Xiang Chunyan, and Wang Jianfei. 2020. "Paper New Allele of HL6 Regulates Trichome Elongation in Rice." *Rice Science* 27 (6): 480–92.

Feng, Lingyang, Muhammad Ali Raza, Zhongchuan Li, Yuankai Chen, Muhammad Hayder Bin Khalid, Junbo Du, Weiguo Liu, et al. 2018. "The Influence of Light Intensity and Leaf Movement on Photosynthesis Characteristics and Carbon Balance of Soybean." *Frontiers in Plant Science* 9: 1952.

Food and Agriculture Organization of the United Nations. 2021. *World Food and Agriculture – Statistical Yearbook 2021*. Food & Agriculture Org.

Francoz, Edith, Philippe Ranocha, Huan Nguyen-Kim, Elisabeth Jamet, Vincent Burlat, and Christophe Dunand. 2015. "Roles of Cell Wall Peroxidases in Plant Development." *Phytochemistry* 112 (April): 15–21.

Franks, P. J., and G. D. Farquhar. 2001. "The Effect of Exogenous Abscisic Acid on Stomatal Development, Stomatal Mechanics, and Leaf Gas Exchange in Tradescantia Virginiana." *Plant Physiology* 125 (2): 935–42.

Franks, Peter J., and David J. Beerling. 2009. "Maximum Leaf Conductance Driven by CO2 Effects on Stomatal Size and Density over Geologic Time." *Proceedings of the National Academy of Sciences of the United States of America* 106 (25): 10343–47.

Franks, Peter J., Joseph A. Berry, Danica L. Lombardozzi, and Gordon B. Bonan. 2017. "Stomatal Function across Temporal and Spatial Scales: Deep-Time Trends, Land-Atmosphere Coupling and Global Models." *Plant Physiology* 174 (2): 583–602.

Franks, Peter J., Paul L. Drake, and David J. Beerling. 2009. "Plasticity in Maximum Stomatal Conductance Constrained by Negative Correlation between Stomatal Size and Density: An Analysis Using Eucalyptus Globulus." *Plant, Cell and Environment* 32 (12): 1737–48.

Franks, Peter J., and Graham D. Farquhar. 2007. "The Mechanical Diversity of Stomata and Its Significance in Gas-Exchange Control." *Plant Physiology* 143 (1): 78–87.

Fujii, Hiroaki, Viswanathan Chinnusamy, Americo Rodrigues, Silvia Rubio, Regina Antoni, Sang-Youl Park, Sean R. Cutler, Jen Sheen, Pedro L. Rodriguez, and Jian-Kang Zhu. 2009. "In Vitro Reconstitution of an Abscisic Acid Signalling Pathway." *Nature* 462 (7273): 660–64.

Galdon-Armero, Javier, Mateu Fullana-Pericas, Pere A. Mulet, Miquel A. Conesa, Cathie Martin, and Jeroni Galmes. 2018. "The Ratio of Trichomes to Stomata Is Associated with Water Use Efficiency InSolanum Lycopersicum(Tomato)." *The Plant Journal* 96 (3): 607-619.

Gao, Yong-Qiang, Wei-Hua Wu, and Yi Wang. 2017. "The K+ Channel KZM2 Is Involved in Stomatal Movement by Modulating Inward K+ Currents in Maize Guard Cells." *The Plant Journal: For Cell and Molecular Biology* 92 (4): 662–75.

García-Plazaola, José Ignacio, Beatriz Fernández-Marín, Stephen O. Duke, Antonio Hernández, Fernando López-Arbeloa, and José María Becerril. 2015. "Autofluorescence: Biological Functions and Technical Applications." *Plant Science: An International Journal of Experimental Plant Biology* 236 (July): 136–45.

Geiger, D., S. Scherzer, P. Mumm, I. Marten, P. Ache, S. Matschi, A. Liese, et al. 2010. "Guard Cell Anion Channel SLAC1 Is Regulated by CDPK Protein Kinases with Distinct Ca2+ Affinities." *Proceedings of the National Academy of Sciences of the United States of America* 107 (17): 8023–28.

Geiger, Dietmar, Tobias Maierhofer, Khaled A. S. Al-Rasheid, Sönke Scherzer, Patrick Mumm, Anja Liese, Peter Ache, et al. 2011. "Stomatal Closure by Fast Abscisic Acid Signaling Is Mediated by the Guard Cell Anion Channel SLAH3 and the Receptor RCAR1." *Science Signaling* 4 (173): ra32.

Geiger, Dietmar, Sönke Scherzer, Patrick Mumm, Annette Stange, Irene Marten, Hubert Bauer, Peter Ache, et al. 2009. "Activity of Guard Cell Anion Channel SLAC1 Is Controlled by Drought-Stress Signaling Kinase-Phosphatase Pair." *Proceedings of the National Academy of Sciences of the United States of America* 106 (50): 21425–30.

Giuliani, Rita, Nuria Koteyeva, Elena Voznesenskaya, Marc A. Evans, Asaph B. Cousins, and Gerald E. Edwards. 2013. "Coordination of Leaf Photosynthesis, Transpiration, and Structural Traits in Rice and Wild Relatives (Genus Oryza)." *Plant Physiology* 162 (3): 1632–51.

Głazowska, Sylwia, Emiko Murozuka, Daniel P. Persson, Pedro Humberto Castro, and Jan K. Schjoerring. 2018. "Silicon Affects Seed Development and Leaf Macrohair Formation in Brachypodium Distachyon." *Physiologia Plantarum* 163 (2): 231–46.

Gomes, D., A. Agasse, P. Thiébaud, S. Delrot, H. Gerós, and F. Chaumont. 2009. "Aquaporins Are Multifunctional Water and Solute Transporters Highly Divergent in Living Organisms." *Biochimica et Biophysica Acta* 1788 (6): 1213–28.

Gommers, Charlotte. 2020. "Keep Cool and Open Up: Temperature-Induced Stomatal Opening." *Plant Physiology* 182 (3): 1188-1189.

González Moreno, Ana, Abel de Cózar, Pilar Prieto, Eva Domínguez, and Antonio Heredia. 2022. "Radiationless Mechanism of UV Deactivation by Cuticle Phenolics in Plants." *Nature Communications* 13 (1): 1786.

Grantz, D. A., and E. Zeiger. 1986. "Stomatal Responses to Light and Leaf-Air Water Vapor Pressure Difference Show Similar Kinetics in Sugarcane and Soybean." *Plant Physiology* 81 (3): 865–68.

Gray, Antonia, Le Liu, and Michelle Facette. 2020. "Flanking Support: How Subsidiary Cells Contribute to Stomatal Form and Function." *Frontiers in Plant Science* 11: 881.

Greve, P., T. Kahil, J. Mochizuki, T. Schinko, Y. Satoh, P. Burek, G. Fischer, et al. 2018. "Global Assessment of Water Challenges under Uncertainty in Water Scarcity Projections." *Nature Sustainability* 1 (9): 486–94.

Grondin, Alexandre, Olivier Rodrigues, Lionel Verdoucq, Sylvain Merlot, Nathalie Leonhardt, and Christophe Maurel. 2015. "Aquaporins Contribute to ABA-Triggered Stomatal Closure through OST1-Mediated Phosphorylation." *The Plant Cell* 27 (7): 1945–54.

Gruber, Benjamin D., Emmanuel Delhaize, Alan E. Richardson, Ute Roessner, Richard A. James, Susan M. Howitt, and Peter R. Ryan. 2011. "Characterisation of HvALMT1 Function in Transgenic Barley Plants." *Functional Plant Biology: FPB* 38 (2): 163–75.

Gruber, Benjamin D., Peter R. Ryan, Alan E. Richardson, Stephen D. Tyerman, Sunita Ramesh, Diane M. Hebb, Susan M. Howitt, and Emmanuel Delhaize. 2010. "HvALMT1 from Barley Is Involved in the Transport of Organic Anions." *Journal of Experimental Botany* 61 (5): 1455–67.

Grünig, Marc, Pierluigi Calanca, Dominique Mazzi, and Loïc Pellissier. 2020. "Inflection Point in Climatic Suitability of Insect Pest Species in Europe Suggests Non-Linear Responses to Climate Change." *Global Change Biology* 26 (11): 6338–49.

Haberstroh, Simon, Jürgen Kreuzwieser, Raquel Lobo-do-Vale, Maria C. Caldeira, Maren Dubbert, and Christiane Werner. 2018. "Terpenoid Emissions of Two Mediterranean Woody Species in Response to Drought Stress." *Frontiers in Plant Science* 9 (July): 1071.

Hachez, Charles, Kyoko Ohashi-Ito, Juan Dong, and Dominique C. Bergmann. 2011. "Differentiation of Arabidopsis Guard Cells: Analysis of the Networks Incorporating the Basic Helix-Loop-Helix Transcription Factor, FAMA." *Plant Physiology* 155 (3): 1458–72.

Hall, Casey R., Vaibhav Dagg, Jamie M. Waterman, and Scott N. Johnson. 2020. "Silicon Alters Leaf Surface Morphology and Suppresses Insect Herbivory in a Model Grass Species." *Plants* 9 (5): 643.

Harley, Peter, Allyson Eller, Alex Guenther, and Russell K. Monson. 2014. "Observations and Models of Emissions of Volatile Terpenoid Compounds from Needles of Ponderosa Pine Trees Growing in Situ: Control by Light, Temperature and Stomatal Conductance." *Oecologia*. 176: 35-55.

Hashimoto-Sugimoto, Mimi, Takumi Higaki, Takashi Yaeno, Ayako Nagami, Mari Irie, Miho Fujimi, Megumi Miyamoto, et al. 2013. "A Munc13-like Protein in Arabidopsis Mediates H+-ATPase Translocation That Is Essential for Stomatal Responses." *Nature Communications* 4: 2215.

Hatfield, Ronald D., David M. Rancour, and Jane M. Marita. 2016. "Grass Cell Walls: A Story of Cross-Linking." *Frontiers in Plant Science* 7: 2056.

Haworth, Matthew, Giovanni Marino, Francesco Loreto, and Mauro Centritto. 2021. "Integrating Stomatal Physiology and Morphology: Evolution of Stomatal Control and Development of Future Crops." *Oecologia* 197: 867-883.

Haworth, Matthew, Charles P. Scutt, Cyril Douthe, Giovanni Marino, Marcos Thiago Gaudio Gomes, Francesco Loreto, Jaume Flexas, and Mauro Centritto. 2018. "Allocation of the Epidermis to Stomata Relates to Stomatal Physiological Control: Stomatal Factors Involved in the Evolutionary Diversification of the Angiosperms and Development of Amphistomaty." *Environmental and Experimental Botany* 151 (July): 55–63.

Heinen, Robert B., Gerd Patrick Bienert, David Cohen, Adrien S. Chevalier, Norbert Uehlein, Charles Hachez, Ralf Kaldenhoff, Didier Le Thiec, and François Chaumont. 2014. "Expression and Characterization of Plasma Membrane Aquaporins in Stomatal Complexes of Zea Mays." *Plant Molecular Biology* 86 (3): 335–50.

Hetherington, Alistair M., and F. Ian Woodward. 2003. "The Role of Stomata in Sensing and Driving Environmental Change." *Nature* 424 (6951): 901–8.

Higaki, Takumi, Mimi Hashimoto-Sugimoto, Kae Akita, Koh Iba, and Seiichiro Hasezawa. 2014. "Dynamics and Environmental Responses of PATROL1 in Arabidopsis Subsidiary Cells." *Plant and Cell Physiology* 55 (4): 773–80.

Higgins, Janet A., Paul C. Bailey, and David A. Laurie. 2010. "Comparative Genomics of Flowering Time Pathways Using Brachypodium Distachyon as a Model for the Temperate Grasses." *PLoS ONE* 5 (4): e10065.

Hill, Kathryn E., Greg R. Guerin, Robert S. Hill, and Jennifer R. Watling. 2014. "Temperature Influences Stomatal Density and Maximum Potential Water Loss through Stomata of Dodonaea Viscosa Subsp. Angustissima along a Latitude Gradient in Southern Australia." *Australian Journal of Botany* 68 (2): 657-665.

Höhner, Ricarda, Viviana Correa Galvis, Deserah D. Strand, Carsten Völkner, Moritz Krämer, Michaela Messer, Firdevs Dinc, et al. 2019. "Photosynthesis in Arabidopsis Is Unaffected by the Function of the Vacuolar K Channel TPK3." *Plant Physiology* 180 (3): 1322-1335.

Holzwart, Eleonore, Apolonio Ignacio Huerta, Nina Glöckner, Borja Garnelo Gómez, Friederike Wanke, Sebastian Augustin, Jana Christin Askani, Ann-Kathrin Schürholz, Klaus Harter, and Sebastian Wolf. 2018. "BRI1 Controls Vascular Cell Fate in the Arabidopsis Root through RLP44 and Phytosulfokine Signaling." *Proceedings of the National Academy of Sciences of the United States of America* 115 (46): 11838–43.

Hõrak, Hanna, Maija Sierla, Kadri Tõldsepp, Cun Wang, Yuh-Shuh Wang, Maris Nuhkat, Ervin Valk, et al. 2016. "A Dominant Mutation in the HT1 Kinase Uncovers Roles of MAP Kinases and GHR1 in CO2-Induced Stomatal Closure." *The Plant Cell* 28 (10): 2493–2509.

Hsia, Mon Mandy, Ronan O'Malley, Amy Cartwright, Rita Nieu, Sean P. Gordon, Sandra Kelly, Tina G. Williams, et al. 2017. "Sequencing and Functional Validation of the JGI Brachypodium Distachyon T-DNA Collection." *The Plant Journal: For Cell and Molecular Biology* 91 (3): 361–70.

Hsu, Po-Kai, Yohei Takahashi, Ebe Merilo, Alex Costa, Li Zhang, Klara Kernig, Katie H. Lee, and Julian I. Schroeder. 2021. "Raf-like Kinases and Receptor-like (Pseudo)Kinase GHR1 Are

Required for Stomatal Vapor Pressure Difference Response." *Proceedings of the National Academy of Sciences of the United States of America* 118 (47): e2107280118.

Hu, Honghong, Aurélien Boisson-Dernier, Maria Israelsson-Nordström, Maik Böhmer, Shaowu Xue, Amber Ries, Jan Godoski, Josef M. Kuhn, and Julian I. Schroeder. 2010. "Carbonic Anhydrases Are Upstream Regulators of CO2-Controlled Stomatal Movements in Guard Cells." *Nature Cell Biology* 12 (1): 87–93; sup pp 1-18.

Hu, Honghong, Mingqiu Dai, Jialing Yao, Benze Xiao, Xianghua Li, Qifa Zhang, and Lizhong Xiong. 2006. "Overexpressing a NAM, ATAF, and CUC (NAC) Transcription Factor Enhances Drought Resistance and Salt Tolerance in Rice." *Proceedings of the National Academy of Sciences of the United States of America* 103 (35): 12987–92.

Hua, Deping, Cun Wang, Junna He, Hui Liao, Ying Duan, Ziqiang Zhu, Yan Guo, Zhizhong Chen, and Zhizhong Gong. 2012. "A Plasma Membrane Receptor Kinase, GHR1, Mediates Abscisic Acid- and Hydrogen Peroxide-Regulated Stomatal Movement in Arabidopsis." *The Plant Cell* 24 (6): 2546–61.

Huang, Shouguang, Rainer Waadt, Maris Nuhkat, Hannes Kollist, Rainer Hedrich, and M. Rob G. Roelfsema. 2019. "Calcium Signals in Guard Cells Enhance the Efficiency by Which Abscisic Acid Triggers Stomatal Closure." *The New Phytologist* 224 (1): 177–87.

Huang, Xin-Yuan, Dai-Yin Chao, Ji-Ping Gao, Mei-Zhen Zhu, Min Shi, and Hong-Xuan Lin. 2009. "A Previously Unknown Zinc Finger Protein, DST, Regulates Drought and Salt Tolerance in Rice via Stomatal Aperture Control." *Genes and Development* 23 (15): 1805–17.

Hughes, Jon, Christopher Hepworth, Chris Dutton, Jessica A. Dunn, Lee Hunt, Jennifer Stephens, Robbie Waugh, Duncan D. Cameron, and Julie E. Gray. 2017. "Reducing Stomatal Density in Barley Improves Drought Tolerance without Impacting on Yield." *Plant Physiology* 174 (2): 776–87.

Humphries, John A., Zuzana Vejlupkova, Anding Luo, Robert B. Meeley, Anne W. Sylvester, John E. Fowler, and Laurie G. Smith. 2011. "ROP GTPases Act with the Receptor-like Protein PAN1 to Polarize Asymmetric Cell Division in Maize." *The Plant Cell* 23 (6): 2273–84.

Hwang, Hyunsik, Jin-Young Yoon, Hana Cho, and Beom-Gi Kim. 2013. "OsKAT2 Is the Prevailing Functional Inward Rectifier Potassium Channels in Rice Guard Cell." *Plant Signaling and Behavior* 8 (12): e26643.

Hwang, Hyunsik, Jinyoung Yoon, Hyun Yeong Kim, Myung Ki Min, Jin-Ae Kim, Eun-Hye Choi, Wenzhi Lan, et al. 2013. "Unique Features of Two Potassium Channels, OsKAT2 and OsKAT3, Expressed in Rice Guard Cells." *PloS One* 8 (8): e72541.

Ikkonen, E. N., T. G. Shibaeva, E. Rosenqvist, and C. O. Ottosen. 2015. "Daily Temperature Drop Prevents Inhibition of Photosynthesis in Tomato Plants under Continuous Light." *Photosynthetica* 53 (3): 389–94.

Imes, Dennis, Patrick Mumm, Jennifer Böhm, Khaled A. S. Al-Rasheid, Irene Marten, Dietmar Geiger, and Rainer Hedrich. 2013. "Open Stomata 1 (OST1) Kinase Controls R-Type Anion Channel QUAC1 in Arabidopsis Guard Cells." *The Plant Journal: For Cell and Molecular Biology* 74 (3): 372–82.

Inamdar, J. A., and R. C. Patel. 1969. "Development of Stomata in Some Solanaceae." *Flora Oder Allgemeine Botanische Zeitung. Abt. B, Morphologie Und Geobotanik* 158 (4): 462–72.

Inoue, Shin-Ichiro, and Toshinori Kinoshita. 2017. "Blue Light Regulation of Stomatal Opening and the Plasma Membrane H+-ATPase." *Plant Physiology* 174 (2): 531–38.

Iurlaro, Andrea, Monica De Caroli, Erika Sabella, Mariarosaria De Pascali, Patrizia Rampino, Luigi De Bellis, Carla Perrotta, et al. 2016. "Drought and Heat Differentially Affect XTH Expression and XET Activity and Action in 3-Day-Old Seedlings of Durum Wheat Cultivars with Different Stress Susceptibility." *Frontiers in Plant Science* 7 (November): 1686.

Jacq, Adélaïde, Clémentine Pernot, Yves Martinez, Frédéric Domergue, Bruno Payré, Elisabeth Jamet, Vincent Burlat, and Valérie B. Pacquit. 2017. "The Arabidopsis Lipid Transfer Protein 2 (AtLTP2) Is Involved in Cuticle-Cell Wall Interface Integrity and in Etiolated Hypocotyl Permeability." *Frontiers in Plant Science* 8 (February): 263.

Jahan, Eisrat, Jeffrey S. Amthor, Graham D. Farquhar, Richard Trethowan, and Margaret M. Barbour. 2014. "Variation in Mesophyll Conductance among Australian Wheat Genotypes." *Functional Plant Biology: FPB* 41 (6): 568–80.

Jangra, Raman, Sabrina C. Brunetti, Xutong Wang, Pooja Kaushik, Patrick J. Gulick, Nora A. Foroud, Shucai Wang, and Jin Suk Lee. 2021. "Duplicated Antagonistic EPF Peptides Optimize Grass Stomatal Initiation." *Development* 148(16): dev199780.

Jasechko, Scott, Zachary D. Sharp, John J. Gibson, S. Jean Birks, Yi Yi, and Peter J. Fawcett. 2013. "Terrestrial Water Fluxes Dominated by Transpiration." *Nature* 496 (7445): 347–50.

Javelle, Marie, Vanessa Vernoud, Peter M. Rogowsky, and Gwyneth C. Ingram. 2011. "Epidermis: The Formation and Functions of a Fundamental Plant Tissue." *The New Phytologist* 189 (1): 17–39.

Jezek, Mareike, and Michael R. Blatt. 2017. "The Membrane Transport System of the Guard Cell and Its Integration for Stomatal Dynamics." *Plant Physiology* 174 (2): 487–519.

Jiang, Wei, Tao Tong, Wen Li, Zhenghong Huang, Guang Chen, Fanrong Zeng, Adeel Riaz, et al. 2022. "Molecular Evolution of Plant 14-3-3 Proteins and Function of Hv14-3-3A in Stomatal Regulation and Drought Tolerance." *Plant and Cell Physiology* 00 (0): 1-16.

Jones, Louise, Jennifer L. Milne, David Ashford, Maureen C. McCann, and Simon J. McQueen-Mason. 2005. "A Conserved Functional Role of Pectic Polymers in Stomatal Guard Cells from a Range of Plant Species." *Planta* 221 (2): 255–64.

Jung, Johannes, and Klaus Grossmann. 1985. "Effectiveness of New Terpenoid Derivatives, Abscisic Acid and Its Methyl Ester on Transpiration and Leaf Senescence of Barley." *Journal of Plant Physiology* 121 (4): 361–67.

Kanaoka, Masahiro M., Lynn Jo Pillitteri, Hiroaki Fujii, Yuki Yoshida, Naomi L. Bogenschutz, Junji Takabayashi, Jian-Kang Zhu, and Keiko U. Torii. 2008. "SCREAM/ICE1 and SCREAM2 Specify Three Cell-State Transitional Steps Leading to Arabidopsis Stomatal Differentiation." *The Plant Cell* 20 (7): 1775–85.

Kapp, Nikki, William J. Barnes, Tom L. Richard, and Charles T. Anderson. 2015. "Imaging with the Fluorogenic Dye Basic Fuchsin Reveals Subcellular Patterning and Ecotype Variation

of Lignification in Brachypodium Distachyon." *Journal of Experimental Botany* 66 (14): 4295–4304.

Karabourniotis, George, Georgios Liakopoulos, Dimosthenis Nikolopoulos, and Panagiota Bresta. 2020. "Protective and Defensive Roles of Non-Glandular Trichomes against Multiple Stresses: Structure–Function Coordination." *Research Journal of Forestry* 31 (1): 1–12.

Kavanová, Monika, Fernando Alfredo Lattanzi, Agustín Alberto Grimoldi, and Hans Schnyder. 2006. "Phosphorus Deficiency Decreases Cell Division and Elongation in Grass Leaves." *Plant Physiology* 141 (2): 766–75.

Kim, Tae-Houn, Maik Böhmer, Honghong Hu, Noriyuki Nishimura, and Julian I. Schroeder. 2010. "Guard Cell Signal Transduction Network: Advances in Understanding Abscisic Acid, CO2, and Ca2+ Signaling." *Annual Review of Plant Biology* 61: 561–91.

Kimura, Sachie, Cezary Waszczak, Kerri Hunter, and Michael Wrzaczek. 2017. "Bound by Fate: The Role of Reactive Oxygen Species in Receptor-Like Kinase Signaling." *The Plant Cell* 29 (4): 638–54.

Kinoshita, T., M. Doi, N. Suetsugu, T. Kagawa, M. Wada, and K. Shimazaki. 2001. "Phot1 and Phot2 Mediate Blue Light Regulation of Stomatal Opening." *Nature* 414 (6864): 656–60.

Koers, Sandra, Aysin Guzel-Deger, Irene Marten, and M. Rob G. Roelfsema. 2011. "Barley Mildew and Its Elicitor Chitosan Promote Closed Stomata by Stimulating Guard-Cell S-Type Anion Channels." *The Plant Journal: For Cell and Molecular Biology* 68 (4): 670–80.

Kohorn, Bruce D., and Susan L. Kohorn. 2012. "The Cell Wall-Associated Kinases, WAKs, as Pectin Receptors." *Frontiers in Plant Science* 3 (May): 88.

Kolbe, Allison R., Thomas P. Brutnell, Asaph B. Cousins, and Anthony J. Studer. 2018. "Carbonic Anhydrase Mutants in Zea Mays Have Altered Stomatal Responses to Environmental Signals." *Plant Physiology* 177 (3): 980–89.

Kollist, Hannes, Maris Nuhkat, and M. Rob G. Roelfsema. 2014. "Closing Gaps: Linking Elements That Control Stomatal Movement." *The New Phytologist* 203 (1): 44–62.

Kong, Dexin, Xuan Pan, Yifeng Jing, Yongping Zhao, Yaping Duan, Juan Yang, Baobao Wang, et al. 2021. "ZmSPL10/14/26 Are Required for Epidermal Hair Cell Fate Specification on Maize Leaf." *The New Phytologist* 230 (4): 1533-1549.

Koornneef, Maarten, and David Meinke. 2010. "The Development of Arabidopsis as a Model Plant." *The Plant Journal: For Cell and Molecular Biology* 61 (6): 909–21.

Kopaczyk, Joanna Maria, Joanna Warguła, and Tomasz Jelonek. 2020. "The Variability of Terpenes in Conifers under Developmental and Environmental Stimuli." *Environmental and Experimental Botany* 180 (December): 104197.

Krämer, Ute. 2015. "Planting Molecular Functions in an Ecological Context with Arabidopsis Thaliana." *ELife* 4 (March): e06100.

Kusumi, Kensuke, Ayana Hashimura, Yoshiko Yamamoto, Juntaro Negi, and Koh Iba. 2017. "Contribution of the S-Type Anion Channel SLAC1 to Stomatal Control and Its Dependence on Developmental Stage in Rice." *Plant and Cell Physiology* 58 (12): 2085–94.

Lamba, Shubhangi, Marianne Hall, Mats Räntfors, Nitin Chaudhary, Sune Linder, Danielle Way, Johan Uddling, and Göran Wallin. 2018. "Physiological Acclimation Dampens Initial Effects of Elevated Temperature and Atmospheric CO2 Concentration in Mature Boreal Norway Spruce." *Plant, Cell and Environment* 41 (2): 300–313.

Lampropoulos, Athanasios, Zoran Sutikovic, Christian Wenzl, Ira Maegele, Jan U. Lohmann, and Joachim Forner. 2013. "GreenGate---a Novel, Versatile, and Efficient Cloning System for Plant Transgenesis." *PloS One* 8 (12): e83043.

Lan, Tao, Yali Zheng, Zilong Su, Shibo Yu, Haibing Song, Xiaoya Zheng, Gege Lin, and Weiren Wu. 2019. "OsSPL10, a SBP-Box Gene, Plays a Dual Role in Salt Tolerance and Trichome Formation in Rice (Oryza Sativa L.)." *G3* 9 (12): 4107–14.

Lau, On Sun, Zhuojun Song, Zimin Zhou, Kelli A. Davies, Jessica Chang, Xin Yang, Shenqi Wang, et al. 2018. "Direct Control of SPEECHLESS by PIF4 in the High-Temperature Response of Stomatal Development." *Current Biology: CB* 28 (8): 1273-1280.e3.

Lawson, Tracy, and Michael R. Blatt. 2014. "Stomatal Size, Speed, and Responsiveness Impact on Photosynthesis and Water Use Efficiency." *Plant Physiology* 164 (4): 1556–70.

Lawson, Tracy, and Jack Matthews. 2020. "Guard Cell Metabolism and Stomatal Function." *Annual Review of Plant Biology* 71:273-302.

Lawson, Tracy, and Silvère Vialet-Chabrand. 2019. "Speedy Stomata, Photosynthesis and Plant Water Use Efficiency." *The New Phytologist* 221 (1): 93–98.

Leakey, Andrew D. B., John N. Ferguson, Charles P. Pignon, Alex Wu, Zhenong Jin, Graeme L. Hammer, and David B. Lobell. 2019. "Water Use Efficiency as a Constraint and Target for Improving the Resilience and Productivity of C3 and C4 Crops." *Annual Review of Plant Biology* 70 (April): 781–808.

Lee, Gun Woong, Sungbeom Lee, Moon-Soo Chung, Yeon Sim Jeong, and Byung Yeoup Chung. 2015. "Rice Terpene Synthase 20 (OsTPS20) Plays an Important Role in Producing Terpene Volatiles in Response to Abiotic Stresses." *Protoplasma* 252 (4): 997–1007.

Lee, Jae-Hyung, Jae-Hoon Jung, and Chung-Mo Park. 2017. "Light Inhibits COP1-Mediated Degradation of ICE Transcription Factors to Induce Stomatal Development in Arabidopsis." *The Plant Cell* 29 (11): 2817–30.

Lee, Miyoung, Yongwook Choi, Bo Burla, Yu-Young Kim, Byeongwook Jeon, Masayoshi Maeshima, Joo-Yeon Yoo, Enrico Martinoia, and Youngsook Lee. 2008. "The ABC Transporter AtABCB14 Is a Malate Importer and Modulates Stomatal Response to CO2." *Nature Cell Biology* 10 (10): 1217–23.

Lee, Sung Chul, Wen-Zhi Lan, Beom-Gi Kim, Legong Li, Yong Hwa Cheong, Girdhar K. Pandey, Guihua Lu, Bob B. Buchanan, and Sheng Luan. 2007. "A Protein Phosphorylation/Dephosphorylation Network Regulates a Plant Potassium Channel." *Proceedings of the National Academy of Sciences of the United States of America* 104 (40): 15959–64.

Leung, Jeffrey, Sylvain Merlot, and Jerome Giraudat. 1997. "The Arabidopsis ABSCISIC ACID-INSENSITIVE2 (ABI2) and ABI1 Genes Encode Homologous Protein Phosphatases 2C Involved in Abscisic Acid Signal Transduction." *The Plant Cell* 9 (5): 759-771.

Li, Jinjie, Bo Tang, Yingxiu Li, Chenguang Li, Minjie Guo, Haiyang Chen, Shichen Han, et al. 2021. "Rice SPL10 Positively Regulates Trichome Development through Expression of HL6 and Auxin-Related Genes." *Journal of Integrative Plant Biology* 63 (8): 1521–37.

Li, Xiangjun, Ying Yang, Jialing Yao, Guoxing Chen, Xianghua Li, Qifa Zhang, and Changyin Wu. 2009. "FLEXIBLE CULM 1 Encoding a Cinnamyl-Alcohol Dehydrogenase Controls Culm Mechanical Strength in Rice." *Plant Molecular Biology* 69 (6): 685–97.

Li, Xi-Dong, Yong-Qiang Gao, Wei-Hua Wu, Li-Mei Chen, and Yi Wang. 2022. "Two Calcium-Dependent Protein Kinases Enhance Maize Drought Tolerance by Activating Anion Channel ZmSLAC1 in Guard Cells." *Plant Biotechnology Journal* 20 (1): 143–57.

Liu, Jing, Fang Zhang, Jinjun Zhou, Fan Chen, Baoshan Wang, and Xianzhi Xie. 2012. "Phytochrome B Control of Total Leaf Area and Stomatal Density Affects Drought Tolerance in Rice." *Plant Molecular Biology* 78 (3): 289–300.

Liu, Tie, Kyoko Ohashi-Ito, and Dominique C. Bergmann. 2009. "Orthologs of Arabidopsis Thaliana Stomatal BHLH Genes and Regulation of Stomatal Development in Grasses." *Development* 136 (13): 2265–76.

Loreto, Francesco, Paola Pinelli, Fausto Manes, and Hannes Kollist. 2004. "Impact of Ozone on Monoterpene Emissions and Evidence for an Isoprene-like Antioxidant Action of Monoterpenes Emitted by Quercus Ilex Leaves." *Tree Physiology* 24 (4): 361–67.

Lowder, Levi G., Dengwei Zhang, Nicholas J. Baltes, Joseph W. Paul 3rd, Xu Tang, Xuelian Zheng, Daniel F. Voytas, Tzung-Fu Hsieh, Yong Zhang, and Yiping Qi. 2015. "A CRISPR/Cas9 Toolbox for Multiplexed Plant Genome Editing and Transcriptional Regulation." *Plant Physiology* 169 (2): 971–85.

Lupanga, Upendo, Rachel Röhrich, Jana Askani, Stefan Hilmer, Christiane Kiefer, Melanie Krebs, Takehiko Kanazawa, Takashi Ueda, and Karin Schumacher. 2020. "The Arabidopsis V-ATPase Is Localized to the TGN/EE via a Seed Plant-Specific Motif." *ELife* 9: eLife.60568.

Ma, Yue, Izabela Szostkiewicz, Arthur Korte, Danièle Moes, Yi Yang, Alexander Christmann, and Erwin Grill. 2009. "Regulators of PP2C Phosphatase Activity Function as Abscisic Acid Sensors." *Science* 324 (5930): 1064–68.

Maierhofer, Tobias, Marion Diekmann, Jan Niklas Offenborn, Christof Lind, Hubert Bauer, Kenji Hashimoto, Khaled A. S Al-Rasheid, et al. 2014. "Site- and Kinase-Specific Phosphorylation-Mediated Activation of SLAC1, a Guard Cell Anion Channel Stimulated by Abscisic Acid." *Science Signaling* 7 (342): ra86.

Marom, Ziv, Ilana Shtein, and Benny Bar-On. 2017. "Stomatal Opening: The Role of Cell-Wall Mechanical Anisotropy and Its Analytical Relations to the Bio-Composite Characteristics." *Frontiers in Plant Science* 8 (December): 2061.

Marten, Holger, Rainer Hedrich, and M. Rob G. Roelfsema. 2007. "Blue Light Inhibits Guard Cell Plasma Membrane Anion Channels in a Phototropin-Dependent Manner." *The Plant Journal: For Cell and Molecular Biology* 50 (1): 29–39.

Matsuda, Shuichi, Sho Takano, Moeko Sato, Kaoru Furukawa, Hidetaka Nagasawa, Shoko Yoshikawa, Jun Kasuga, et al. 2016. "Rice Stomatal Closure Requires Guard Cell Plasma Membrane ATP-Binding Cassette Transporter RCN1/OsABCG5." *Molecular Plant* 9 (3): 417–27.

Matthews, Jack S. A., Silvere Vialet-Chabrand, and Tracy Lawson. 2018. "Acclimation to Fluctuating Light Impacts the Rapidity of Response and Diurnal Rhythm of Stomatal Conductance." *Plant Physiology* 176 (3): 1939–51.

Matthews, Jack S. A., Silvere R. M. Vialet-Chabrand, and Tracy Lawson. 2017. "Diurnal Variation in Gas Exchange: The Balance between Carbon Fixation and Water Loss." *Plant Physiology* 174 (2): 614–23.

McAdam, Scott A. M., and Timothy J. Brodribb. 2012. "Stomatal Innovation and the Rise of Seed Plants." *Ecology Letters* 15 (1): 1–8.

McAdam, Scott A. M., Jeffrey G. Duckett, Frances C. Sussmilch, Silvia Pressel, Karen S. Renzaglia, Rainer Hedrich, Timothy J. Brodribb, and Amelia Merced. 2021. "Stomata: The Holey Grail of Plant Evolution." *American Journal of Botany* 108 (3): 366–71.

McAusland, Lorna, Silvère Vialet-Chabrand, Philip Davey, Neil R. Baker, Oliver Brendel, and Tracy Lawson. 2016. "Effects of Kinetics of Light-induced Stomatal Responses on Photosynthesis and Water-use Efficiency." *The New Phytologist* 211 (4): 1209–20.

Mega, Ryosuke, Fumitaka Abe, June-Sik Kim, Yuuri Tsuboi, Keisuke Tanaka, Hisato Kobayashi, Yoichi Sakata, et al. 2019. "Tuning Water-Use Efficiency and Drought Tolerance in Wheat Using Abscisic Acid Receptors." *Nature Plants* 5 (2): 153–59.

Merilo, Ebe, Pirko Jalakas, Kristiina Laanemets, Omid Mohammadi, Hanna Hõrak, Hannes Kollist, and Mikael Brosché. 2015. "Abscisic Acid Transport and Homeostasis in the Context of Stomatal Regulation." *Molecular Plant* 8 (9): 1321–33.

Merilo, Ebe, Indrek Jõesaar, Mikael Brosché, and Hannes Kollist. 2014. "To Open or to Close: Species-Specific Stomatal Responses to Simultaneously Applied Opposing Environmental Factors." *The New Phytologist* 202 (2): 499–508.

Meyer, Stefan, Patrick Mumm, Dennis Imes, Anne Endler, Barbara Weder, Khaled A. S. Al-Rasheid, Dietmar Geiger, Irene Marten, Enrico Martinoia, and Rainer Hedrich. 2010. "AtALMT12 Represents an R-Type Anion Channel Required for Stomatal Movement in Arabidopsis Guard Cells." *The Plant Journal: For Cell and Molecular Biology* 63 (6): 1054–62.

Miao, Yuxuan, Yao Cai, Hao Wu, and Dan Wang. 2021. "Diurnal and Seasonal Variations in the Photosynthetic Characteristics and the Gas Exchange Simulations of Two Rice Cultivars Grown at Ambient and Elevated CO2." *Frontiers in Plant Science* 12: 651606.

Mnich, Ewelina, Nanna Bjarnholt, Aymerick Eudes, Jesper Harholt, Claire Holland, Bodil Jørgensen, Flemming Hofmann Larsen, et al. 2020. "Phenolic Cross-Links: Building and de-Constructing the Plant Cell Wall." *Natural Product Reports* 37 (7): 919–61.

Moose, Stephen P., Nick Lauter, and Shawn R. Carlson. 2004. "The Maize Macrohairless1 Locus Specifically Promotes Leaf Blade Macrohair Initiation and Responds to Factors Regulating Leaf Identity." *Genetics* 166 (3): 1451–61.

Motulsky, Harvey J., and Ronald E. Brown. 2006. "Detecting Outliers When Fitting Data with Nonlinear Regression - a New Method Based on Robust Nonlinear Regression and the False Discovery Rate." *BMC Bioinformatics* 7 (March): 123.

Muller, Bertrand, Gildas Bourdais, Beat Reidy, Christelle Bencivenni, Agnès Massonneau, Pascal Condamine, Gaëlle Rolland, Geneviève Conéjéro, Peter Rogowsky, and François Tardieu.

2007. “Association of Specific Expansins with Growth in Maize Leaves Is Maintained under Environmental, Genetic, and Developmental Sources of Variation.” *Plant Physiology* 143 (1): 278–90.

Mumm, Patrick, Dennis Imes, Enrico Martinoia, Khaled A. S. Al-Rasheid, Dietmar Geiger, Irene Marten, and Rainer Hedrich. 2013. “C-Terminus-Mediated Voltage Gating of Arabidopsis Guard Cell Anion Channel QUAC1.” *Molecular Plant* 6 (5): 1550–63.

Mumm, Patrick, Thomas Wolf, Jörg Fromm, M. Rob G. Roelfsema, and Irene Marten. 2011. “Cell Type-Specific Regulation of Ion Channels within the Maize Stomatal Complex.” *Plant & Cell Physiology* 52 (8): 1365–75.

Munemasa, Shintaro, Felix Hauser, Jiyoung Park, Rainer Waadt, Benjamin Brandt, and Julian I. Schroeder. 2015. “Mechanisms of Abscisic Acid-Mediated Control of Stomatal Aperture.” *Current Opinion in Plant Biology* 28 (December): 154–62.

Murata, Yoshiyuki, Izumi C. Mori, and Shintaro Munemasa. 2015. “Diverse Stomatal Signaling and the Signal Integration Mechanism.” *Annual Review of Plant Biology* 66 (1): 369–92.

Nguyen, Thanh Hao, Shouguang Huang, Donaldo Meynard, Christian Chaine, Rémy Michel, M. Rob G. Roelfsema, Emmanuel Guiderdoni, Hervé Sentenac, and Anne-Aliénor Véry. 2017. “A Dual Role for the OsK5.2 Ion Channel in Stomatal Movements and K+ Loading into Xylem Sap.” *Plant Physiology* 174 (4): 2409–18.

Nieves-Cordones, Manuel, Farrukh Azeem, Yuchen Long, Martin Boeglin, Geoffrey Duby, Karine Mouline, Eric Hosy, et al. 2022. “Non-Autonomous Stomatal Control by Pavement Cell Turgor via the K+ Channel Subunit AtKC1.” *The Plant Cell*, koac038.

Niinemets, Ulo, Markus Reichstein, Michael Staudt, Günther Seufert, and John D. Tenhunen. 2002. “Stomatal Constraints May Affect Emission of Oxygenated Monoterpenoids from the Foliage of Pinus Pinea.” *Plant Physiology* 130 (3): 1371–85.

Nunes, Tiago, Paulo Cardoso, Rosa Freitas, and Etelvina Figueira. 2018. “Protective Effects of Farnesol on a Rhizobium Strain Exposed to Cadmium.” *Ecotoxicology and Environmental Safety* 165 (December): 622–29.

Nunes, Tiago D. G., Magdalena W. Slawinska, Heike Lindner, and Michael T. Raissig. 2022. "Quantitative Effects of Environmental Variation on Stomatal Anatomy and Gas Exchange in a Grass Model." *Quantitative Plant Biology* 3: e6.

Nunes, Tiago D. G., Zhang, Dan and Raissig, Michael T. 2020. "Form, Development and Function of Grass Stomata." *The Plant Journal: For Cell and Molecular Biology* 101 (4): 780–99.

Nurit-Silva, Kiriaki, Rafael Costa-Silva, Ionaldo J. L. D. Basílio, and Maria de Fátima Agra. 2012. "Leaf Epidermal Characters of Brazilian Species of Solanum Section Torva as Taxonomic Evidence." *Botany* 90 (9): 806–14.

Obiremi, E. O., and F. A. Oladele. 2001. "Water Conserving Stomatal Systems in Selected Citrus Species." *South African Journal of Botany: Official Journal of the South African Association of Botanists = Suid-Afrikaanse Tydskrif Vir Plantkunde: Amptelike Tydskrif van Die Suid-Afrikaanse Genootskap van Plantkundiges* 67 (2): 258–60.

Ormeño, E., J. P. Mévy, B. Vila, A. Bousquet-Mélou, S. Greff, G. Bonin, and C. Fernandez. 2007. "Water Deficit Stress Induces Different Monoterpene and Sesquiterpene Emission Changes in Mediterranean Species. Relationship between Terpene Emissions and Plant Water Potential." *Chemosphere* 67 (2): 276–84.

Papanatsiou, Maria, Anna Amtmann, and Michael R. Blatt. 2017. "Stomatal Clustering in Begonia Associates with the Kinetics of Leaf Gaseous Exchange and Influences Water Use Efficiency." *Journal of Experimental Botany* 68 (9): 2309–15.

Park, Sang-Youl, Pauline Fung, Noriyuki Nishimura, Davin R. Jensen, Hiroaki Fujii, Yang Zhao, Shelley Lumba, et al. 2009. "Abscisic Acid Inhibits Type 2C Protein Phosphatases via the PYR/PYL Family of START Proteins." *Science* 324 (5930): 1068–71.

Passardi, F., C. Cosio, C. Penel, and C. Dunand. 2005. "Peroxidases Have More Functions than a Swiss Army Knife." *Plant Cell Reports* 24 (5): 255–65.

Passardi, Filippo, David Longet, Claude Penel, and Christophe Dunand. 2004. "The Class III Peroxidase Multigenic Family in Rice and Its Evolution in Land Plants." *Phytochemistry* 65 (13): 1879–93.

Passardi, Filippo, Claude Penel, and Christophe Dunand. 2004. "Performing the Paradoxical: How Plant Peroxidases Modify the Cell Wall." *Trends in Plant Science* 9 (11): 534–40.

Penny, M. G., and D. J. Bowling. 1974. "A Study of Potassium Gradients in the Epidermis of Intact Leaves of Commelina Communis L. in Relation to Stomatal Opening." *Planta* 119 (1): 17–25.

Penny, M. G., L. S. Kelday, and D. J. Bowling. 1976. "Active Chloride Transport in the Leaf Epidermis of Commelina Communis in Relation to Stomatal Activity." *Planta* 130 (3): 291–94.

Pichersky, Eran, and Robert A. Raguso. 2018. "Why Do Plants Produce so Many Terpenoid Compounds?" *The New Phytologist* 220 (3): 692–702.

Pillitteri, Lynn Jo, and Juan Dong. 2013. "Stomatal Development in Arabidopsis." *The Arabidopsis Book / American Society of Plant Biologists* 11 (June): e0162.

Pitaloka, Mutiara K., Emily L. Harrison, Christopher Hepworth, Samart Wanchana, Theerayut Toojinda, Watchara Phetluan, Robert A. Brench, et al. 2021. "Rice Stomatal Mega-Papillae Restrict Water Loss and Pathogen Entry." *Frontiers in Plant Science* 12 (June): 677839.

Postiglione, Anthony E., and Gloria K. Muday. 2020. "The Role of ROS Homeostasis in ABA-Induced Guard Cell Signaling." *Frontiers in Plant Science* 11 (June): 968.

Qi, Guo-Ning, Fen-Yong Yao, Hui-Min Ren, Shu-Jing Sun, Yan-Qiu Tan, Zhong-Chun Zhang, Bao-Sheng Qiu, and Yong-Fei Wang. 2018. "The S-Type Anion Channel ZmSLAC1 Plays Essential Roles in Stomatal Closure by Mediating Nitrate Efflux in Maize." *Plant and Cell Physiology* 59 (3): 614–23.

Ragel, Paula, Reyes Ródenas, Elena García-Martín, Zaida Andrés, Irene Villalta, Manuel Nieves-Cordones, Rosa M. Rivero, et al. 2015. "CIPK23 Regulates HAK5-Mediated High-Affinity K Uptake in Arabidopsis Roots." *Plant Physiology* 169 (4): 2863-2873.

Raissig, M. T., J. L. Matos, M. X. A. Gil, and A. Kornfeld. 2017. "Mobile MUTE Specifies Subsidiary Cells to Build Physiologically Improved Grass Stomata." *Science* 355 (6330): 1215-1218.

Raissig, Michael T., Emily Abrash, Akhila Bettadapur, John P. Vogel, and Dominique C. Bergmann. 2016. "Grasses Use an Alternatively Wired BHLH Transcription Factor Network to Establish Stomatal Identity." *Proceedings of the National Academy of Sciences of the United States of America* 113 (29): 8326–31.

Raissig, Michael T., and Daniel P. Woods. 2022. "The Wild Grass Brachypodium Distachyon as a Developmental Model System." *Current Topics in Developmental Biology* 147 (March): 33–71.

Rancour, David M., Jane M. Marita, and Ronald D. Hatfield. 2012. "Cell Wall Composition throughout Development for the Model Grass Brachypodium Distachyon." *Frontiers in Plant Science* 3 (December): 266.

Ranjan, Aashish, Stephen Dickopf, Kristian K. Ullrich, Stefan A. Rensing, and Ute Hoecker. 2014. "Functional Analysis of COP1 and SPA Orthologs from Physcomitrella and Rice during Photomorphogenesis of Transgenic Arabidopsis Reveals Distinct Evolutionary Conservation." *BMC Plant Biology* 14 (1): 178.

Raschke, K., and M. P. Fellows. 1971. "Stomatal Movement in Zea Mays: Shuttle of Potassium and Chloride between Guard Cells and Subsidiary Cells." *Planta* 101 (4): 296–316.

Resco de Dios, Víctor. 2017. "Circadian Regulation and Diurnal Variation in Gas Exchange." *Plant Physiology* 175 (1): 3–4.

Rho, Hyungmin, Victor Van Epps, Nicholas Wegley, Sharon L. Doty, and Soo-Hyung Kim. 2018. "Salicaceae Endophytes Modulate Stomatal Behavior and Increase Water Use Efficiency in Rice." *Frontiers in Plant Science* 9 (March): 188.

Roelfsema, M. Rob G., Stefan Hanstein, Hubert H. Felle, and Rainer Hedrich. 2002. "CO2 Provides an Intermediate Link in the Red Light Response of Guard Cells." *The Plant Journal: For Cell and Molecular Biology* 32 (1): 65–75.

Roelfsema, M. Rob G., and Rainer Hedrich. 2002. "Studying Guard Cells in the Intact Plant: Modulation of Stomatal Movement by Apoplastic Factors." *The New Phytologist* 153 (3): 425–31.

Rogers, Louisa A., and Malcolm M. Campbell. 2004. "The Genetic Control of Lignin Deposition during Plant Growth and Development." *The New Phytologist* 164 (1): 17–30.

Ronzier, Elsa, Claire Corratgé-Faillie, Frédéric Sanchez, Karine Prado, Christian Brière, Nathalie Leonhardt, Jean-Baptiste Thibaud, and Tou Cheu Xiong. 2014. "CPK13, a Noncanonical Ca2+-Dependent Protein Kinase, Specifically Inhibits KAT2 and KAT1 Shaker K+ Channels and Reduces Stomatal Opening." *Plant Physiology* 166 (1): 314–26.

Rosenzweig, Cynthia, Joshua Elliott, Delphine Deryng, Alex C. Ruane, Christoph Müller, Almut Arneth, Kenneth J. Boote, et al. 2014. "Assessing Agricultural Risks of Climate Change in the 21st Century in a Global Gridded Crop Model Intercomparison." *Proceedings of the National Academy of Sciences of the United States of America* 111 (9): 3268–73.

Roussel, Magali, Erwin Dreyer, Pierre Montpied, Grégoire Le-Provost, Jean-Marc Guehl, and Oliver Brendel. 2009. "The Diversity of 13C Isotope Discrimination in a Quercus Robur Full-Sib Family Is Associated with Differences in Intrinsic Water Use Efficiency, Transpiration Efficiency, and Stomatal Conductance." *Journal of Experimental Botany* 60 (8): 2419-2431.

Rui, Yue, Yintong Chen, Baris Kandemir, Hojae Yi, James Z. Wang, Virendra M. Puri, and Charles T. Anderson. 2018. "Balancing Strength and Flexibility: How the Synthesis, Organization, and Modification of Guard Cell Walls Govern Stomatal Development and Dynamics." *Frontiers in Plant Science* 9 (August): 1202.

Rui, Yue, Chaowen Xiao, Hojae Yi, Baris Kandemir, James Z. Wang, Virendra M. Puri, and Charles T. Anderson. 2017. "POLYGALACTURONASE INVOLVED IN EXPANSION3 Functions in Seedling Development, Rosette Growth, and Stomatal Dynamics in Arabidopsis Thaliana." *The Plant Cell* 29 (10): 2413–32.

Sabillón, Danelia, and Lázaro V. Cremades. 2001. "Diurnal and Seasonal Variation of Monoterpene Emission Rates for Two Typical Mediterranean Species (Pinus Pinea and Quercus Ilex) from Field Measurements—Relationship with Temperature and PAR." *Atmospheric Environment* 35(25): 4419-4431.

Saez, Angela, Nadia Robert, Mohammad H. Maktabi, Julian I. Schroeder, Ramón Serrano, and Pedro L. Rodriguez. 2006. "Enhancement of Abscisic Acid Sensitivity and Reduction of Water Consumption in Arabidopsis by Combined Inactivation of the Protein Phosphatases Type 2C ABI1 and HAB1." *Plant Physiology* 141(4): 1389-1399.

Sakoda, Kazuma, Wataru Yamori, Tomoo Shimada, Shigeo S. Sugano, Ikuko Hara-Nishimura, and Yu Tanaka. 2020. "Higher Stomatal Density Improves Photosynthetic Induction and Biomass Production in Arabidopsis Under Fluctuating Light." *Frontiers in Plant Science* 11 (October): 589603.

Sampaio, V. S., N. D. Araújo, and M. F. Agra. 2014. "Characters of Leaf Epidermis in Solanum (Clade Brevantherum) Species from Atlantic Forest of Northeastern Brazil." *South African Journal of Botany: Official Journal of the South African Association of Botanists = Suid-Afrikaanse Tydskrif Vir Plantkunde: Amptelike Tydskrif van Die Suid-Afrikaanse Genootskap van Plantkundiges* 94 (September): 108–13.

Sasaki, Takayuki, Izumi C. Mori, Takuya Furuichi, Shintaro Munemasa, Kiminori Toyooka, Ken Matsuoka, Yoshiyuki Murata, and Yoko Yamamoto. 2010. "Closing Plant Stomata Requires a Homolog of an Aluminum-Activated Malate Transporter." *Plant & Cell Physiology* 51 (3): 354–65.

Sato, Aiko, Yuki Sato, Yoichiro Fukao, Masayuki Fujiwara, Taishi Umezawa, Kazuo Shinozaki, Takao Hibi, et al. 2009. "Threonine at Position 306 of the KAT1 Potassium Channel Is Essential for Channel Activity and Is a Target Site for ABA-Activated SnRK2/OST1/SnRK2.6 Protein Kinase." *Biochemical Journal* 424 (3): 439–48.

Schäfer, Nadine, Tobias Maierhofer, Johannes Herrmann, Morten Egevang Jørgensen, Christof Lind, Katharina von Meyer, Silke Lautner, et al. 2018. "A Tandem Amino Acid Residue Motif in Guard Cell SLAC1 Anion Channel of Grasses Allows for the Control of Stomatal Aperture by Nitrate." *Current Biology: CB* 28 (9): 1370-1379.e5.

Scharwies, Johannes Daniel, and José R. Dinneny. 2019. "Water Transport, Perception, and Response in Plants." *Journal of Plant Research* 132 (3): 311–24.

Seidl-Adams, I., A. Richter, K. B. Boomer, N. Yoshinaga, J. Degenhardt, and J. H. Tumlinson. 2015. "Emission of Herbivore Elicitor-Induced Sesquiterpenes Is Regulated by Stomatal Aperture in Maize (Zea Mays) Seedlings." *Plant, Cell and Environment* 38 (1): 23–34.

Serna, Laura. 2021. "The Role of Grass MUTE Orthologs in GMC Progression and GC Morphogenesis." *Frontiers in Plant Science* 12 (June): 678417.

Sexauer, Moritz, Defeng Shen, Maria Schön, Tonni Grube Andersen, and Katharina Markmann. 2021. "Visualizing Polymeric Components That Define Distinct Root Barriers across Plant Lineages." *Development* 148 (23): dev199820.

Shah, G. L., and B. V. Gopal. 1969. "Development of Stomata in Some Papilionaceae." *Canadian Journal of Botany* 47(3): 387-393.

Shigeto, Jun, and Yuji Tsutsumi. 2016. "Diverse Functions and Reactions of Class III Peroxidases." *The New Phytologist* 209 (4): 1395–1402.

Shimizu, Takafumi, Yuri Kanno, Hiromi Suzuki, Shunsuke Watanabe, and Mitsunori Seo. 2021. "Arabidopsis NPF4.6 and NPF5.1 Control Leaf Stomatal Aperture by Regulating Abscisic Acid Transport." *Genes*. 12 (6): 885.

Shtein, Ilana, Yaniv Shelef, Ziv Marom, Einat Zelinger, Amnon Schwartz, Zoë A. Popper, Benny Bar-On, and Smadar Harpaz-Saad. 2017. "Stomatal Cell Wall Composition: Distinctive Structural Patterns Associated with Different Phylogenetic Groups." *Annals of Botany* 119 (6): 1021–33.

Sierla, Maija, Hanna Hõrak, Kirk Overmyer, Cezary Waszczak, Dmitry Yarmolinsky, Tobias Maierhofer, Julia P. Vainonen, et al. 2018. "The Receptor-like Pseudokinase GHR1 Is Required for Stomatal Closure." *The Plant Cell* 30 (11): 2813–37.

Sierla, Maija, Cezary Waszczak, Triin Vahisalu, and Jaakko Kangasjärvi. 2016. "Reactive Oxygen Species in the Regulation of Stomatal Movements." *Plant Physiology* 171 (3): 1569–80.

Singh, Rachana, Parul Parihar, Samiksha Singh, Rohit Kumar Mishra, Vijay Pratap Singh, and Sheo Mohan Prasad. 2017. "Reactive Oxygen Species Signaling and Stomatal Movement: Current Updates and Future Perspectives." *Redox Biology* 11 (April): 213–18.

Sonawane, Balasaheb V., Nuria K. Koteyeva, Daniel M. Johnson, and Asaph B. Cousins. 2021. "Differences in Leaf Anatomy Determines Temperature Response of Leaf Hydraulic and Mesophyll CO 2 Conductance in Phylogenetically Related C 4 and C 3 Grass Species." *New Phytologist* 230 (5): 1802-1814.

Spiegelhalder, Roxane P., and Michael T. Raissig. 2021. "Morphology Made for Movement: Formation of Diverse Stomatal Guard Cells." *Current Opinion in Plant Biology* 63 (October): 102090.

Stangl, Zsofia R., Lasse Tarvainen, Göran Wallin, Nerea Ubierna, Mats Räntfors, and John D. Marshall. 2019. "Diurnal Variation in Mesophyll Conductance and Its Influence on Modelled Water-Use Efficiency in a Mature Boreal Pinus Sylvestris Stand." *Photosynthesis Research* 141 (1): 53–63.

Stebbins, G. L., and S. S. Shah. 1960. "Developmental Studies of Cell Differentiation in the Epidermis of Monocotyledons: II. Cytological Features of Stomatal Development in the Gramineae." *Developmental Biology* 2 (6): 477–500.

Strömberg, Caroline A. E., Verónica S. Di Stilio, and Zhaoliang Song. 2016. "Functions of Phytoliths in Vascular Plants: An Evolutionary Perspective." *Functional Ecology* 30 (8): 1286–97.

Suh, Su Jeoung, Yong-Fei Wang, Annie Frelet, Nathalie Leonhardt, Markus Klein, Cyrille Forestier, Bernd Mueller-Roeber, Myeon H. Cho, Enrico Martinoia, and Julian I. Schroeder. 2007. "The ATP Binding Cassette Transporter AtMRP5 Modulates Anion and Calcium Channel Activities in Arabidopsis Guard Cells." *The Journal of Biological Chemistry* 282 (3): 1916–24.

Sun, Guiling, Mingzhang Xia, Jieping Li, Wen Ma, Qingzeng Li, Jinjin Xie, Shenglong Bai, et al. 2022. "The Maize Single-Nucleus Transcriptome Comprehensively Describes Signaling Networks Governing Movement and Development of Grass Stomata." *The Plant Cell*, February, koac047.

Sun, Shenshen, Wenqiang Fan, and Zixin Mu. 2017. "The Spatio-Temporal Specificity of PYR1/PYL/RCAR ABA Receptors in Response to Developmental and Environmental Cues." *Plant Signaling and Behavior* 12 (11): e1214793.

Sun, Shu-Jing, Guo-Ning Qi, Qi-Fei Gao, Hui-Qin Wang, Fen-Yong Yao, Jamshaid Hussain, and Yong-Fei Wang. 2016. "Protein Kinase OsSAPK8 Functions as an Essential Activator of S-Type Anion Channel OsSLAC1, Which Is Nitrate-Selective in Rice." *Planta* 243 (2): 489–500.

Sun, Wenqiang, Dawei Gao, Yin Xiong, Xinxin Tang, Xiongfeng Xiao, Chongrong Wang, and Sibin Yu. 2017. "Hairy Leaf 6, an AP2/ERF Transcription Factor, Interacts with OsWOX3B and Regulates Trichome Formation in Rice." *Molecular Plant* 10 (11): 1417–33.

Sun, Yanqi, Fei Yan, Xiaoyong Cui, and Fulai Liu. 2014. "Plasticity in Stomatal Size and Density of Potato Leaves under Different Irrigation and Phosphorus Regimes." *Journal of Plant Physiology* 171 (14): 1248–55.

Takeshima, Akira, Hyungjun Kim, Hideo Shiogama, Ludwig Lierhammer, John F. Scinocca, Øyvind Seland, and Dann Mitchell. 2020. "Global Aridity Changes Due to Differences in Surface Energy and Water Balance between 1.5 °C and 2 °C Warming." *Environmental Research Letters: ERL [Web Site]* 15 (9): 0940a7.

Takeuchi, Jun, Masanori Okamoto, Ryosuke Mega, Yuri Kanno, Toshiyuki Ohnishi, Mitsunori Seo, and Yasushi Todoroki. 2016. "Abscinazole-E3M, a Practical Inhibitor of Abscisic Acid 8'-Hydroxylase for Improving Drought Tolerance." *Scientific Reports* 6 (November): 37060.

Toda, Yosuke, Yin Wang, Akira Takahashi, Yuya Kawai, Yasuomi Tada, Naoki Yamaji, Jian Feng Ma, Motoyuki Ashikari, and Toshinori Kinoshita. 2016. "Oryza Sativa H + -ATPase (OSA) Is Involved in the Regulation of Dumbbell-Shaped Guard Cells of Rice." *Plant & Cell Physiology* 57 (6): 1220–30.

Tognolli, Michael, Claude Penel, Hubert Greppin, and Patrice Simon. 2002. "Analysis and Expression of the Class III Peroxidase Large Gene Family in Arabidopsis Thaliana." *Gene* 288 (1–2): 129–38.

Tokunaga, Naohito, Tsuyoshi Kaneta, Seiichi Sato, and Yasushi Sato. 2009. "Analysis of Expression Profiles of Three Peroxidase Genes Associated with Lignification in Arabidopsis Thaliana." *Physiologia Plantarum* 136 (2): 237–49.

Toreti, Andrea, Davide Bavera, Carmelo Cammalleri, Tania Cota, Alfred de Jager, Ricardo Deus, Chiara Di Ciollo, et al. 2022. *Drought in Western Mediterranean February 2022*. Luxembourg: EUR 31026 EN, Publications Office of the European Union.

Torii, Keiko U. 2021. "Stomatal Development in the Context of Epidermal Tissues." *Annals of Botany* 128 (2): 137-148.

Umezawa, Taishi, Naoyuki Sugiyama, Masahide Mizoguchi, Shimpei Hayashi, Fumiyoshi Myouga, Kazuko Yamaguchi-Shinozaki, Yasushi Ishihama, Takashi Hirayama, and Kazuo Shinozaki. 2009. "Type 2C Protein Phosphatases Directly Regulate Abscisic Acid-Activated Protein Kinases in Arabidopsis." *Proceedings of the National Academy of Sciences of the United States of America* 106 (41): 17588–93.

Urban, Josef, Miles Ingwers, Mary Anne McGuire, and Robert O. Teskey. 2017a. "Stomatal Conductance Increases with Rising Temperature." *Plant Signaling and Behavior* 12 (8): e1356534.

Urban, Josef, Miles W. Ingwers, Mary Anne McGuire, and Robert O. Teskey. 2017b. "Increase in Leaf Temperature Opens Stomata and Decouples Net Photosynthesis from Stomatal Conductance in Pinus Taeda and Populus Deltoides x Nigra." *Journal of Experimental Botany* 68 (7): 1757–67.

Ursache, Robertas, Tonni Grube Andersen, Peter Marhavý, and Niko Geldner. 2018. "A Protocol for Combining Fluorescent Proteins with Histological Stains for Diverse Cell Wall Components." *The Plant Journal: For Cell and Molecular Biology* 93 (2): 399–412.

Vahisalu, Triin, Hannes Kollist, Yong-Fei Wang, Noriyuki Nishimura, Wai-Yin Chan, Gabriel Valerio, Airi Lamminmäki, et al. 2008. "SLAC1 Is Required for Plant Guard Cell S-Type Anion Channel Function in Stomatal Signalling." *Nature* 452: 487-491.

Vahisalu, Triin, Irina Puzõrjova, Mikael Brosché, Ervin Valk, Martin Lepiku, Heino Moldau, Priit Pechter, et al. 2010. "Ozone-Triggered Rapid Stomatal Response Involves the Production of Reactive Oxygen Species, and Is Controlled by SLAC1 and OST1." *The Plant Journal: For Cell and Molecular Biology* 62 (3): 442–53.

Vernoud, Vanessa, Guillaume Laigle, Frédérique Rozier, Robert B. Meeley, Pascual Perez, and Peter M. Rogowsky. 2009. "The HD-ZIP IV Transcription Factor OCL4 Is Necessary for Trichome Patterning and Anther Development in Maize." *The Plant Journal* 59 (6): 883-894.

Vinnakota, Rajesh, Anantha Maharasi Ramakrishnan, A. Samdani, M. Anjali Venugopal, B. Sri Ram, S. Navaneetha Krishnan, Dhandapani Murugesan, and Kavitha Sankaranarayanan. 2016. "A Comparison of Aquaporin Function in Mediating Stomatal Aperture Gating among Drought-Tolerant and Sensitive Varieties of Rice (Oryza Sativa L.)." *Protoplasma* 253 (6): 1593–97.

Voelker, Camilla, Diana Schmidt, Bernd Mueller-Roeber, and Katrin Czempinski. 2006. "Members of the Arabidopsis AtTPK/KCO Family Form Homomeric Vacuolar Channels in Planta." *The Plant Journal: For Cell and Molecular Biology* 48 (2): 296–306.

Vogel, John. 2008. "Unique Aspects of the Grass Cell Wall." *Current Opinion in Plant Biology* 11 (3): 301–7.

Vogel, John P. 2016. "The Rise of Brachypodium as a Model System." In *Genetics and Genomics of Brachypodium*, edited by John P. Vogel, 1–7. Cham: Springer International Publishing.

Wang, Chung-Yi, Yu-Wei Chen, and Chih-Yao Hou. 2019. "Antioxidant and Antibacterial Activity of Seven Predominant Terpenoids." *International Journal of Food Properties* 22 (1): 230–38.

Wang, Hai, Shijuan Yan, Hongjia Xin, Wenjie Huang, Hao Zhang, Shouzhen Teng, Ya-Chi Yu, et al. 2019. "A Subsidiary Cell-Localized Glucose Transporter Promotes Stomatal Conductance and Photosynthesis." *The Plant Cell* 31 (6): 1328–43.

Wang, Haibo, Shuang Zhao, Ke Mao, Qinglong Dong, Bowen Liang, Chao Li, Zhiwei Wei, Mingjun Li, and Fengwang Ma. 2018. "Mapping QTLs for Water-Use Efficiency Reveals the Potential Candidate Genes Involved in Regulating the Trait in Apple under Drought Stress." *BMC Plant Biology* 18 (1): 136.

Wang, Hongliang, Siyi Guo, Xin Qiao, Jianfei Guo, Zuliang Li, Yusen Zhou, Shenglong Bai, et al. 2019. "BZU2/ZmMUTE Controls Symmetrical Division of Guard Mother Cell and Specifies Neighbor Cell Fate in Maize." *PLoS Genetics* 15 (8): e1008377.

Wang, Xuening, Shuo Lv, Xiangyu Han, Xiongjuan Guan, Xiong Shi, Jingke Kang, Luosha Zhang, et al. 2019. "The Calcium-Dependent Protein Kinase CPK33 Mediates Strigolactone-Induced Stomatal Closure in Arabidopsis Thaliana." *Frontiers in Plant Science* 10 (December): 1630.

Wei, Hongbin, Dexin Kong, Juan Yang, and Haiyang Wang. 2020. "Light Regulation of Stomatal Development and Patterning: Shifting the Paradigm from Arabidopsis to Grasses." *Plant Communications* 1 (2): 100030.

Wei, Pengcheng, Su Chen, Xiuqing Zhang, Ping Zhao, Yanmei Xiong, Wenlong Wang, Jia Chen, and Xuechen Wang. 2011. "An α-Expansin, VfEXPA1, Is Involved in Regulation of Stomatal Movement in Vicia Faba L." *Chinese Science Bulletin = Kexue Tongbao* 56 (33): 3531–37.

Wei, Peng-Cheng, Xiu-Qing Zhang, Ping Zhao, and Xue-Chen Wang. 2011. "Regulation of Stomatal Opening by the Guard Cell Expansin AtEXPA1." *Plant Signaling & Behavior* 6 (5): 740–42.

Wei, Shuya, Wei Hu, Xiaomin Deng, Yingying Zhang, Xiaodong Liu, Xudong Zhao, Qingchen Luo, et al. 2014. "A Rice Calcium-Dependent Protein Kinase OsCPK9 Positively Regulates Drought Stress Tolerance and Spikelet Fertility." *BMC Plant Biology* 14 (May): 133.

Worthen, Jennifer M., Maria V. Yamburenko, Jeewoo Lim, Zachary L. Nimchuk, Joseph J. Kieber, and G. Eric Schaller. 2019. "Type-B Response Regulators of Rice Play Key Roles in Growth, Development and Cytokinin Signaling." *Development* 146 (13): dev174870.

Wu, Alex, Graeme L. Hammer, Al Doherty, Susanne von Caemmerer, and Graham D. Farquhar. 2019. "Quantifying Impacts of Enhancing Photosynthesis on Crop Yield." *Nature Plants* 5 (4): 380–88.

Wu, Qiqi, Mei Wang, Jianlin Shen, Donghua Chen, Yu Zheng, and Wei Zhang. 2019. "ZmOST1 Mediates Abscisic Acid Regulation of Guard Cell Ion Channels and Drought Stress Responses." *Journal of Integrative Plant Biology* 61 (4): 478–91.

Wu, Xingwen, Antony Bacic, Kim L. Johnson, and John Humphries. 2020. "The Role of Brachypodium Distachyon Wall-Associated Kinases (WAKs) in Cell Expansion and Stress Responses." *Cells* 9 (11): 2478.

Wu, Zhongliang, Liang Chen, Qi Yu, Wenqi Zhou, Xiaoping Gou, Jia Li, and Suiwen Hou. 2019. "Multiple Transcriptional Factors Control Stomata Development in Rice." *The New Phytologist* 223 (1): 220–32.

Xiang, Yang, Xiujuan Sun, Xiangli Bian, Tianhui Wei, Tong Han, Jingwei Yan, and Aying Zhang. 2020. "The Transcription Factor ZmNAC49 Reduces Stomatal Density and Improves Drought Tolerance in Maize." *Journal of Experimental Botany* 72 (4): 1399–1410.

Xiong, Zhuang, Dongliang Xiong, Detian Cai, Wei Wang, Kehui Cui, Shaobing Peng, and Jianliang Huang. 2022. "Effect of Stomatal Morphology on Leaf Photosynthetic Induction under Fluctuating Light across Diploid and Tetraploid Rice." *Environmental and Experimental Botany* 194(2022): 104757.

Xu, Muyun, Benjamin D. Gruber, Emmanuel Delhaize, Rosemary G. White, Richard A. James, Jiangfeng You, Zhenming Yang, and Peter R. Ryan. 2015. "The Barley Anion Channel, HvALMT1, Has Multiple Roles in Guard Cell Physiology and Grain Metabolism." *Physiologia Plantarum* 153 (1): 183–93.

Xu, Zhenzhu, and Guangsheng Zhou. 2008. "Responses of Leaf Stomatal Density to Water Status and Its Relationship with Photosynthesis in a Grass." *Journal of Experimental Botany* 59 (12): 3317–25.

Yamasaki, Takenobu, Tomokazu Yamakawa, Yoshihiro Yamane, Hiroyuki Koike, Kazuhiko Satoh, and Sakae Katoh. 2002. "Temperature Acclimation of Photosynthesis and Related Changes in Photosystem II Electron Transport in Winter Wheat." *Plant Physiology* 128 (3): 1087–97.

Yamauchi, Shota, Atsushi Takemiya, Tomoaki Sakamoto, Tetsuya Kurata, Toshifumi Tsutsumi, Toshinori Kinoshita, and Ken-Ichiro Shimazaki. 2016. "The Plasma Membrane H -ATPase AHA1 Plays a Major Role in Stomatal Opening in Response to Blue Light." *Plant Physiology* 171 (4): 2731-2743.

Yamori, Wataru, Kensaku Suzuki, K. O. Noguchi, Masato Nakai, and Ichiro Terashima. 2006. "Effects of Rubisco Kinetics and Rubisco Activation State on the Temperature Dependence of the Photosynthetic Rate in Spinach Leaves from Contrasting Growth Temperatures." *Plant, Cell and Environment* 29 (8): 1659-1670.

Yan, Longfeng, Xi Cheng, Ruiling Jia, Qianqian Qin, Liping Guan, Hang Du, and Suiwen Hou. 2014. "New Phenotypic Characteristics of Three Tmm Alleles in Arabidopsis Thaliana." *Plant Cell Reports* 33 (5): 719–31.

Yaneff, Agustín, Victoria Vitali, and Gabriela Amodeo. 2015. "PIP1 Aquaporins: Intrinsic Water Channels or PIP2 Aquaporin Modulators?" *FEBS Letters* 589 (23): 3508–15.

Yang, Xuanshong, Jiazheng Yuan, Wenbin Luo, Mingyue Qin, Jiahan Yang, Weiren Wu, and Xiaofang Xie. 2020. "Genome-Wide Identification and Expression Analysis of the Class III Peroxidase Gene Family in Potato (Solanum Tuberosum L.)." *Frontiers in Genetics* 11 (December): 593577.

Yao, Lingya, Xuan Cheng, Zongying Gu, Wei Huang, Shou Li, Linbo Wang, Yong-Fei Wang, Ping Xu, Hong Ma, and Xiaochun Ge. 2018. "The AWPM-19 Family Protein OsPM1 Mediates Abscisic Acid Influx and Drought Response in Rice." *The Plant Cell* 30 (6): 1258–76.

Yao, Yaqin, Xiping Liu, Zhenzhen Li, Xufeng Ma, Heinz Rennenberg, Xin Wang, and Haichao Li. 2013. "Drought-Induced H2O 2 Accumulation in Subsidiary Cells Is Involved in Regulatory Signaling of Stomatal Closure in Maize Leaves." *Planta* 238 (1): 217–27.

Ye, Wenxiu, Daichi Muroyama, Shintaro Munemasa, Yoshimasa Nakamura, Izumi C. Mori, and Yoshiyuki Murata. 2013. "Calcium-Dependent Protein Kinase CPK6 Positively Functions in Induction by Yeast Elicitor of Stomatal Closure and Inhibition by Yeast Elicitor of Light-Induced Stomatal Opening in Arabidopsis." *Plant Physiology* 163 (2): 591-599.

You, Jun, Wei Zong, Honghong Hu, Xianghua Li, Jinghua Xiao, and Lizhong Xiong. 2014. "A STRESS-RESPONSIVE NAC1-Regulated Protein Phosphatase Gene Rice *Protein Phosphatase18* Modulates Drought and Oxidative Stress Tolerance through Abscisic Acid-Independent Reactive Oxygen Species Scavenging in Rice." *Plant Physiology* 166 (4): 2100-2114

You, Jun, Wei Zong, Xiaokai Li, Jing Ning, Honghong Hu, Xianghua Li, Jinghua Xiao, and Lizhong Xiong. 2013. "The SNAC1-Targeted Gene OsSRO1c Modulates Stomatal Closure and Oxidative Stress Tolerance by Regulating Hydrogen Peroxide in Rice." *Journal of Experimental Botany* 64 (2): 569–83.

Zandalinas, Sara I., Itay Hamus Cohen, Felix B. Fritschi, and Ron Mittler. 2020. "Coordinated Systemic Stomatal Responses in Soybean." *Plant Physiology* 183 (4): 1428–31.

Zhang, An, Hui-Min Ren, Yan-Qiu Tan, Guo-Ning Qi, Fen-Yong Yao, Gui-Li Wu, Lu-Wen Yang, Jamshaid Hussain, Shu-Jing Sun, and Yong-Fei Wang. 2016. "S-Type Anion Channels SLAC1 and SLAH3 Function as Essential Negative Regulators of Inward K+ Channels and Stomatal Opening in Arabidopsis." *The Plant Cell* 28 (4): 949–55.

Zhang, Bo, Bernadette Sztojka, Sacha Escamez, Ruben Vanholme, Mattias Hedenström, Yin Wang, Halbay Turumtay, András Gorzsás, Wout Boerjan, and Hannele Tuominen. 2020. "PIRIN2 Suppresses S-Type Lignin Accumulation in a Noncell-Autonomous Manner in Arabidopsis Xylem Elements." *The New Phytologist* 225 (5): 1923–35.

Zhang, Guangqiang, Junjiao Yang, Xiaoyu Zhao, Qinxue Li, Yunzhen Wu, Fangyuan Li, Yong Wang, Qunqun Hao, and Wei Wang. 2021. "Wheat TaPUB1 Protein Mediates ABA

Response and Seed Development through Ubiquitination." *Plant Science: An International Journal of Experimental Plant Biology* 309 (August): 110913.

Zhang, Li, Dongyang Li, Yaqin Yao, and Suiqi Zhang. 2020. "H2O2, Ca2+, and K+ in Subsidiary Cells of Maize Leaves Are Involved in Regulatory Signaling of Stomatal Movement." *Plant Physiology and Biochemistry: PPB / Societe Francaise de Physiologie Vegetale* 152 (July): 243–51.

Zhang, Lirong, Shiping Wang, Xiaoxia Yang, Xiaoyong Cui, and Haishan Niu. 2021. "An Intrinsic Geometric Constraint on Morphological Stomatal Traits." *Frontiers in Plant Science* 12: 628.

Zhang, Qiangqiang, Shaobing Peng, and Yong Li. 2019. "Increase Rate of Light-Induced Stomatal Conductance Is Related to Stomatal Size in the Genus Oryza." *Journal of Experimental Botany* 70 (19): 5259–69.

Zhang, Xiu-Qing, Peng-Cheng Wei, Yan-Mei Xiong, Yi Yang, Jia Chen, and Xue-Chen Wang. 2011. "Overexpression of the Arabidopsis α-Expansin Gene AtEXPA1 Accelerates Stomatal Opening by Decreasing the Volumetric Elastic Modulus." *Plant Cell Reports* 30 (1): 27–36.

Zhao, Daqiu, Yuting Luan, Xing Xia, Wenbo Shi, Yuhan Tang, and Jun Tao. 2020. "Lignin Provides Mechanical Support to Herbaceous Peony (Paeonia Lactiflora Pall.) Stems." *Horticulture Research* 7 (1): 213.

Zhou, Haoran, Ming Xu, Hongli Pan, and Xiubo Yu. 2015. "Leaf-Age Effects on Temperature Responses of Photosynthesis and Respiration of an Alpine Oak, Quercus Aquifolioides, in Southwestern China." *Tree Physiology* 35 (11): 1236–48.

Zhu, Ting, Fang Xin, Shuwei Wei, Yue Liu, Yucui Han, Jiao Xie, Qin Ding, and Lingjian Ma. 2019. "Genome-Wide Identification, Phylogeny and Expression Profiling of Class III Peroxidases Gene Family in Brachypodium Distachyon." *Gene* 700 (March): 149–62.